STRENGTHENING OF BRICK INFILLED RC FRAMES WITH DIFFERENT ASPECT RATIOS BY MEANS OF CFRP OVERLAYS

by

Savaş Atmaca

B.S., in Civil Engineering, Dokuz Eylul University, 1997

M.S., in Civil Engineering, Boğaziçi University, 2001

Submitted to the Institute for Graduate Studies in
Science and Engineering in partial fulfillment of
the requirements for the degree of
Doctor of Philosophy

Graduate Program in Civil Engineering

Boğaziçi University

2008

To my dearest family

ACKNOWLEDGEMENTS

I would like to express my sincere gratitude to Assistant Prof. Dr. Şevket Özden of Kocaeli University for his help, encouragement and continuous support throughout this dissertation. It would be very difficult to finish this dissertation without his invaluable contribution and great experience.

I owe special thanks to Prof. Dr. Cengiz Karakoç of Bogazici University for his guidance, endless help and generous support throughout this dissertation. I also would like to thank to him for managing BU Scientific Research Fund Projects (03HA401, 04A403D and 05A403).

I am also grateful to the members of my thesis committee, Prof. Dr. Turan Özturan, Prof. Dr. Serap Kahraman of Dokuz Eylul University, Assistant Prof. Dr. Cem Yalçın, and Assistant Prof. Dr. Kutay Orakçal for their suggestions, encouragement and criticism.

I would like to thank BU Structures Laboratory research assistants and technicians for their assistance during the strengthening procedure of the specimens and tests. I am grateful to Osman Kaya for his support and friendship throughout the tests.

I am indebted to my dear friend L. Christina Heath for her support, friendship, and proofreading skills. A special thanks to my dear friend Halim Alanyalı for his support and encouragement.

Finally, I would like to thank my dad, my mom and my sister for their endless help, support, encouragement and love.

ABSTRACT

STRENGTHENING OF BRICK INFILLED RC FRAMES WITH DIFFERENT ASPECT RATIOS BY MEANS OF CFRP OVERLAYS

The effects of aspect ratio on the engineering properties (stiffness, strength, energy dissipation, ductility…etc.) of infilled RC frames with or without CFRP were evaluated experimentally and analytically. Ten single-bay, two-story specimens at 1/3 scale were tested in a vertical position under quasi-static reversed cyclic seismic loading. Vertical and lateral loads were applied concurrently. Two out of ten specimens were control specimens (with no CFRP) and the rest of them were strengthened with CFRP unidirectional overlays in various configurations. The specimens had some deficiencies commonly seen in pre-1998 Turkish construction. The specimens had detailing deficiencies; such as insufficient confinement, 90^0 hooks, no transverse reinforcement in the joints, design deficiencies; such as weak column-strong beam, and construction deficiencies; such as poor material quality, and inadequate lap splice length. To eliminate the existing deficiencies of the specimens and improve their seismic performance, unidirectional CFRP overlays were applied in the form of vertical strips and/or cross diagonals on both sides of the infill panel and anchored to the surrounding RC frames. Local rehabilitation techniques such as confinement of the frame members were also used for some of the specimens. The application of CFRP overlays improved the load carrying capacity and the energy dissipation capacity significantly. Generally, as the peak loads increased, their corresponding drifts also increased. Some stiffness improvements were also recorded depending on the configuration of the CFRP overlays and the aspect ratio of the frames. The test results were compared with the numerical results obtained from the nonlinear static pushover analysis. The analytical model incorporated the equivalent diagonal compression strut concept for the infill panel. A new stress-strain model for the infill panel was proposed and calibrated by using test data. The numerical model predicted global behavior satisfactorily.

ÖZET

FARKLI UZUNLUK/YÜKSEKLİK ORANLARINA SAHİP TUĞLA DOLGU DUVARLI BETONARME ÇERÇEVELERİN KARBON FİBER ESASLI KOMPOZİT YAYGILARLA GÜÇLENDİRİLMESİ

Karbon fiberli kompozitlerle güçlendirilmiş veya güçlendirilmemiş dolgulu betonarme çerçevelerin mühendislik özellikleri (rijitlik, dayanım, enerji yutma, düktilite…vs.) deneysel ve nümerik olarak değerlendirilmiştir. 1/3 ölçekli, tek açıklıklı, iki katlı ve düşey olarak test alanına yerleştirilen 10 numune statik tersinir yanal yükler altında deneye tabi tutulmuştur. Düşey ve yatay yükler birbirinden bağımsız olarak numuneye etkittirilmiştir. 10 numuneden ikisi kontrol numunesidir (fiberli kompozit yaygısız). Diğer numuneler ise tek yönlü karbon fiberli kompozit yaygılarla çeşitli konfigürasyonlarda güçlendirilmiştir. Numuneler 1998'den önce Türkiye'de yapılan yapılarda yaygın bir şekilde görülen kusurlara sahiptir. Bu kusurlar yetersiz sargı, 90^0 kanca ve birleşim bölgelerinde etriye bulunmaması gibi detay kusurları, zayıf kolon-güçlü kiriş gibi dizayn kusurları ve düşük malzeme kalitesi, yetersiz bindirme boyu gibi yapım kusurlarıdır. Bu mevcut kusurları azaltmak ve numunelerin sismik performanslarını arttırmak için tek yönlü karbon fiberli kompozit yaygılar düşey şeritler ve/veya eğik diyagonaller biçiminde dolgu duvarın her iki tarafına da yapıştırılmış ve betonarme çerçeveye ankrajlanmıştır. Bazı numunelerde, çerçeve elemanlarının sarılması gibi bölgesel güçlendirme teknikleri de uygulanmıştır. Karbon fiberli kompozit yaygılar numunelerin yük taşıma ve enerji yutma kapasitelerini önemli ölçüde arttırmıştır. Maksimum yüklere tekabül eden yatay deplasmanlar da artmıştır. Ayrıca numunelerin uzunluk/yükseklik oranlarına ve karbon fiberli kompozit yaygıların konfigürasyonlarına bağlı olarak bazı rijitlik artımları da kaydedilmiştir. Test sonuçları monotonik olarak artan yanal yükler altında yapılan ve doğrusal olmayan analizden elde edilen sonuçlarla karşılaştırılmıştır. Eşdeğer diyagonal basınç çubuğu kavramı kullanılarak yığma duvarlar modellenmiştir. Yığma duvarlar için yeni bir gerilme-birim deformasyon modeli önerilmiş ve test verileriyle kalibre edilmiştir. Nümerik model global davranışı yeterli bir yakınsaklıkla tahmin etmiştir.

TABLE OF CONTENTS

LIST OF FIGURES

LIST OF TABLES

LIST OF SYMBOLS/ABBREVIATIONS

b_{column}	Column section width
b_{FRP}	Width of FRP
d_1, d_2	Undeformed dimensions of the dial-gages which were placed in "X" configuration
D_1, D_2	Deformed dimensions of the dial-gages which were placed in "X" configuration
d_{column}	Column effective depth
E_{bm}	The modulus of elasticity of the masonry infill
E_{bmp}	The modulus of elasticity of the plastered infill wall
E_c	The modulus of elasticity of concrete in the frame
E_p	The modulus of elasticity of the plaster
E_s	Modulus of elasticity of re-bars
f_{bm}	Compressive strength of masonry (excluding plaster)
f_{bmp}	Compressive strength of masonry (including plaster)
f_{bmpF}	Compressive strength of the strengthened infill wall
f_{ck}	Characteristic compressive strength of concrete
f_{ctk}	Characteristic tensile strength of concrete
f_m'	The prism compressive strength of the masonry
f_p, f_m, f_{mortar}	Nominal compressive strength of 50x50x50mm mortar cubes
f_s	Maximum stress in the re-bars of the tension column
f_{sp}	Splitting tensile strength of concrete
f_u	Characteristic ultimate strength of rebars
f_{yk}	Characteristic yield strength of re-bars
h_1	Story height
h_{bmp}, h_m	Height of the infill wall
h_{column}	Column section height
H_{ult}	Corner crushing strength of the infill
I_g	Moment of inertia of column
k	Modification factor

K_{ult}	Empirical constant
l, L_f	Length of the frame between centers of the columns
l_b	Insufficient lap splice length
l_{bmp}, l_m	Length of the infill wall
N_d	Axial load on the column
P	Overturning failure load
R_c	Diagonal compression failure force
R_s	Diagonal compression strut force
R_{strut}	Capacity of the equivalent compression strut
s	Spacing of the transverse reinforcement
t	The thickness of the infill
t_{bm}	Thickness of the infill wall excluding plaster
t_{frp}	Thickness of CFRP overlay
t_p	Thickness of the plaster
V_{column}	Shear capacity of the column (either tension or compression)
$V_{cr\text{-}compression}$	Shear resistance of concrete under compression
$V_{cr\text{-}tension}$	Shear resistance of concrete under tension
V_f	The maximum shear force resisted by the wall
$V_{f\text{-}column}$	Total shear force carried by column
V_i	The sliding shear capacity of the infilled frame
V_w	Shear strength contribution of transverse steel
z_{clm}	Vertical contact length between masonry panel and the column
ε_y	Yield strain of re-bars
μ	Coefficient of friction
θ, θ_{strut}	Inclination of the diagonal compressive strut
θ_{FRP}	Inclination of the cross FRP diagonals
τ_{bm}	Shear strength of masonry (excluding plaster)
τ_p, τ_m	Shear strength of plaster or mortar
ASTM	American Society for Testing and Materials
CFRP	Carbon Fiber Reinforced Plastic

FEMA	Federal Emergency Management Agency
LVDT	Linear Variable Differential Transducers
RC	Reinforced Concrete
RCMRF	Reinforced Concrete Moment Resisting Frame
TDY	Turkish Earthquake Code

1. INTRODUCTION

1.1. General

The reconnaissance reports and previous earthquakes (1992 Erzincan, 1995 Dinar, 1998 Ceyhan, 1999 Marmara ve Düzce, ve 2003 Bingöl) revealed that most of the building stock in Turkey which was constructed prior to 1998 can suffer from severe strong ground motions due to design and implementation deficiencies. The existing buildings mostly have inadequate stiffness, strength and ductility and they were designed excluding the effect of the infill walls. In general, hollow clay tile (HCT) infills are used in the buildings as interior and exterior partitions. HCT infills have brittle behavior and very limited ductility. They exhibit poor performance during a seismic event due to rapid degradation in stiffness and strength. Numerous experimental and analytical studies show that infill walls interact with the surrounding frame if they are not isolated from the structural system completely.

Infills in the frames not only change the dynamic characteristics of the infilled frames but also influence the stiffness, strength and energy dissipation capacities remarkably. Adding infill to the structure increases mass which in turn increases period and increases stiffness which in turn reduces the period. In general, net result is the reduced period of the building. Reduced period also increases the demand of earthquake on the building.

The frame and infill flexibility is one of the major parameters which affects the behavior of the infilled frame. The behavior of infilled frames and bare frames are very different. Infilled frames attract relatively higher shear forces due to the stiffening effect of the infill. Addition of infills improves the stiffness and load carrying capacity of infilled frames and decreases deformation capacity as compared to bare frame. In some cases decreasing deformations may be advantageous, especially for the frames with limited lateral load capacity and designed mainly for gravity loads. This leads to less damage to the structure in case of an earthquake. Location of infilled frames in the building and the number of infilled frames are also important. Poor arrangement of infills results in torsional effects and soft story conditions.

Infill and frame act together at small displacement levels and low loads [1 and 2]. As the deformations increase, separation between frame and panel and redistribution of internal forces take place. Decreasing stiffness and increasing cracking under increasing load and deformations point out the incipient failure of the infilled frame. Relative stiffness and aspect ratio of the frame can be used as parameters to define failure modes [3]. For the same aspect ratio, presence of a strong panel and a strong frame improves behavior and causes full formation of load resisting mechanisms. However, a strong panel in the non-ductile frame leads to undesirable failure modes such as shear failure of columns. If infill fails following high shear forces developed in the infilled frame, redistribution of forces takes place and the surrounding frame, which is not designed for severe seismic forces, is damaged. If the infill panel fails before developing high lateral forces, the surrounding frame can resist the additional forces due to redistribution. In this case, the beneficial effect of infill walls can be observed because infill walls limit deformation and dissipate energy. In some cases, stress distribution on the frame due to the interaction between frame and infill creates some weak locations on the frame by changing critical regions of the frame, hence poor seismic behavior occurs.

Poor seismic behavior of low to mid-rise existing buildings necessitates the rehabilitation of these buildings. The term rehabilitation includes both the repair (post-earthquake) and the strengthening (pre-earthquake). There are several strengthening techniques that may successfully be applied. However, the large number of vulnerable buildings to be strengthened force engineers to figure out new and more efficient techniques. At this point Fiber Reinforced Plastic (FRP) materials emerge as an alternative strengthening material. FRP materials have several excellent features such as their ease of application, minimum changes in member sizes, minimum disturbance to dwellers, minimum additional weight for the building, and competitive mechanical properties. Although FRP materials have excellent advantages, some issues such as long term behavior and susceptibility to environmental factors should be studied further.

FRP attracts attention both architecturally and structurally. However, it is critical that more research on the behavior of FRP-strengthened infilled frames be carried out to accentuate the contribution of FRP on the infilled frames. Furthermore, time-saving, easy and accurate numerical models should be proposed.

1.2. Deficiency and Vulnerability of Existing Buildings

The level of damage to existing buildings is mainly determined by the characteristics of strong ground motions, soil conditions, and deficiencies of the superstructures. Deficiencies of existing buildings are in the scope of this study. Damage to existing buildings was mostly the result of insufficient application of code requirements. The first Turkish Earthquake Code (TDY) was published in 1944. The issues of the code before 1975 did not sufficiently take into account detailing and the buildings designed before 1975 were basically tailored for gravity loads without or with little attention to lateral load [4]. The code which was revised in 1975 was comparatively good for its time. The transverse reinforcement details included 135^0 degree hooks, and nominal shear stresses at the joints were limited to the value of $0.8\sqrt{f_{ck}}$ [4 and 5]. However this code allowed the use of Allowable Stress Design (ASD) for both steel and reinforced concrete structures. In addition, strong beam-weak column construction was not prevented which can cause column side-sway mechanism. The 1975 issue was revised in 1998 and most recently in 2007. These versions did not allow the use of ASD for reinforced concrete structures [6 and 7]. Most of the low to medium-rise existing buildings which were constructed before 1998 exhibited poor seismic performance in terms of lateral stiffness, strength and ductility. Some of the common deficiencies observed in the reinforced concrete buildings can be listed as follows:

- Soft story and/or weak story;

These deficiencies are the result of inadequate stiffness and insufficient lateral strength of one story as compared to the neighboring stories respectively. Column hinging induced collapse can be caused by the presence of taller members and lack of infills at that specified story.

- Short columns;

Presence of large openings (such as windows, etc.) extending from one column to another in the HCT infilled frames generally cause a decrease in the effective length of the column. The column undergoes large seismic forces and experiences brittle shear failure (an undesirable failure mode) since these columns generally are not designed for such excessive demands.

- Strong beam-weak column construction;

In the current code (TDY'07), columns are adequately stronger than the joining beams at a joint. This is necessary to develop a desirable beam side-sway mechanism. However, it is observed that most of the existing buildings have larger beam sizes and small column sizes. This situation lead to strong beam-weak column construction which is one of the inherent properties of Gravity Load Design (GLD) Reinforced Concrete (RC) frames. Presence of strong beam-weak column joints in the frame causes formation of plastic hinges at column ends. This triggers non-ductile soft story mechanism [8 and 9].

- Torsion created by poor arrangement of infills and load carrying elements;

- Inadequate confinement, insufficient splice lengths;

Observations have shown that most of the existing buildings have insufficient transverse reinforcement and inadequate or no joint transverse reinforcement. Also, the transverse reinforcement is anchored into the core by bending the ends by 90^0 degrees. This improper and insufficient reinforcement detailing deteriorates the confinement effect which is necessary for ductility. Wide spacing and lack of adequate anchorage of transverse reinforcement result in the buckling of longitudinal reinforcement and the column shear failures. For columns with low axial load levels, the flexural strength was reached prior to the shear failure [10]. Moreover, the shear failure was followed by the axial load failure or the compression failure at high drift levels [10]. At high axial load levels, the shear compression failure which is brittle and sudden is observed [10].

Inadequate splice length in column longitudinal reinforcement is one of the important deficiencies. Observations showed that these splices were generally located at the floor level and there were generally widely spaced ties at these regions. Moreover plain bars which bond is mostly due to friction and adhesion were widely used in the existing buildings. Provision of short, inadequate lapped splice lengths prevents the development of yield strength of the re-bar. Brittle failure with no energy dissipation capacity was reported when there were inadequate lapped splices [11].

- Poor material qualities (Low concrete strength, Plain bars);
- Lack of inspection.

Since most of the low to medium-rise existing buildings have the common deficiencies mentioned above, a quick and robust vulnerability assessment is important. Various strategies or methods were developed to rank the vulnerable buildings. Ranking the vulnerable buildings can be done by using some basic information such as dimensions of the structure [12 and 13]. In addition some statistical methods are also developed for vulnerability assessments [14]. Vulnerability assessment is important to determine seismic risk and the steps which can be taken to reduce loss of human lives. Strengthening of buildings with the addition of structural walls is one of the methods to decrease vulnerability of the existing buildings [15]. However, the huge number of existing buildings arise the need to find a quick, reliable, and an efficient strengthening technique. Externally applied FRP on low to medium-rise masonry infilled RC buildings has emerged as a promising technique.

1.3. Objective

The main targets of this study are listed as follows:

- to investigate the aspect ratio effect on the behavior of CFRP strengthened HCT infilled RC frames
- to examine the efficiency and effectiveness of FRP application on the infilled frames with low quality concrete and with deficiencies observed in practice
- to develop an analytical model by using micro modeling based on finite element methods and/or macro modeling based on equivalent diagonal strut (so that simple, fast and time saving analysis can be possible).

1.4. Scope and Organization of the Dissertation

This study is limited to planar single-bay and two-story infilled frames. The specimens included beams, columns, and masonry panels as well as strengthening materials for the strengthened frames. One third scale models were tested under reversed cyclic loading up to failure.

The second chapter in this study is a survey of the existing literature on the topic. The third chapter gives information about materials and test set-up. Chapters four and five examine test results and their evaluation. Chapter six describes the macro-model for predicting the capacity and response of the strengthened specimens. Chapter seven gives conclusions and recommendations for the future studies.

2. LITERATURE REVIEW

2.1. Previous Experimental and Numerical Research on Infilled Frames

In literature, the behavior of infilled frames were investigated considering various parameters such as presence of opening and/or gap, presence of connectors between panel and frame, infill and frame types, presence of vertical loads, loading types and the scale of the specimens. Some numerical simulations were also performed and compared with the experimental results. In this section, selected papers on masonry walls and infilled frames were summarized in the chronological order to highlight the behavior of infilled frames.

In 1958, Benjamin and Williams published one of the earliest papers on brick masonry infill walls [16]. They tested model walls with and without reinforced concrete and steel frames under monotonic lateral loading. Moreover, they also investigated the effect of openings in the brick masonry infilled steel frames but inconclusive results were obtained. The scale of the specimens shifted from 1.0 to 0.34. No axial load was used. Due to the large variation in the performance of the unit masonry composite, the researchers limited the mathematical studies in the brick walls. Frictional resistance, frame properties and test procedure were found to be effective on the post ultimate behavior. Some of the significant results were the following: aspect ratio (the length to height ratio) was very important considering ultimate strength and rigidity. Workmanship influenced ultimate load and the rigidity significantly. Regarding causes of error, the influence of workmanship seriously outweighed that of the scale effect. Noticeable strength increase in brick masonry panels could be obtained by confining the panel with a surrounding frame.

In 1961, Holmes [17] investigated the behavior of infilled (brick and concrete) steel frames by using small-scale, single-bay and single-story specimens. Numerical predictions for calculating the ultimate racking load and corresponding side sway deflection of infilled steel frames were carried out and compared with the test results. An equivalent diagonal strut model was used to model the wall panel. Horizontal load and deflections were calculated based on the strength of materials methods. The width of the equivalent strut was one third of the diagonal length (d/3). The comparison of the theoretical and

experimental values revealed that ultimate load predictions were in the range of 14% in regards to the majority of the tests. However deflection predictions scattered. Holmes [17] stated that the formulas must be revised outside of the h/l=0.7~1.4 range. Moreover, openings in the brickwork infilling adversely affected the ultimate loads (leading to a 30%~40% drop at failure load). In 1963, Holmes [18] revised the previously proposed formulas and investigated the effect of combined loading (lateral and vertical) on infilled frames analytically and experimentally. 5 single-story single-bay steel frames with and without concrete infilling (S1~S5) and 5 single-bay two-story steel frames with and without brick and concrete infilling (S6~S10) were tested to compare the predicted results. Some of the noticeable conclusions were as follows: Presence of vertical load in addition to the horizontal load decreased lateral load carrying capacity about 13%; Semi-emprical methods can be revised by additional test data; The higher compressive strength of the concrete determined that the ultimate load of concrete infilled steel frames was higher than that of the brick infilled steel frames.

In 1962, Smith investigated the lateral stiffness of infilled frames with an equivalent strut concept and compared the theoretical results with the experimental ones [19]. The mortar panels which had three different aspect ratios (l/h=1, 1.5, 2) were tested under a diagonal compression load to determine the stiffness of the panels and the strain distribution along the diagonal. Theoretically and analytically obtained strains were in good agreement especially at the center of the panel. The difference at the loaded corners was partly attributed to the decrease in the modulus of elasticity of the panel material. Effective width of the panels were stated in terms of diagonal length of the panels and shifted from 0.25d for an aspect ratio of 1.0 to d/11 for an aspect ratio of 5. One story, one bay and two-story one bay infilled frames were tested in back to back arrangement under monotonic loading and stiffness values were calculated analytically. Stiffness of the infilled frames was calculated based on the findings on the infill panel stiffness and the rigidity of the surrounding frame. The formulations did not take into account the contribution of bending stiffness of the frame and the change in effective width of the strut for multi-story infilled frames. Experimental and numerical stiffness ratios for single story single-bay mortar infilled frames with aspect ratios of 1.0, 1.5, and 2.0 were in the range of 16%. Smith [19] concluded that lack of fit or initial slackness and foundation stiffness affected initial stiffness and deflection calculations.

In 1966, Smith [20] investigated the behavior of square infilled frames. Diagonally loaded small scale mortar infilled and rigidly connected steel frames were tested under monotonically increasing compression forces. Frame thickness was variable. He proposed a non-dimensional parameter to define relative stiffness of the infill to the frame. This parameter was stated as a function of the contact length. Contact length increased as the frame stiffness increased. Moreover a relation between effective width of the equivalent strut and contact length was established by using the finite difference method. The results showed that effective width increased as the contact length increased. Diagonal cracking and compressive failure were defined as infill failure modes. The tests on diagonally-loaded infilled frames extended to the laterally loaded single and double story infilled frames due to the similarities between deflected shapes. Test results were evaluated by using equivalent pin jointed frame approach to predict lateral stiffness of the infilled frames. The stiffness predictions for multistory infilled frames were close to the ones obtained experimentally at the second story but differed at the first story. Smith [20] proposed a method to predict strength and sequence of the failure of the infill and stated that this method was in good agreement with the experimental results.

In 1967, Mallick and Severn proposed a new method by using FEM tools based on a complementary energy [21]. The effect of slip on the behavior was shown experimentally and included in the model as well as stress distribution along the contact lengths. A decrease in slip due to shear connectors increased the stiffness. Several tests on single-story and single-bay infilled steel frames were done to evaluate stiffness and strength values and compare them with the theoretical results. Failure was mostly due to the crushing of the infill material. Back to back arrangement or tandem method of testing was used for the infilled frames with span to height ratios of 1.0, 1.5, and 2.0. They found the method to be not feasible for multistory infilled frames. That’s why, a relatively simple method was introduced based on the concept of shear structure. Satisfactory results were reported.

Mallick and Severn also investigated dynamic properties of infilled frames in terms of natural frequency, mode shape and damping of infilled frames [22]. The sources of damping were material damping or internal friction, friction between infill and the surrounding frame, friction between the cracked surfaces of the infill and rocking of the

infill inside the frame. Two types of tests were performed to determine dynamic characteristics of the infilled frames; namely half-cyclic load tests and forced vibration tests. 8 single-bay single-story infilled frames with and without shear connectors were tested in tandem configuration under half cyclic loading. Presence of shear connectors improved stiffness, decreased deterioration between consecutive cycles and damping capacity. Damping for integral infilled frames was due to viscous damping whereas for non-integral frames it was partly due to solid friction. Forced vibration tests were performed on the specimens with one, two, three and four story specimens. Damping obtained from half cyclic loading tests was noticeably higher than that obtained from forced vibration tests due to the large amplitudes. They proposed two simple methods in addition to complex finite element method. When the frequencies of single story and single-bay infilled frames were compared, good agreement between experimental and analytical results was reported in terms of frequencies calculated by using shear model. However, the same tendency was not observed for the 3 and 4 story specimens. Bending model which allowed shear and axial deformations predicted mode shapes and frequencies better than shear model for multistory infilled frames.

Later, Smith and Carter proposed an analysis method to predict stiffness and strength of the laterally loaded infilled frames by using the equivalent strut concept [23]. The method was proposed for the non-integral and unbonded infilled frames. Bending in the frame members was not taken into account. They stated that contact length, aspect ratio, applied load level, mechanical properties of the infill influenced equivalent strut width significantly. The elevation of the infill panel also affected the equivalent strut width. Analytical predictions were compared with the 3-story full scale brick infilled RC frame test results and satisfactory estimations were noted.

Liauw investigated many aspects of infilled frames and compared the test results with analytical predictions. In 1970, Liauw published a paper on elastic behavior of infilled frames [24]. Full bond or full contact was assumed at the frame and infill interface. Photo-elastic experiments were done and experimental and analytical results were satisfactory in the elastic range of the materials. Liauw [24] stated that the stiffer the frame was, the higher shear forces it attracted. Stress distribution at the beam column and panel interface was non-linear whereas it was almost linear at the beam panel interface of the mid-span.

In 1971, Ersoy and Uzsoy studied the behavior of RC infilled RC frames [25]. One specimen out of nine specimens was a bare frame. The rest were infilled frames. 1/4 scale single bay-single story specimens were tested in tandem configuration under monotonically increasing loading in horizontal position. Frame aspect ratio of the specimens was about 2.0 and beam to column rigidity ratio was in the range of 2.0~4.0. Presence of vertical load on beam mid-span and the ratio of vertical load to horizontal load, relative rigidities of frame members, infill thickness (30 mm and 50 mm) and frame-wall interface type (30 mm long anchor dowels were used) were the investigated parameters. Some of the noticeable conclusions were as follows: RC infills increased the lateral load carrying capacity as much as 7 times and decreased deformation at failure about 65% as compared to the bare frame; also, RC infill improved initial stiffness (500%) and first cracking load (30-35 fold) considerably; the effect of rigidity ratios between beam and column on the behavior of infilled frames was minimal; although presence of vertical load decreased the rigidity of the infilled frame, the considerable increase of the ratio between vertical and horizontal load enhanced lateral load carrying capacity; presence of connection did not affect the load carrying capacity (approximately 20% increase) and the rigidity of infilled frame (slight increase) noticeably. The researchers used equivalent strut concept to predict the behavior of the infilled frames. The pin support connection was used for the equivalent strut if the strut width was less than one fifth of the diagonal length. They recommended that the width of the equivalent strut can be accepted in the range of 11%-13% of the diagonal length for the infilled frames without vertical loads. Strut width was recommended in the range of 7.0%-8.5% for the infilled frames with high vertical loads.

In 1971, Mallick and Garg investigated the effect of an opening on the lateral stiffness and the capacity of infilled frames [26]. 16 single story single-bay mortar infilled steel frames, 8 of which had shear connectors, were tested under monotonic loading. Back to back arrangement was used. Positioning of each opening and the presence of shear connectors were among the variables. Square openings were used for the ease of calculations. Test results were compared with the analytical ones done by using a FEM and good agreement was reported. Relatively simpler equivalent strut approach with an effective width of d/3 was used to calculate stiffness of the integral frames and good, comparable results were obtained. Mallick and Garg [26] recommended the use of shear

connectors due to failure mode which gave warning prior to collapse, high stiffness as compared to the infilled frames without connectors and the lesser probability of lack of fit. The spacing of connectors did not influence stiffness and load carrying capacity significantly. They suggested that location of openings be very important and openings not be placed at either end of the loaded diagonal.

In 1971, Mainstone tested 1/6 scale steel frames with brickwork or micro-concrete infills [27]. In addition, the researcher tested walls with no frames surrounding them and 3 full-scale brickwork infilled frames. Failure of these specimens was sudden and either by a single diagonal crack for brickwork or by crushing of one of the loaded corners in micro-concrete walls. Failure of the infilled frames triggered by the formation of a diagonal crack and crushing failure was observed. He reported similar behavior for the scaled and full scale tests. Mainstone [27] proposed three different empirical curves to determine equivalent strut with related to stiffness, cracking and ultimate strength.

In 1977, Liauw and Lee investigated the behavior of multi-story infilled frames. 4-story micro-concrete infilled steel frames were tested under uniformly distributed lateral load [28]. Presence of connectors between frame and infill, presence of opening, span to height ratio (2.0, 2.5, and 3.0) and opening area were among the variables. Presence of an opening changed the behavior significantly, especially when it crossed the compression diagonal. Slip-induced separation between panel and frame increased remarkably due to presence of an opening. Stiffness and strength characteristics were adversely affected as the opening area increased, especially in case of non-integral frames. Minimal or no slip between panel and the frame and increased number of cracks in the infill were the results of shear connectors. Two analytical methods were used to predict the experimental results of integral and non-integral infilled frames. In the equivalent strut method, rigid arms were used to connect equivalent beams and columns of the infill. Equivalent diagonal strut method used for non-integral frames produced unsatisfactory results considering failure load; mainly due to idealization of material properties and concentrated contact forces assumption between frame and panel. Equivalent frame method approach was introduced for integral infilled frames. A modular ratio for frame and infill was used to establish the equivalent frame. Strength predictions done by using the latter method produced better

results that the former method. They reported comparable results between experimental and analytical ones in terms of stiffness, and failure mode.

Wood studied wall-frame interaction and proposed a method based on plastic theory for the infilled frames in 1978 [29]. Shear mode (strong frame –weak panel), shear rotation mode (medium strength walls), diagonal compression mode (strong wall-weak frame) and corner crushing mode (very weak frame) were defined as failure modes. The plastic analysis method was verified by using full scale and model test results and good agreement was reported in terms of failure load and failure modes. The researcher proposed a penalty factor to calibrate the analytical results. Wood emphasized the importance of the bending strength of the frame.

In 1978, Klingner and Bertero tested a one third scale subassemblage (1-1/2 bays wide and 3-1/2 stories high) of an 11 story building [30]. Four specimens, one of which was a bare frame, were tested under reversed cyclic loading. Lateral load was applied at the top of the specimens. The specimens were tested horizontally. Hollow core concrete and clay block units were bonded to the surrounding frame to obtain firm contact between the panel and the frame. Load controlled and displacement controlled types of loading were used. They drew several conclusions: Load-displacement graphs of the infilled specimens showed pinching behavior and a sudden drop prior to the gradual drop in the strength due to a decrease in the infill resistance; the behavior of infilled frames was improved in terms of stiffness at service levels, strength, and energy absorption and dissipation capacity. Klingner and Bertero [30] believed that positive effects of the engineered infills suppressed the disadvantages created by increased inertial forces due to changes in stiffness and period values. Adding infills decreased P-Δ effects and the risk of incremental collapse due to high energy dissipation through the hysteretic behavior. They compared the experimental results with the numerical ones obtained from macro-modeling of the specimens based on equivalent strut concept. Tensile strength of the struts were relatively low due to low tensile strength of the infill material and low contribution of panel steel. Although bond-slip behavior was not included in the model, the results were quite good because the behavior of the infill determined the behavior of the infilled frame.

Kahn and Hanson investigated the behavior of infilled non-ductile RC frames [31]. Five half-scale, single-bay and single story specimens were tested under reversed cyclic loading. There were no vertical loads on the columns. Two specimens were a bare frame (specimen 5) and a monolithically cast RC infilled frame (specimen 1). The other frames included a cast in place panel (specimen 2), a mechanically connected single unit precast panel (specimen 3) and a mechanically connected multiple precast panel (specimen 4). There was a gap between the panel and the columns in the RC frames with a precast panel to prevent column shear failure due to the panel. Some of the remarkable conclusions are as follows: interface connection affected the behavior significantly. Although the ultimate load of specimen 4 was approximately half of that of specimen 2, specimen 2 dissipated the same amount of cumulative energy and exhibited higher ductility. Shear failure of the compression column was observed after yielding of the wall at the base in specimen 1. In specimen 2, connection failure followed by column shear failure was observed. In specimen 3, failure of the bolted connection caused beam shear failure. The gap between the panel and the columns caused a ductile behavior and eliminated shear failure of the columns. In specimen 4, shear failure at the panels followed by diagonal shear failure at the ends of the columns was observed. Inadequate confinement of columns accelerated load degradation. They stated that each strengthening technique is unique to that structure.

Later in 1979, Liauw investigated multistory infilled frames under dynamic loading [32]. Four story single-bay micro-concrete infilled steel frames were tested under lateral loading. The load was applied at the top of the frames at different frequencies. Presence of shear connectors and openings, and span to height ratio were among the variables. Liauw [32] drew the following conclusions: Shear connectors increased stiffness and strength of the multistory infilled frames with respect to the non-integral infilled frames. Moreover, shear connectors led to increase the number of the cracks and raised the dissipated energy due to extensive cracking as compared to the energy dissipation of non-integral frames due to slip and separation. Presence of opening caused early cracks around the top corners of the opening and resulted in a reduction in the stiffness and strength with respect to the solid infilled frames. Failure was due to diagonal compression for solid infilled non-integral frames and due to shear between the frame and the panel for integral infilled frames. Presence of an opening shifted the failure mode from the bending in lintel beams for non-integral frames to the shear in the lintel beams for integral frames.

In 1983, Bertero and Brokken examined the effects of various kinds of masonry infills to retrofit existing RCMRF [33]. Test specimens, scale, and set up were similar to the ones given in reference 19. Eighteen specimens one of which was bare frame were tested under reversed cyclic or monotonic loading. The infill types were reinforced hollow unit masonries (clay and concrete blocks) split brick with exterior welded wire fabric (WWF) reinforcement and lightweight concrete panels. Supply of the building and demand of the earthquake were influenced by infills. The results showed that unreinforced masonry infills increased lateral strength of the bare frame 2.82 times when all the frames were infilled. The highest supplied strength, which was approximately 7.72 times that of bare frame, was obtained when reinforced lightweight concrete infills were used. The increase in strength demand due to decreased period was in the range of 1.86-2.41 times that of bare frame when all the frames were infilled. Peak effective acceleration values for ductile and non-ductile unreinforced masonry infilled frames were limited to 0.26g and 0.12g respectively. These values were high for other reinforced infill types. They stated that infill type, anchorage details and loading history influenced hysteretic behavior significantly. The best hysteretic behavior and least amount of debris was exhibited by solid masonry infills externally reinforced with WWF covered with cement mortar.

In 1984, Liauw and Kwan published a paper on nonlinear behavior of non-integral infilled frames [34]. Two four-story micro-concrete infilled steel frames with a span to height ratio of 2.0 were tested under displacement controlled type of loading. Lateral load was applied at the top of the specimens. A guard rail at the fourth story was used to eliminate possible twisting and buckling. Failure of the specimens was due to the crushing of the infill. Nonlinear finite element analysis was performed to predict experimental results. Three types of elements namely panel, frame, and interface elements were used. Friction, separation, and slip were modeled by using an interface element. They examined the stresses at panel, frame, and interface and concluded that an increase in frame moments took place following the yielding of the panel corners due to increasing moment arm of the contact stresses. Moreover, the capacity of the non-integral infilled frame was closely related to the flexural strength of the frame. A uniaxial stress distribution was reported along the loaded diagonal. The higher stress concentrations were, the smaller the contact area was. Based on these observations and previous studies, Liauw and Kwan [34] proposed equation (2.1) for the effective strut width (w). h and λh represented story height

and relative stiffness parameter respectively. This equation does not take into account the effect of friction. A parametric study on the initial slackness and friction showed that lack of fit was unimportant when a strong contact between panel and frame was established. Friction affected the behavior especially in the nonlinear range after the peak load and increased the dissipated energy.

$$\frac{w}{h \times \cos\theta} = \min(\ 0.45\ or\ \frac{0.86}{\sqrt{\lambda h}}\ ) \tag{2.1}$$

Liauw and Kwan published a paper on plastic design of infilled frames in 1984 and later extended the study and proposed an analysis method for integral, semi-integral and non-integral infilled frames [35, 36]. A gap between panel and columns were introduced in semi-integral infilled frames. In other words, the integral connection between the panel and the frame was constructed by beams. Slip and separation between frame and panel, crushing of the infill wall, and flexural failure in the frame members were observed to be the reasons for the nonlinear behavior for non-integral infilled frames. Yielding of the interface connection, cracking and crushing of the panel and flexural failure of the frame members were the sources of the non-linear behavior of integral infilled frames. Based on the failure modes observed, plastic theory was developed and failure shear force was calculated. The model also included stress redistribution prior to collapse. Diagonal crushing and corner crushing were defined in two basic and two complementary failure modes. Compressive strength of the infill and shear strength of the connection determined the collapse shear for integral infilled frames. Relative strength of the frame and the wall controlled the failure load of the non-integral infilled frames whereas shear strength of the connection determined the collapse shear of semi-integral ones. The method was applicable to both single and multi-story infilled frames. They reported a satisfactory agreement between the available test results and the proposed analysis in regards to the ultimate strengths and the failure modes.

In 1988, Liauw and Lo investigated the behavior of multi-bay infilled frames [37]. This study was an extension of the previous study published in 1982 on single-bay and multi-story infilled frames [38]. Single story, single-bay and single story two bays micro concrete infilled steel frame with span to height ratio of 1.5 were tested under monotonic loading up to the failure. Integral and non-integral test specimens were tested vertically.

Column dimension, presence of shear connectors between frame and the infill were among the variables of the small scale models. The specimens were modeled by using non-linear FEA. The researchers drew several conclusions: Failure of the non-integral infilled frame was governed by the formation of plastic hinges prior to crushing. Whereas in the case of integral infilled frames, formation of extensive cracking due to tensile and shearing stresses at the interface was followed by the formation of plastic hinges and sometimes the shear failure at the interface. The magnitude of interface stresses decreased in the second panel. When integral and non-integral infilled frames were compared, the average increase in the ultimate load due to shear connectors was reported as 1.41 and 1.47 for single and two bays infilled frames respectively. Doubling of the bay produced greater ultimate loads but the ratio was smaller than 2. Test results verified the proposed method up to the failure.

Altin, Ersoy and Tankut investigated the hysteretic behavior of RC infilled RC frames [39]. Fourteen infilled frames which were one third scale, one-bay and two-story were tested under reversed cyclic loading. One specimen was a bare frame. Lateral load was applied at the second story. Specimens were tested horizontally. The main variables were type of infill reinforcement, interface connection between frame and panel, flexural capacity of columns, axial load and concrete strength. Diagonal reinforcement (Type A), regular mesh reinforcement (Type M, B and D) and concentrated boundary reinforcement (Type C) were the reinforcement patterns. The failure mode was a combination of flexure and shear sliding. Specimens which behaved elastically up to the peak load showed some ductility with reduced capacity due to yielding of horizontal panel reinforcement for monolithic specimens or due to deterioration of the interface connections for infilled specimens. Provision of anchorage between frame and panel improved the hysteretic behavior significantly. Presence of RC infills which did not have any anchorage at the interface increased ultimate load approximately 2.4 times with respect to bare frame. Provision of axial load increased the capacity between 13%-30% depending on infill type and connection type as well as stiffness. Type B infills improved strength and energy dissipation better than the other types. They reported that number of infilled frames and location of them influenced the dynamic characteristics of the prototype building.

In 1996, Mehrabi et al. examined the effect of infills on the seismic performance of RC frames [3]. Two types of frame specimens, one of which represented older structures,

were examined. Aspect ratios (h/l) were 1/1.5 for strong frames and 1/1.5 and 1/2 for weak frames. Solid and hollow core concrete units were used as infill materials. 12 one half scale single-bay, single-story specimens, one of which was bare frame, were tested under either cyclic or monotonic loading. The columns had continuous reinforcement. Distribution of vertical loads, loading history (load or displacement controlled for cyclic loading), height to span ratio, frame type, and infill type were among the variables. They stated that failure and frame panel interaction was governed by relative strengths of the panel and the frame. Ultimate load ratios with respect to the bare frame for weak frame infilled with hollow and solid concrete units were 1.5 and 2.3 respectively. Those values for ductile infilled frames with respect to the ductile virgin frame (the capacity of the virgin frame was calculated as 145 kN) were predicted as 1.4 and 3.2 respectively. Hysteretic energy dissipation of solid masonry units infilled frames was better than that of hollow masonry units infilled frames both for weak and strong frames. The increase in span to height ratio increased the ultimate loads about 10% for strong infils and 17% for weak infills. Mehrabi et al. [3] believed that this observation may be wrong if changes in aspect ratio resulted in different failure mode. Vertical load distribution between frame and panel did not affect the load carrying capacity. However, a 50% increase in vertical load increased stiffness 30% and lateral load capacity 25% for solid concrete infilled weak frames with aspect ratio of 1/2. Shear failure of the columns, generally seen in specimens with weak frames and strong infills, obstructed the development of an effective load resisting mechanism. An effective load resisting mechanism was observed in the solid concrete blocks infilled ductile frames. Moreover, presence of strong infills decreased the drift levels which shear cracks was observed with respect to the specimens with weak infills.

In 1997, Marjani examined the behavior of infilled frames experimentally and analytically [40]. Four 1/3 scale single bay two story brick infilled frames and 2 bare frames were tested in tandem configuration under reversed cyclic loading. Presence of plaster (4 mm) and concrete strength (12.5 MPa, 25 MPa, 31 MPa, and 35 MPa) were among the variables. Aspect ratio of the specimens was about 1.7. Lateral load applied at the second story level and vertical loads on the columns were kept constant (50% of the balanced load) throughout the tests. The specimens were code-compliant (1975 Turkish Seismic Code) and cross-sectional dimensions of the beam and column members were the same (150 mm*150 mm). Column longitudinal bars were continuous. The frames were

cast horizontally but brick were laid up after the frames were brought in an upright position. Some of the remarkable results were as follows. Presence of plastered infill improved the load carrying capacity about 3 times as compared to the bare frame. Presence of plaster increased initial stiffness as much as 1.8 times compared to the infilled frame without plaster. The increase in concrete strength (24% increase) did not affect stiffness (5.1% increase) and load carrying capacity considerably. Presence of plaster directly affected the first cracking load and lateral load capacity (25% increase). Marjani [40] stated that the stiffness and strength of the infilled frame can be predicted accurately by using linear and nonlinear FEM if infill properties were determined correctly.

In 1997, Mosalam et al. examined unreinforced solid concrete masonry infilled gravity load designed steel frames under quasi-static cyclic lateral loads [41]. The number of bays, relative material strengths of concrete units and mortar joints, and opening area size and configuration, were the investigated parameters. 5 single story, 1/4 scale specimens were tested up to failure. Mosalam et al. [41] drew several conclusions: failure shifted from corner crushing to mortar cracking when relative strength of concrete blocks and mortar joints increased. Failure mode changed the ultimate load approximately 10% in this study. Doubling the bays increased ultimate load about 2 times and initial stiffness about 1.7 times. Presence of openings resulted in less stiffness, larger deformations and more ductile behavior compared to the solid infilled frames. Presence of door opening in one wall decreased ultimate load approximately 20 %. However, presence of window opening did not change ultimate loads significantly. The width of the equivalent strut was not uniform; it decreased towards the loaded corners. They proposed a hysteresis model with physically meaningful parameters based on test results.

Schneider et al. examined the effect of large openings on the seismic behavior of brick infilled steel frames in 1998 [42]. Pier width between the column and window opening and the number of wythes were among the variables. Five large scale specimens which simulated interior steel column with infill on each side were tested under cyclic loading. The ratio of window opening height to pier width (h/b) was in the range of 1.44-2.88. End conditions of the interior column were fixed-fixed and full contact between wall and surrounding steel elements was ensured. Vertical loads were applied to the infill through the steel rods to simulate gravity and live loads. They drew several conclusions:

the brick infills had an average ultimate shear stress of 0.96 MPa. However failure modes may not be determined from average ultimate shear stresses. The inclination of the strut formed in the pier decreased as the ratio between opening height to pier width decreased. Flaking and crushing of the infill were delayed when the number of wythes increased. Effective stiffness degradation was approximately 70% at 0.2 % drift, which caused the first observable flexural cracks in the wall. Pier width and number of wythes did not seem to influence effective stiffness degradation. Ductility of narrow piers and thick piers was greater than that of wider ones or single wythe infills respectively. Ultimate load increased as number of the wythes or b/h increased.

In 1998, Turk examined the effect of adding cast in-place infill on the behavior damaged and undamaged RC frames [43]. 1/3 scale, single span and two-story RC frames were tested to a certain damage level and then they were strengthened and tested up to failure under reversed cyclic loading. One bare frame out of five was not damaged. Two bare frames were code compliant (1975 Turkish Seismic Code) and did not have lapped splices whereas three bare frames were non-compliant with insufficient lapped splices. Deformed bars for frame members and plain bars for panel were used. No rehabilitation was applied to the frame members. The thickness of the panels was 50 mm. Some of the noticeable conclusions are as follows; interaction between frame and panel influenced lateral load capacity of the specimen. Application of axial load improved the behavior of the infilled frames. Inadequate lapped splices resulted in unsatisfactory behavior of infilled frames. Overall behavior of the infilled frame did not noticeably depend on level of damage in the bare frame. Addition of infill made the lateral strength 8-13 times stronger than the bare frame, and the initial stiffness 19-24 times greater than the bare frame and increased energy dissipation capacity significantly. The numerical results, which were based on both the equivalent strut concept and plastic analysis method, were satisfactorily compared with the test results.

In 1999 Chaker and Cherifati investigated dynamic characteristics of HCT infilled RC buildings on site [44]. The vibration records were gathered from 2 adjacent 3-story code-compliant buildings one of which was without infills. They concluded that infills affected the dynamic characteristics significantly. Stiffness of the infilled building was approximately 7 times greater than that of the bare building and frequency of the infilled

building was higher than that of bare building (2.3 times greater in the transverse direction and 2.4 times greater in the longitudinal direction). Chaker and Cherifati [44] stated that plane stress model represented frequencies better than the diagonal truss models at small strains.

In 1999, Flanagan and Bennett investigated the behavior of large scale HCT infilled steel frames under cyclic loading [45]. Infills were bonded to the surrounding frame by snugly packing mortar. Aspect ratio (1.0, 1.25, 1.5), relative stiffness of the panel to the frame, and thickness of the wall were among the variables. No axial load was applied. Some of the more interesting results were as follows: corner crushing type of failure was observed and ultimate load did not seem dependent on frame characteristics. The load deflection diagram showed pinching behavior due to interface degradation between frame and the wall and plastic deformations in the masonry. They proposed an equation to determine corner crushing strength of the infill, (H_{ult}), based on the assumption that frame properties and geometry did not influence the corner crushing strength of the wall. These equations demonstrated good agreement with experimental results. Moreover, they determined equivalent strut area, (A), based on an empirical constant, (C). The formulations were given in equations (2.2) and (2.3). The variables t and f_m' represented the thickness of the infill and the prism compressive strength of the masonry respectively.

$$H_{ult} = K_{ult} \times t \times f'_m \tag{2.2}$$

$$A = \frac{\pi \times t}{C \times \lambda \times \cos\theta} \tag{2.3}$$

Lateral load was transferred to the infill through column bearing and friction along the top beam interface. Most of the shear was transferred through friction between beam and panel. In case of provision of stronger columns, the load transferred through column bearing increased. They stated that presence of initial gap between panel and column decreased the initial stiffness but this stiffness is higher than bare frame stiffness. After full contact between panel and column occurred, stiffness increased significantly. This gap did not alter capacity considerably. However, Seah [46] showed that presence of initial gap between panel and beam adversely affected peak load and stiffness. Flanagan and Bennett

[45] stated that eccentric placement of infill decreased ultimate load 25% and initial stiffness 30%.

In 2002, Al-Chaar et al. investigated the behavior of single story and single or multi-bay non-ductile infilled frames [47]. 5 half scale, single story with variable bays specimens were tested under monotonic loading. Longitudinal steel of the columns was continuous whereas bottom longitudinal steel of the beams at the joint region was discontinuous. The number of bays and the type of masonry (concrete or brick units) were among the variables. Height-to-span ratio (h/l) of the frames was 0.75. Some of the notable observations and conclusions were as follows: first cracking of the single span infilled frames occurred at the same drift level regardless of the infill type but first cracking load of brick infilled frames was higher. Two bay concrete masonry infilled frames had the least drift level for the first cracking. An increase in the number of bays resulted in a nonlinear increase in peak load, initial stiffness, first cracking load and residual strength. They reported that infilled frames showed a ductile behavior due to presence of infill. However this observation may not be correct for the infilled frames with inadequate lap splice lengths in the columns. Presence of a surrounding frame increased shear stress of the infill due to confining effect. Moreover shear stress in the front panel which was close to the loading side was half of that in the second panel for two bay infilled frames. This was an indicator of non-uniform stress distribution. Test results were compared with the numerical ones and good correlation was reported in terms of peak load.

In 2003, Asteris presented a parametric study on the infilled frames with openings [48]. He developed a FE technique. One story and one bay brick infilled frames were analyzed under monotonic loading. The study also covered single span multistory infilled frames with and without openings. Asteris [48] drew the following conclusions. Stiffness reduction factor decreased as the opening area increased and the stiffness reduction factor was stabilized for opening percentages exceeding 50%. The decrease in stiffness was 87% for 100% opening percentage. The location of the opening influenced stiffness significantly. If an opening is located above the diagonal, the influence on stiffness was minimal. If an opening was located below the diagonal, contact length between panel and beam increased as it decreased for other options. Contact length between panel and column increased if an opening was located above the diagonal. However contact length between

panel and column decreased if an opening was located on the diagonal or below the diagonal. Infills in multistory frames generally decreased lateral displacement and shear forces on the columns. Nonetheless, shear forces in the columns were very high in case of infilled frames with soft story.

In 2003, Canbay et al. tested a 1/3 scale, two-story and three bay RC frame up to a roof drift level of 1.6% under reversed cyclic loading [15]. Then they strengthened the frame by adding RC infill to the middle bay of the frame and tested up to the same drift level. The damaged frame was not repaired. Their aim was to determine internal force distribution between frame members and the infill. The specimen had the deficiencies observed at site such as inadequate lapped splices at the floor level. Plain bars were used for frame and infill whereas deformed bars were used to anchor the panel into the frame. Lateral and vertical loads were applied at the second story level. Some of the conclusions are as follows: the test set-up instrumentation and specially developed transducers were satisfactory. No cracks were observed at the second story infill. At low load levels the lateral load was carried by the infills 99%. In the last loading cycle this value was 90 %. The maximum lateral load shifted from 14 kN to 53 kN. Test results were compared with analytical results and good comparison was obtained. They recommended partial strengthening to use full capacity of infills.

Sonuvar et al. presented a paper on eliminating adverse effects of local deficiencies in the splice region and improving seismic behavior of non-ductile RC frames with lapped splices in 2004 [49]. 1/3 scale, single-bay and two-story RC frames were moderately damaged under reversed cyclic loading. Damaged frames were rehabilitated by introducing RC infills and some local strengthening techniques. Four specimens out of five had short inadequate lapped splices (12ϕ). The specimens were tested horizontally in a back to back arrangement under vertical and horizontal loading. Partial steel jacketing, addition of longitudinal bars at the boundaries of the infill, and additional boundary columns at the both ends of the infills were the local strengthening techniques. The more important conclusions are as follows: the addition of infills improves stiffness, strength and energy dissipation capacities of the infilled frames and decreased lateral drift remarkably. Connection failure was not observed. Provision of local strengthening improved the behavior of the infilled frame, prevented local failure, and increased energy dissipation

capacity, stiffness and strength. Jacketing and additional boundary columns were superior in terms of energy dissipation capacity. Sonuvar [50] compared the test results with the numerical ones by using equivalent strut concept and stated that the method can be used efficiently for the preliminary analysis.

In 2006, Kara and Altin examined the behavior of partially infilled non-ductile RC frames [51]. 1/3 scale, single-bay, and two-story specimens were tested under reversed cyclic loading. One specimen out of seven was a bare frame. Only lateral load was applied to the specimens at the story levels in the form of inverted triangle. Aspect ratio and configuration of RC infill were the main parameters. All frame members had deformed bars without lapped splices above the floor level. However infill walls and edge members had orthogonal plain bars. Connection between frame members and panels was satisfied by inserting dowels into the epoxy injected holes. The thickness of the infills was 50 mm. Specimens were cast in horizontal position and tested upright. Both load controlled and displacement controlled types of loading was applied. Some of the noticeable conclusions were as follows: Load degradation in partially infilled frames was more gradual than fully infilled frame. Initial stiffness, strength and energy dissipation capacity was proportional to aspect ratio of the infill. Presence of connection between panel and column increased initial stiffness about 45% and energy dissipation capacity about 36% for the aspect ratio of 0.87 (l/h). The position of partial infills affected strength degradation and lateral drift. Load displacement diagrams exhibited significant pinching at high drift levels. Failure was at the first story in all the strengthened frames. Failure mode was governed either by web crushing or sliding shear between wall and foundation. No connection failure was observed. They suggested that frame members should be strengthened to eliminate premature failure of the specimen. Macro-model analytical results were compared with the experimental ones and good correlation was reported in terms of ultimate strength.

In the literature many parameters related to infills and infilled frames were investigated. For example, infill type, presence of connector, type of loading history, and failure modes were among the examined parameters on scaled or full scale models. Table 2.1 presented the summary of the investigated parameters and some insightful comments. Micromodels, mesomodels and macromodels were developed in order to predict the behavior of infilled frames. The micromodels generally incorporate nonlinear finite

element methods and models interface, wall and frame elements in detail. Many researchers attempted to verify the test results of masonry infilled frames by using micromodels [52, 53 and 54]. However micromodelling is very time-consuming for practical applications and system studies and requires detailed calibration [55]. In addition, it was reported that three dimensional FEM had some numerical difficulties and exhibited poor performance in the inelastic range [56]. Macromodelling is very fast and relatively easier. Nonlinear behavior of the structure can be evaluated satisfactorily by using macromodels [57, 58 and 59]. Although macromodels are not able to examine local effects, they are practical and appropriate for analysis and design applications.

Table 2.1. Summary of the investigated parameters

Year	Researcher	Frame Type	Infill Type	Scale	Opening	Initial Gap	Connector	Loading Type	Aspect Ratio (l/h)	Number of Story	Notes
1958	Benjamin and Williams	RC or Steel	Brick	0.34~1.0	Yes **	No	No	Monotonic	1.5~2.0	1	
1961	Holmes	Steel	Brick and concrete	Small	No	No	No	Monotonic	1.0~1.5	1	
1962	Smith	Steel	Mortar infill	Small	No	No	No	Monotonic	1.0, 1.5, 2.0	1, 2	
1963	Holmes	Steel	Brick and concrete	Large	No	No	No	Monotonic	0.5~1.0	1, 2	
1966	Smith	Steel	Mortar infill	Small	No	No	No	Monotonic	1.0	1, 2	
1967	Mallick and Severn	Steel	Mortar infill	Small	No	No	No	Monotonic	1.0, 1.5, 2.0	1	FEM was done and applied to multi-story infilled frames
1968	Mallick and Severn	Steel	Mortar infill	Small	No	No	Yes"	Half-cyclic, Forced Vibration	1	1~4	Dynamic Characteristics of infilled frames were evaluated.
1971	Ersoy and Uzsoy	RC	RC infill	1/4	No	No	Yes"	Monotonic	2.0	1	
1971	Mallick and Garg	Steel	Mortar infill	Small	Yes **	No	Yes"	Monotonic	1	1	Presence of opening at either end of the loaded diagonal decreased ultimate load about 75 % and stiffness about 85 % Provision of connectors improved stiffness and changed the failure mode
1971	Mainstone	Steel	Brickwork and micro-concrete	1/6 , 1.0	No	Yes---	No	Monotonic (LC and DC)	0.5~2.0	1, 2	

Table 2.1. Summary of the investigated parameters (continued)

Year	Researcher	Frame Type	Infill Type	Scale	Opening	Initial Gap	Connector	Loading Type	Aspect Ratio (l/h)	Number of Story	Notes
1977	Liauw and Lee	Steel	Micro-concrete	Small	Yes **	No	Yes"	Monotonic	2.0, 2.5, 3.0	4	Connectors prohibited slip and separation and increased stiffness and strength.
1978	Klingner and Bertero	RC	(Clay or Concrete) hollow core blocks (reinforced)	1/3	No	No	No	Reversed Cyclic Loading	2.2	3.5	
1979	Kahn and Hanson	RC	RC and precast infill	½	No	Yes---	Yes	Reversed Cyclic Loading	1.6	1	
1979	Liauw	Steel	Micro-concrete	Small	Yes **	No	Yes"	Dynamic	2.0, 3.0	4	
1983	Bertero and Brokken	RC	Unreinforced masonry, Reinforced hollow masonry, Soid Brick Rinforced with WWF, Reinforced Lightweight concrete	1/3	No	No	Yes"	Reversed Cyclic and Monotonic	2.2	3.5	
1984	Liauw and Kwan	Steel	Micro-concrete	Small	No	No	No	Monotonic, (Displacement Controlled (DC))	2.0	4	Initial lack of fit was observed, Nonlinear FEA was proposed.
1992	Altin et al.	RC	RC infill	1/3	No	No	Yes"	Reversed Cyclic Loading	1.73	2	
1996	Mehrabi et al.	RC	Solid and hollow core concrete units	½	No	No	No	Cyclic or monotonic	1.5, 2.0	1	

Table 2.1. Summary of the investigated parameters (continued)

Year	Researcher	Frame Type	Infill Type	Scale	Opening	Initial Gap	Connector	Loading Type	Aspect Ratio (l/h)	Number of Story	Notes
1997	Marjani	RC	Hollow Clay Tile	1/3	No	No	No	Reversed Cyclic Loading	1.7	2	Specimens were tested horizontally
1997	Mosalam et al.	RC	Solid concrete unit	1/4	Yes **	No	No	Reversed Cyclic Loading	1.9	1	
1998	Turk	RC	RC infill	1/3	No	No	Yes	Reversed Cyclic Loading	1.73	2	The damage level in the bare frame did not influence the overall behavior of infilled frame.
1999	Flanagan and Bennett	Steel	Hollow Clay Tile	Large	Yes **	Yes---	No	Reversed Cyclic Loading	1.0, 1.25, 1.5	1	Initial gap did not change the ultimate load.
2002	Al-Chaar et al.	RC	Concrete or Brick masonry unit	1/2	No	No	No	Monotonic	1.33	1	
2003	Canbay et al.	RC	RC infill	1/3	No	No	Yes	Reversed Cyclic Loading	0.62 (at 1st story) 1.05 (at 2nd story)	2	
2004	Sonuvar et al.	RC	RC infill	1/3	No	No	Yes	Reversed Cyclic Loading	1.73	2	
2006	Kara and Altin	RC	RC infill	1/3	Yes **	Yes---	Yes	Reversed Cyclic Loading	1.73	2	The effect of partial infill was investigated.

Note: ** means some specimens have an opening

Note: " means some specimens have connectors

Note: --- means some specimens have initial gaps

2.2. Rehabilitation of Masonry Structures with FRP Materials

Rehabilitation is unavoidable if the system or members do not have adequate stiffness, strength, or ductility. The term rehabilitation includes both pre-earthquake and post-earthquake improvement. Rehabilitation can be investigated in two parts; system rehabilitation and member rehabilitation. If the number of rehabilitated elements is limited, member rehabilitation such as jacketing of beams and columns can be used. However, if the number of elements is high and the system has some drift problems, then system strengthening will be feasible. Addition of structural walls, steel braces, and shotcrete can be effectively used for system strengthening. High cost, necessity for foundation improvement, additional mass and inertial forces, architectural and functional disturbance and disturbance to occupants (evacuation may be necessary) are among the main disadvantages of the conventional methods.

Advanced composite materials emerged as a new rehabilitation material. Strengthening with FRP (fiber reinforced plastic or fiber reinforced polymer) is relatively new and challenging issue in civil engineering. Lower cost, good mechanical performance, high strength to mass ratio and high stiffness to mass ratio, ease of application and fewer disturbances to dwellers are among the advantages of FRP. Long term behavior and fire resistance of FRP materials should be further investigated. In addition, presence of moisture adversely influences FRP-strengthened system and may cause delamination or debonding [60]. FRP materials are mostly used in the form of laminate, sheet and bars in structures. They generally consist of glass, aramid and carbon fibers as load carrying elements and resin matrix as binding elements. Resin matrix is used to protect fibers from the ambient conditions, sticks the FRP to the substrate, and distributes the load among the fibers [61]. To reiterate, this study is limited to externally bonded unidirectional CFRP application. In this study, FRP applied on both sides of masonry wall and anchored to the surrounding frame. Hand lay-up procedure in which FRP was bonded to the surface by using epoxy resin was used. In the following pages, selective papers on FRP strengthening are summarized.

In 1997, Ehsani et al. examined shear behavior of solid clay brick infill strengthened with FRP [62]. Test specimens included 3 standard solid clay bricks. The middle one was

elevated from the base and placed between two pieces of lubricated plywood. The aim of the lubricated plywood located between bricks was to eliminate shear resistance provided by mortar and to investigate the effect of the gap between the bricks on the shear strength of the woven fabric placed on both sides of the specimen. 37 specimens were tested under displacement controlled static loading. Strength of the fabric, fiber orientation, and anchorage length were the investigated parameters. Some of the results were as follows: fabric strength and fabric length influenced the failure mode. Specimens with higher density fabrics exhibited the delamination type of failure at the middle brick region or at the outer edges. The failure mode of the specimens with shorter fabrics was due to shear failure at the joint and delamination of the fabric at the outer edges whereas failure mode for specimens with long fabrics was due to shear along one of the bed joints. An increase in fabric strength shifted failure mode from shear along one of the bed joints to delamination at the middle brick region and caused limited usage of the capacity of the fabric. Two fiber orientations were used at 45^0 and 90^0 with respect to the applied load. The 45^0 orientation produced slightly higher ultimate load, lower displacement at ultimate load, more linear behavior, and less ductile failure. In order to obtain full strength of the material, the length should be adequate. Test results were compared with analytical ones and satisfactory agreement was reported for the orientation of 45^0.

In 1998, Triantafillou proposed an analysis method on FRP strengthened masonry structures and carried out tests to show the validity of these formulations [63]. These formulations were developed for out-of-plane bending with axial load, in plane bending with axial load, and in plane shear with axial load. Twelve small wall specimens which consisted of perforated clay units were tested statically in four point bending. Six of them were tested in plane bending and the rest were tested in out of plane bending. Two specimens in each group were unreinforced masonry walls. The main test variables were loading configuration of the small walls, FRP area and distribution of FRP. Some of the notable conclusions were as follows. The failure mode of the strengthened specimens tested in out of plane bending was due to crushing of the masonry in compression region (flexural failure). The test results verified the analytical ones for the out of plane bending. The failure mode of the strengthened specimens tested in in plane bending was due to peeling off of the CFRP laminates which resulted from short length of the specimens and inadequate bond development length. Analytical results were found to be satisfactory for

the in plane bending case. He stated that FRP improved bending capacity of the walls (both in plane and out of plane) and in plane shear capacity considerably.

In 1998, Kolsch developed a method for out of plane rehabilitation of masonry infill walls [64]. The strengthening was done by using carbon fabrics embedded in a cement based matrix. Full scale strengthened masonry walls were tested in out of plane bending under cyclic loading applied with a pressure bag. Kolsch [64] stated that the capacity of the wall increased approximately 3 times with respect to the unreinforced masonry wall. Test results exhibited that carbon fiber cement matrix (CFCM) system eliminated partial or complete collapse of the panel.

In 2000, Velazquez-Dimas et al. investigated out of plane behavior of solid clay brick masonry panels strengthened with GFRP strips [65]. Four half scale specimens were tested under reversed cyclic loading. The main variables were the number of wythes and reinforcement ratio of GFRP strips. Height to thickness ratio of wall specimens was 28. Wet lay-up procedure was followed to bond the strips with epoxy resin. The width of the strips changed depending on the reinforcement ratio of FRP but the number of the strips was kept constant. Some of the conclusions were as follows. Rehabilitation of masonry walls with GFRP strips improved the stiffness, strength (5-24 times weight of the wall) and deformation (up to 5% of the wall height) parameters. As the reinforcement ratio increased, the maximum supported pressure also increased. Depending on the reinforcement ratio, failure mode shifted from delamination or tension or combination of both for the single wythe to peeling off of the strips and splitting of the wythes for the double wythe specimens respectively. They suggested that upper limit of the reinforcement ratio of the FRP should be limited to two times that of the balanced reinforcement ratio to obtain a good hysteretic performance. Later in 2000, Velazquez-Dimas and Ehsani proposed an analytical method to predict out of plane behavior of infill walls strengthened with FRP [66]. Velazquez-Dimas and Ehsani stated that the results of linear elastic approach were better than those of ultimate strength approach in terms of the flexural capacity of strengthened walls [66].

In 2001, Albert et al. tested 12 FRP rehabilitated masonry walls and one unreinforced wall to investigate the behavior of the specimens subjected to out of plane flexural loads

[67]. The variables were the type of FRP (GFRP or CFRP), the amount and configuration of FRP, axial load, and loading type (cyclic or monotonic). Height to thickness ratio of the walls was approximately 21. Some of the noticeable conclusions were as follows. Strengthening with FRP improved strength and ductility of the masonry walls. Presence of axial load increased the first phase stiffness of the load versus mid-span deflection graphs and deteriorated the second or last phase stiffness. In case of cyclic loading, unloading stiffness decreased as deformations increased. Type and amount of FRP influenced the stiffness of the second phase of load mid-span deflection diagram and the change in stiffness was directly proportional to the fiber type and amount of the fiber. They stated that the layout of the FRP reinforcement were effective on the behavior of the local joint strain behavior. Axial load had beneficial effect for the first phase stiffness and detrimental effect for the second phase stiffness. Test results were compared with the analytical ones and good correlation was reported in terms of transitional level load and corresponding deflection and stiffness of the second phase of the behavior as well.

In 2001, Hamilton and Dolan investigated out of plane behavior of the normal or lightweight concrete masonry walls strengthened with GFRP [68]. Reinforcement ratio of vertically applied GFRP was under the balanced reinforcement ratio. The main variables were wall height and type of concrete masonry unit. 4 short walls and 2 tall walls were tested statically up to failure using an air bag. It was concluded that bonding GFRP strips on the wall individually allowed the system to increase deformation capacity due to increased integrity. Developed flexural design formulations based on basic flexural strength design predicted failure loads within the range of 20%. The observed failure modes were GFRP fracture, delamination or a combination of GFRP fracture and delamination.

In 2002, Valluzzi et al. presented a paper on shear strengthening of masonry panels with FRP laminates [69]. Carbon, glass, and polyvinyl-alcohol unidirectional fiber embedded in epoxy resin were used to strengthen the masonry panels. 33 panels, 9 of which were unreinforced, were tested under monotonic loading. Test variables were the amount, arrangement and the type of FRP and eccentricity created by FRP application (single side or both sides). They stated that the effectiveness of the single sided strengthening was limited. Double side configurations resulted in less brittle failure and

higher ultimate loads. The efficiency of diagonal configuration was higher than that of grid configuration. Grid configuration produced less brittle failure and better stress redistribution. Failure mode of double side configuration was delamination or a combination of delamination and FRP rupture. Mainly splitting type of failure was observed for single side strengthening.

In 2002, Hanoglu carried out a series of tests on 1/3 scale HCT brick infilled RC frames [70]. 2 specimens were bare frames and 2 specimens were infilled frames. 4 specimens were strengthened with biaxial woven GFRP sheet or a combination of GFRP sheet and CFRP laminates. Strengthening was applied only one side of the specimens. One story one bay specimens were tested horizontally in tandem configuration under reversed cyclic loading. Four specimens out of 8 were code compliant. Some of the remarkable conclusions were as follows. Rehabilitation of infilled frames with FRP materials increased load carrying capacity significantly. Moreover the displacement capacity of strengthened frames decreased and deficiencies seen in non-compliant frames were eliminated. Corner crushing type of failure was observed in all strengthened specimens. Strengthening of infilled frames with FRP enhanced the probability of sudden and brittle failures.

In 2003, Akguzel investigated the behavior of 1/3 scale single-bay and two-story infilled frames strengthened with CFRP overlays [71]. One of the most important deficiencies was inadequate lapped splices just above the floor levels. 5 specimens were tested under reversed cyclic loading. One of the specimens was bare frame and another one was unstrengthened infilled frames. Uniaxial CFRP sheets were used to strengthen the specimens. Depending on the strengthening configuration, the failure mode shifted from corner crushing to shear sliding. The strengthening scheme included cross diagonals, corner flags, and confinement FRP around lap splice region. Some of the results were as follows. Lateral load carrying capacity and dissipated energy increased considerably. Maximum increase in peak load was about 94% compared to the infilled frame. The change in stiffness was not noticeable but stiffness degradation of strengthened specimens was quite fast compared to the bare frame. Deformation capacity decreased but deformation capacity tended to increase for the specimens with columns confined with CFRP overlays around the lap splice regions. Moreover, he stated that inadequate lapped

splice deficiency was eliminated by the scheme in which columns were confined with CFRP overlays around the lap splice regions.

In 2003, Ozcebe et al. published a technical report on strengthening of brick infilled RC frames with CFRP [72]. Seven 1/3 scale one-bay and two-story infilled frames with common deficiencies seen in practice were subjected to vertical and horizontal loads and tested in tandem configuration under reversed cyclic loading. Lap splices were provided only at the second story. Six specimens out of seven were strengthened. Presence of anchors between frame and panel, the number of treated surfaces, the amount and configuration of FRP were among the variables. Some of the conspicuous conclusions were as follows. Strengthening with CFRP increased strength and energy dissipation capacity significantly. Cross (X) configuration of FRP was seen as an economical solution for rehabilitating existing structures. Anchors were necessary to use CFRP effectively. Local strengthening of columns with lap splices prevented local failures and improved behavior. However, local strengthening at the bottom ends of the first story columns (with no lap splice) shifted the failure from flexure into brittle shear failure. The change in stiffness due to CFRP strengthening was limited. Thus the increase in strength demand which was directly related to the stiffness of the system was limited.

In 2004, Stratford et al. investigated the behavior of clay and concrete brick walls strengthened with GFRP under monotonic loading [73]. Six square masonry walls, 2 of which were unreinforced, were tested under lateral and vertical loads up to failure. One side of the specimens was completely covered with biaxial GFRP sheets. They stated that load carrying capacity of strengthened clay brick specimens increased 65%. In the case of concrete masonry walls, it increased between 38% and 63%. Stiffness and deformation capacity of the strengthened walls remained the same as the unreinforced specimens. Debonding of GFRP was observed in all strengthened specimens. They stated that at ultimate limit state, eliminating premature failure of strengthened specimens resulted in a ductile failure within the masonry. Thus the need to have high strength adhesive might turn into high strain adhesive which could be inflammable if the design is based on debonded FRP.

In 2004, El-Dakhakhni et al. investigated the behavior of GFRP retrofitted hollow concrete masonry infilled steel frames [74]. 3 full scale single-bay and single-story infilled steel frames were rehabilitated with GFRP laminates. 6 specimens, one of which was a bare frame, were tested under displacement controlled reversed cyclic loading. The main variables were the presence of openings and the number of strengthened sides. 2 layers of GFRP covered only the masonry infill. No vertical load was applied. They drew the following conclusions. Stiffness, strength, and energy dissipation capacities of retrofitted specimens were higher than those of unretrofitted counterparts. The increase in load carrying capacity was 23% when strengthened and unreinforced specimens with door openings were compared whereas it was 39% for the case of retrofitted and unreinforced solid infilled frames. Solid infilled frames which were strengthened on both sides dissipated the most energy and had highest initial stiffness. Presence of GFRP improved the postpeak behavior. The panel's structural integrity inhibited out of plane spalling and increased in plane loads. Failure of the retrofitted specimens was gradual with an apparent post peak capacity. El-Dakhakhni et al. [74] stated that retrofitting with GFRP seemed a quick and cost effective solution.

In 2006, Yuksel et al. investigated the behavior of 1/2 scale, single bay and two-story Hollow Clay Tile (HCT) infilled RC frames [75]. Aspect ratio (frame span length/story height) of the specimens was approximately 1.7. Two out of six specimens were RC bare frames. Four out of six specimens, two of which were strengthened with CFRP overlays, were HCT infilled RC frames. One specimen in each group had 20ϕ lap splices just above the story levels and longitudinal reinforcement of the specimens was plain bars. The specimens were tested under quasi-static reversed cyclic loading and displacement controlled type of loading was applied. Specimens underwent one full cycle at each displacement amplitude. Vertical loads on the columns which were 23% of the capacity of the columns were applied prior to the application of the lateral loads which were in the form of inverted triangle and vertical loads were kept constant throughout the test. Strengthening scheme involved CFRP overlays in the form of cross diagonals. Cross diagonals were anchored to the surrounding RC frames. Vertical FRP strips applied on the outer faces of the columns were utilized to eliminate lap splice deficiency then these strips were wrapped with FRP sheets in transverse direction. The vertical strips at the foundation level were anchored to the foundation with CFRP anchors (20 cm depth). Some of the

noticeable conclusions are as follows: No significant damage was observed on the second story of the specimens due to the test set-up. Presence of infill influenced the behavior of the specimens significantly and shifted the frame type behavior to the shear wall type behavior. The peak load of the infilled specimen with lap splices was 15% higher than that of the infilled specimen without lap splices. It was attributed to the higher compressive strength of the former specimen. The infilled specimens lost their load carrying capacity following the crushing of the infill corners whereas rupturing of the cross diagonals of the strengthened specimens resulted in significant load drop in their load carrying capacity. Retrofitting of the infilled specimens with CFRP improved strength and energy dissipation capacities of the unstrengthened counterparts.

In 2006, Erdem et al. investigated the performance of two strengthened RC frames [76]. 1/3 scale 3 bays and 2 story strengthened frames were tested under reversed cyclic loading. The frames had common deficiencies seen in Turkish practice. The middle bays of the frames were strengthened with either RC infills or diagonally applied FRP on the hollow clay tile infills. The thickness of RC infill was 70 mm and steel anchor dowels were used to connect the RC infill to the surrounding frame. The thickness of HCT with plaster was 90 mm. CFRP strips were placed diagonally and anchored to the surrounding frame with CFRP anchors. In addition, the splice regions of the interior columns were wrapped with uniaxial CFRP in two orthogonal directions in FRP strengthening case. Lateral load was applied on the second story and vertical loads were applied on each column at the second story. Some of the remarkable conclusions were as follows. Load deformation diagrams exhibited pinching behavior. Failure of the FRP strengthened specimen was due to premature failure of FRP anchor at the foundation level. Thus the amount and effectiveness of FRP anchors influenced the strengthened frame significantly. The increase in ultimate load was as much as 5 times and 4.6 times for the RC infilled frame (S1) and FRP strengthened frame (S2) respectively when compared to the bare frame. Initial stiffness of S1 and S2 was in the range of ten times to thirteen times that of the bare frame respectively. Strength degradation of S2 was faster than that of S1 due to premature failure of FRP anchors. If system strengthening was done by applying FRP on masonry or RC infills to the selected bays, member strengthening could be eliminated.

In 2007, ElGawady et al. investigated the behavior of FRP strengthened hollow clay masonry walls [77]. One side of three damaged and one undamaged walls was rehabilitated and specimens tested in plane under cyclic loading. The axial load of the half scale specimens was kept constant. Test variables were axial rigidity of FRP and effective moment to shear ratio. Bidirectional or double layer unidirectional FRP was applied to the specimens. They stated that FRP improved stiffness, strength and energy dissipation of the unreinforced specimens. The increase in lateral load was in the range of 42% for low axial rigidity and high moment to shear ratio and 493% for high axial rigidity and low moment to shear ratio respectively. The damage level and type of damage adversely influenced the maximum load of the retrofitted specimens. As the axial rigidity increased, the probability of occurrence of brittle failure mode increased. ElGawady et al. [77] stated that numerical failure loads obtained from simple analytical models predicted experimental failure load satisfactorily.

3. EXPERIMENTAL PROGRAM

3.1. Introduction

Recent earthquakes and revised codes indicate that most of the existing building stock in Turkey need rehabilitation ([78], [79], and [80]). Low to mid-rise buildings which were in the scope of this dissertation were among the most vulnerable buildings. These buildings were damaged for several reasons including but not limited to; the presence of strong beams and weak columns, detailing deficiencies, and poor material properties. When upgrading the structural systems, the most widespread strengthening technique was to construct new shear walls within the frames. Some restrictions such as construction time, cost, changing in functionality and dwellers comfort, called for new technologies. Recently, thanks to developments in the FRP industry, application of FRP materials have emerged as an alternative for repair and strengthening purposes. The main objective of this experimental study was to investigate the behavior as well as strength, stiffness, and energy dissipation characteristics of FRP strengthened R.C. infilled frames. Moreover, the efficiency and effectiveness of the strengthened infilled frames with different aspect ratios were investigated. For this purpose, specimens with identical columns, beams and infills were produced. Different strengthening schemes for different aspect ratios were evaluated. Based on the previous studies ([39], [43], and [71]) done in Bogazici University and Middle East Technical University (METU), three different frame aspect ratio of infilled frames were tested. The specimens were designed and detailed considering existing deficiencies faced in practice. It is believed that the observed failure modes, characteristics of the behavior, and the parameters investigated, like the frame aspect ratio, will be an important step for future studies.

3.2. Selection of Specimens

In order to simulate the behavior of a subassembly, full scale tests should be performed. In other words a true model should be preferred to a scale model. However, this was not feasible as it would require great facilities and larger budgets. Instead, scaled tests were performed to understand the behavior and to obtain general relations which were

applicable to real structures. Scaled tests can explain the behavior of a subassembly and were performed by applying dimensional analysis and similitude requirements. The relation between the model and the prototype were established by using scale factors which derived from similitude requirements [81]. The scale factors and quantities were illustrated in Table 3.1 [81]. To construct this table, it was assumed that time dependent effects which affected the behavior were negligible [81]. In this table, length scale parameter was independent whereas stress scale parameter was one. It meant that the stress-strain curves of model and prototype must be the same [81]. In this table, quantities, dimensions, true model, and practical model scale factors for different quantities were illustrated.

Table 3.1. Scale factors for the practical model (based on the study of Harris et al. [81])

Group	Quantity	Dimensions	True Model	Practical Model
Material	Stress	F/L^2	S_σ	1
	strain	---	1	1
	Modulus of Elasticity	F/L^2	S_σ	1
	Poison's Ratio	---	1	1
	Specific Weight	F/L^3	S_σ/S_L	$1/S_L=3$
Geometry	Linear Dimension	L	S_L	$S_L=1/3$
	Linear Displacement	L	S_L	$S_L=1/3$
	Angular Displacement	---	1	1
	Area	L^2	S_L^2	$S_L^2=1/9$
Loading	Concentrated Load	F	$S_\sigma*S_L^2$	$S_L^2=1/9$
	Line Load	F/L	$S_\sigma*S_L$	$S_L=1/3$
	Pressure	F/L^2	S_σ	1
	Moment	F*L	$S_\sigma*S_L^3$	$S_L^3=1/27$
Note 1: S_s and S_L represented scale factors for length and stress respectively.				
Note 2: S_L was 1/3 for the test specimens.				
Note 3: F and L represented force and length respectively.				

When scaled models were used some problems arose such as size effect, and errors occurred during construction. The strength of the specimen tends to increase when the size is decreased. The smaller specimens had larger scatter in strength [81]. It was also difficult to obtain identical bond stresses in prototype and scaled models. Moreover, surface conditions of the given size should be taken into account in regards to bond properties [81]. Cracking was also influenced by decreased model size. Change in crack width, decrease in number of cracks, and an increase in first cracking load could be expected [81]. Although there were clear disadvantages to use scaled models, (some of which listed above) full

scale tests were not always possible. Carefully and appropriately scaled models can satisfactorily describe the behavior and other parameters of real structures.

Based on previous studies three different frame aspect ratios (l/h), namely 1.0, 1.7, 2.3, were used. A four-storey frame building with three bays in each direction [43] was used as a basis of the aspect ratio of 1.7. The details of the prototype building were given in Figure 3.1. All test specimens were designed and detailed considering deficiencies faced in practice. All test specimens were two-story, one bay, one-third scale reinforced concrete infilled frames. Axial load on the columns was given considering column capacities.

Dimensions of the columns and beams were 100/150 mm and 150/150 mm respectively. The thickness of the infill was about 70 mm excluding plaster. Details of the frame members were illustrated in Table 3.2. Strong beam-weak column design philosophy which was prohibited in the current code was employed to simulate previous applications. The height of the specimens from the foundation level was 1800 mm with various spans. The spans of the specimens between column outer faces for aspect ratios 1.0, 1.7, and 2.3 were 930 mm, 1500 mm, and 2000 mm respectively. Column and beam stirrups were Φ4@95mm, and Φ4@100mm respectively.

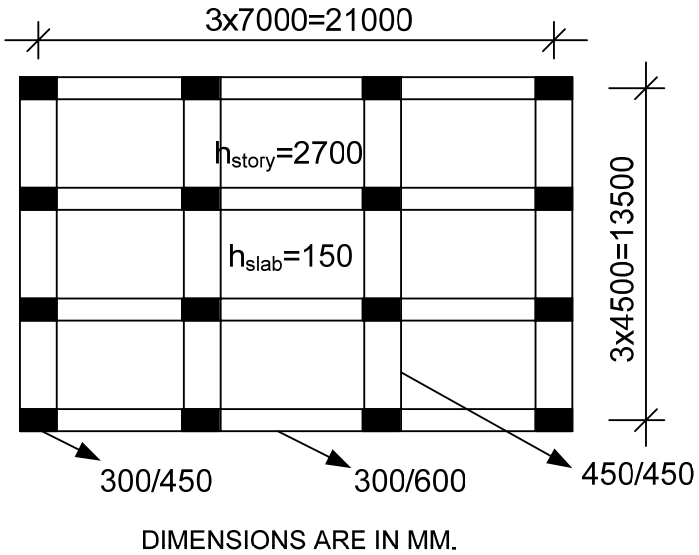

Figure 3.1. Details of the prototype building

Table 3.2. Properties of the test specimens

Specimen	Strengthening Scheme	Column Longitudinal Reinforcement	Beam Longitudinal Reinforcement	f_{ck} (MPa)	f_{mortar} (MPa)	f_{yk} (MPa)	$\frac{N}{N_0}$ (%)	$\frac{M_b}{M_c}$
SA1.0	N/A	4Φ8 (ρ=0.0134) Tie Φ4@95 mm	6Φ8 (ρ=0.0074) Tie Φ4@100 mm	8.0	12.6	347	14	4.2
SA1.0-CV	Cross FRP Vertical FRP			8.9	5.2		11	4.2
SA1.0-C2V	Cross FRP Doubled Vertical FRP			16.9	7.0		9	2.9
SA1.0-CVL	Cross FRP Vertical FRP Around Columns			15.3	7.5		10	2.4
SA1.7-D	Cross FRP Vertical FRP			13.7	5.2		11	3.1
SA1.7-S	Cross FRP Vertical FRP			10.2	6.7		10	4.0
SA2.3	N/A			11.0	6.5		11	3.6
SA2.3-CCM	Doubled Cross FRP			16.0	10.5		10	2.9
SA2.3-CV	Cross FRP Vertical FRP			15.8	7.0		9	3.0
SA2.3-CFM	Doubled Cross FRP Wrapping of Columns			18.0	6.5		10	2.7

3.3. Test Variables

During the production of the specimens, it was intended that all specimens had the same deficiencies common in practice. The deficiencies of the specimens were;

- Low quality concrete,
- Insufficient confinement,
- Hooks with 90^0 ends,
- Plain bars and inadequate lap splice length in columns and beam bottom reinforcement,
- No transverse steel in the joints,
- Strong beams-weak columns

Longitudinal plain reinforcing bars in the columns were Φ8 with a lap splice length of 20Φ. Spacing and the diameter of the stirrups are illustrated in Table 3.2. The ratio of flexural moment capacities of the frame members, (beam vs. column), were also indicated in the last column of Table 3.2. Capacity loss due to inadequate lap splice length was taken into consideration during the calculation of the column flexural capacity. Inadequate confinement was also a common practice in the existing buildings. The main objectives were;

- To investigate the aspect ratio effect on the Fiber Reinforced Polymer (FRP)-strengthened hollow clay tile (HCT) infilled reinforced concrete (RC) frames in terms of stiffness, energy dissipation characteristics, ductility, and load carrying capacity,
- To highlight an effective and efficient strengthening scheme for the frames with different aspect ratios.

10 specimens were prepared and tested to fulfill the intended objective. These specimens can be evaluated in three different groups as illustrated in Figure 3.2. The numbers 1.0, 1.7, and 2.3 which represent the aspect ratio are followed by the capital letters which represents the strengthening scheme. In the case of SA1.7-S and SA1.7-D, S and D stood for the name of the manufacturers. C and V represent the diagonally and vertically applied overlays respectively. CM and FM represent the coarse and fine meshes created by diagonally placed fabrics. In this case the number of diagonally placed parallel fabrics was 2 folds in one face of the first story. L stands for the vertical strips located around column lap splices and 2V depicts that the thickness of vertical strips were doubled.

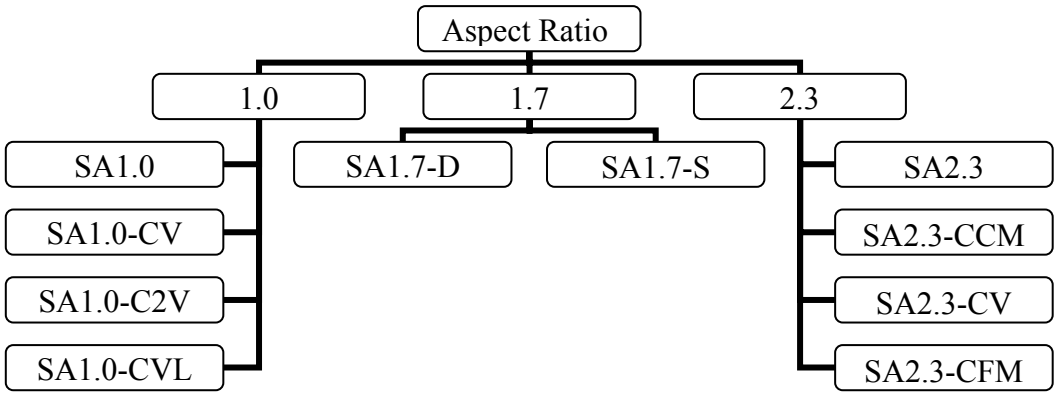

Figure 3.2. The list of the specimens

3.4. Materials

3.4.1. Concrete

Concrete mix was prepared in the laboratory in order to produce a low nominal compressive strength concrete. To fulfill this aim, a high water to cement ratio was used. Two types of mix design were used. The mix design values for the specimens are listed in Table 3.3. In order to determine the compressive and tensile strength of concrete, cylinder samples with a diameter of 150 mm and height of 300 mm were used. Nominal compressive strength and splitting tensile strength values of 150*300 mm cylinder specimens were determined in accordance with ASTM C39-96 [82] and ASTM C496-96 [83] respectively and listed in Table 3.4.

Table 3.3. Concrete mix proportions

For Specimens SA1.7-D, SA1.7-S, SA1.0, SA1.0-CV	
Material	Weight for m^3 (kg/m^3)
Cement, (PKC/B 32.5-R)	270
Water	262
0-3 Sand	450
3-7 Sand (Crushed Sand)	450
7-15 Gravel (Coarse Aggregate)	916
For Specimens SA1.0-C2V, SA1.0-CVL, SA2.3, SA2.3-CCM, SA2.3-CV, SA2.3-CFM	
Material	Weight for m^3 (kg/m^3)
Cement, (PKC/B 32.5-R)	270
Water	233
0-3 Sand	450
3-7 Sand (Crushed Sand)	450
7-15 Gravel (Coarse Aggregate)	916
Super plasticizer	0.8

Table 3.4. Material properties of concrete

Specimen	f_{ck} (MPa)	f_{sp} (MPa)
SA1.0	8.0	0.76
SA1.0-CV	8.9	0.82
SA1.0-C2V	16.9	1.55
SA1.0-CVL	15.3	1.44
SA1.7-D	13.7	1.14
SA1.7-S	10.2	0.83
SA2.3	11.0	0.95
SA2.3-CCM	16.0	1.19
SA2.3-CV	15.8	1.19
SA2.3-CFM	18.0	1.61
Test Method	ASTM C39-96	ASTM C496-96

3.4.2. Reinforcing Steel

Plain bars with different nominal diameters were used for the longitudinal reinforcement, stirrups and ties. Longitudinal bars with a diameter of 8 mm were used for beams and columns. The plain wires with a diameter of 4 mm were used as stirrups and ties. The tests were done in accordance with ASTM A706/A706M-06a [84]. Characteristic values for these bars are given in Table 3.5.

Table 3.5. Material properties of reinforcement

Diameter	Category	f_{yk} (MPa)	E_s (MPa)	f_u (MPa)	ε_y
ϕ8	Longitudinal Steel	347	195000	448	0.0018
ϕ4	Stirrup, Tie	241	198600	423	0.0012

3.4.3. Plaster and Mortar

The same mix design was used for both mortar and the plaster. The plaster thickness was approximately 10 mm while the thickness of mortar between bricks was approximately 3 mm. The mix design is given in Table 3.6. In order to determine the compressive strength of mortar, 50 mm*50 mm*50 mm cube specimens were prepared and tested in accordance with ASTM C109/C109M-95 [85]. Nominal compressive strength of mortar cubes are listed in Table 3.7 for each specimen.

Table 3.6. Mortar mix proportions

Material	Ratio in the mix (by Weight,%)
0-3 Sand	60
Lime	11
Cement	11
Water	18

Table 3.7. Compressive strength of mortar cubes

Specimen	f_{mortar} (MPa)	Test Method
SA1.0	12.6	ASTM C109/C109M-95
SA1.0-CV	5.2	“
SA1.0-C2V	7.0	“
SA1.0-CVL	7.5	“
SA1.7-D	5.2	“
SA1.7-S	6.7	“
SA2.3	6.5	“
SA2.3-CCM	10.5	“
SA2.3-CV	7.0	“
SA2.3-CFM	6.5	“

3.4.4. Masonry Subassemblies

RC frames were infilled with hollow clay tiles (HCTs). Dimensions of the infill material are given in Figure 3.3. In order to determine the shear and compressive strength of the infilling material quadlet and triplet tests were performed respectively. Triplet tests were performed in accordance with ASTM E447-97 [86]. Quadlet test set-up was based on the one given in Angel’s PhD dissertation [87]. Triplet and quadlet test set-up is illustrated in Figure 3.4. Material properties of the masonry are given in Table 3.8.

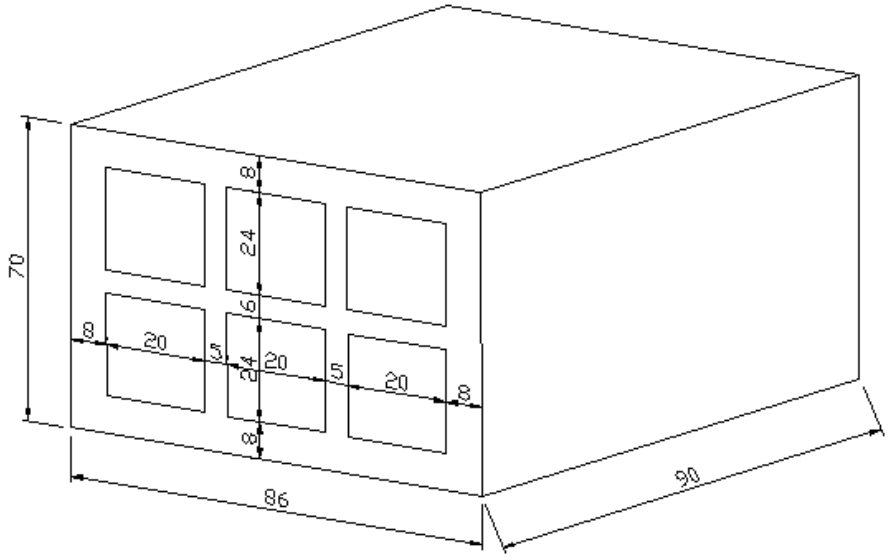

Figure 3.3. Dimensions of the hollow clay tile

Figure 3.4. Test set-up for compressive and shear strengths of a masonry subassembly

Table 3.8 Masonry material properties

Specimen	f_m	f_{bm}* (MPa)	τ_{bm}* (MPa)	τ_p* (MPa)
SA1.0	12.6	5.23	0.46	0.57
SA1.0-CV	5.2	4.44	0.43	0.23
SA1.0-C2V	7.0	4.63	0.44	0.32
SA1.0-CVL	7.5	4.68	0.44	0.34
SA1.7-D	5.2	4.44	0.43	0.23
SA1.7-S	6.7	4.60	0.44	0.30
SA2.3	6.5	4.58	0.44	0.29
SA2.3-CCM	10.5	5.00	0.46	0.47
SA2.3-CV	7.0	4.63	0.44	0.32
SA2.3-CFM	6.5	4.58	0.44	0.29
* The values were calculated based on a linear regression obtained by compressive and shear tests				

3.4.5. Carbon Fiber Reinforced Polymer (CFRP)

Fiber reinforced polymer is a polymer matrix reinforced with fibers. E-glass, kevler/aramid, and carbon are among the most commonly used continuous fibers. Resins can be divided into two parts namely thermoset (polyester, epoxy, vinylester etc.) and thermoplastic (nylon, PET etc.). Although reinforcing fibers are the main constituent in the composite, polymer matrix is also very important. It holds fibers together, helps transferring stresses between fibers and the surrounding structure, and preserves fibers from ambient conditions. There are several fabricating processes for FRP materials some of which are sheet molding compound, filament winding, pultrusion, vacuum compaction, and matched mold processes. Depending on the product, the fabricating process can be chosen. The performance of the FRP composite mainly depends on the materials used and the interaction between fibers and the polymer matrix. For example fiber orientation, length shape, and composition of the fibers, mechanical properties of fiber and the resin matrix, and bond between resin matrix and the fibers are among the parameters that influence the performance of the composite [88].

Low weight, high strength and modulus, improved corrosion resistance, ease of application, minimum disturbance to the dwellers, less space necessity are among the advantages of FRP. Low fire resistance, weakness for ultraviolet light and some chemicals

are among the disadvantages [88]. In civil engineering structures, FRP has large application areas such as bridges, buildings (beams, columns, masonry), bridge decks etc. In this dissertation CFRP which has unidirectional fibers was used. Since it is anisotropic, orientation of fibers where they are used is very important to get the highest advantage. SA1.7-D was strengthened by using Mbrace Fibre and saturant. Sikadur hex C230 and sikadur 330 were used for the rest of the strengthened specimens. The details of the CFRP and saturant were obtained from the manufacturers and given in Tables 3.9, 3.10, and 3.11. The main differences between these FRPs were the fiber overlay thickness and the elongation at break values. The color of the adhesives one of which was blue and viscosity of the mix were also different. The fluidity of the blue one was higher than that of the grey one.

Table 3.9. Properties of Sikadur 330 impregnation resin

SIKADUR-330 TWO PART EPOXY IMPREGNATION RESIN	
APPEARANCE	Resin Part A: white Hardener Part B: grey Part A+B mixed: light grey
PACKAGING	5 kg (A+B) Pre-dosed units
SHELF LIFE	24 months in original packaging at temperatures between +5 ^{0}C and +25 ^{0}C
DENSITY	Mixed Resin: 1.31 kg/l (at 23^{0}C)
TENSILE STRENGTH (DIN 53455)	30 N/mm^2 (7 days at 23^{0}C)
E-MODULUS (DIN 53455)	Tensile: 4500 MPa (7 days at 23^{0}C)
ELONGATION AT BREAK (DIN 53455)	0.9% (7 days at 23^{0}C)
MIXING	Part A: part B=4:1 by weight

Table 3.10. Product data for Sikawrap Hex-230C CFRP overlays

SIKAWRAP HEX-230 C WOVEN CARBON FIBER FIBRIC FOR STRUCTURAL STRENGTHENING	
DESCRIPTION	A unidirectional woven carbon fiber fabric for the dry application process
TYPE	Mid strength carbon fibers
CONSTRUCTION	Fiber orientation:0^0 (unidirectional) Warp: black carbon fibers (99% of total areal weight) Weft: white thermoplastic heat-set fibers
FABRIC WIDTH;LENGTH/ROLL	300/600 mm ≥ 50 m
STORAGE	24 months from date of production if stored properly
AREAL WEIGHT	225 gr/m2
DESIGN THICKNESS	0.13 mm (based on fiber content)
TENSILE STRENGTH	3500 MPa (nominal)
TENSILE E-MODULUS	230000 MPa (nominal)
ELONGATION AT BREAK	1.5% (nominal)

Table 3.11. Properties of CFRP, primer and epoxy based saturant used for SA1.7-D

MBRACE PRIMER	
COLOUR	Transparent
TENSILE STRENGTH	>12 MPa
TENSILE E-MODULUS	>700 MPa
MIXING (BY WEIGHT)	Component A:77% Component B:23%
MBRACE ADESIVO (SATURANT)	
COLOUR	Blue
DENSITY	1.02+-0.024 kg/lt
COMPRESSIVE STRENGTH	>80 MPa
TENSILE STRENGTH	>50 MPa
TENSILE E-MODULUS	>3000 MPa
ELONGATION AT BREAK	2.50%
MIXING (BY WEIGHT)	Component A:76% Component B:24%
PACKAGING (PER SET)	10 liters
MBRACE FIBRE C1-30	
TYPE	High strength carbon fibers
THICKNESS	165 micron
FABRIC WIDTH;LENGTH/ROLL	50 cm x 100 m (roll)
TENSILE STRENGTH	>3430 MPa
E-MODULUS	230000 MPa
ELONGATION AT BREAK	1.5%

3.5. Details of the Specimens

The production and the reinforcement details of specimens as well as the strengthening procedure and details are explained herein. The production phase can be clarified in four parts; preparation of steel cage, casting of concrete, laying of bricks and application of plaster, and strengthening of specimens with unidirectional CFRP materials.

As mentioned before, plain bars of 8 mm diameter were used as longitudinal reinforcement for beams and columns. In columns there were the lap splices with a length of approximately 16 cm at floor levels. Moreover, there was no any transverse reinforcement at the joints. Plain bars used for beams had hooks of 135^0. Plain wires of 4 mm diameter were used as ties and stirrups. Transverse reinforcement had 90^0 hook ends. The arrangement of longitudinal and transverse steel was the same for all the specimens. The details of reinforcement were drawn and illustrated in Figures 3.5, 3.6, and 3.7.

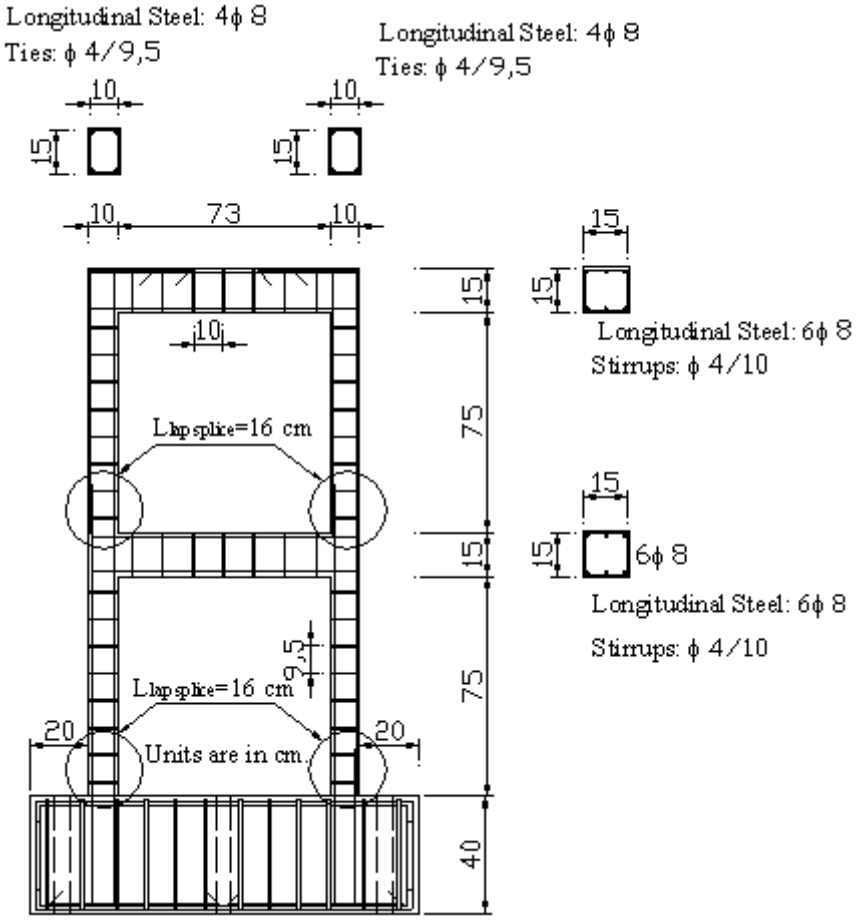

Figure 3.5. Reinforcement detail of the specimens with an aspect ratio of 1.0

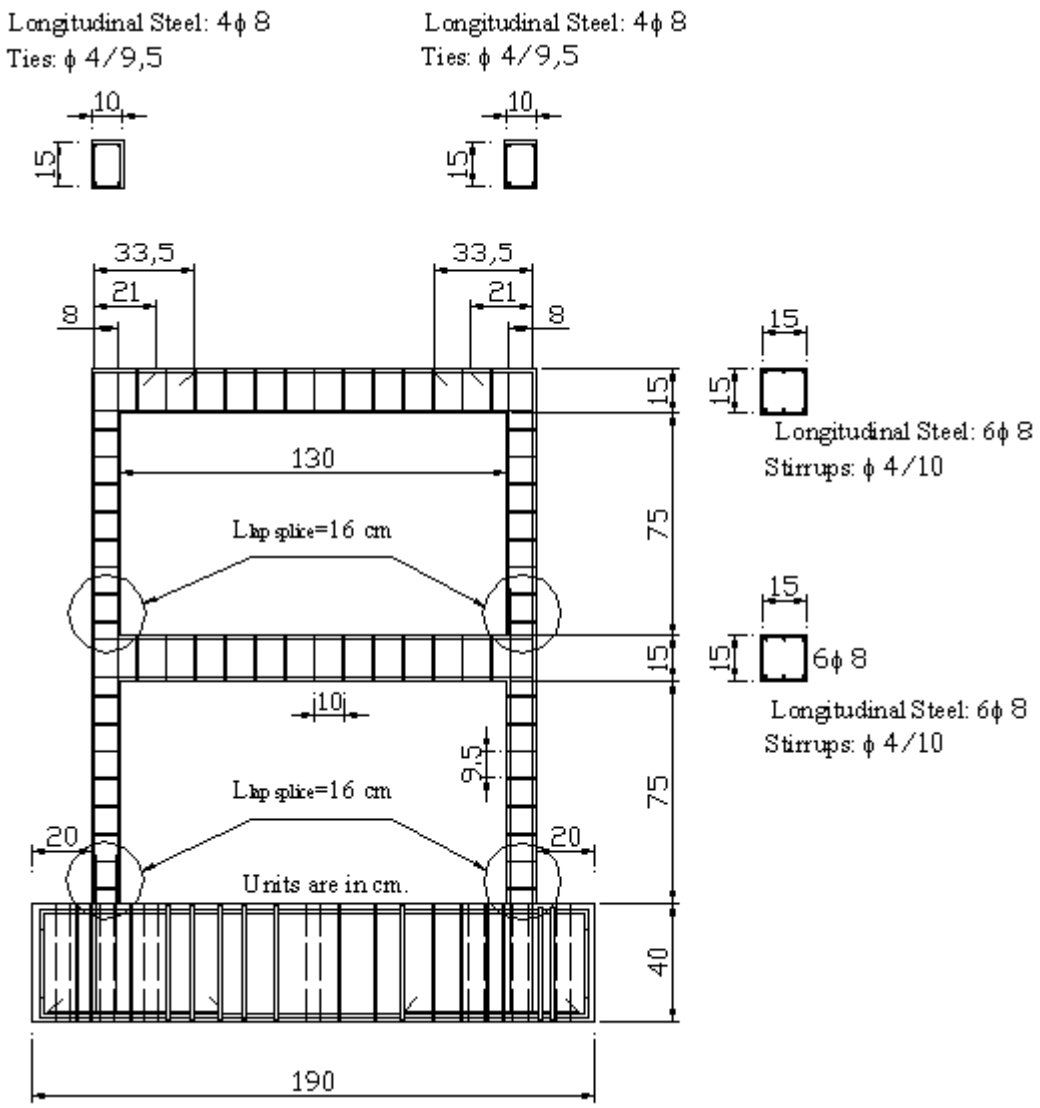

Figure 3.6. Reinforcement detail of the specimens with an aspect ratio of 1.7

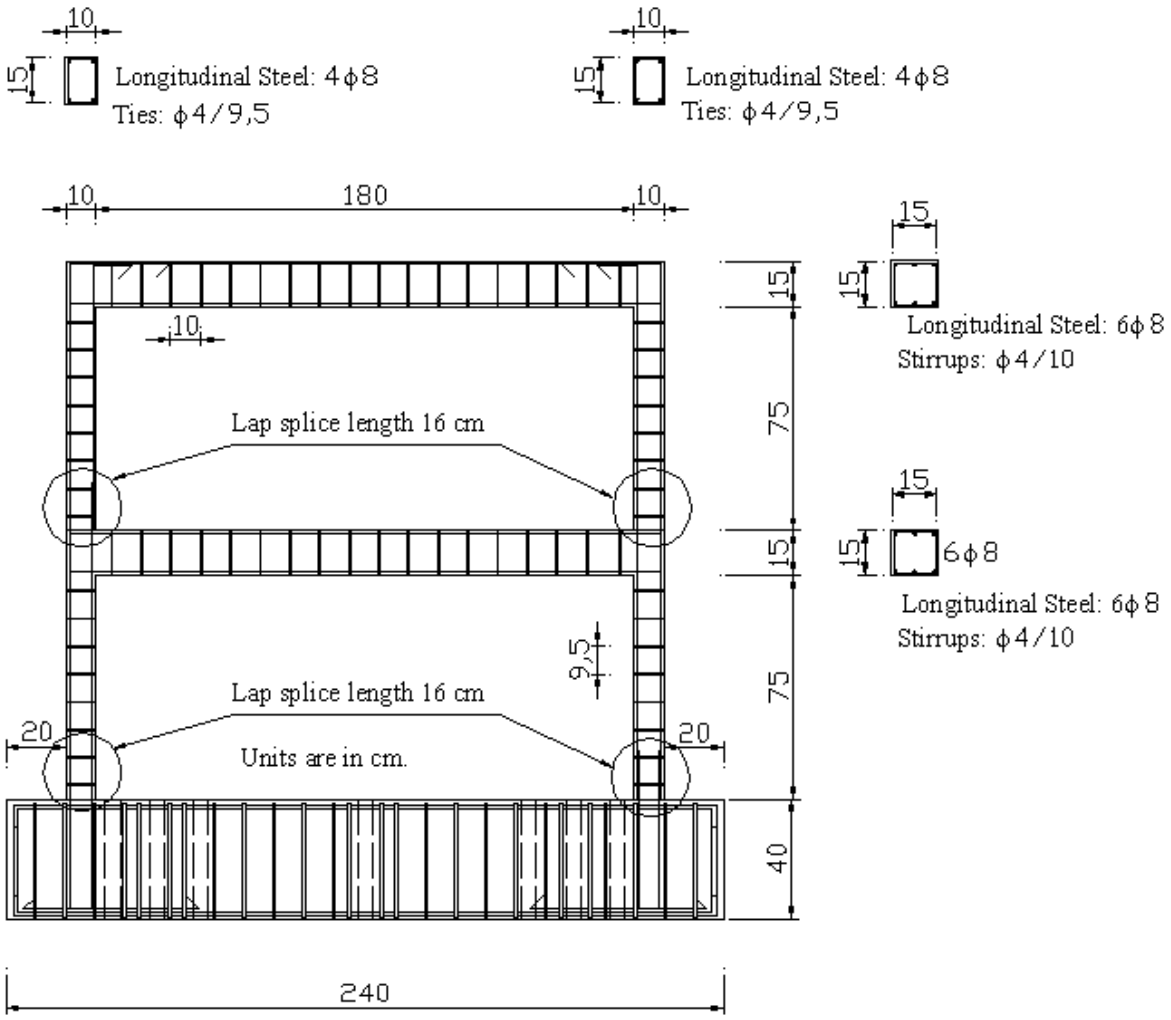

Figure 3.7. Reinforcement detail of the specimens with an aspect ratio of 2.3

Figure 3.8. Picture of reinforcement cage prior to casting of concrete.

The second part included casting of concrete. The specimens were cast in a horizontal position unlike the practice as shown in Figure 3.8. This might result in some imperfections like retention of air voids or bubbles around the reinforcing steel which deteriorated the bond between steel and concrete. To eliminate this, extra care was given while pouring the concrete. Vibrators and a rubber hammer were used to place concrete appropriately. Although segregation, in practice, is indispensable for high w/c ratio, extra care was taken during the production of the specimens to eliminate or minimize segregation. After curing of the specimens for 5 days, the mold was removed and the specimen was raised to upright position.

The third process was laying the bricks and plastering the specimen. Bricks were flush to one side of the specimens. While they were laying, the cores were kept vertical to the bed joints. A professional mason was hired to lay the bricks so they would correspond to brickwork laid in practice. The thickness of the bricks was about 70 mm. The pictures related to this phase are given in Figure 3.9. The thickness of the plaster was between 8.5 mm-10 mm. In order to have an identical plaster thickness, long narrow strips of wood were used.

Figure 3.9. Laying of bricks and plastering of the brick wall

The strengthening procedure followed the completion of brickwork and plastering. Strengthening was achieved by applying CFRP. Depending on the aspect ratio and previous test results, different strengthening schemes were used. The procedure can be summarized as follows. The place of the anchor holes were determined and drilled into predefined depths. The holes were cleaned by using an air compressor to remove any dust or loose materials. This was done to eliminate any inconvenience for the bond between concrete surface and epoxy impregnated CFRP anchors as shown in Figure 3.10. As any surface eccentricity could cause early failure of CFRP, any roughness on the surface of the specimens was smoothed by sandpaper. All CFRP were cut in previously determined dimensions prior to application. All strengthened specimens had flag fabrics on the corners and cross diagonal overlays. Some specimens had flags at the mid-span of the beams as well. In some applications, columns were beveled with a radius of about 20 mm. The differences considering CFRP details were illustrated while the strengthening scheme was explained.

During the strengthening process Sikadur 330, a two component epoxy based impregnating resin, was first applied to the substrate by using a brush and a roller. Before the application of the epoxy resin, dew point, substrate, ambient temperature, and moisture

Figure 3.10. Cleaning of the anchor holes

content were checked. The preparation of the two-component epoxy impregnation resin was done by using a mixing spindle attached to a slow speed electric drill as illustrated in Figure 3.11. The mix was stirred at slow speed three or four minutes conforming to the manufacturer's recommendations. Depending on the ambient temperature and application speed, the mix amount was determined because potlife of the mixture started as soon as the components mixed together and it was directly a function of ambient temperature. In the strengthening procedure, corner flag fabrics were stacked preceding the placement of cross diagonals or other overlays (vertical strips, wrapping of columns etc.). Since the fabric was unidirectional, two layers of flags were used horizontally and vertically respectively as shown in Figure 3.12. As soon as CFRP was placed on the wall, a special plastic impregnating roller was used parallel to the fiber direction so that the epoxy resin was evenly distributed over the whole fabric surface and the fabric was not folded. Before the application of second layer of the flag fabric which was parallel to the column axis, the two component epoxy impregnation resin was applied on the previous fabric. Then cross diagonal overlays were stack on the infill wall at both faces. Excessive amount of the fabric on the corners was cut with a special scissors to fit the corner geometry and to facilitate the anchor application. Application of vertical strips was illustrated in Figure 3.13. Anchor application started following the application of cross diagonals and vertical strips. The holes were filled with the two-component epoxy impregnation resin and the anchors were impregnated with the two-component impregnation resin prior to putting the

anchors into the holes. Two anchors, one of which was placed completely, were shown in Figure 3.14. The specimens were left to cure for about 7 days following to the CFRP placement.

Figure 3.11. Preparation of the epoxy resin

Figure 3.12. Application of corner flags

Figure 3.13. Application of vertical strips

Figure 3.14. Placement of anchors

The first strengthened specimen was SA1.7-D. The strengthening scheme included cross diagonal fabrics with 200 mm width and vertical strips with a width of 50 mm. Specimens SA1.7-S, SA1.0-CV, SA1.0-C2V, SA2.3-CV had the same strengthening scheme. However, vertical strips of the specimen SA-C2V were doubled as compared to the other specimens with the same scheme. Dimensions of the anchors and strips were illustrated in Table 3.12. In order to determine the CFRP anchor widths, it was assumed that 30 to 40% of the anchorage capacity was effectively used. The anchor depth, hole diameter, concrete quality, workmanship, eccentricity on the applied load influenced the performance of the anchors [89]. The detailed information can be found elsewhere [89].Since the anchor depths were kept constant, CFRP anchor widths were a function of CFRP strip widths. The hole patterns were identical for specimen SA1.7-D and SA1.7-S. However the depth of the holes at the foundation level shifted from 8 cm to 15 cm. Figures 3.15, and 3.16 illustrated the strengthening pattern of specimens SA1.0-CV and SA1.0-C2V. Close ups of the anchors were shown in Figure 3.17 for the specimens SA1.0-CV, SA1.0-C2V, SA1.7-S and SA2.3-CV. Strengthening pattern of specimen SA1.7-D was illustrated in Figures 3.18, and 3.19. Since the span of the specimen increased, the number of holes on the wall was also raised from 3 to 5. The close-ups of the typical holes are shown in Figure 3.20. Although specimen SA1.7-S had the same strengthening technique with SA1.7-D, it differed from SA1.7-D in terms of anchorage depth at the foundation level and materials used. The strengthening scheme and details are illustrated in Figures 3.21 and 3.22. SA2.3-CV had the same strengthening pattern with SA1.7-S but more holes were used on the wall due to the increased span of the specimen. The necessary details of the strengthening pattern for SA2.3-CV are given in Figures 3.23 and 3.24.

Figures 3.25 and 3.26 illustrated the strengthening scheme of SA1.0-CVL. The pattern changed slightly. The strips; which were used to eliminate deficiencies created by inadequate lap splices; shifted from vertical strips on the masonry wall to vertical strips around columns. Close-up of FRP anchors, dimension and location of vertical strips as well as close up of vertical FRP around columns are illustrated in Figures 3.27, 3.28, and 3.29. To prevent any misunderstanding, vertical strips around columns and anchors used for these strips are shown in Figure 3.28. These anchors (12cm*44cm) were bonded to the vertical sheets on the outer face of the columns which were underneath the vertical strips around the columns. To reiterate, fiber direction of the strips around columns was

Table 3.12. Dimensions of CFRP anchor fabrics

		Hole	CFRP anchor	
Specimen	Anchor Detail	Depth (mm)	Width (mm)	Length (mm)
SA1.0-C2V	A	120	120	340
	B	80	80	260
	C	90	80	190
	D	50	80	200
	E	150	80	440
	F	60	80	220
	G	150	120	440
SA1.0-CV SA1.7-S SA2.3-CV SA2.3-CCM	A	120	80	340
	B	80	80	260
	C	90	80	190
	D	50	80	200
	E	150	80	440
	F	60	80	220
	G	150	80	440
SA1.7-D	A	120	80	340
	B	80	80	260
	C	90	80	190
	D	50	80	200
	E	80	80	260
	F	60	80	220
	G	80	80	260
SA1.0-CVL	A	50	80	200
	B	80	80	260
	C	90	80	190
	D	50	80	200
	E	150	80	440
	F	60	80	220
	G	150	80	440
SA2.3-CFM	A	120	100	340
	B	80	100	260
	C	90	80	190
	D	50	80	200
	E	150	100	440
	F	60	80	220
	G	150	100	440

perpendicular to horizontal axis. These vertical strips were connected to the foundation beam by using two CFRP anchors for each column. Moreover, CFRP strips under these vertical CFRPs were used to increase continuity between different story levels at lap splice regions.

Specimen SA2.3-CCM had cross diagonals extended from column-foundation corners to the mid span of the specimen. The same pattern was used for the second story as well. New flag fabrics were introduced at the mid-span in this specimen. The aim was to increase the shear strength of the beams and to confine masonry at the end of the cross diagonals in order to prevent possible early crushing of the masonry panel. Similar to corner flags, the flags with horizontal fibers were placed prior to the placement of the second layer of FRP fabrics. Second layer flags had fibers vertical with respect to the first layer fibers. Vertical and horizontal flags at mid-span had the same dimensions. The scheme and necessary dimensions are illustrated in Figures 3.30 and 3.31. Close-ups of typical FRP anchors of specimen SA2.3-CCM were seen in Figure 3.32.

Specimen SA2.3-CFM had evenly distributed cross diagonals with a width of 80 mm and overlay which confined the columns throughout the story. Moreover, new flag fabrics were introduced as in the case of SA2.3-CCM. Since cross diagonals were evenly distributed on the wall the middle flags were extended into 1400 mm. The fabrics with horizontal fibers were not used for the beams in the middle region. To confine middle region of the wall horizontal flags with a depth of 100 mm were used on the top of the vertical flags which lied underneath. In other words horizontal flags in the middle region had a depth of 100 mm both in the front and back faces of the specimen. Moreover these horizontal flags were used only on the infill wall because they were found to be ineffective on the beam due to horizontal fiber direction. It may be necessary to reiterate that the width of the cross diagonals of all the other specimens were 200 mm. The width of FRP anchors was determined according to their capacities and illustrated in Table 3.12. Front and back views of FRP scheme and necessary dimensions were shown in Figures 3.33 and 3.34. The Figures 3.35 and 3.36 depicted close-ups of CFRP anchors and details of the confinement CFRP used on the columns.

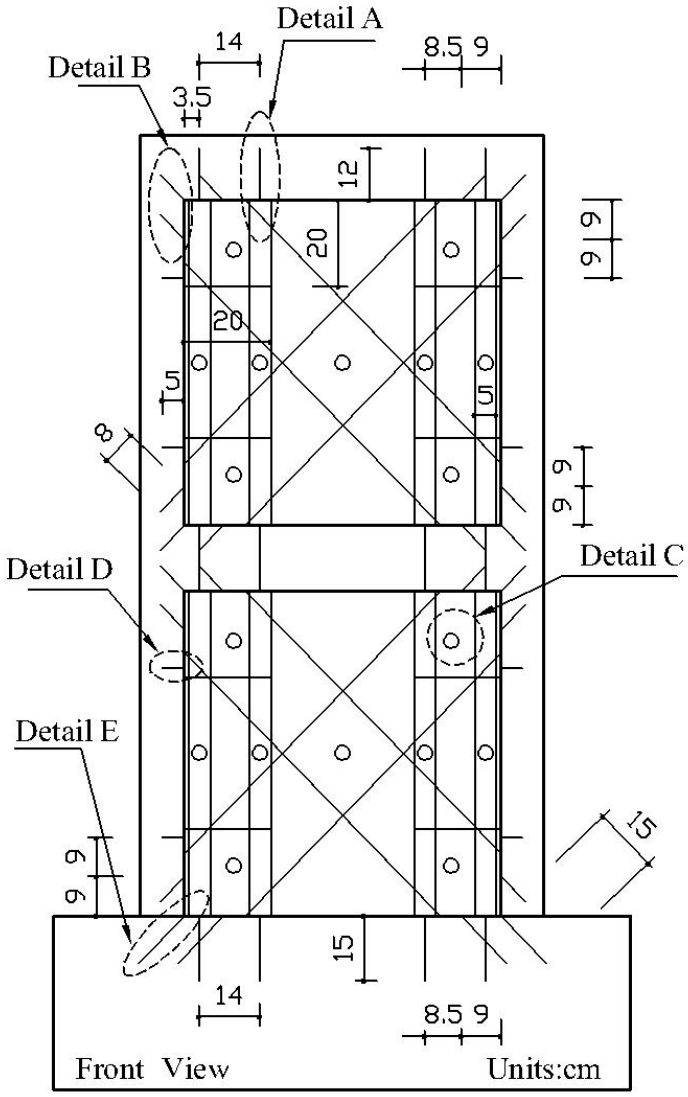

Figure 3.15. Front view of specimens SA1.0-CV and SA1.0-C2V

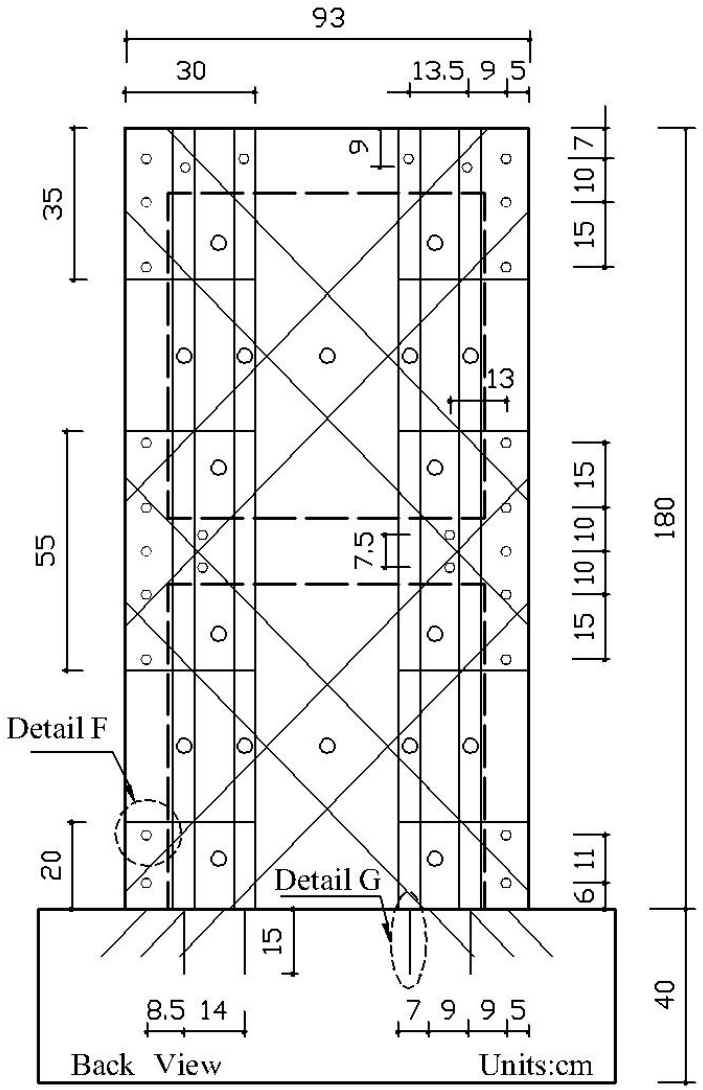

Figure 3.16. Back view of specimens SA1.0-CV and SA1.0-C2V

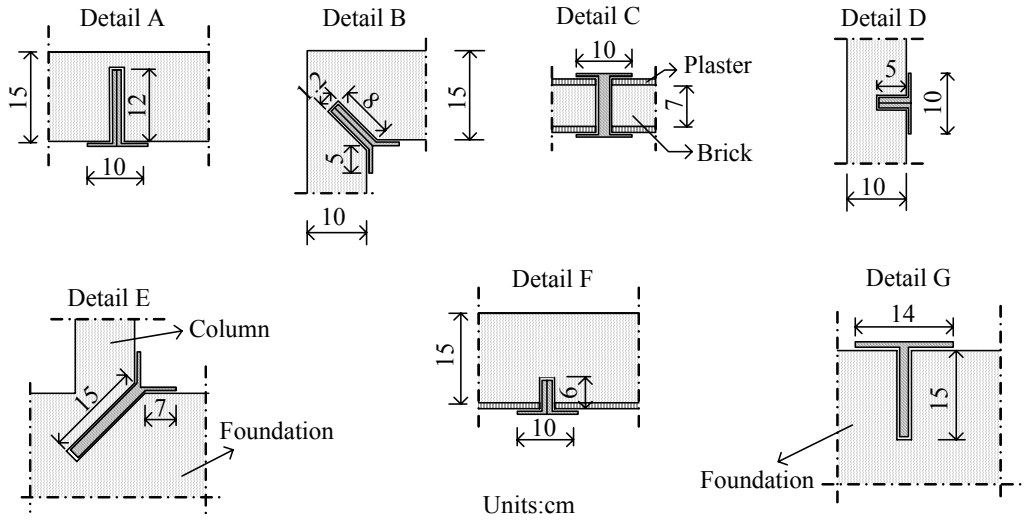

Figure 3.17. SA1.0-CV, SA1.0-C2V, SA1.7-S and SA2.3-CV anchor details

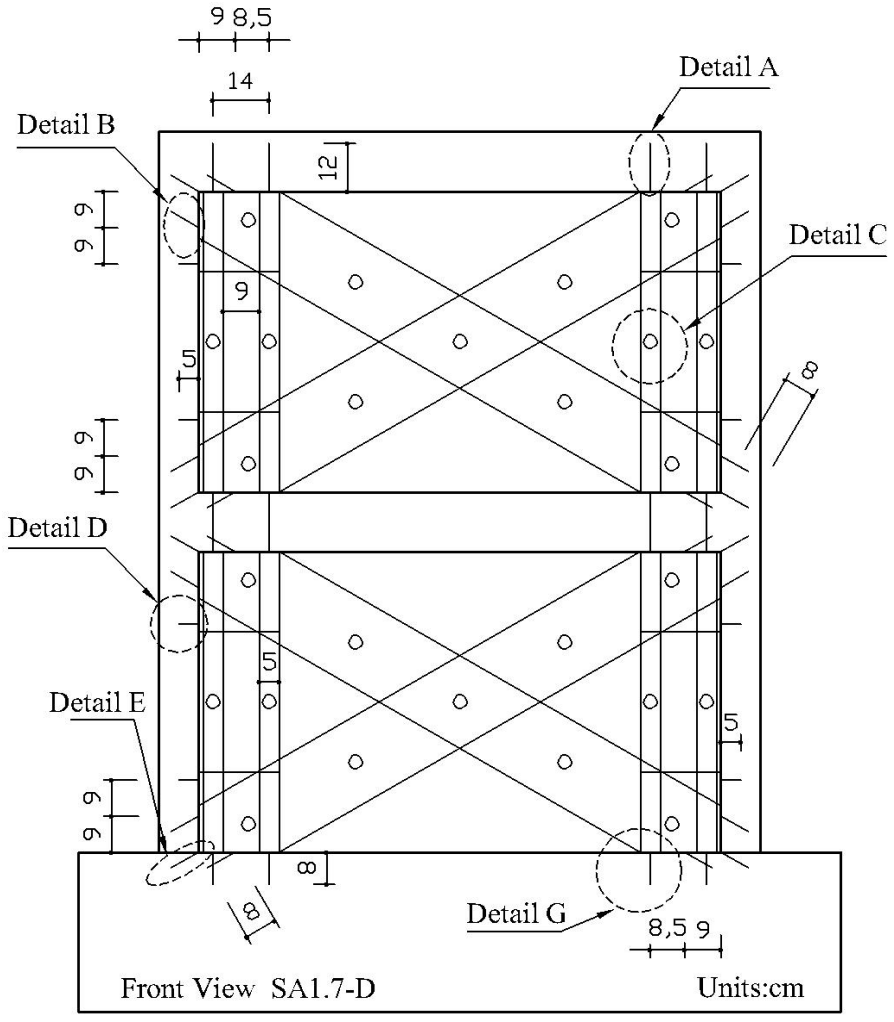

Figure 3.18. Front view of specimen SA1.7-D

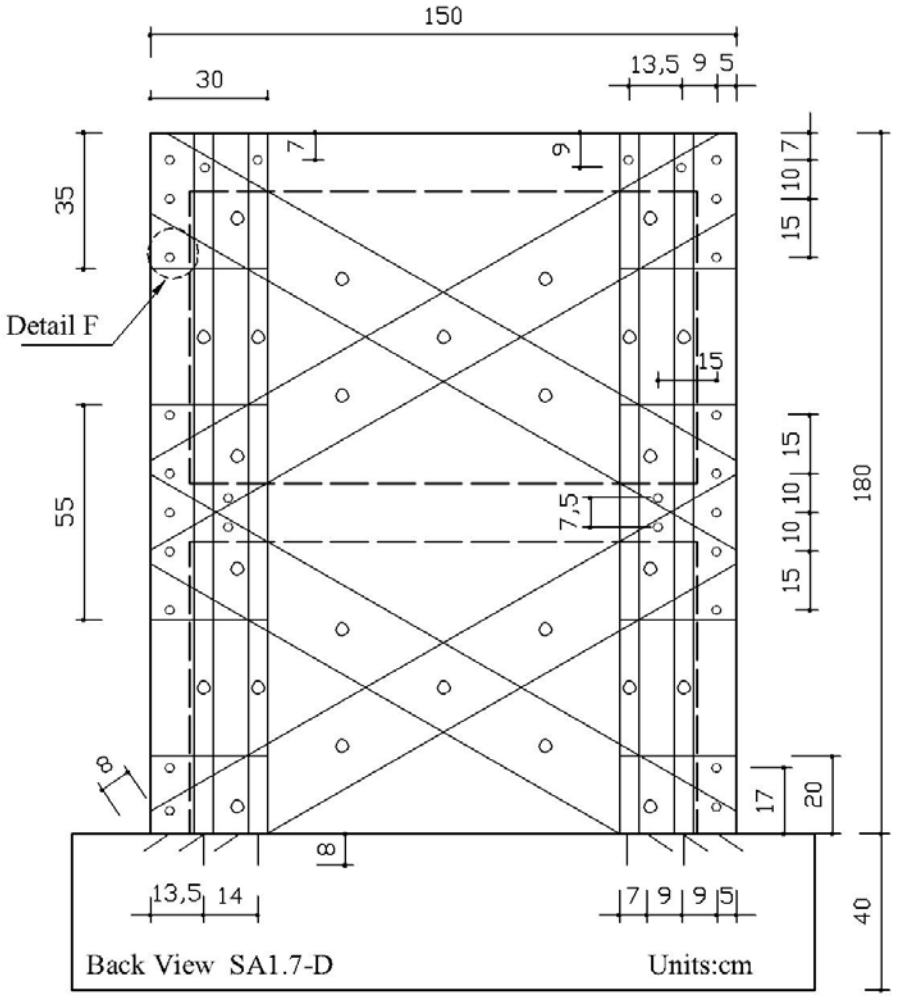

Figure 3.19. Back view of specimen SA1.7-D

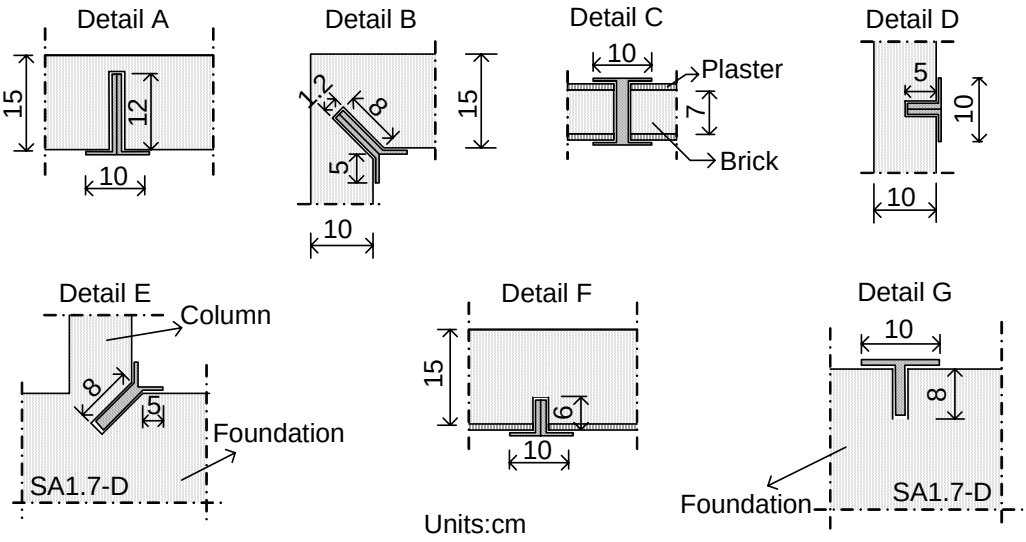

Figure 3.20. Anchor details of specimen SA1.7-D

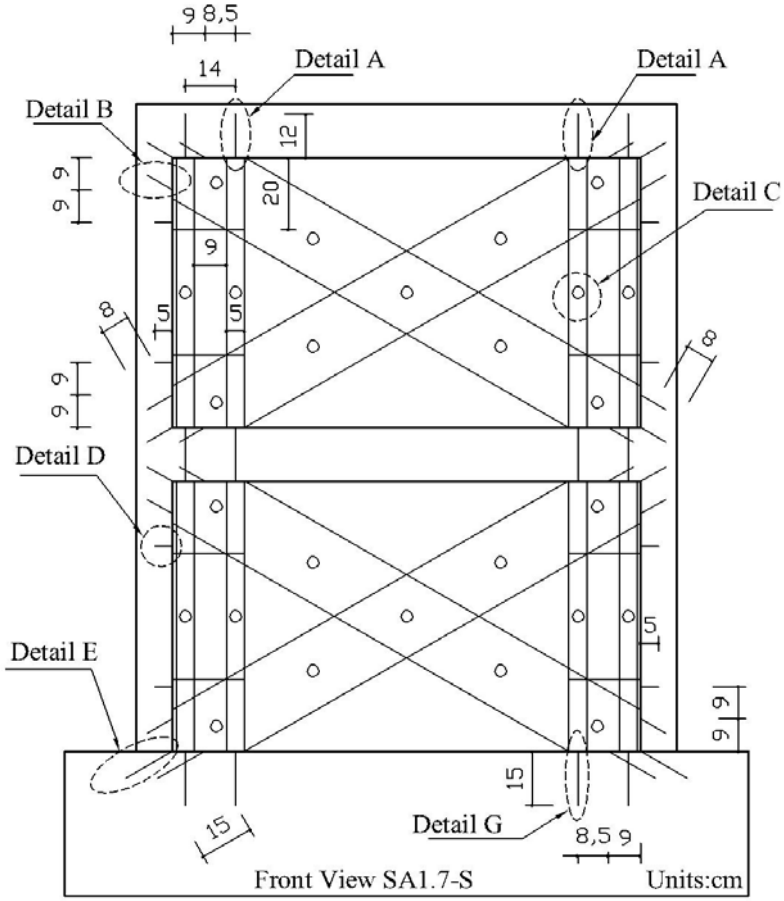

Figure 3.21. Front side of specimen SA1.7-S

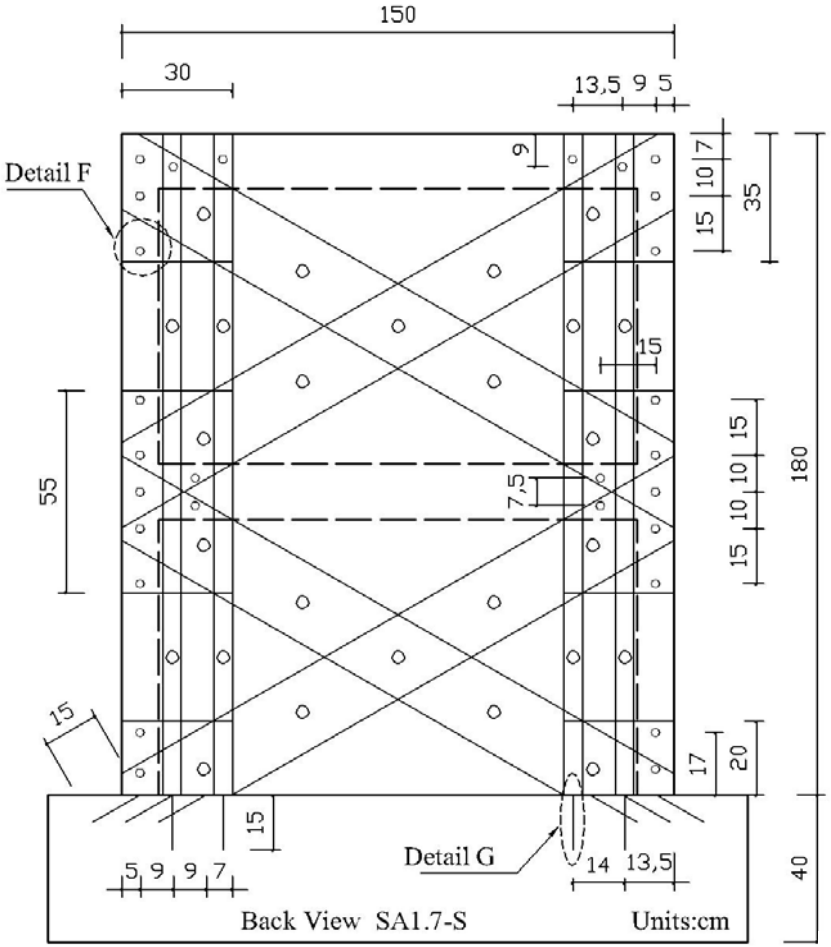

Figure 3.22. Back side of specimen SA1.7-S

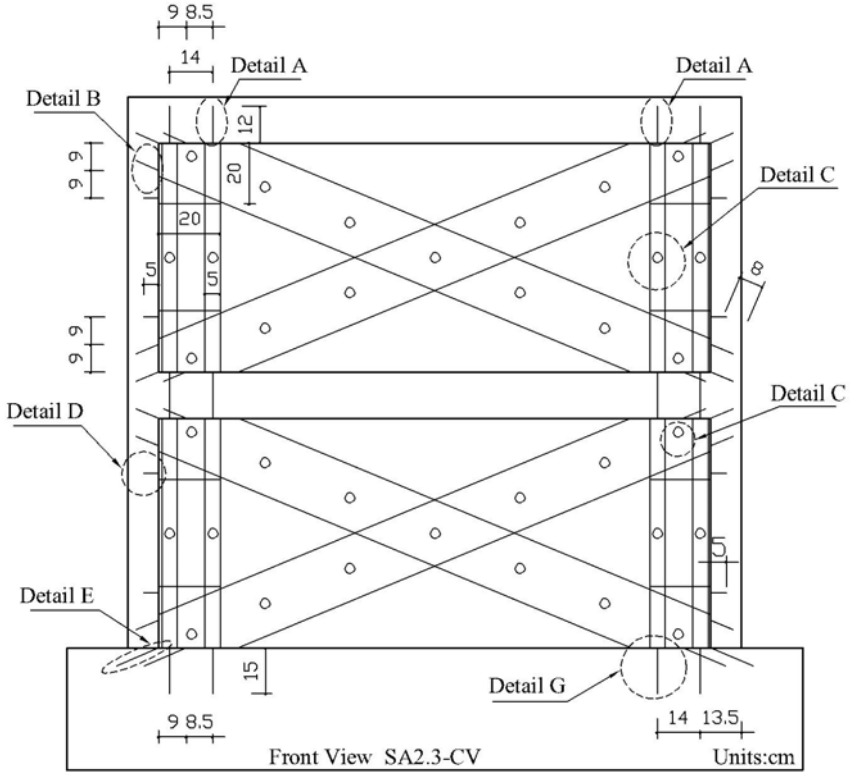

Figure 3.23. Front view of strengthening details of specimen SA2.3-CV

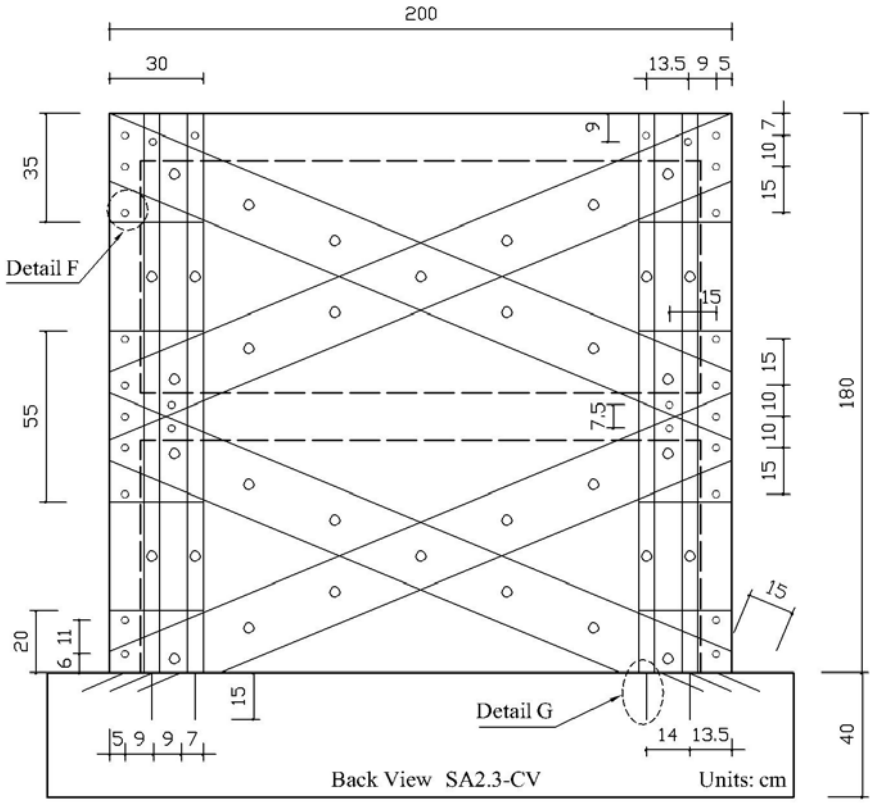

Figure 3.24. Back view of strengthening details of specimen SA2.3-CV

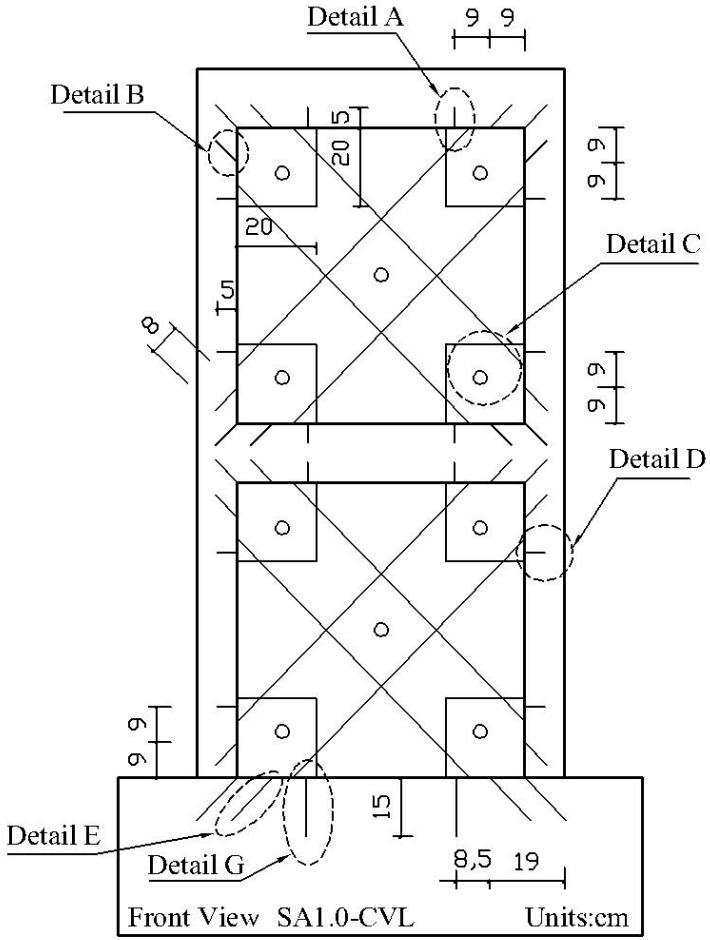

Figure 3.25. Front view of strengthening details of SA1.0-CVL

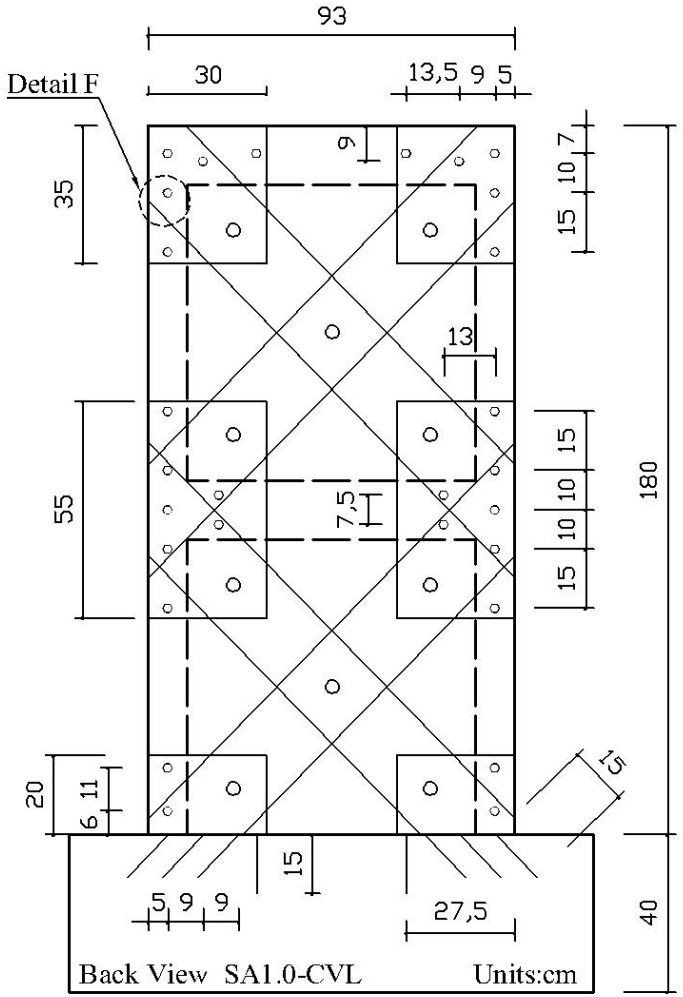

Figure 3.26. Back view of strengthening details of SA1.0-CVL

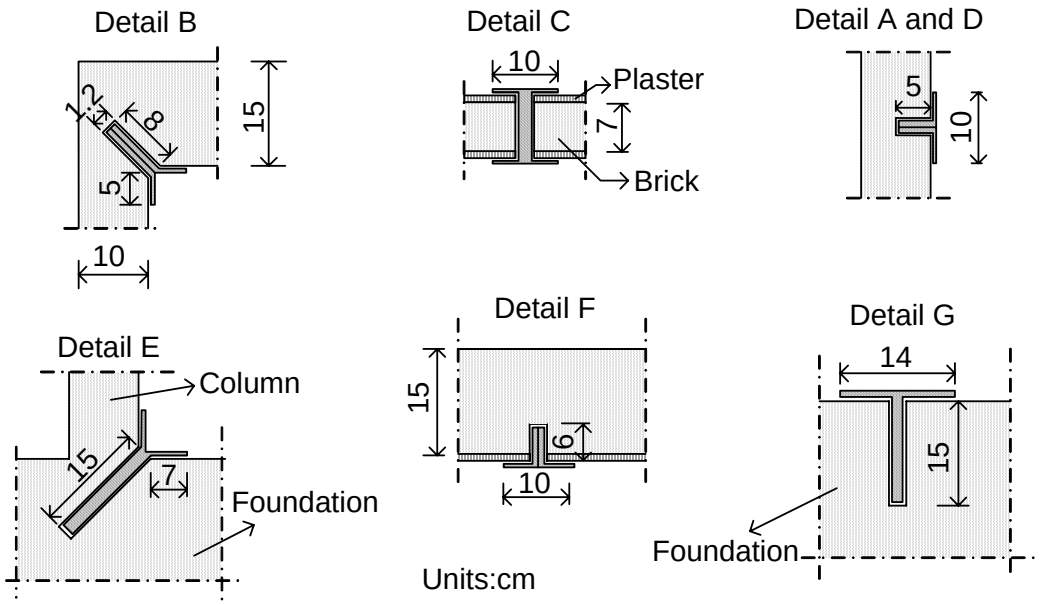

Figure 3.27. Close-up of anchor details of SA1.0-CVL

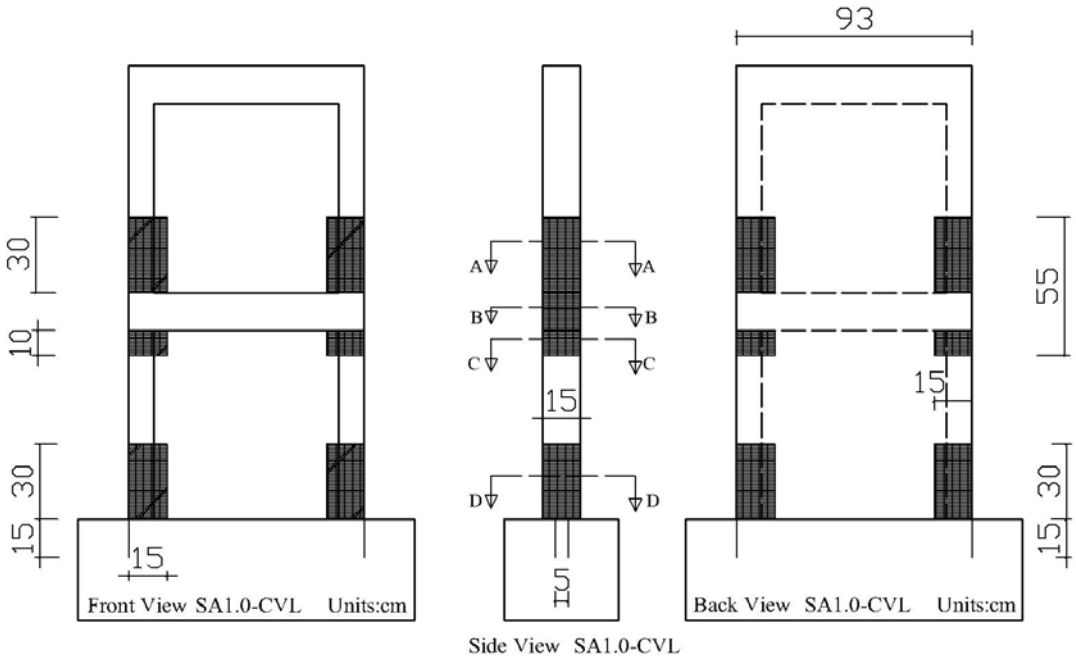

Figure 3.28. Dimensions and locations of vertical FRPs around columns

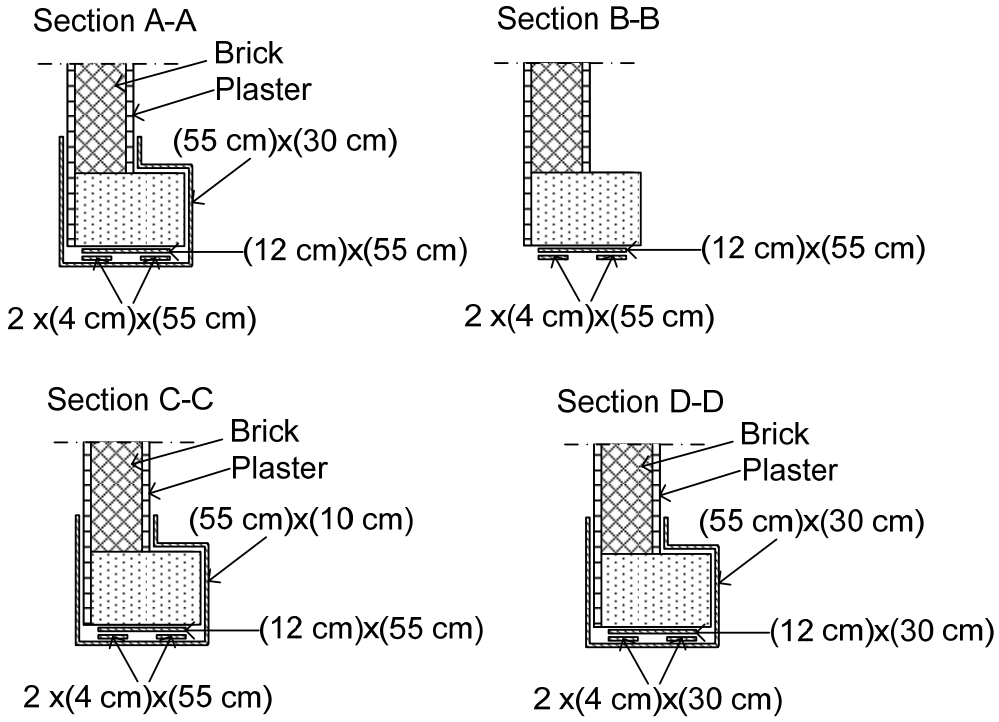

Figure 3.29. Close ups of vertical FRPs around the columns for specimen SA1.0-CVL

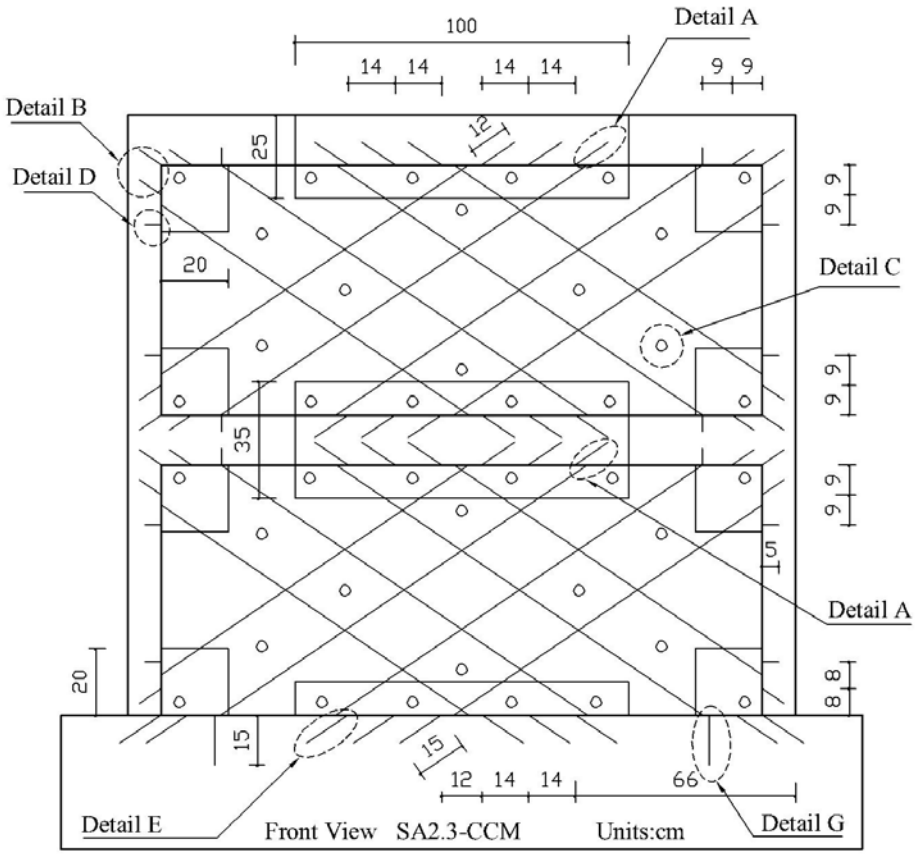

Figure 3.30. Front view of strengthening details of specimen SA2.3-CCM

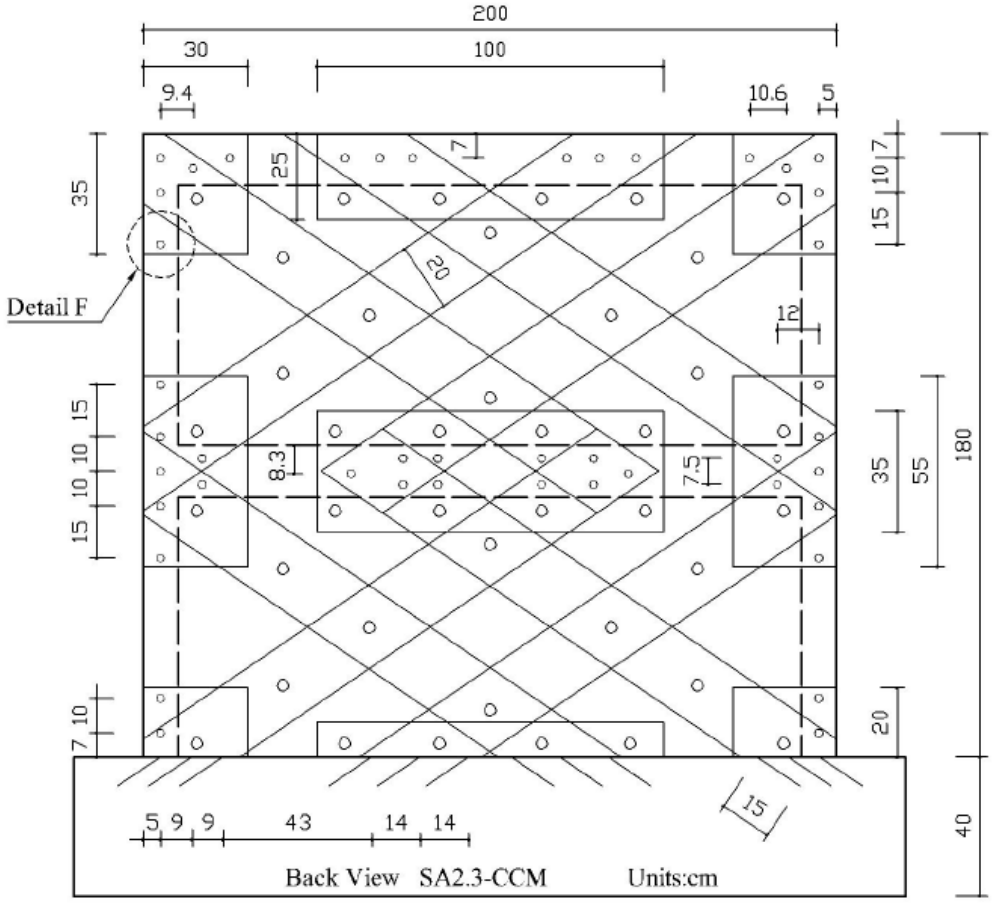

Figure 3.31. Back view of strengthening details of specimen SA2.3-CCM

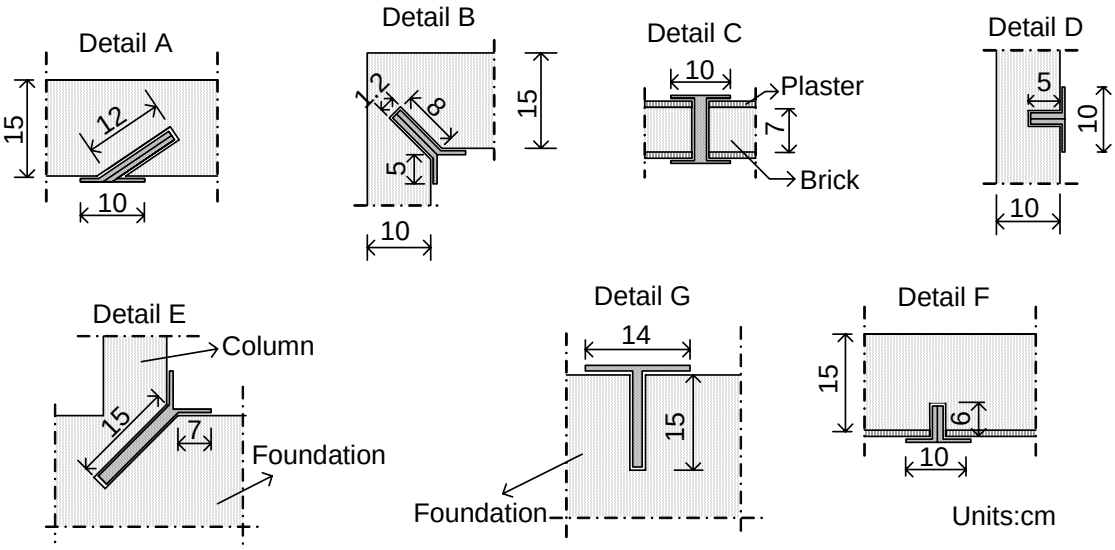

Figure 3.32. Close ups of FRP anchors of specimen SA2.3-CCM

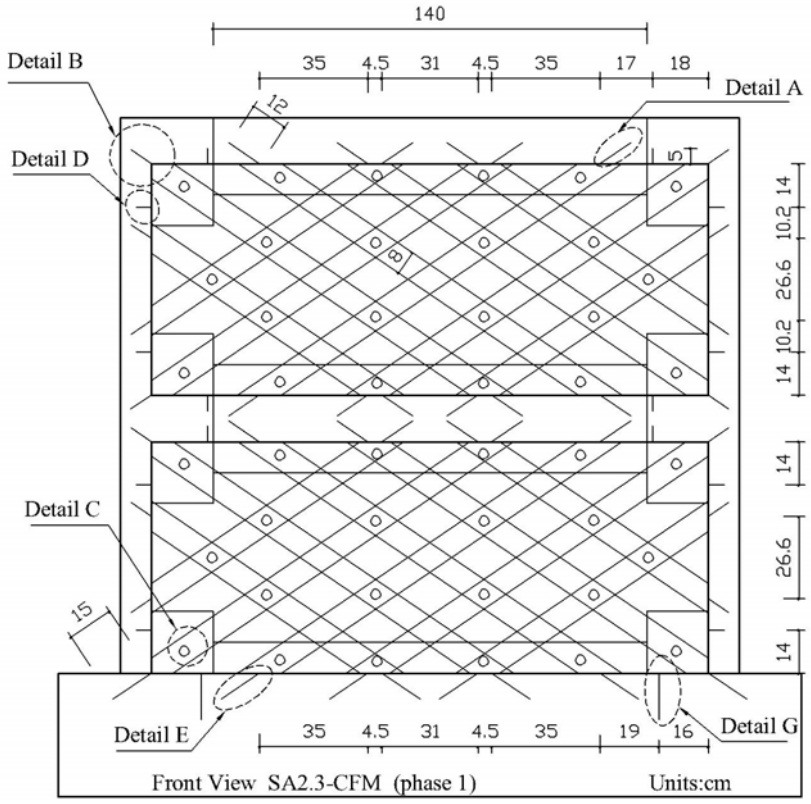

Figure 3.33. Front view of strengthening details of SA2.3-CFM

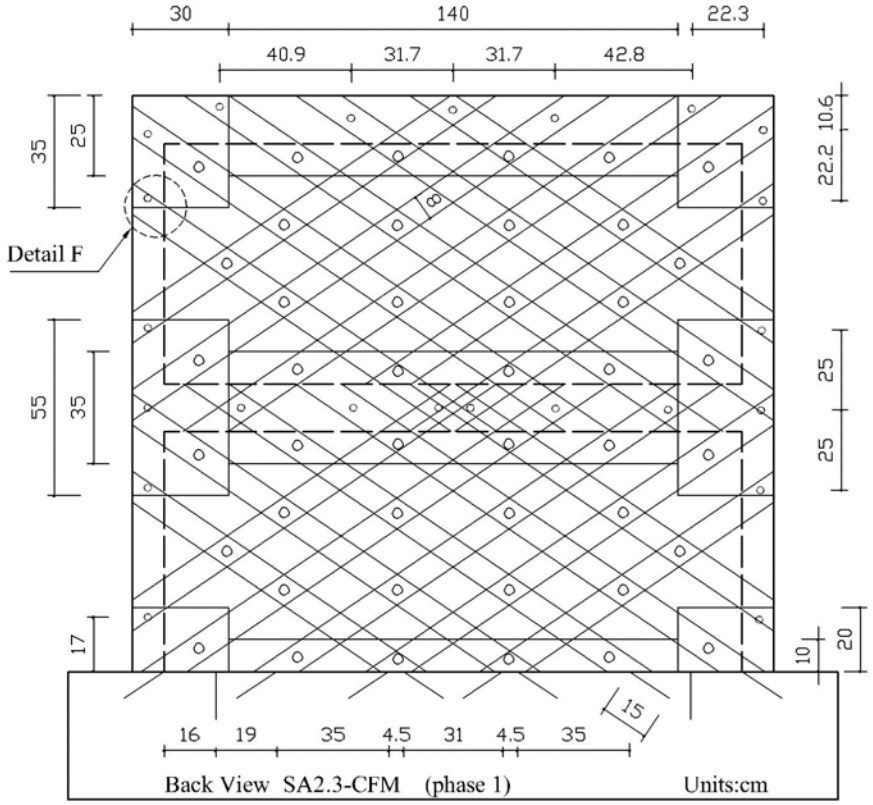

Figure 3.34. Back view of strengthening details of SA2.3-CFM

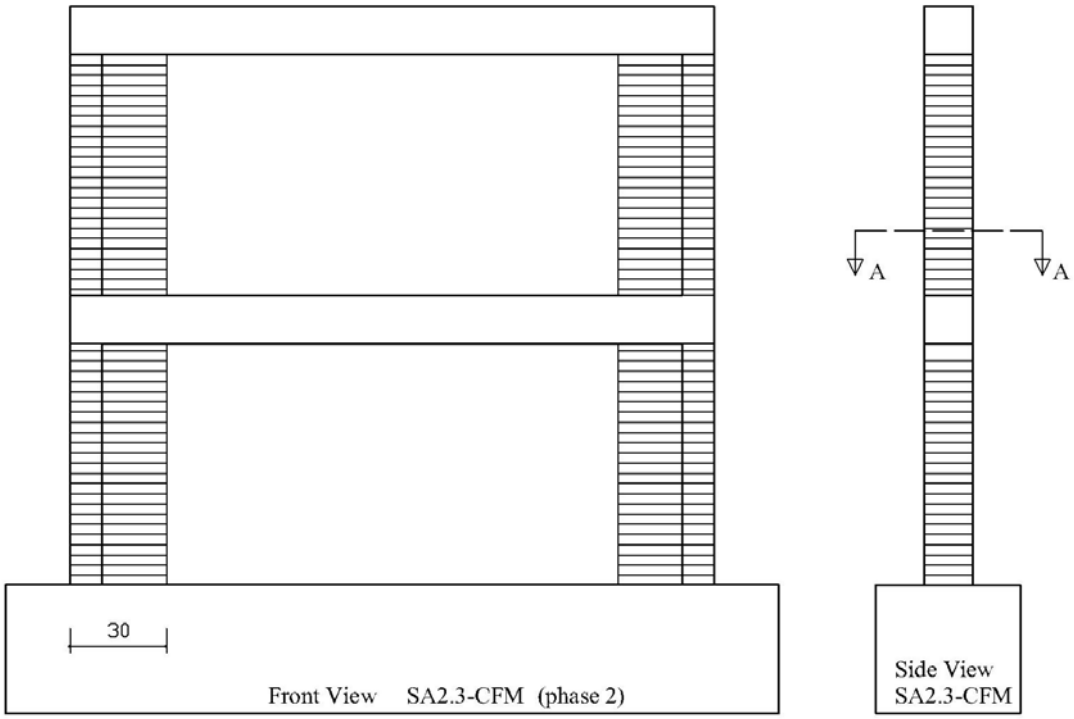

Figure 3.35. Confinement of the columns of SA2.3-CFM

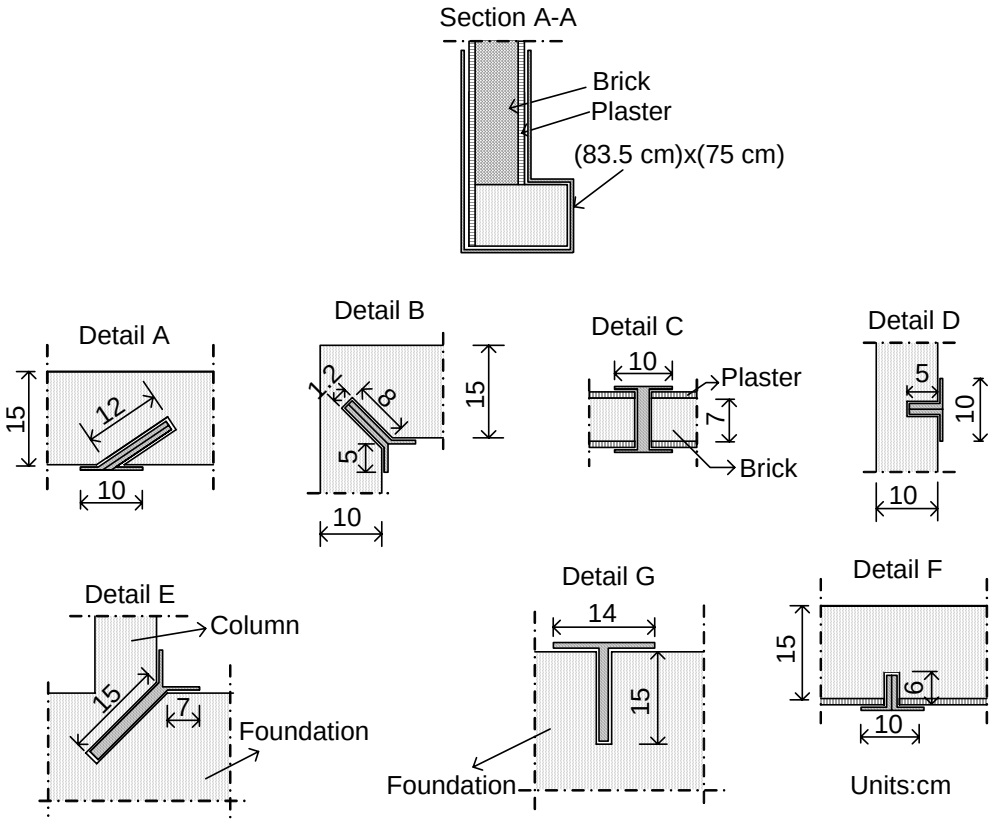

Figure 3.36. Close-ups of CFRP anchors and wrapping of columns with CFRP

3.6. Test Set up and Instrumentation

The test specimens were attached to the strong floor and loaded until failure. Horizontal and vertical loadings were independently applied throughout the test. Test set up consisted of an auxiliary foundation used to fix the specimen into the strong floor, a steel reaction wall to apply the cyclic horizontal loading, a hydraulic ram and a pumping equipment to apply the vertical load, a 250 kN displacement controlled hydraulic actuator attached to the reaction wall, horizontal and vertical steel spreader beams, restrainers to prevent out of plane deformation of the specimen and a data acquisition system. Each cured specimen was carried into the test rig and prepared for the test. Test set-up is shown in Figure 3.37. The horizontal load was applied by using the 250 kN dynamic actuator which was mounted to the steel reaction wall. One third of the horizontal load was given to the first story and two thirds of the horizontal load was given to the second story by using the horizontal steel spreader beam. Eight steel rods fixed four thick plates on the beam levels to apply the horizontal load. A 40 ton capacity hydraulic ram was placed between two horizontal steel spreader beams over the specimen. One of these spreader beams was placed in the plane of the specimen. The other horizontal spreader beam was located on the top of the hydraulic ram and fixed to the hinge support by using four steel bars. The hinge supports were placed on the auxiliary foundation. Axial load was applied on the columns by using the manually controlled hydraulic ram and steel bars and kept constant throughout the test. Vertical load was applied prior to test. Application systems of the horizontal and vertical loads were independent. The load obtained by dynamic actuator was not directly used in the calculations. The effect of the axial load on the horizontal force was also calculated and the corrected horizontal load was used in the calculations. To calculate the corrected horizontal load, it was assumed that horizontal load was always horizontal and vertical load had Cartesian components due to horizontal deflection. In other words the horizontal component of the vertical load decreased the effect of the load obtained by the actuator. The corrected horizontal load was calculated in accordance with the Equation 3.1. The variables were shown in Figure 3.38.

$$H_{corrected} = P_{actuator} - N_{vertical} \times \sin(\arctan(\frac{\Delta}{h})) \tag{3.1}$$

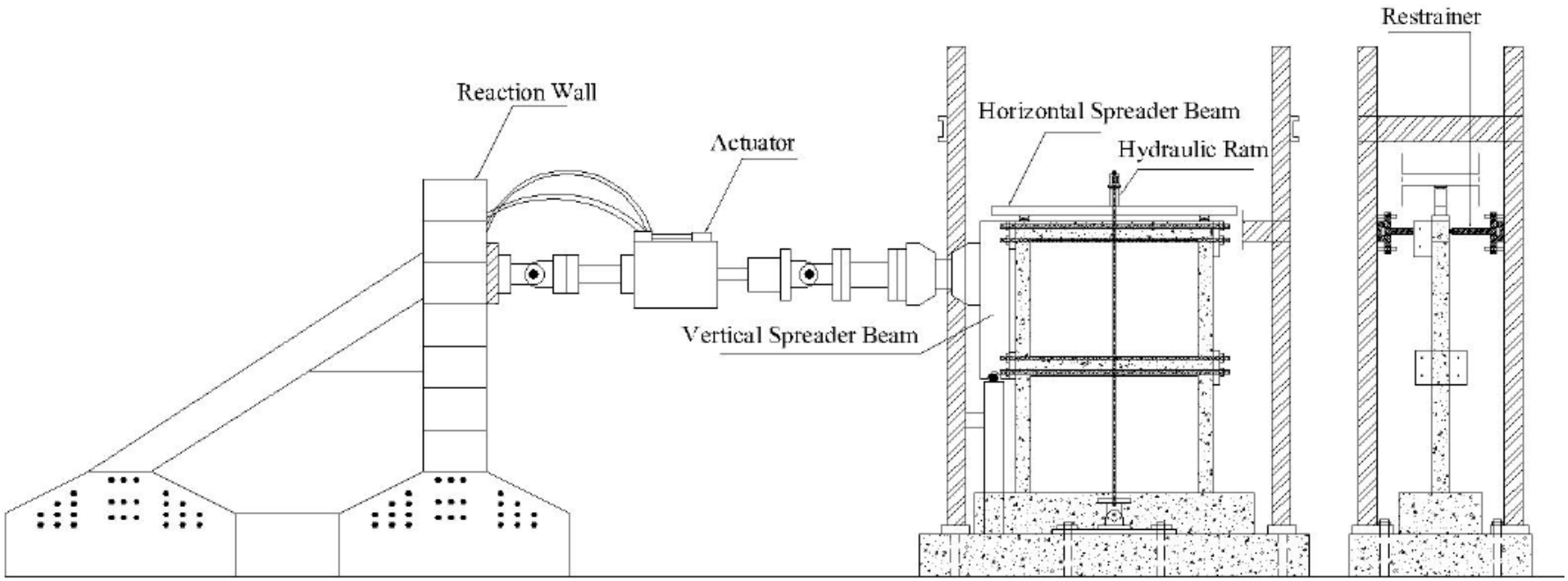

Figure 3.37. Test set-up

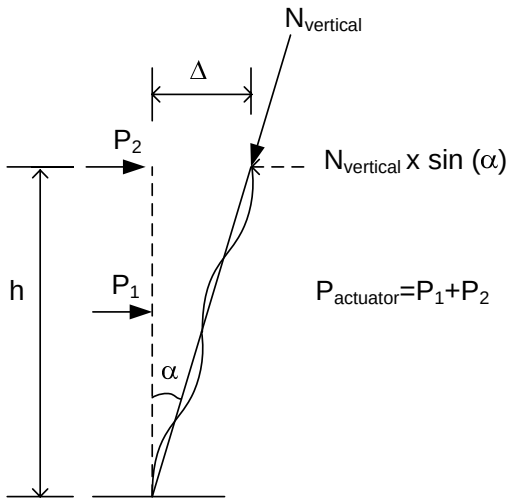

Figure 3.38. Calculation of the corrected load

$P_{actuator}$: Total base shear

$N_{vertical}$: Total applied vertical load

h : Height from the hinge support to the top of the specimen

$H_{corrected}$: Corrected base shear

In order to eliminate possible out of plane deformations a steel frame was constructed and steel restrainers were attached to this steel frame. Small steel spherical balls were placed to the ends of these steel restrainers to prevent any frictional forces to develop between the specimen and the steel frame. A total of four restrainers were used at the second story beam level to prevent or limit twisting of the specimen. Installation of loading system preceded the placing of measuring devices (Linear Variable Differential Transducers, dialgages and straingages). Straingages were glued on the CFRP materials. The location of LVDTs and dialgages are schematically given in Figure 3.39.

In order to measure horizontal displacements (drifts) at the first and second story levels 4 LVDTs, two of which were on the second floor level, were mounted on the specimen (1, 2, 3, 4 in Figure 3.39). The measurement frame was mounted on the foundation of the specimen. Thus all measurements were relative to the foundation of the specimen. Two dialgages were located on the lower part of the left and right columns so that they measured horizontal slip just above the foundation level (6, 8 in Figure 3.39).

Two dialgages were located on the bottom outer face of the columns to measure rotation or base rocking of the overall specimens (5, 7 in Figure 3.39). Two dialgages were mounted on the specimen to determine potential out of plane deformations (9, 10 in Figure 3.39). Four dialgages, two of which were in the second story infill panel, were used to measure the shear deformations on the infill panel (11, 12, 13, 14 in Figure 3.39). Specimens with an aspect ratio of 2.3 had two extra dialgages on the infill panel to better understand shear deformations. The dialgages mounted to measure shear deformations were placed in an X configuration on the masonry panel. In order to determine the shear deformations the following formulations (3.2) and (3.3) proposed by Massone L.M. and John W. Wallace [90] was used. The deformed shape and variables were illustrated in Figure 3.40. Undeformed shape was seen in dashed lines. The influence of flexural deformations was assumed to be zero. Average shear deformation and average shear deformation angle were calculated in accordance with the Equations 3.2 and 3.3 respectively [90]. In these formulations diagonal lengths were calculated by using the average height and length values. The locations of the dialgages and necessary measurements were given in APPENDIX-A. Shear deformation angle was also calculated by using the formulation proposed by Melek et al. [91]. The formulation is given in Equation 3.4.

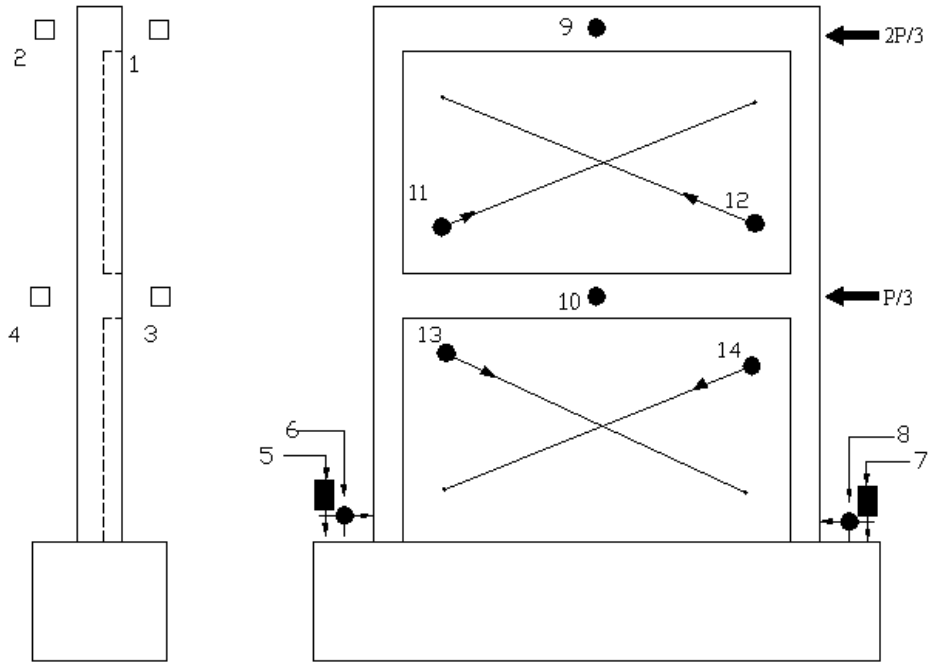

Figure 3.39. Schematical View of LVDTs and Dialgages

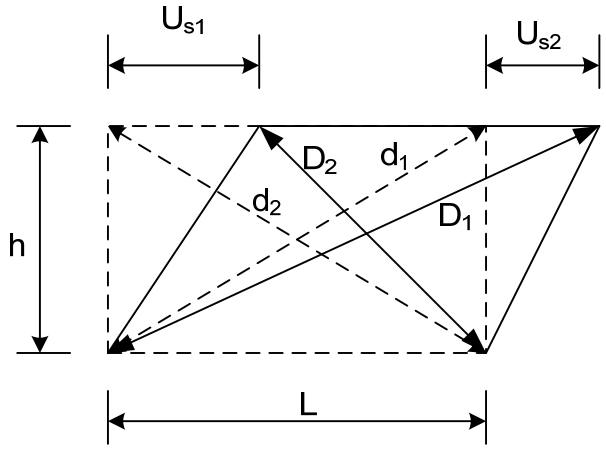

Figure 3.40. Calculation of shear deformation

$$U_{s\_average} = \frac{\sqrt{D_1^2 - h^2} - \sqrt{D_2^2 - h^2}}{2} \tag{3.2}$$

$$\gamma_{average} = \tan^{-1}\left(\frac{U_{s\_average}}{h}\right) \tag{3.3}$$

$$\gamma_{average} = \frac{(D_1 - d_1)\times d_1 - (D_2 - d_2)\times d_2}{2\times h\times L} \tag{3.4}$$

Straingages were also used on the CFRP overlays to measure strain values at each displacement level, and these measurements were also recorded by using data acquisition system.

3.7. Test Procedure

First the load transfer mechanism was placed, then the instrumentation was mounted on the specimens to the predetermined points, and finally the data acquisition system was connected to the instruments. The data acquisition system included a TML 602 data logger and actuator control panel. All values of the LVDTs, dialgages and straingages were recorded in this data logger until the test was terminated. During the test, the cracks were marked on the specimen and observations were recorded at each drift level. The specimens were tested in an upright position whereas they were cast in horizontal position.

Loading history was very important for the behavior especially in the nonlinear range. Although it was intended to use the same loading history to do better comparison, it was not possible due to nature of the specimens. In other words failure types of the specimens affected loading history significantly. While flexure dominant systems such as specimens with an aspect ratio of 1.0 can undergo displacement controlled type of loading, shear dominant systems must experience load controlled type of loading in the initial cycles. Load controlled type of loading was followed by displacement controlled type of loading for the specimens with aspect ratios of 1.7 and 2.3. Loading histories are given in the following chapter for each specimen. Previous test results done in Bogazici University [71] and the document of ACI T1.1-01 [92] were used to find an appropriate loading pattern to be used for displacement controlled phase of the loading. The loading pattern was determined considering the following points:

- The initial drift ratio should be within the linear elastic range,
- The ratio between two consecutive drift amplitudes should be in the range of 1.25 and 1.50,
- Three full reversed cycles should be applied at each displacement amplitude.

When load controlled type of loading was used, it was intended to avoid softening caused by loading repetitions. That's why previously determined displacement amplitudes and drift ratios were checked at each drift ratio and the decision was made to shift from load controlled type of loading to the displacement controlled type of loading. Loading increments were approximately 5 kN.

The test was halted when the specimens experienced a significant change in ultimate load. Photos were taken during and after the test. Important stages of the test were recorded by using a video camera.

4. TEST RESULTS

Before deciding about the strengthening scheme, non-strengthened infilled specimens (SA1.0 and SA2.3) were tested in order to highlight the possible cracking patterns. CFRP overlays for strengthening were applied in such a way to either stop or delay the formation of cracks observed in non-strengthened specimens. The loading for all specimens consists of reversed cyclic loading, and three full cycles were applied at each load step. Observations during testing as well as the crack patterns, loading history and base shear versus specimen drift graphs for each specimen are shown in the following pages. Photographs showing the final stage damage level are also given. Load versus drift values in the relevant tables consist of the values attained at the third cycle of each loading step, while the discussions on specimen response are made based on the first cycle values of each loading step.

Some definitions about failure modes must be given before explaining the behavior of specimens. As the aspect ratio of the specimen is decreased rocking type of behavior started to govern the behavior as seen in specimen SA1.0. When the aspect ratio increased, specimen behavior changed from a flexure dominant rocking response into a shear dominant one and formation of compression struts became more conspicuous as in the case of specimen SA2.3. Sometimes this rocking action occurred in the strengthened specimens above the foundation level due to the configuration of CFRP cross diagonals. When the specimen started to rock, contact surface started to decrease and this incident triggered the sliding, and a contact surface sliding type of failure developed. Sliding occurred at the plane where moment of cross diagonals' vertical components was minimum. This generally coincided with the mid-height of the strengthened specimens. Vertical strips around columns helped to transfer the load from FRP to longitudinal bars at the lap splice region. This occurrence increased the advantages or benefits of the strengthening due to positive effects of continuity. Another failure mode was governed by the anchorage length of FRP anchors into the foundation beam. If the embedment length of the FRP anchors was not sufficient to develop tensile strength of FRP or debonding initiated before developing tensile strength, pull-out type of failures were observed. The slope of cross diagonals

changed as the aspect ratio increased. This affected shear force and normal force interaction of the cross diagonal FRPs and changed the specimens' failure modes.

4.1. Specimen SA1.0

SA1.0 was an unstrengthened, infilled specimen whose frame aspect ratio was 1.0. The aspect ratio of the infill was 0.97 (h/l), where h and l represents the clear length and the clear height of the infill. Displacement controlled (DC) type of loading was applied to the specimen SA1.0 (Figure 4.1). Vertical load on each column was approximately 14% of the column capacity (17 kN). The total axial load applied to the columns was 34 kN and kept constant throughout the test. Maximum applied horizontal load was 25.7 kN for the forward cycle (Figure 4.2).

In the 1st load cycle, the maximum applied load for the forward half cycle was 12.0 kN with a corresponding drift of 0.000169 (0.017%). No damage was observed in this cycle.

The first visible cracks were observed in the 6th load cycle at a load level of 25.7 kN (0.099% drift). Flexural cracks were observed in this cycle and were concentrated to the top and bottom ends of the first story columns. The cracks observed at the bottom of the columns encircled the perimeters of the columns. Hairline horizontal cracks were observed at the lap splice regions and at the interface between the first story panel and the foundation. Blisters between the first story panel and the first story beam were also observed in this cycle.

In the 8th cycle, at a load level of 22.3 kN (0.19% drift), previous cracks extended and crack width of the second crack (Figure 4.3) located on the left column which was 6 cm away from the foundation reached 1 mm. Also, new flexural cracks formed on the top of the 1st story columns. Some new cracks appeared on the interfaces of the 1st story panel and left column and of the 1st story panel and foundation near to the right column.

In the 9th cycle, at a load level of 22.7 kN (0.24% drift), hairline cracks between right column and 1st story panel were observed. Previous cracks extended and some cracks

joined together. Crack widths of the second and fifth cracks reached about 1.5 mm and 1.2 mm respectively.

In the 10th cycle, at a load level of 23.3 kN (0.29% drift), previous cracks widened and extended. 1st story panel separated from the surrounding frame with some hairline cracks.

In the 11th and 12th cycles, maximum crack widths of the second and fifth cracks reached 3 mm. Maximum loads and corresponding drift values for the forward half cycles were 21.7 kN (0.37% drift), and 20.4 kN (0.45% drift) respectively.

In the 13th and 14th cycles, crack widths of the second and fifth cracks increased. Vertical cracks between the first story panel and the first story columns on the back of the specimen were observed (Figure 4.4). Maximum loads and corresponding drift values were 20.0 kN (0.60% drift), and 19.3 kN (0.89% drift) respectively.

In the 15th and 16th cycles, the cracks at the interface of the first story panel and left column and at the interface of the first story panel and beam merged. This observation showed that first story masonry panel and surrounding reinforced concrete frame separated totally. Shear cracks formed on the back of the specimen at the first story beam level. The maximum loads and corresponding drift values for the forward half cycles were 18.5 kN (1.24% drift) and 17.4 kN (1.73% drift) respectively. Test was terminated at the end of the 16th cycle. Maximum displacement and corresponding load values are given in Table 4.1 for each successive drift level.

There was not any remarkable damage on the second story infill panel and reinforced concrete members as depicted in Figure 4.5. Cracks accumulated on the first story. Failure was mainly due to the inadequate lap splice length (20ϕ) in columns. Thus a tensile failure of the columns at the bottom ends was observed as seen in Figure 4.6. Rocking type of behavior was observed in the last loading cycles. Although crushing of the infill panel in the compression region was not observed, cracks observed in the compression regions showed that crushing would be imminent if the failure mode was different than the rocking type.

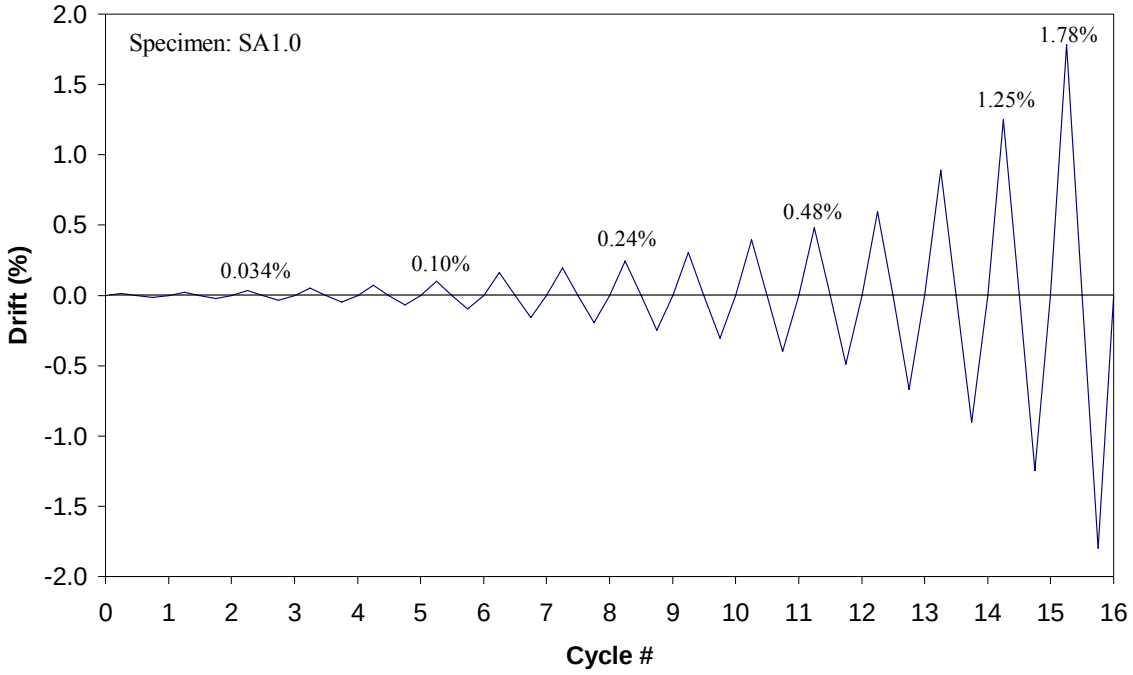

Figure 4.1. Load pattern applied for specimen SA1.0

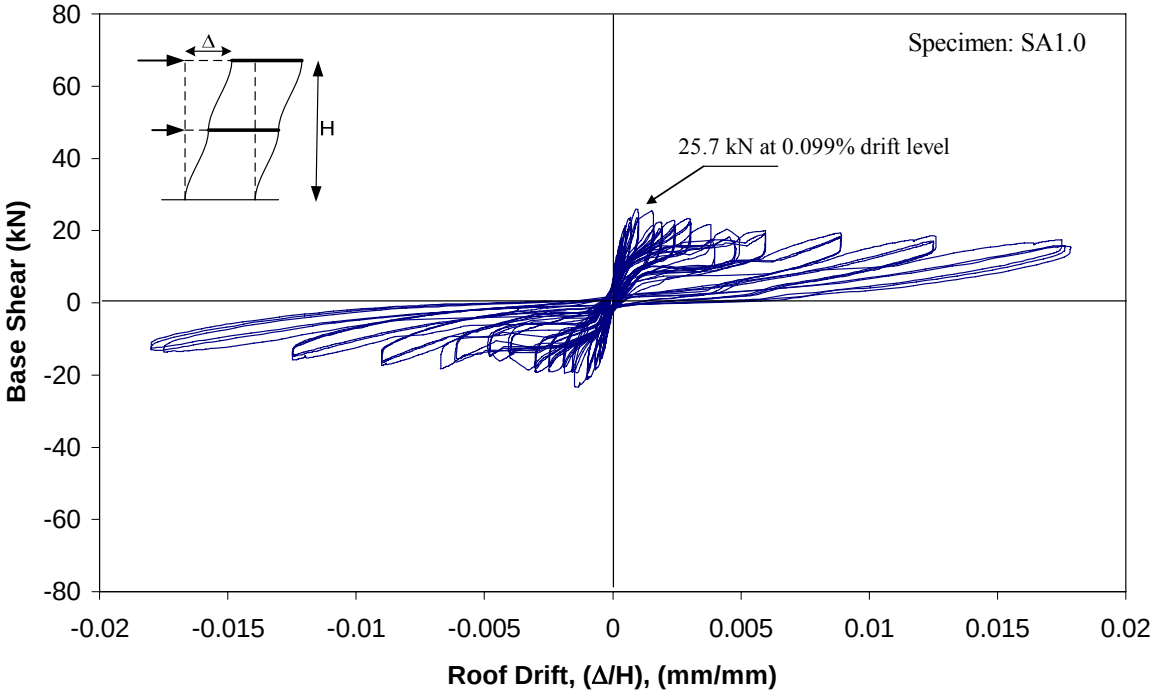

Figure 4.2. Base shear-top drift diagram for specimen SA1.0

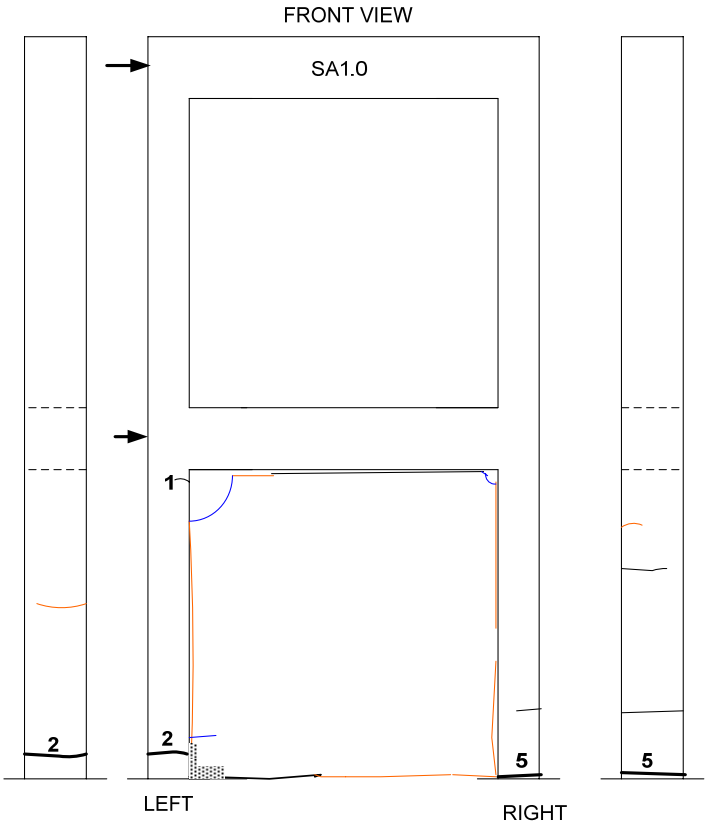

Figure 4.3. Crack distribution at the end of the test for front view

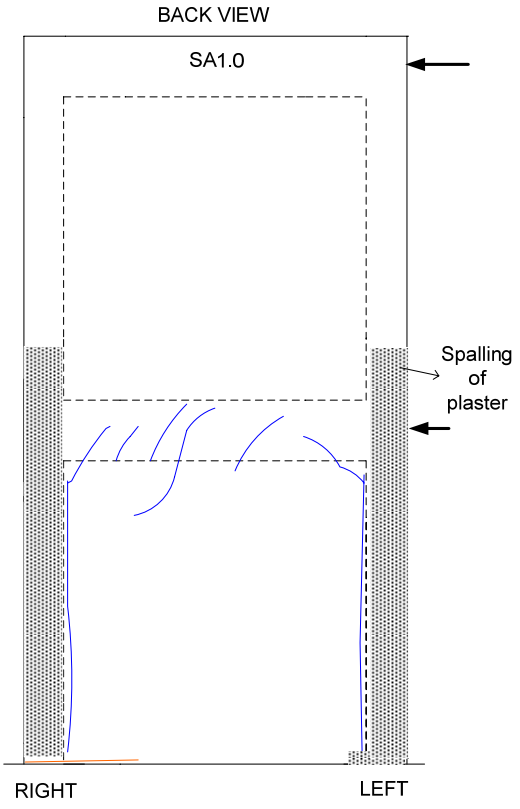

Figure 4.4. Crack distribution at the end of the test for back side of the specimen

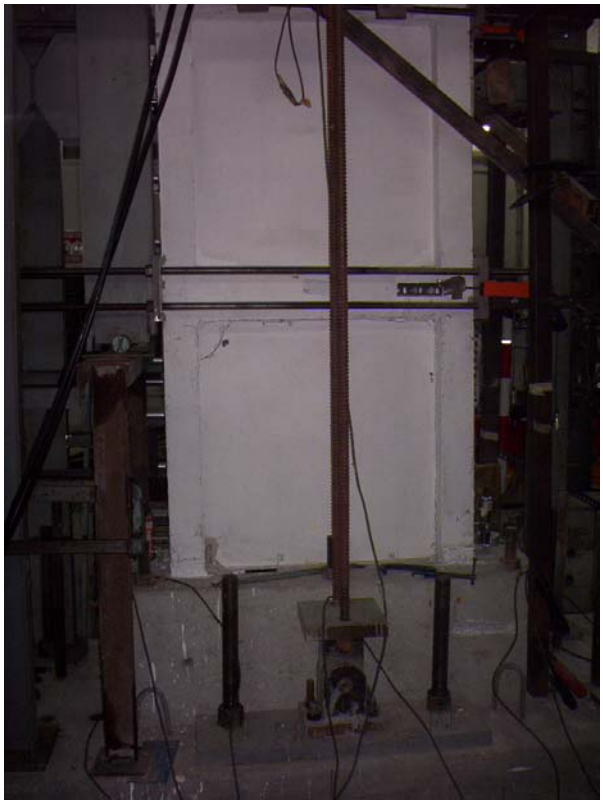

Figure 4.5. Specimen SA1.0 at the end of the test

Figure 4.6. Close-up of specimen SA1.0 at the end of the test

Table 4.1. Maximum displacements and corresponding loads for specimen SA1.0

Specimen: SA1.0					
Cycle #	Control Type	Maximum Displacement Δ_{max} (mm)	Corresponding Load P_{max} @ Δ_{max} (kN)	Minimum Displacement Δ_{min} (mm)	Corresponding Load P_{min} @ Δ_{min} (kN)
1	DC	0.23	8.52	-0.27	-6.44
2	DC	0.39	13.73	-0.41	-9.03
3	DC	0.59	14.94	-0.60	-12.50
4	DC	0.90	19.74	-0.84	-14.50
5	DC	1.25	21.72	-1.19	-17.43
6	DC	1.75	22.76	-1.69	-19.28
7	DC	2.77	19.74	-2.72	-19.01
8	DC	3.31	20.19	-3.34	-17.67
9	DC	4.21	20.92	-4.27	-17.11
10	DC	5.26	21.88	-5.22	-17.91
11	DC	6.83	15.77	-6.86	-14.31
12	DC	8.25	15.19	-8.38	-12.41
13	DC	10.24	18.98	-11.54	-18.22
14	DC	15.30	17.59	-15.51	-16.23
15	DC	21.50	16.69	-21.45	-14.44
16	DC	30.68	15.50	-30.95	-11.61
Note 1: The values given were obtained from the third consecutive cycle of each drift level.					
Note 2: The measurement height was 1720 mm.					
Note 3: DC represents displacement controlled type of loading.					

4.2. Specimen SA1.0-CV

The first strengthened specimen with an aspect ratio (h/l) of 1.0 was SA1.0-CV. CFRP overlays were applied in the form of cross diagonals and vertical strips. These CFRP overlays were anchored to the predetermined holes on the surrounding frame by using CFRP anchors. Displacement controlled type of loading was applied to specimen SA1.0-CV. The loading protocol is given in Figure 4.7. Constant axial load of 14.5 kN (N/N_0=0.11) was applied on each column throughout the test. Base shear versus roof drift response of SA1.0-CV is given in Figure 4.8.

The first visible crack on specimen SA1.0-CV was observed in cycle 5. This flexural crack with a length of 8 cm was on the left column outer face and located 42 cm away from the foundation level (nearly half height of column). Maximum applied load for the forward half cycle was about 21.2 kN (0.05% drift). Maximum applied load and corresponding drift for the backward half cycle was about -22.2 kN and -0.049% respectively.

In cycle 7, previous cracks extended and new cracks formed. Maximum applied loads and corresponding drifts for the forward and backward cycles were 31.7 kN (0.10% drift) and -32.2 kN (-0.097% drift) respectively. Horizontal cracks at different elevations on the left column and right column formed. Crack lengths changed between 6 cm and 10 cm. Moreover, a crack with a length of 4 cm at the intersection of right column outer face and the foundation appeared. The first shear crack with a length of 12 cm was observed at a height of 54 cm on the right column outer face.

In cycle 9, maximum applied push load for the forward half cycle and corresponding drift were about 43.2 kN and 0.19%. Some of the previous cracks extended while vertical and diagonal cracks between cross diagonals and horizontal cracks at various elevations between vertical strips appeared. New horizontal cracks at the right column and left column front face at different elevations were observed. The first inclined crack group, 8 cm away from the foundation, formed in the front of the specimen during the forward half cycle (Figure 4.9).

In cycle 10, maximum applied load and corresponding drift for the forward half cycle were about 46.8 kN and 0.24% respectively. On the back of the specimen, a horizontal crack with a length of 6 cm was observed between vertical strips which were near to the right column (47 cm away from the foundation level). The second inclined crack group which were perpendicular to the first one formed in the backward half cycle showing the effectiveness of the cross FRP diagonals.

In cycle 11, maximum applied load and corresponding drift for the forward half cycle were 48.4 kN and 0.30% respectively. Previously formed cracks, 42 cm and 15 cm away from the foundation level on the left column, extended throughout the left column front face. Observations showed that tensile strength of RC columns was started to be exceeded and horizontal cracks encircled the columns. In addition new flexural cracks on the left column at about 52 cm and 71 cm away from the foundation level formed. A new shear crack with a length of 25 cm was observed on the back of the specimen at the 1st story beam level. The third inclined crack group with a length of 5 cm formed at a distance of 65 cm from the foundation in the first story panel during the forward half cycle.

In cycle 12, maximum applied push load and corresponding drift were 52.2 kN and 0.38% respectively. Previously formed cracks forked out and inclined cracks between vertical strips formed at a level 38 cm and 40 cm away from the foundation beam in the front face of the specimen. A new shear crack which was perpendicular to the one observed on the back of the specimen at the 1st story beam level formed.

In cycle 13, maximum load on the forward half cycle and corresponding drift were 55.5 kN and 0.458% respectively. Some of the previous cracks extended and a new flexural crack with a length of 8 cm on the right column front face was observed at a distance of 13 cm from the foundation. Also 3 horizontal cracks formed on the masonry panel. One of them with a length of 12 cm was located 19 cm away from the foundation on the back of the specimen. The others appeared at the foundation and the first story panel interface between X diagonals. These two cracks located at the front and the back of the specimen were parallel to each other and indicated a separation between masonry panel and foundation.

In cycle 14, maximum recorded load and corresponding drift for the forward half cycle were 55.2 kN and 0.60% respectively. Separation between plaster and left column back face was observed. A slight load drop was observed at this drift level among 3 consecutive cycles.

In cycle 15, the 7th vertical strip (Figure 4.10) which was on the back of the frame and 13.5 cm away from the outer face of the right column ruptured in the forward-half-cycle. Afterwards, the 5th vertical strip which was in the front of the specimen and 27.5 cm away from the outer face of left column ruptured in the backward half cycle. Specimen failed by the rupture of all vertical strips and cross diagonals. Vertical strips ruptured just below mid height of the first story. Maximum applied loads and corresponding drifts for forward and backward cycles were 58.0 kN (0.77% drift) and -60.0 kN (-0.72% drift) respectively. After reaching maximum load, the specimen lost its strength suddenly especially in the backward half cycle. Loading type, maximum displacement and corresponding loads for each successive drift level are recapulated in Table 4.2.

The test was terminated at a drift level of 0.0177 at the end of the 17th cycle. Figures 4.11 and 4.12 showed the final situation of the specimen. Failure would be attributed to tensile failure of columns at lap splice region, and rupturing of vertical FRPs under the axial FRP stresses. Separation between infill and columns around was observed significantly. Masonry infill separated into two main parts due to mid-height rocking action of the specimen after rupturing of vertical FRPs as shown in Figure 4.13. On the other hand, formation of horizontal cracks on the infill implied a horizontal movement of the frame. Spalling of unconfined concrete was observed especially at the bottom ends of the columns around lap splices. Although the specimen failed with the rupture of vertical FRP strips, the top deformation of the frame was influenced by a sliding shear type of deformation took place at midheight of the first story. This resulted in a so- called ductility and anticipated pinching behavior in the hysteretic loops. The development of sliding shear surface will be discussed in SA2.3-CCM.

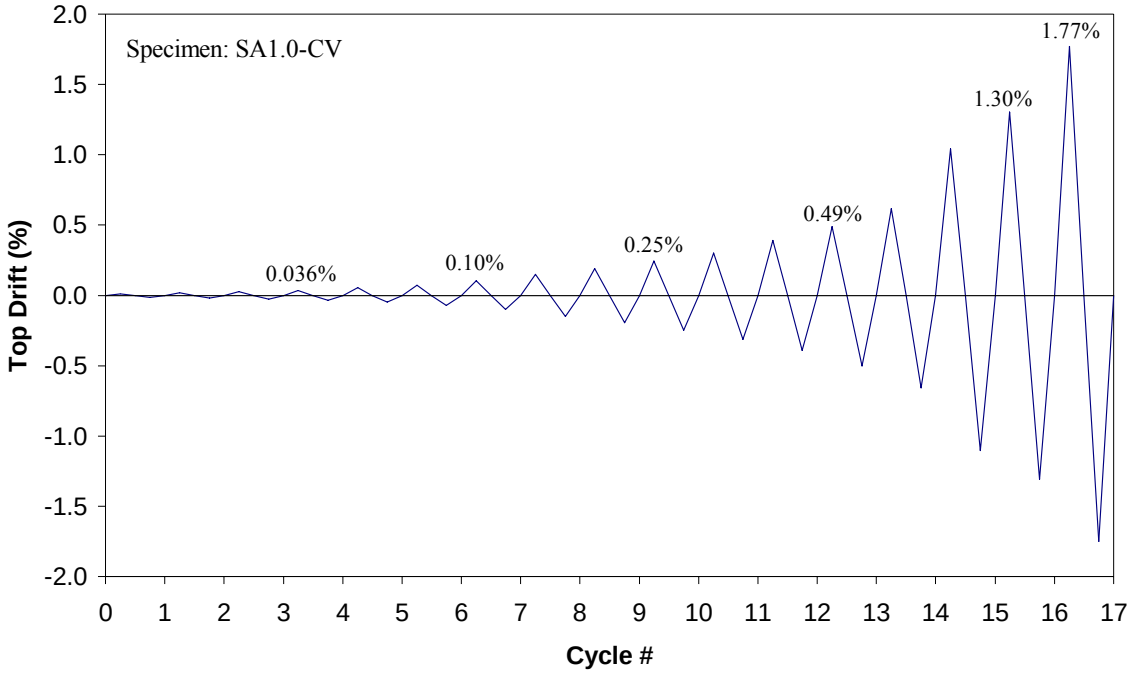

Figure 4.7. Load pattern applied for specimen SA1.0-CV

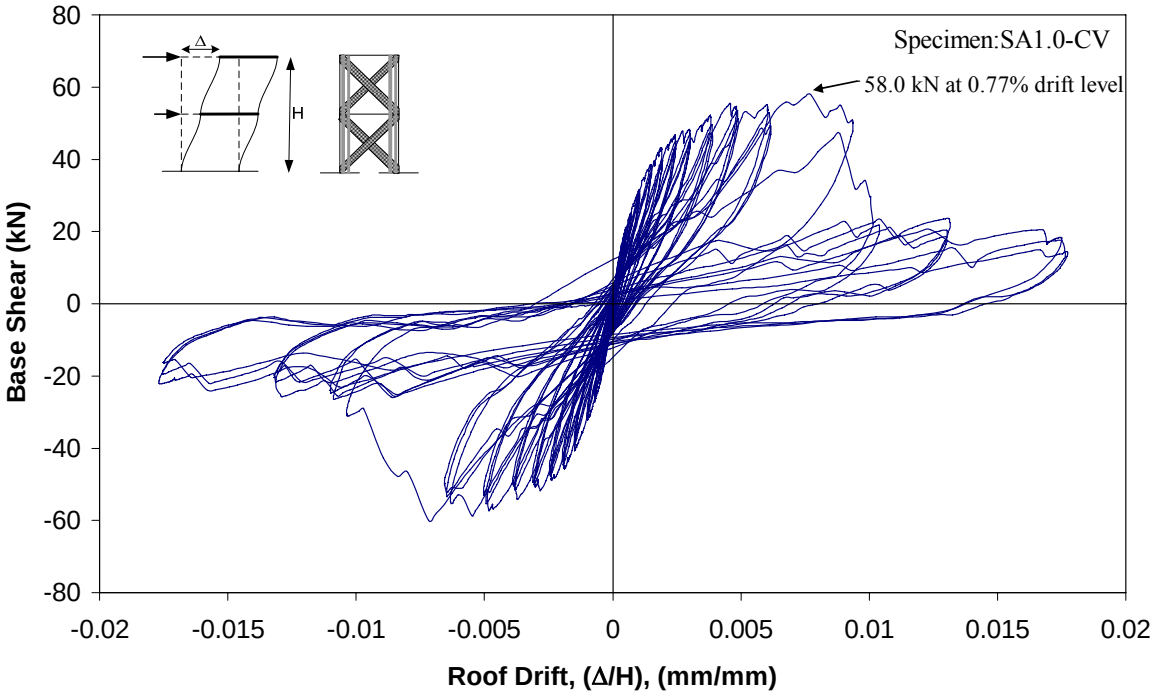

Figure 4.8. Base shear-top drift diagram for specimen SA1.0-CV

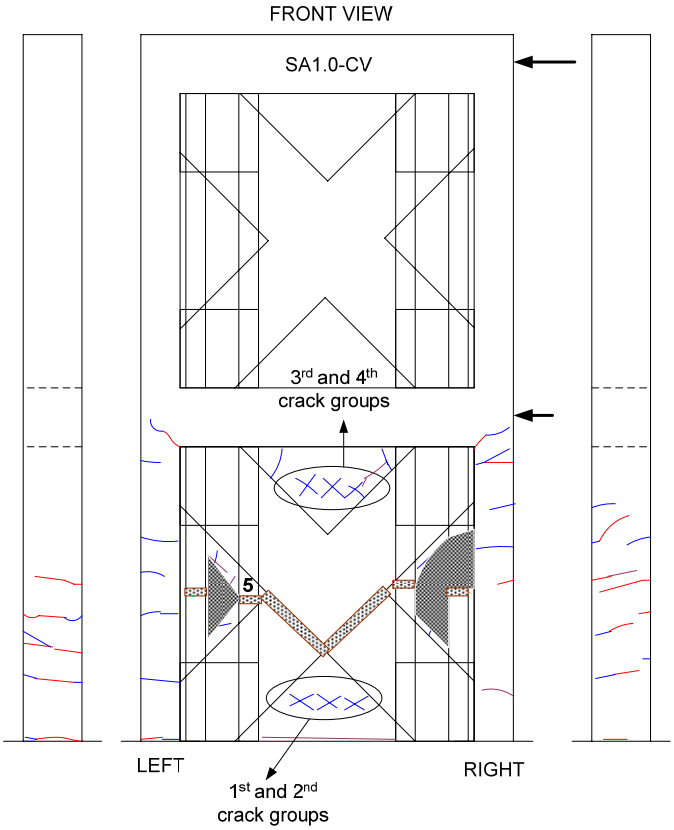

Figure 4.9. Crack distribution at the end of the test for front view

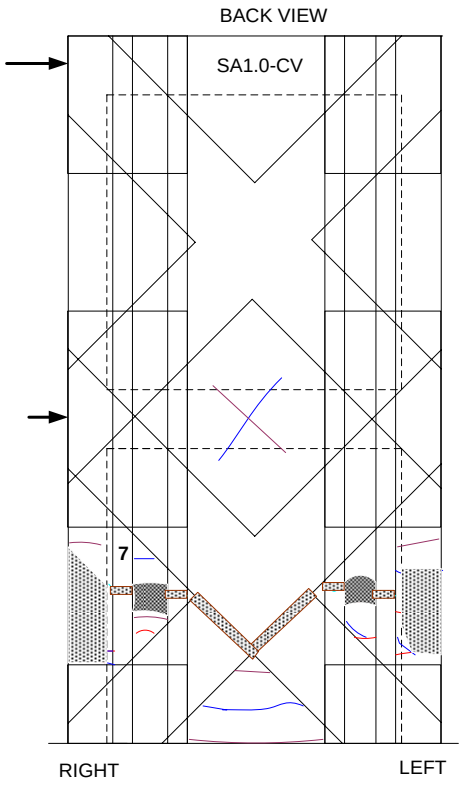

Figure 4.10. Crack distribution at the end of the test for back side of the specimen

Figure 4.11. Specimen SA1.0-CV at the end of the test

Figure 4.12. Close-up of the right column outer face

Figure 4.13. Cracking planes at different elevations during the failure of the specimen

Table 4.2. Maximum displacements and corresponding loads for specimen SA1.0-CV

Specimen: SA1.0-CV					
Cycle #	Control Type	Maximum Displacement Δ_{max} (mm)	Corresponding Load P_{max} @ Δ_{max} (kN)	Minimum Displacement Δ_{min} (mm)	Corresponding Load P_{min} @ Δ_{min} (kN)
1	DC	0.16	3.97	-0.23	-8.37
2	DC	0.28	7.91	-0.30	-8.39
3	DC	0.43	11.46	-0.42	-12.43
4	DC	0.61	15.46	-0.59	-16.16
5	DC	0.91	19.56	-0.83	-21.05
6	DC	1.20	24.27	-1.21	-25.66
7	DC	1.78	30.43	-1.70	-31.43
8	DC	2.54	35.41	-2.56	-38.57
9	DC	3.26	38.03	-3.33	-43.66
10	DC	4.18	42.50	-4.21	-46.89
11	DC	5.15	43.30	-5.33	-48.02
12	DC	6.64	45.47	-6.64	-49.11
13	DC	8.35	51.10	-8.58	-51.96
14	DC	10.52	48.64	-11.18	-49.78
15	DC	17.75	20.27	-18.78	-24.00
16	DC	22.21	17.27	-22.29	-18.88
17	DC	30.22	14.35	-29.86	-16.27
Note 1: The values given were obtained from the third consecutive cycle of each drift level.					
Note 2: The measurement height was 1705 mm.					
Note 3: DC represents displacement controlled type of loading.					

4.3. Specimen SA1.0-C2V

Although the strengthening scheme was the same as SA1.0-CV the cross-sectional area of each vertical strip doubled with respect to SA1.0-CV. Displacement controlled type of loading was applied to specimen SA1.0-C2V (Figure 4.14). Constant axial load of 24 kN (N/N_0=0.09) was applied on each column throughout the test. Base shear versus roof drift response of specimen SA1.0-C2V is given in Figure 4.15.

In the first cycle, maximum applied load and corresponding drift for the forward half cycle were about 8.2 kN and 0.00009 respectively. The specimen behaved elastically in the first cycles. No visible damage was observed in the first 7 cycles.

In cycle 8, the first visible cracks were observed both on the left and right columns. In the forward half cycle, two flexural cracks which were on the right column outer face at a height of 13.5 cm and 23 cm from the foundation. In the backward half cycle, one flexural crack, 15 cm in length on the left column outer face, formed at a height of 33 cm from the foundation. Width of this crack was measured as 0.1 mm. Moreover, cracking sounds were heard at this drift level. Maximum applied load and corresponding drift were 34.8 kN and 0.098% respectively.

In cycle 9, new crack formation continued increasingly. On the right column, new horizontal or slightly inclined cracks with various lengths formed at different elevations of 1.5 cm, 35 cm and 43 cm. The first shear crack, 10 cm long, on the left column outer face was observed 16 cm away from the foundation. A new flexural crack on the front face of the left column observed 61 cm away from the foundation. Two inclined cracks which intersected cross diagonals perpendicularly formed in the front of the masonry panel 34 cm and 33 cm away from the left column and right column respectively. These cracks illustrated the restraining effect of FRP and started from the bottom face of the first story beam. Maximum load and corresponding drift for the forward half cycle were 43.7 kN and 0.15% respectively.

In cycle 10, maximum applied load and corresponding drift for the forward half cycle were 49.1 kN and 0.19% respectively. Previous cracks extended and new cracks on

the surrounding frame were observed. First shear cracks on the both left and right beam-column joints formed. A new shear crack 10 cm long on the outer face of the left column was observed during the backward half cycle.

In cycle 12, maximum applied load and corresponding drift for the forward half cycle were 60.0 kN and 0.30% respectively. Cracks were generally located on both front and back of the masonry panel. The cracks on the masonry panel generally formed between vertical strips. Some of the cracks on the front face of the masonry panel were parallel to the 9^{th} and 10^{th} cross diagonals (Figure 4.16). A new 30 cm-long crack which pointed out the sign of separation between first story masonry panel and first story beam was observed. Moreover, another horizontal crack with a length of 10 cm and at a height of 19 cm formed on the back of the masonry panel. Shear cracks on the first story beam level formed on the back of the specimen both in the forward and backward half cycles.

In cycle 14, maximum applied load and corresponding drift for the forward half cycle were 68.6 kN and 0.48% respectively. All cracks observed in this cycle were formed in the front and on the back of the masonry panel. The cracks were generally both parallel and perpendicular to FRP diagonals and strips. 1^{st} vertical strip and 11^{th} cross diagonal tended to bulge (Figure 4.16 and Figure 4.17).

In cycle 15, maximum applied load and corresponding drift for the forward half cycle were 71.6 kN and 0.60% respectively. Crack width on the right column reached 1 mm whereas it was 2.5 mm on the left column during backward cycle. Cracks were generally perpendicular to the FRP overlays. Protrusion of 4^{th}, 9^{th}, 5^{th}, 10^{th}, 1^{st} FRPs was observed.

In cycle 16, maximum loads and corresponding drifts for the forward and backward half cycles were 75.2 kN (0.69%) and -71.7 kN (-0.705%) respectively. Some cracks were observed at the end of anchorages on the foundation. In the forward half cycle, 1^{st}, 2^{nd} and 5^{th} vertical strips ruptured. After failing of these vertical strips, load dropped significantly as can be seen from base shear versus top drift diagram. 10^{th} cross diagonal started to be broken about 5 cm in the beginning of the overlap region with cross diagonal 9. The initiation of the rupture was parallel to the 9^{th} cross diagonal. A crack which was parallel to

the FRP fibers on the 10th cross diagonal was observed. After rupturing 10th cross diagonal completely and rupturing 12th cross diagonal partially, load dropped drastically in the forward half cycles. In the first backward cycle, 8th, 4th and 7th vertical strips ruptured completely except 4th one. However, significant load drop was not observed in the backward half cycles. At the end of this cycle, all FRPs ruptured except 11th, 9th and 3rd FRPs. Also, 12th cross diagonal didn't rupture completely.

In cycle 17, 12th FRP ruptured completely. In the backward cycle, all FRP overlays ruptured and load dropped drastically. Maximum applied loads and drifts for the forward and backward cycles were 36.2 kN (1.1%) and -68.5 kN (-1.06%) respectively. Table 4.3 summurized the loading type, maximum displacement and corresponding loads for the forward and backward cycles of each successive drift level. Test was terminated in the 18th cycle at a drift level of 1.75%. A sliding plane on the masonry mid-height formed. Shear-sliding type of failure was observed. Debonding of cross diagonals and vertical strips as well as separation of infill from the beam and column faces were observed as can be seen from Figure 4.18. Close inspection of the specimen after the test revealed that shear failure of columns were followed by an axial load failure because of the relatively small vertical movement of the specimen. Vertical strips failed mostly in tension whereas cross diagonals failed under the combined action of shear and axial tensile forces.

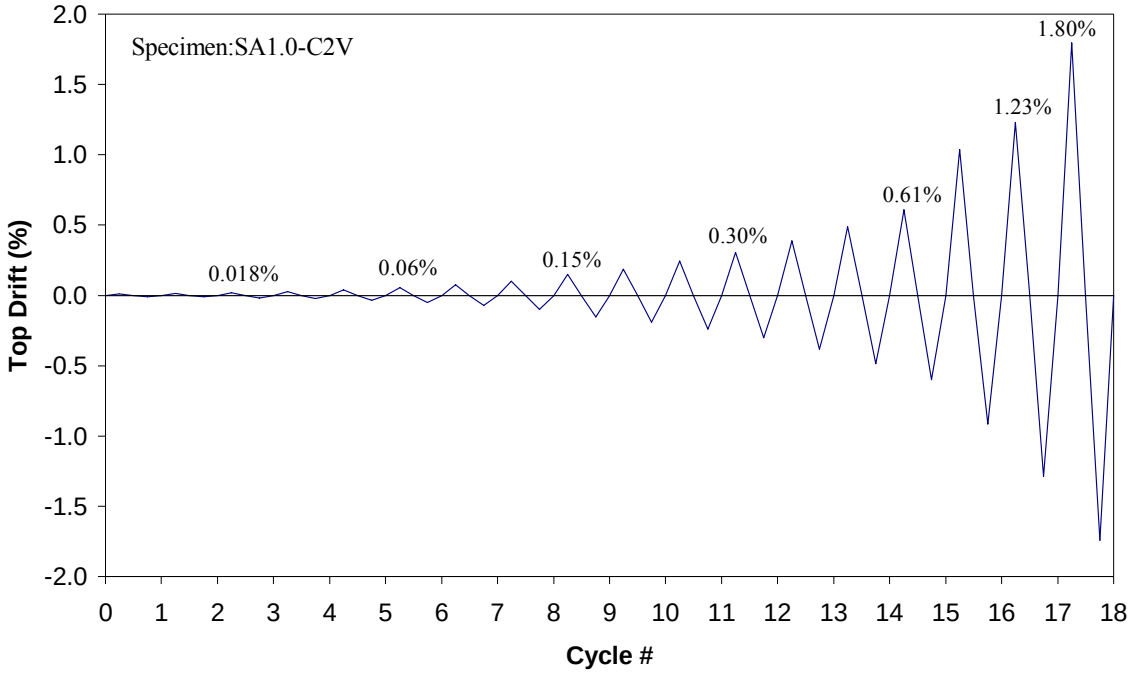

Figure 4.14. Load pattern applied for specimen SA1.0-C2V

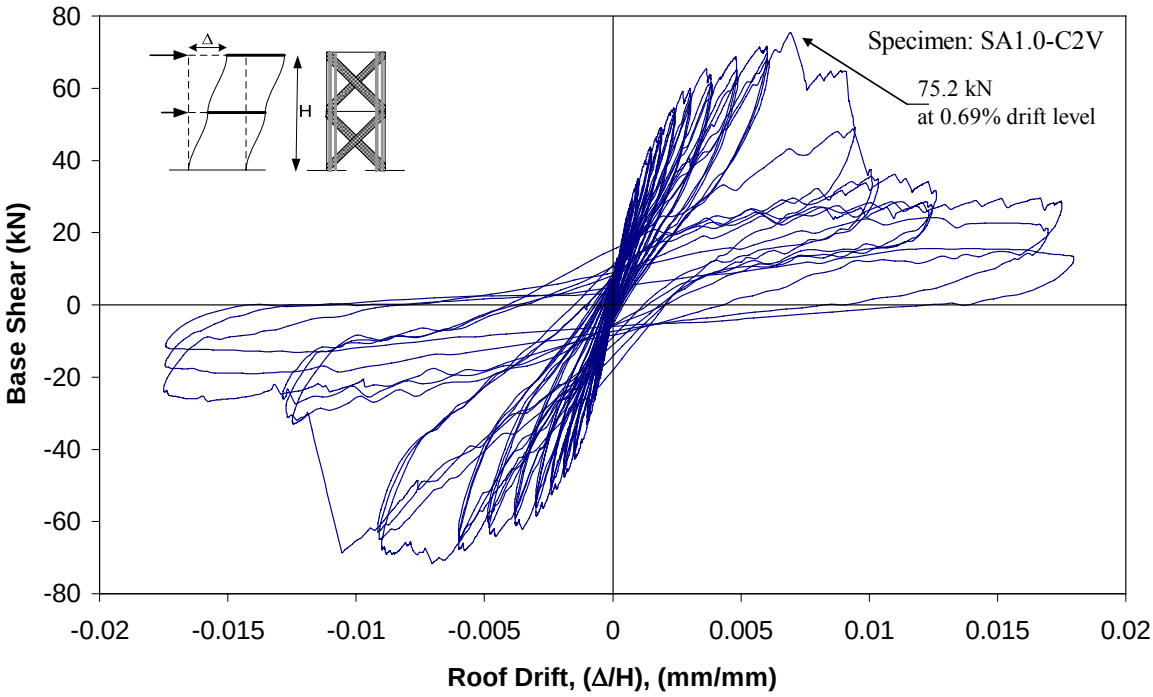

Figure 4.15. Base shear-top drift diagram for specimen SA1.0-C2V

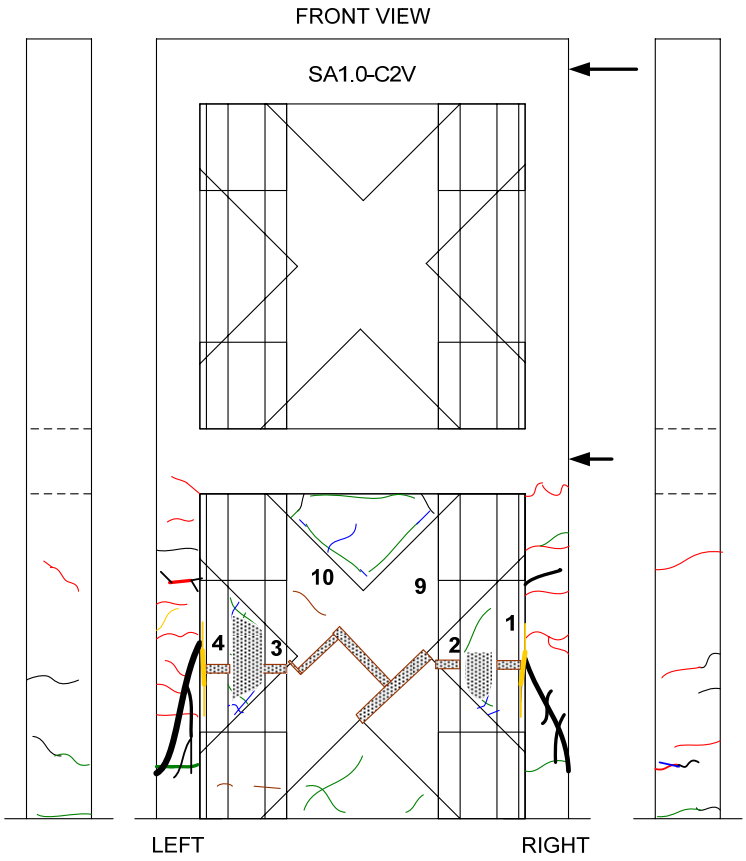

Figure 4.16. Crack distribution at the end of the test for front view

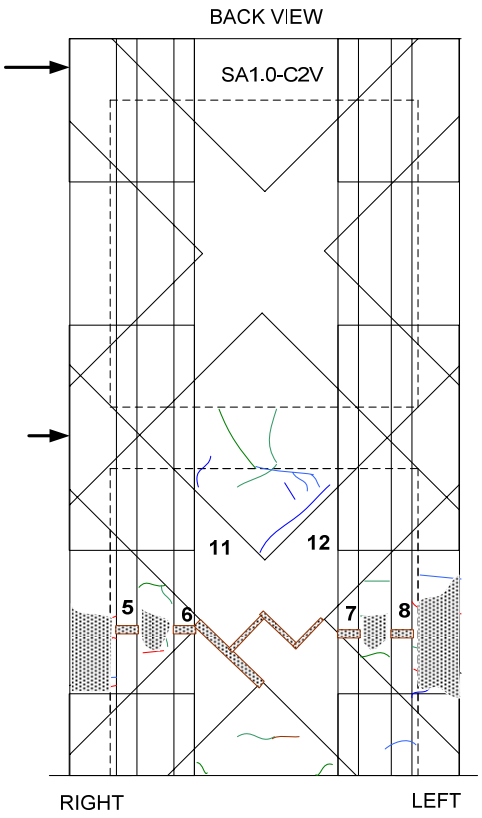

Figure 4.17. Crack distribution at the end of the test for back side of the specimen

Figure 4.18. Specimen SA1.0-C2V at the end of the test

Table 4.3. Maximum displacements and corresponding loads for specimen SA1.0-C2V

Specimen: SA1.0-C2V					
Cycle #	Control Type	Maximum Displacement Δ_{max} (mm)	Corresponding Load P_{max} @ Δ_{max} (kN)	Minimum Displacement Δ_{min} (mm)	Corresponding Load P_{min} @ Δ_{min} (kN)
1	DC	0.15	7.81	-0.20	-4.16
2	DC	0.22	9.58	-0.21	-4.55
3	DC	0.30	12.74	-0.29	-5.31
4	DC	0.45	14.01	-0.42	-10.94
5	DC	0.67	18.71	-0.58	-14.22
6	DC	0.95	24.10	-0.87	-19.41
7	DC	1.28	29.10	-1.23	-25.40
8	DC	1.74	34.46	-1.69	-31.58
9	DC	2.59	42.02	-2.61	-41.29
10	DC	3.20	46.27	-3.27	-45.66
11	DC	4.16	52.91	-4.12	-48.67
12	DC	5.22	57.15	-5.15	-52.86
13	DC	6.63	60.16	-6.57	-56.51
14	DC	8.34	63.08	-8.33	-59.66
15	DC	10.44	67.34	-10.28	-63.34
16	DC	17.73	34.22	-15.67	-62.03
17	DC	21.08	25.99	-22.03	-25.35
18	DC	30.75	12.33	-29.82	-11.44
Note 1: The values given were obtained from the third consecutive cycle of each drift level.					
Note 2: The measurement height was 1712 mm.					
Note 3: DC represents displacement controlled type of loading.					

4.4. Specimen SA1.0-CVL

The strengthening scheme included cross diagonals on the masonry infill and vertical strips in the lap splice regions of the columns. Displacement controlled type of loading was applied to specimen SA1.0-CVL (Figure 4.19). Constant axial load of 23 kN (N/N_0=0.10) was applied on each column throughout the test. Base shear-roof drift diagram is shown in Figure 4.20.

In the first cycle, maximum applied load and corresponding drift for the forward half cycle were about 7.6 kN and 0.00009 respectively. No visible damage was observed in the first 6 loading cycles. However some cracking sounds were heard in the fifth cycle at the drift level of 0.036% (16.7 kN).

In the 7^{th} cycle, the first visible hairline crack was observed 46 cm away from the foundation on the left column outer face in the backward half cycle. This crack was in the form of several small horizontal cracks propagating downward. In the forward half cycle, counterpart of the previous crack formed 43 cm away from the foundation on the right column outer face. Maximum applied load and corresponding drift for the forward half cycle were 26.8 kN and 0.07% respectively.

In cycle 8, maximum applied load and corresponding drift for the forward half cycle were 32.9 kN and 0.099% respectively. On the right column outer face, two cracks one of which was shear-flexure crack formed 50 cm and 45 cm away from the foundation. On the right column outer face, one flexural crack which was 7 cm in length formed just above the column FRP strip. The horizontal cracks formed on the masonry panel were located at the mid-height of the first story.

In cycle 12, previous cracks extended and forked out. Crack width on the left column reached 1.4 mm whereas it attained 1.2 mm on the masonry panel near to left column. Formation of new cracks decreased but previous cracks extended and widened. On the right column outer face, a shear- flexural crack with a length of 11 cm formed 60 cm away from the foundation. One of the cracks on the right column which was above the vertical strips around columns encircled the column. A new vertical crack with a length of 7 cm on

the left column corner between outer face of the column and back of the specimen formed on the vertical strips around columns. The first shear crack at the first story beam level was observed on the back of the specimen. Maximum load and corresponding drift for the forward half cycle were 57.9 kN and 0.30% respectively.

In cycle 15, maximum load and corresponding drift for the forward half cycle were 54.6 kN and 0.60% respectively. The cracks indicating separation between left column-first story masonry panel and first story beam-first story panel intersections were observed. The lengths of these cracks were 11 cm and 8 cm respectively. Formation of new cracks on the masonry panel and development of pre-formed cracks continued. Some of the cracks propagated parallel to the cross diagonals after reaching the cross diagonals.

In cycle 16, maximum load and corresponding drift for the forward half cycle were 60.8 kN and 0.89% respectively. Maximum lateral loads were attained both in the forward and backward cycles. Some of the previous cracks extended and joined together. Extensive cracks induced on the masonry panel at the end of this cycle. New vertical cracks on the outer corner of the right column and inner corner of the left column formed on these vertically applied FRPs. On the other hand, the vertical strips around columns began to peel off. 2nd cross diagonal bulged in the backward half cycle (Figure 4.21). Spalling at the intersection of the right column and in the front of the masonry panel was observed.

In cycle 17, maximum applied load and corresponding drift for the forward and backward half cycles were 58.5 kN (1.08%) and -52.8 kN (-0.90%) respectively. Some protrusion on the second story cross diagonal was observed. 2nd cross diagonal ruptured in the forward cycle and a sudden load drop was observed. Also some cracks parallel to FRP fibers were observed on the 1st cross diagonal during the forward half cycle. In the backward cycle some part of 3rd cross diagonal ruptured (Figure 4.22). However load drop was gradual. Sliding on the first story masonry was monitored at the mid-height of the first story masonry panel. Rupturing of cross diagonals followed a zigzag path in the mid-height of the panel. Table 4.4 illustrated the loading type, maximum displacement and corresponding loads for each successive drift level of specimen SA1.0-CVL.

Test was terminated at a drift level of 0.0177 at the end of the 18th cycle. Front view of the specimen and close-ups of the right and left columns were illustrated in Figures 4.23, 4.24 and 4.25. Failure was due to shear sliding failure with rupturing of cross diagonals under the combined action of axial tension and shear (Figure 4.23). Debonding of cross diagonals was observed. Formation of plastic hinges on the left and right column upper ends were observed due to block movement of infills (Figures 4.24 and 4.25). Vertical strips around columns prevented lap splice failure induced damage to a certain load level. It is observed that the load transfer between column lap splices through the vertical CFRP strips bonded on columns failed at a drift level of 0.0030. This observation was shown in the forward half cycle clearly. After that point minimal sliding observed. Hence, the cross FRP diagonals are stretched resulting load capacity enhancement. It was believed that these vertical strips around column lap splices helped to transfer failure plane on the masonry towards mid-height part of the first story panel. Loss of core concrete which implied gravity load collapse was not observed. Base shear-top drift diagram revealed that pinching behavior took place due to opening and closure of cracks especially after the failing of vertical strips around the lap splice region of the columns.

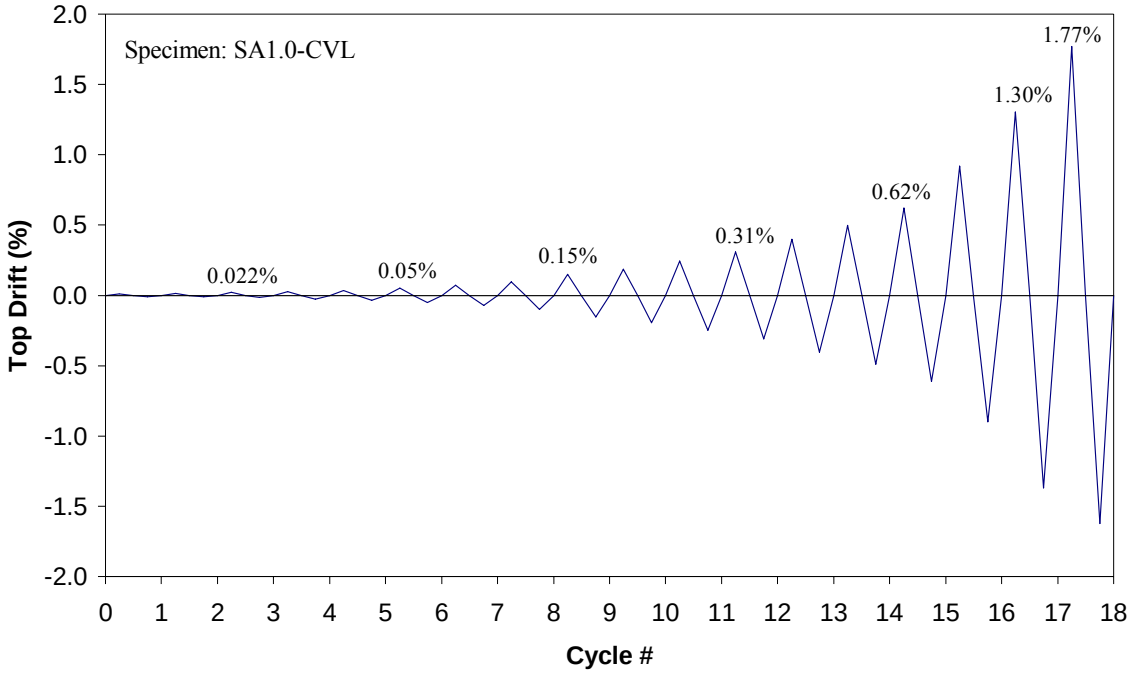

Figure 4.19. Load pattern applied for specimen SA1.0-CVL

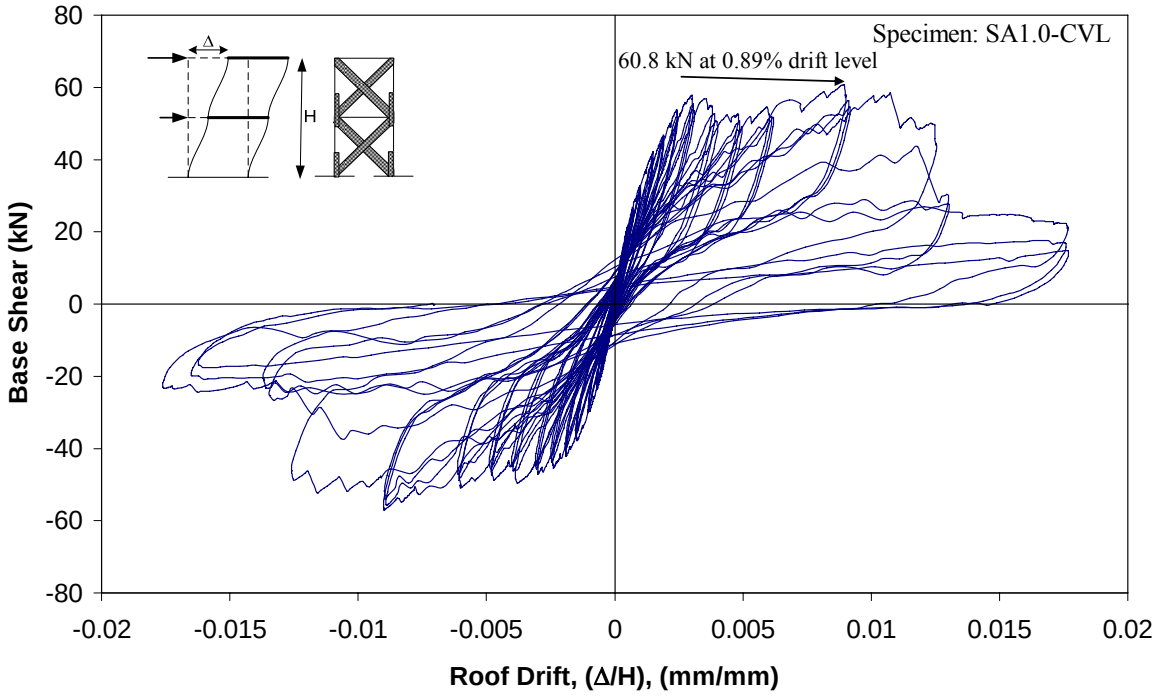

Figure 4.20. Base shear-roof drift diagram for specimen SA1.0-CVL

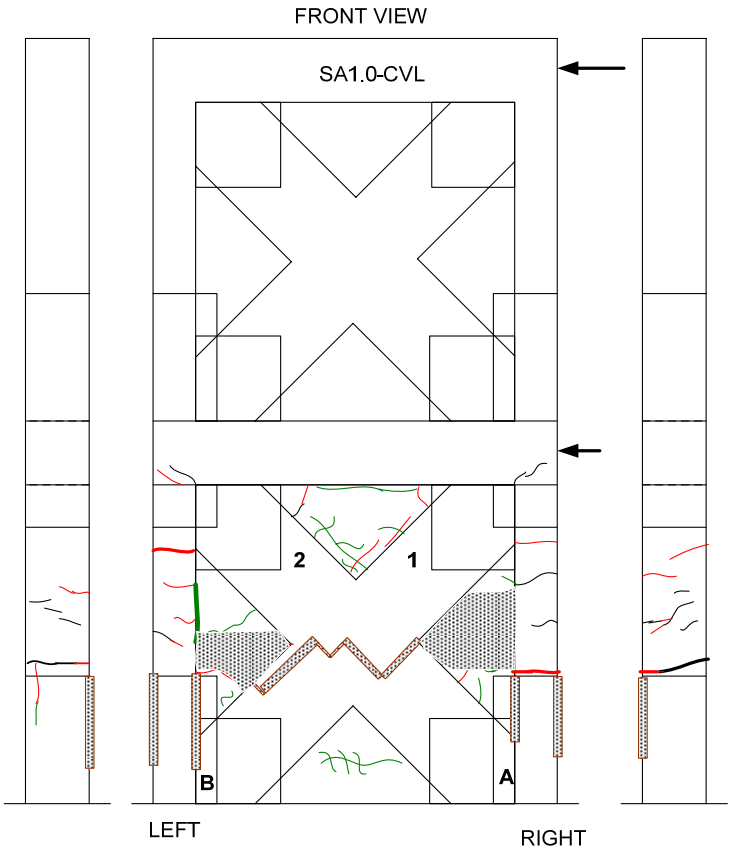

Figure 4.21. Crack distribution at the end of the test for front view

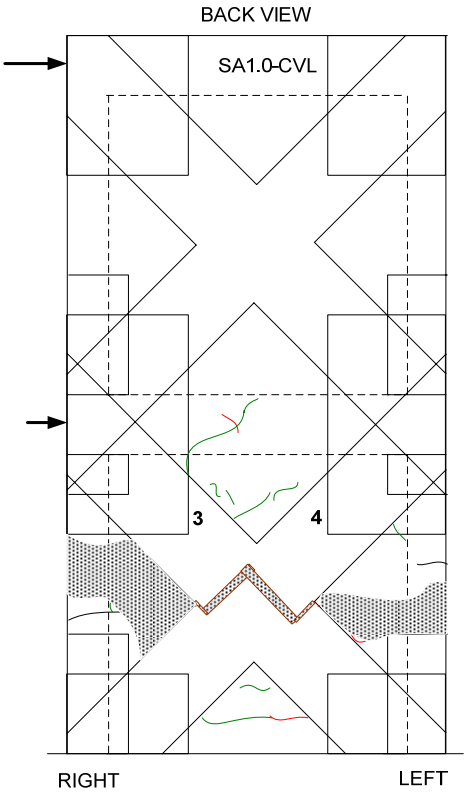

Figure 4.22. Crack distribution at the end of the test for back side of the specimen

Figure 4.23. Front view of specimen SA1.0-CVL at the 18th cycle

Figure 4.24. Right column in the 18th forward half cycle

Figure 4.25. Left column at the 18th cycle

Table 4.4. Maximum displacements and corresponding loads for specimen SA1.0-CVL

Specimen: SA1.0-CVL					
Cycle #	Control Type	Maximum Displacement Δ_{max} (mm)	Corresponding Load P_{max} @ Δ_{max} (kN)	Minimum Displacement Δ_{min} (mm)	Corresponding Load P_{min} @ Δ_{min} (kN)
1	DC	0.15	7.58	-0.19	-3.05
2	DC	0.28	7.33	-0.18	-5.59
3	DC	0.38	8.11	-0.28	-7.96
4	DC	0.46	12.79	-0.45	-10.46
5	DC	0.61	15.47	-0.60	-13.41
6	DC	0.85	20.97	-0.86	-18.04
7	DC	1.22	24.56	-1.21	-23.03
8	DC	1.68	29.83	-1.75	-28.87
9	DC	2.53	39.53	-2.63	-34.93
10	DC	3.23	44.67	-3.31	-39.95
11	DC	4.17	50.87	-4.28	-42.71
12	DC	5.32	53.54	-5.32	-44.64
13	DC	6.88	49.30	-6.90	-44.94
14	DC	8.52	48.97	-8.40	-44.61
15	DC	10.61	51.58	-10.52	-45.75
16	DC	15.76	53.95	-15.41	-51.69
17	DC	22.38	27.66	-23.52	-20.48
18	DC	30.36	13.96	-27.86	-16.47
Note 1: The values given were obtained from the third consecutive cycle of each drift level.					
Note 2: The measurement height was 1716 mm.					
Note 3: DC represents displacement controlled type of loading.					

4.5. Specimen SA1.7-D

Aspect ratio of specimen SA1.7-D was 1.7 whereas aspect ratio of the masonry was 1.73, and was a strengthened specimen with CFRP overlays. CFRP overlays were applied in the form of cross diagonals and vertical strips. These CFRP overlays were anchored to the predetermined locations on the surrounding reinforced concrete frame by using CFRP anchors. Previous test results [71] and strengthening schemes were investigated to determine the strengthening scheme of specimen SA1.7-D. Load controlled and displacement controlled type of loading were applied to specimen SA1.7-D to simulate earthquake forces (Figure 4.26). Constant axial load of 22.5 kN (N/N_0=0.11) was applied on each column throughout the test. Load increments for the load controlled cycles were 5 kN in forward and backward directions. Base shear versus roof drift diagram is shown in Figure 4.27.

Load controlled type of loading was applied in the first cycle. Maximum applied load and the corresponding drift for the forward half cycle was 26.9 kN (0.019% drift). No visible cracks were observed in this cycle. The first visible cracks formed in the 2nd cycle. Maximum load and corresponding drift values were 31.9 kN and 0.026% respectively. The first visible crack, crack 1, formed at the interface of the left column outer face and foundation as shown in Figure 4.28. Following that, two new flexural cracks formed on the left column outer face at a distance of 20 cm and 40 cm away from the foundation level during the backward half cycles (crack 2 and 3 respectively).

In the third cycle, a new crack between right column outer face and foundation was observed. Also a crack (crack 6) between first story panel and the first story beam occurred in this cycle implying an initial separation of infill and the frame as shown in Figure 4.28. Maximum load for the forward half cycle was 34.6 kN (0.036% drift).

In cycle 5, maximum load and corresponding drift for the forward half cycle were 43.9 kN and 0.057% respectively. Previous cracks extended and new flexural cracks at different elevations formed on the right column outer face. Also the crack between the first story panel and beam extended over the beam length. The first inclined crack on the back of the specimen at the first story beam level was observed.

In cycle 10, maximum load and corresponding drift were 67.3 kN and 0.159% respectively. A new crack formed between second story panel and second story beam with a length of 21 cm. In the 12th cycle, maximum load and corresponding drift were 78.7 kN and 0.24% respectively. Some of the previous cracks extended and spalling of plaster on the back of the specimen about the first story beam level started. A new shear crack with a length of 8 cm on the second story right column appeared (crack 33). Formation of flexural cracks decreased whereas formation of inclined cracks on the masonry panels accelerated.

In cycle 14, displacement controlled type of loading was started. A new shear crack with a length of 16 cm on the first story beam was observed at a distance of 25 cm from the right column. Bulging of X diagonal FRP was observed in the forward half cycle near to the first story beam-right column joint (FRP# 1 of Figure 4.28). Maximum applied load for the forward half cycle and corresponding drift values were 86.2 kN and 0.338% respectively.

In the 16th cycle, previous cracks extended, strength degradation initiated and inclined cracks which were parallel to the X diagonal FRPs on the first story panel were observed. Maximum load and corresponding drift were 82.8 kN and 0.48% respectively.

Test was terminated at a drift level of 0.0175 at the end of the 19th cycle. The loading type, maximum displacement and corresponding loads for the forward and backward cycles of each successive drift level is given in Table 4.5. Crack distribution at the back of the specimen is shown in Figure 4.29. X diagonal FRPs didn't fail under reversed cyclic loading in this specimen. Nonetheless, anchorages separated from the foundation and caused stiffness and strength deterioration. Figures 4.30, 4.31, 4.32, 4.33 and 4.34 showed status of the specimen at the end of the test. Sliding due to anchorage separation can be seen in base shear-roof drift diagram especially at the 18th cycle. Failure was due to inadequate anchorage length at the foundation level (Figure 4.34). Due to early failure of the anchors, the specimen didn't develop the whole capacity of the FRPs. Also after the test, the final state of anchorages were closely examined and pull out type of failure observed in most of the anchorages due either to inadequate anchorage depth (approximately 6 cm to 8 cm) or inability to sufficiently clean the holes from the dust.

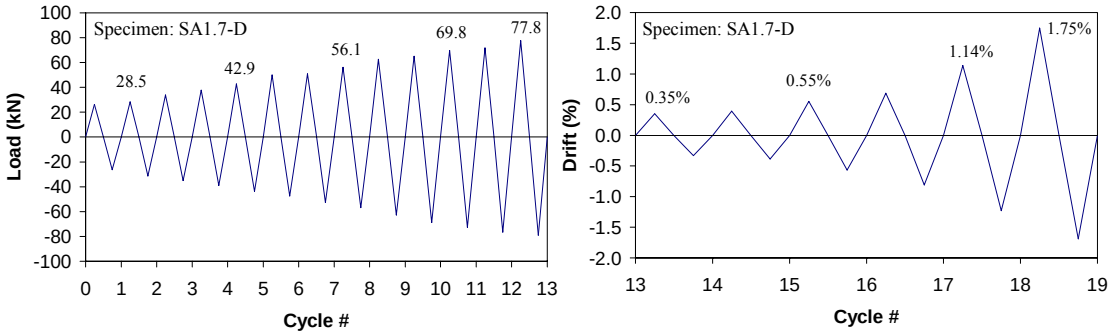

Figure 4.26. Load pattern applied for specimen SA1.7-D

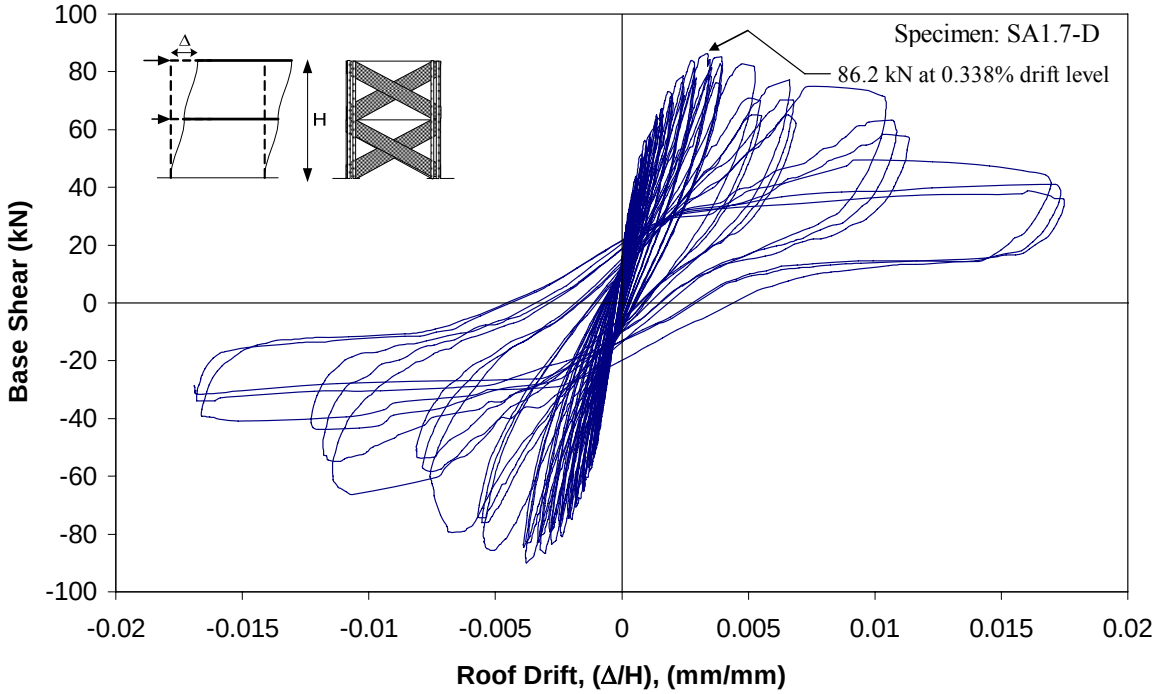

Figure 4.27. Base shear-top drift diagram for specimen SA1.7-D

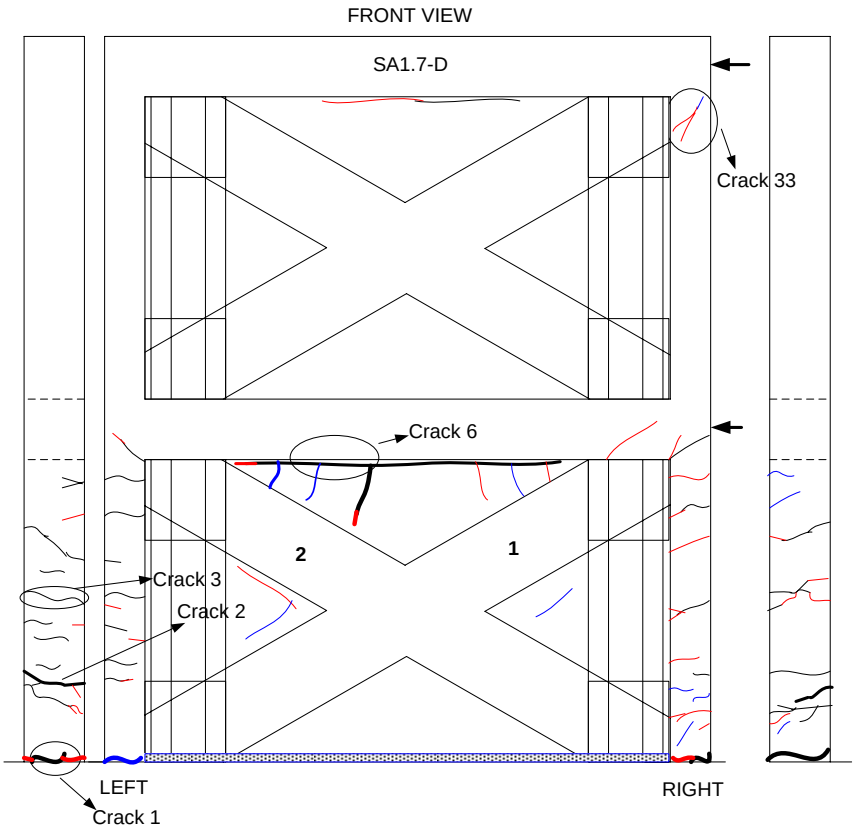

Figure 4.28. Crack distribution for the front view at the end of the test

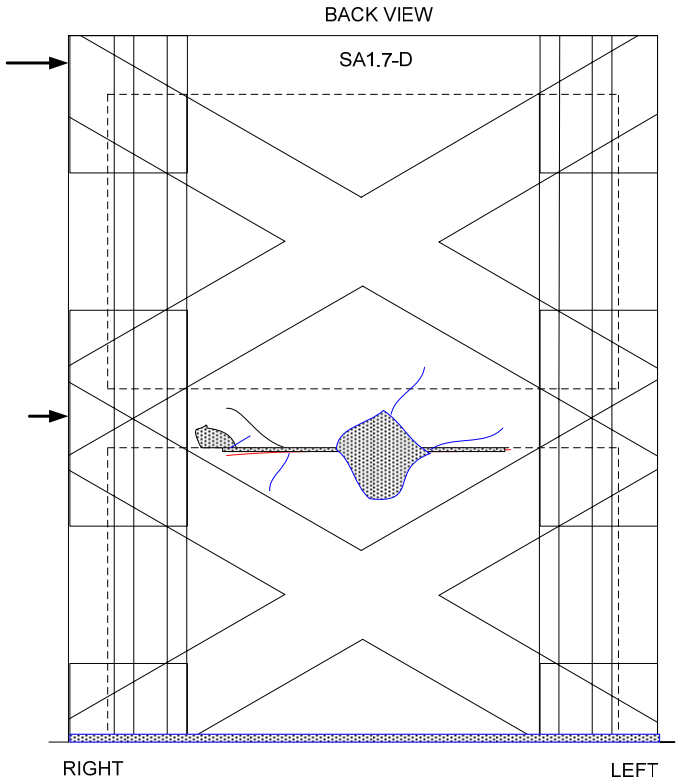

Figure 4.29. Crack distribution at the end of the test for back side of the specimen SA1.7-D

Figure 4.30. Front view of specimen SA1.7-D at the end of the test

Figure 4.31. Close-up of the right column

Figure 4.32. Close-up of the left column

Figure 4.33. Close-up of the base level

Figure 4.34. Close-up of anchorages around left column at the end of the test

Table 4.5. Maximum values for specimen SA1.7-D

Specimen: SA1.7-D					
Cycle #	Control Type	Maximum Load P_{max} (kN)	Corresponding Displacement Δ_{max} @ P_{max} (mm)	Minimum Load P_{min} (kN)	Corresponding Displacement Δ_{min} @ P_{min} (mm)
1	LC	26.38	0.30	-26.41	-0.98
2	LC	28.46	0.48	-31.23	-1.13
3	LC	33.97	0.58	-35.07	-1.26
4	LC	37.78	0.73	-38.96	-1.37
5	LC	42.88	0.98	-43.78	-1.53
6	LC	49.96	1.34	-47.48	-1.75
7	LC	50.88	1.54	-52.62	-1.92
8	LC	56.13	1.92	-56.84	-2.22
9	LC	62.64	2.33	-62.91	-2.60
10	LC	65.02	2.79	-68.74	-3.11
11	LC	69.75	3.34	-72.67	-3.63
12	LC	71.69	4.19	-76.67	-4.25
13	LC	77.77	5.04	-79.07	-4.91
Specimen: SA1.7-D					
Cycle #	Control Type	Maximum Displacement Δ_{max} (mm)	Corresponding Load P_{max} @ Δ_{max} (kN)	Minimum Displacement Δ_{min} (mm)	Corresponding Load P_{min} @ Δ_{min} (kN)
14	DC	6.05	78.18	-5.71	-79.54
15	DC	6.76	75.39	-6.69	-83.51
16	DC	9.49	64.91	-9.77	-74.03
17	DC	11.80	62.16	-13.93	-51.11
18	DC	19.50	56.65	-21.08	-41.52
19	DC	30.02	34.18	-29.00	-28.52
Note 1: The values given were obtained from the third consecutive cycle of each drift level.					
Note 2: The measurement height was 1716 mm.					
Note 3: LC represents load controlled type of loading.					
Note 4: DC represents displacement controlled type of loading.					

4.6. Specimen SA1.7-S

Aspect ratio (h/l) of specimen SA1.7-S was 1.7, and the specimen details were exactly the same as those of specimen SA1.7-D. The differences were the type of CFRP material and increased anchorage length at the foundation level. CFRP overlays were applied in the form of cross diagonals and vertical strips. These CFRP overlays were anchored to the predetermined locations on the surrounding frame by using CFRP anchors. Previous test results [71] and strengthening schemes were used to decide about the strengthening scheme of this specimen. Both load controlled and displacement controlled type of loading were applied at different load cycles. Constant axial load of 15 kN (N/N_0=0.10) was applied on each column throughout the test. Load increments for the load controlled cycles were approximately 5 kN in the load controlled forward and backward cycles (Figure 4.35). Base shear versus roof drift diagram is shown in Figure 4.36.

In the first cycle, the maximum applied push load was 19.2 kN and the corresponding displacement was 0.30 mm (0.018% drift). In this cycle, no visible cracks were observed.

In cycle 4, first visible cracks were observed. These hairline cracks were flexural cracks. The first visible hairline crack was observed in this cycle between left column outer face and the foundation. The length of this crack was about 3 cm long. The next hairline crack was between right column outer face and the foundation with a length of 3 cm. The third crack was on the left column outer face. Elevation of this 4 cm-long flexural crack was about 42 cm from the foundation. Maximum applied load and corresponding drift for the forward half cycle were 36.0 kN and 0.041% in turn.

In cycle 7, maximum applied push load was 48.7 kN (0.08% drift). Previous cracks extended and formation of new cracks accelerated. A new shear crack with a length of 4 cm at the right column and beam joint occurred. Some flexural cracks on the top of the columns were observed as well as a shear-flexural crack, 24 cm away from the foundation, at the lower part of the left column. Also, some shear cracks at the back of the specimen were observed on the first story beam level during the forward and backward half cycles. Load controlled type of loading was terminated at the end of this cycle.

In the 13th cycle, previous cracks extended and some of them passed the second vertical strip. Some cracks on the panel and columns forked out. Crack width of a crack on the right column reached 1 mm for the forward half cycle. Crack width on the left column reached 2.5 mm for the backward cycle. New cracks which were parallel to diagonal FRPs and perpendicular to vertical strips occurred on the first story panel. Moreover, hairline cracks which were 45 degree with respect to horizontal were observed on the first story panel located 10 cm below the first story beam and between cross diagonal FRPs. Protrusion on the diagonal FRP which were on the left of the first story panel was observed. Strain at the second vertical strip on the first story panel reached 2265 με. Maximum load and corresponding drift for the forward half cycle were 81.5 kN and 0.38% respectively. Maximum load and corresponding drift for the backward half cycle were -86.2 kN and 0.38% respectively. Ultimate load for the backward cycle were reached in this cycle.

In the 14th cycle, crack width at the joint between the first story beam and right column reached 0.8 mm (crack 9) as shown in Figure 4.37. A new flexural crack with a length of 10 cm formed on the right column (front face), 34 cm above the foundation level. Cross diagonal on the first story panel was torn apart approximately 4 cm. 3 vertical strips (4th, 7th, 8th) which were closer to left column were completely failed under tension. Two of them were at the back of the specimen and one was on the front of the specimen which was 3.5 cm away from the left column. In addition, some protrusion on the vertical strip which was in the back of the frame and 3.5 cm away from the right column was observed. The elevation of the protrusion was about 24 cm from the foundation level. Maximum loads and corresponding drifts for the forward and backward cycles were 82.1 kN (0.47% drift) and -85.4 kN (-0.46% drift) respectively. As indicated, load capacity in the forward cycles tended to increase whereas it decreased for the backward half cycles significantly due to rupturing of the FRP strips (approximately 25% reduction).

In cycle 15, the 3rd vertical strip whose center line was 17.5 cm away from the left column inner face ruptured. This strip located in the front of the specimen. At the end of this cycle, vertical strips around the left column were broken hence the load carrying capacity of the frame decreased significantly in the backward cycles. However, there was not any significant drop in load carrying capacity of the FRP-strengthened infilled frame in

the forward cycles. Maximum loads and corresponding drifts for the forward and backward cycles were 83.7 kN (0.59% drift) and -64.4 kN (-0.59% drift) respectively.

In cycle 17, 3 cross diagonals (2, 1, 1') ruptured as illustrated in Figures 4.37 and 4.38. Maximum loads and corresponding drifts were 60.8 kN (0.92% drift) and -62.6 kN (-1.19% drift) respectively. Last cross diagonal (2') was broken in cycle 18 during the forward cycle and the test was terminated at the end of 18^{th} cycle. These diagonals were torn apart with very little time intervals resulting significant capacity losses. The loading type, maximum displacement and corresponding loads for the forward and backward cycles of each successive drift level are given in Table 4.6.

Failure could be attributed to the formation of lap splice failure of column longitudinal bars along with the axial tension failure of the vertical FRP strips (Figures 4.39 and 4.40). Flag FRP configuration at the corners of the masonry impeded the crushing remarkably. On the other hand failure of vertical strips let the specimen to a rocking and sliding type of movement resulting high distress on diagonal FRP strips. Sliding of specimen was observed after the failure of vertical strips and before the failure of diagonal ones. On the other hand sliding was not predominant on the failure. This sliding is observed as a so-called ductility on the pull part of hysteretic curve. The observations done after the test illustrated that FRP anchorages on the columns caused cone failure cracks which were vertical as shown in Figure 4.41.This cone failure cracks and dowel cracks, which were formed by different sliding surfaces on the masonry panel and RC columns, could be among the possible reasons of spalling of the cover concrete. The close-up of the rigth column upper end is depicted in Figure 4.42. Sliding, shear failure of the right column (Figure 4.42) and lap splice failure of the columns' bottom ends (Figure 4.39) may be listed as the reasons of pinched hysteretic behavior of the specimen especially after 0.5% - 0.6% drift level.

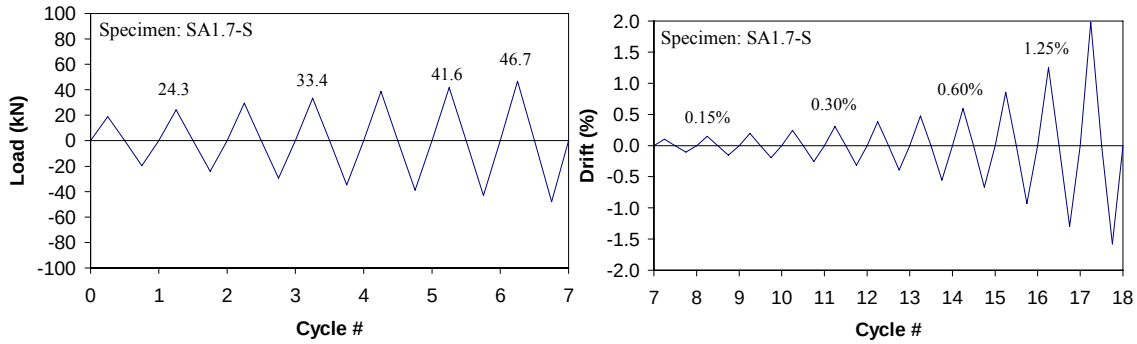

Figure 4.35. Load pattern applied for specimen SA1.7-S

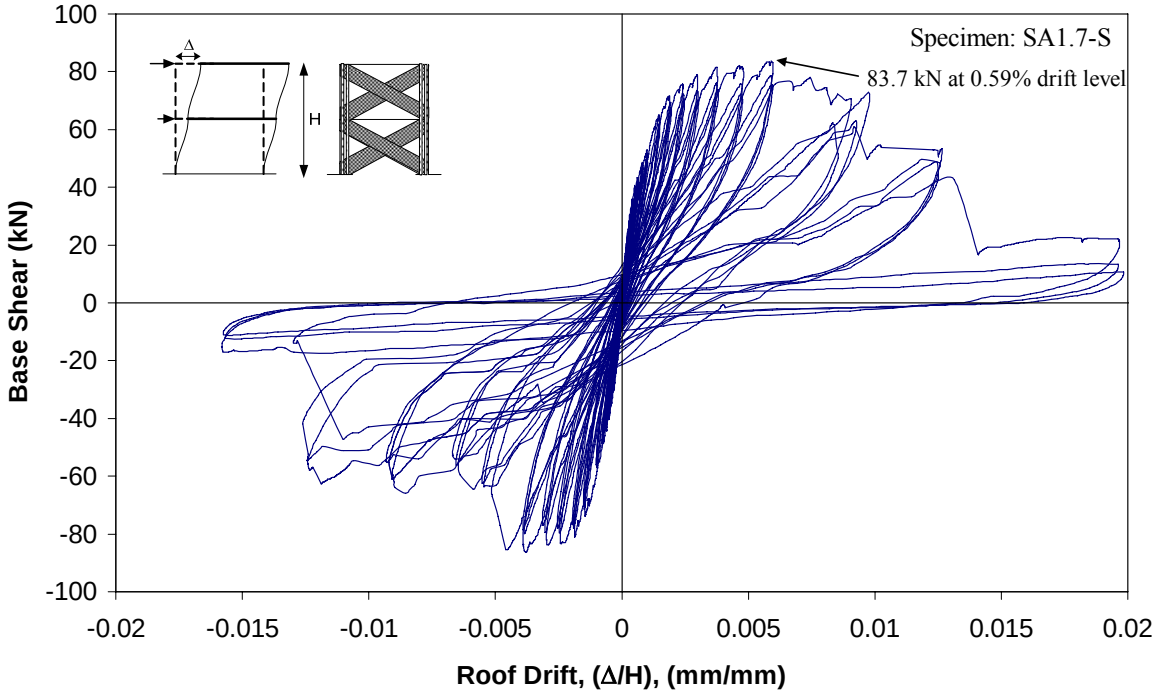

Figure 4.36. Base shear-top drift diagram for specimen SA1.7-S

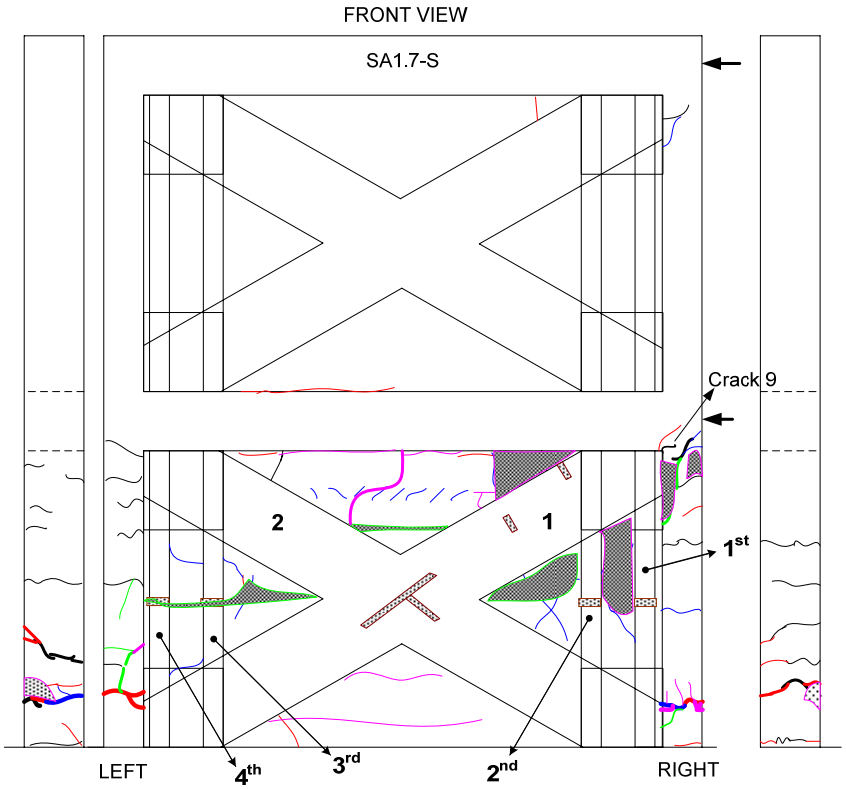

Figure 4.37. Crack distribution for the front view at the end of the test

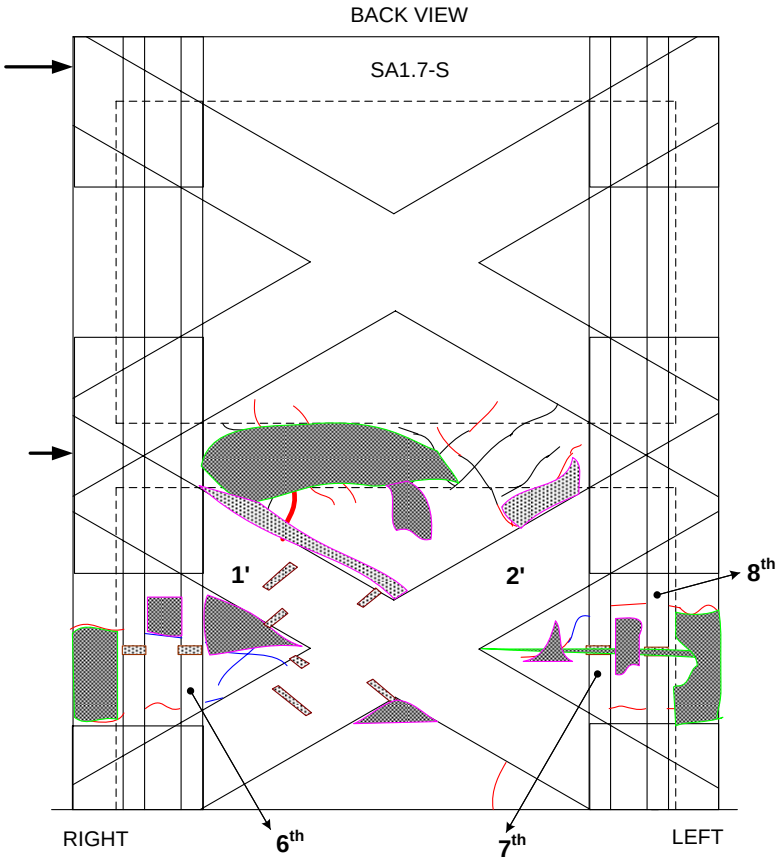

Figure 4.38. Crack distribution at the end of the test for back side of the specimen SA1.7-S

Figure 4.39. Front view of specimen SA1.7-S at the final state

Figure 4.40. Close-up of the left column

Figure 4.41. Close-up of the right column bottom end

Figure 4.42. Close-up of the right column top end

Table 4.6. Maximum Values for Specimen SA1.7-S

Specimen: SA1.7-S					
Cycle #	Control Type	Maximum Load P_{max} (kN)	Corresponding Displacement Δ_{max} @ P_{max} (mm)	Minimum Load P_{min} (kN)	Corresponding Displacement Δ_{min} @ P_{min} (mm)
1	LC	18.85	0.29	-19.75	-0.31
2	LC	24.25	0.42	-24.04	-0.42
3	LC	29.57	0.56	-29.43	-0.57
4	LC	33.43	0.70	-34.68	-0.74
5	LC	38.59	0.93	-39.01	-0.91
6	LC	41.61	1.09	-43.03	-1.08
7	LC	46.65	1.41	-47.88	-1.31
Specimen: SA1.7-S					
Cycle #	Control Type	Maximum Displacement Δ_{max} (mm)	Corresponding Load P_{max} @ Δ_{max} (kN)	Minimum Displacement Δ_{min} (mm)	Corresponding Load P_{min} @ Δ_{min} (kN)
8	DC	1.74	47.70	-1.75	-55.89
9	DC	2.57	59.37	-2.61	-70.36
10	DC	3.37	66.07	-3.35	-75.91
11	DC	4.24	69.67	-4.37	-76.86
12	DC	5.23	69.95	-5.37	-76.29
13	DC	6.55	72.91	-6.71	-77.32
14	DC	8.18	70.45	-9.49	-61.28
15	DC	10.23	74.86	-11.48	-52.86
16	DC	14.68	51.56	-15.99	-54.65
17	DC	21.47	43.52	-22.28	-13.90
18	DC	34.04	10.26	-27.05	-11.00
Note 1: The values given were obtained from the third consecutive cycle of each drift level.					
Note 2: The measurement height was 1716 mm.					
Note 3: LC represents load controlled type of loading.					
Note 4: DC represents displacement controlled type of loading.					

4.7. Specimen SA2.3

Aspect ratio of SA2.3 was 2.3 while the aspect ratio of the infill only was about 2.4. No strengthening was applied to this specimen in order to observe the non-strengthened response. The axial load applied to each column using a steel spreader beam was about 18.5 kN (N/N_0=0.11) and kept constant throughout the test. In this specimen, load controlled (LC) type of loading and displacement controlled (DC) type of loading were used at different loading cycles as shown in Figure 4.43. Load increments for the load controlled cycles were 5 kN in the forward and backward cycles. The loading type, maximum displacement and corresponding loads for the forward and backward cycles of each successive drift level is given in Table 4.7. Base shear versus roof drift diagram is depicted in Figure 4.44.

In the first cycle, maximum applied load and the corresponding drift for the forward half cycle were 16.4 kN and 0.0000058 respectively. No visible damage was observed in this cycle. Load controlled type of loading was applied in this cycle.

The first visible hairline cracks were observed at the 3rd cycle and were located at the interface of the back of first story panel and the right column starting from the foundation level as shown in Figure 4.45. Maximum applied push load for the forward half cycle was 25.0 kN (0.000029 drift).

In cycle 6, crack width of the first crack reached 0.3 mm and formation of compression strut at the backward cycle was observed. Maximum load for the forward half cycle and corresponding drift were 39.6 kN and 0.039% respectively.

In cycle 7, at a load level of 45.0 kN and corresponding drift of 0.064%, a crack between right column and the foundation was observed and it encircled the column in the forward half cycle. Also, some shear cracks were observed at the joints of the first story beam-column regions. Crack width of the first crack in this cycle reached 0.8 mm. Previous cracks extended and the one located at the interface of the left column and foundation encircled the column. Sliding of the frame which was relative to the foundation was observed.

In cycle 8, maximum applied load and corresponding drift for the forward half cycle were 50.0 kN and 0.099% respectively. Previous cracks extended. Some cracks between second story panel and surrounding frame were observed in the front of the specimen as illustrated in Figure 4.46. On the left column inside face a flexural crack with a length of 5 cm appeared at a distance of 49 cm from the foundation level. Crushing of the first story panel began in the lower left corner adjacent to the foundation and left column. Load controlled type of loading was terminated at the end of this cycle.

In cycle 9, at a load level of 51.0 kN (0.133% drift), displacement controlled type of loading was started. Ultimate load for the forward half cycle was reached in this cycle. Crack width between left column and masonry panel reached 1.4 mm. A new vertical crack with a length of 11 cm on the first story panel, 55 cm away from the left column outer face was observed. Moreover, hairline cracks were observed between the second story panel and the second story beam and columns. Shear cracks on the back of the specimen at the first story beam level formed. Some plaster spalling between the first story beam and first story panel was also observed.

In the 11^{th} and 12^{th} cycles, ultimate loads decreased significantly while drifts increased. Maximum loads and corresponding drift values for the forward half cycles were 39.1 kN (0.27% drift) and 34.4 kN (0.32% drift) respectively. Previous cracks extended. Shear cracks on the first story panel which explained formation of compression strut in the region which was closer to left column appeared in the forward cycles as shown in Figure 4.47. New flexural cracks on the front and on the outer side of the left column formed. Also, new shear cracks on the left beam-column joint region and right column–first story beam joint region were observed. Moreover, in the forward cycles new flexural cracks on the right column were observed at a distance of 40 cm and 60 cm to the foundation level. Crushing of the panel corner at the right column-beam interface was also observed as illustrated in Figure 4.48.

In cycle 14, at a load level of 32.8 kN (0.53% drift), previous cracks extended and forked out. 2 horizontal cracks about 65 cm and 63.5 cm away from the foundation level appeared on the first story panel starting from the left column panel interface and right column panel interface respectively. These two cracks propagated and defined the crushing

borders of the first story masonry panel corners. After this cycle, stiffness degradation increased significantly mainly due to separation of the infill from the surrounding frame.

In cycle 16, at load level of 25.1 kN (1.175% drift) right column and first story masonry panel separated about 1 cm. Previous cracks extended. On the right column outer face inclined cracks appeared at a distance of 28 cm from the foundation.

Test was terminated at the end of the 18th cycle. Failure was due to excessive flexural cracks observed on first story columns following crushing of the infill panel at the compression regions. Compression strut formed on the masonry, near to the left column, had an average angle of 54 degree with respect to the foundation beam as shown in Figures 4.46 and 4.47. Aspect ratio played an important role on the failure mechanism. Failure mechanism altered mainly from the lap splice deficiency problem (as in the case of SA1.0 specimens) into failure of the masonry strut. Close-up of the specimen at the end of the test was illustrated in Figure 4.49. Formation of plastic hinges was observed to a certain degree at the end of the lap splice region, although it was not dominant in the failure mode. In other words, splice tensile strength was not as important as the specimens with lower aspect ratios.

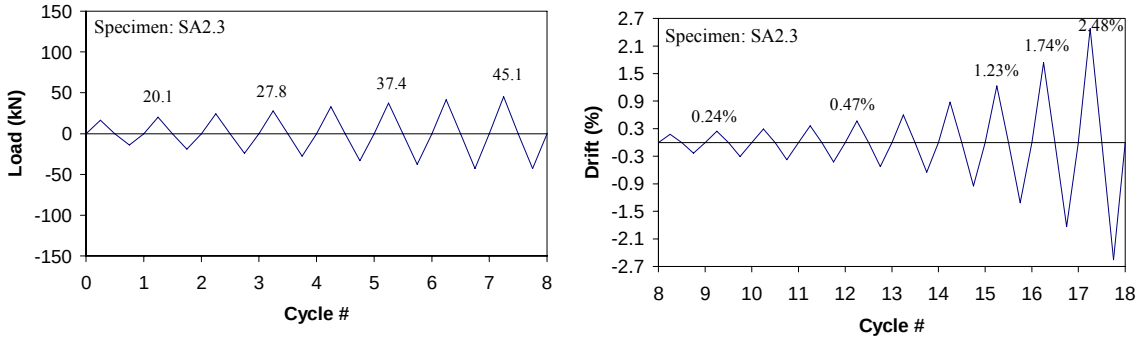

Figure 4.43. Load pattern applied for specimen SA2.3

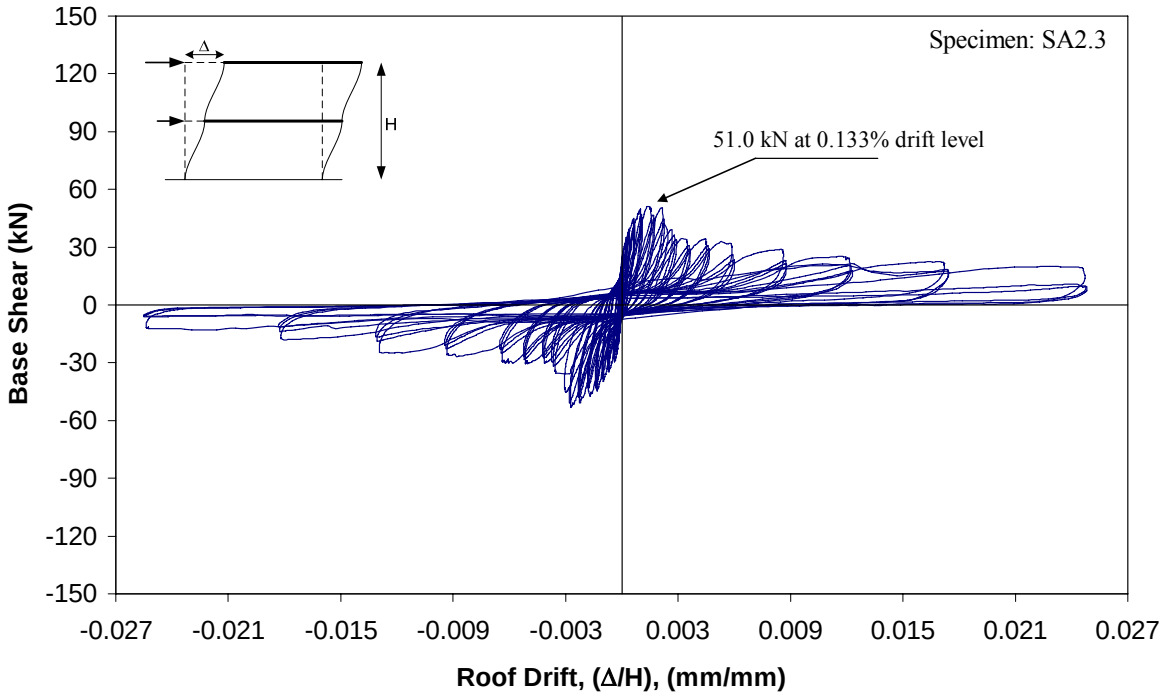

Figure 4.44. Base shear-top drift diagram for specimen SA2.3

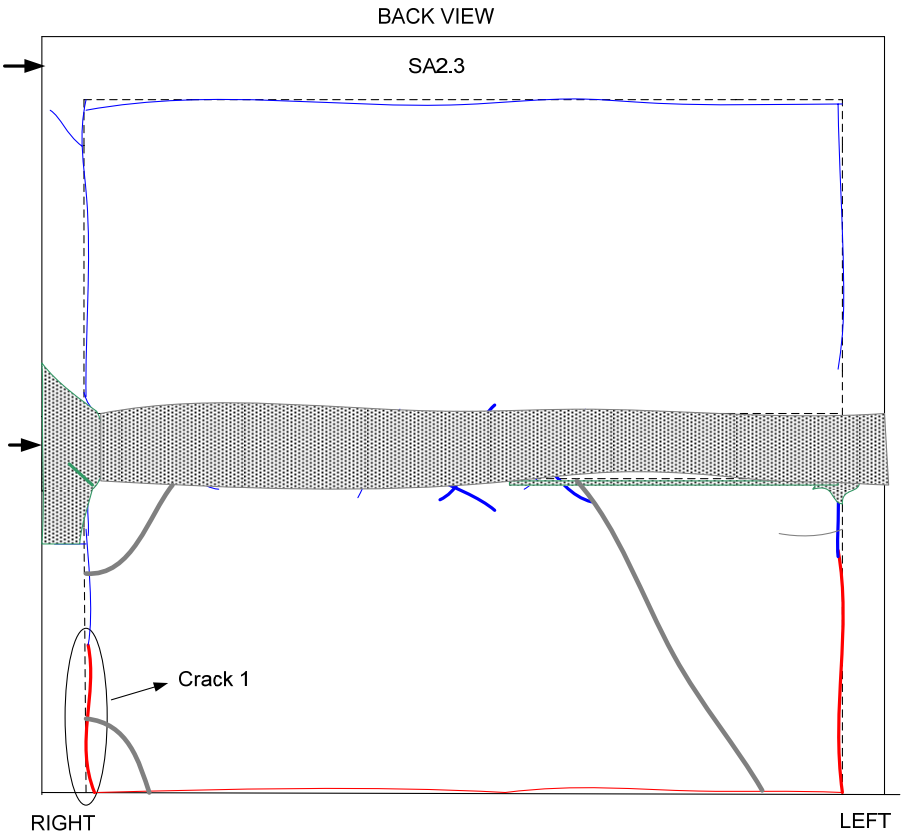

Figure 4.45. Crack distribution at the end of the test for back side of the specimen

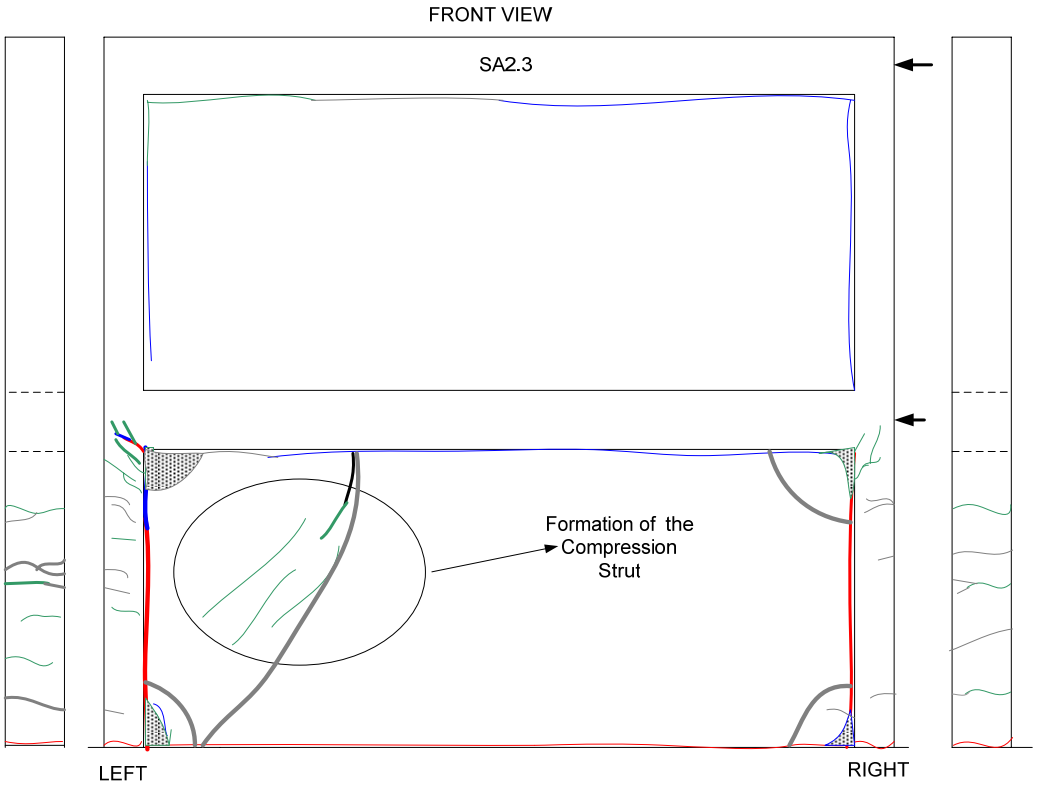

Figure 4.46. Crack distribution at the end of the test for front view

Figure 4.47. Formation of compression strut and formation of crushing around left column

Figure 4.48. Front view of the specimen around right column after the test

Figure 4.49. Close-up of the specimen at the end of the test

Table 4.7. Maximum values for specimen SA2.3

Specimen: SA2.3					
Cycle #	Control Type	Maximum Load P_{max} (kN)	Corresponding Displacement Δ_{max} @ P_{max} (mm)	Minimum Load P_{min} (kN)	Corresponding Displacement Δ_{min} @ P_{min} (mm)
1	LC	16.41	0.01	-14.09	-0.22
2	LC	20.08	0.02	-19.19	-0.31
3	LC	24.31	0.04	-24.16	-0.45
4	LC	27.82	0.14	-27.67	-0.76
5	LC	32.91	0.44	-33.17	-1.30
6	LC	37.37	0.67	-37.86	-1.81
7	LC	41.57	1.14	-42.73	-2.41
8	LC	45.14	1.88	-42.72	-3.12
Specimen: SA2.3					
Cycle #	Control Type	Maximum Displacement Δ_{max} (mm)	Corresponding Load P_{max} @ Δ_{max} (kN)	Minimum Displacement Δ_{min} (mm)	Corresponding Load P_{min} @ Δ_{min} (kN)
9	DC	3.01	44.97	-4.01	-45.80
10	DC	4.21	33.90	-5.27	-38.34
11	DC	5.03	33.11	-6.49	-25.52
12	DC	6.30	28.92	-7.30	-26.27
13	DC	8.06	29.08	-9.05	-26.61
14	DC	10.36	23.35	-11.21	-22.31
15	DC	15.15	19.75	-16.31	-20.27
16	DC	21.21	17.67	-22.65	-16.73
17	DC	30.01	17.90	-31.61	-11.40
18	DC	42.72	9.03	-44.02	-5.53
Note 1: The values given were obtained from the third consecutive cycle of each drift level.					
Note 2: The measurement height was 1725 mm.					
Note 3: LC represents load controlled type of loading.					
Note 4: DC represents displacement controlled type of loading.					

4.8. Specimen SA2.3-CCM

Specimen SA2.3-CCM had an aspect ratio of 2.3 (l/h=2.3). CFRP overlays were applied in the form of double cross diagonals and flag sheets were introduced at the end of diagonals on the specimen. Load controlled and displacement controlled type of loading were applied to specimen SA2.3-CCM to simulate the seismic action. Loading protocol is given in Figure 4.50. Constant axial load of 24.0 kN (N/N_0=0.10) was applied on each column throughout the test. Base shear roof drift diagram is shown in Figure 4.51.

Load controlled type of loading was applied in the first cycle. Maximum applied load and corresponding drift for the forward half cycle was 15.9 kN and 0.000023 respectively. Load increment of the consecutive cycles for the load controlled loading was about 5 kN in forward and backward cycles. There were no visible cracks in the first seven cycles.

In cycle 8, maximum applied load and corresponding drift for forward half cycle was about 49.7 kN and 0.015% respectively. The first cracking sound was heard at this load cycle. First visible cracks were on the left column outer face and propagated about 8 cm horizontally. This flexural crack was 32 cm away from the foundation level.

In cycle 12, formation of new cracks accelerated. The maximum recorded load and corresponding drift for the forward half cycle were 70.1 kN and 0.024% respectively. New flexural cracks were observed on the right column outer face at different elevations of 41.5 cm, 22.5 cm and 14.5 cm. Furthermore, horizontal cracks on the masonry panel formed in this load cycle.

In cycle 14, maximum applied load and corresponding drift for the forward half cycle were 80.0 kN and 0.032% respectively. The first crack on the right column beam-column joint region appeared with a length of 7 cm. Also a flexural crack with a length of 5 cm was observed on the right column front face at a height of 69 cm from the foundation level. Cracking on the interface between right column and foundation became visible.

In cycle 15, maximum applied load and corresponding drift for the forward half cycle were 86.2 kN and 0.037% respectively. Two new cracks which developed parallel to

the 1st cross FRP diagonal in the front of the masonry panel were observed. These were located 46 cm and 37 cm away from the foundation. Moreover, a new flexural hairline crack, 3 cm in length, formed on the right column outer face at a distance of 59 cm from the foundation. In this cycle and in the following cycles, displacement controlled type of loading was applied.

In cycle 19, maximum applied load and corresponding drift were 101.3 kN and 0.15% respectively. Crack width of the 4th crack in the backward half cycle reached 1 mm whereas crack width of the 11th crack was recorded as 1.8 mm in the forward half cycle as seen in Figure 4.52 and 4.53. All cracks observed in these cycles were distributed on the masonry panel.

In cycle 22, maximum applied load and corresponding drift for the forward half cycle were 120.2 kN and 0.31% respectively. Crack width of the 3rd crack attained about 3.5 mm in the backward half cycle. Cracks which were parallel and next to FRP cross diagonals formed. This illustrated that FRP cross diagonals began to bulge and peel off. Cracking was observed on the masonry panel rather than surrounding frame.

In cycle 24, maximum applied load and corresponding drift for the forward half cycle were 132.2 kN and 0.48% in turn. Cracks were mainly on the masonry panel. However some shear and flexural cracks were observed on the left column. The first hairline crack with a length of 3 cm on the left column beam-column joint was observed in the backward half cycle. Some cracks on the 8th cross diagonals formed in the direction of the fibers. Protrusion on the 6th FRP increased.

In cycle 25, maximum applied load and corresponding drift for the forward half cycle were 142.3 kN and 0.62% in turn. Cross FRP diagonals began to rupture. In the forward cycle, 2nd and 6th FRPs were ruptured 13 cm and 12 cm respectively. Then 6th FRP was ruptured completely resulting a load drop in the forward cycles.

In cycle 26, maximum applied loads and corresponding drifts for the forward and backward half cycles were 106.9 kN (0.77% drift) and -143.2 kN (-0.77% drift) respectively. In the forward half cycle, 2nd FRP was ruptured completely and some cracks

on the 1st FRP were observed in the longitudinal direction or fiber direction. Also 8th FRP began to rupture. Considerable load drop in the forward half cycles was observed. However, drastical load drop in the backward half cycle was observed because of the rupturing of 7th and 3rd FRPs.

In cycle 27, all the cross diagonals were ruptured both in the forward and backward cycles. Load drop was seen clearly in the base shear-roof drift diagram in Figure 4.51. Test was terminated at a drift level of 1.82% in the 28th cycle. Loading type, maximum displacement and corresponding loads and maximum loads and corresponding displacement values were given in Table 4.8. A sliding surface formed at the midheight of the first story. Shear sliding type of failure followed by gravity collapse of the columns as shown in Figures 4.54, 4.55 and 4.56. There were several reasons why specimen slided at the mid-height of the masonry panel. One of them was FRP orientation. Since we applied FRP in the form of cross diagonals, contribution of FRPs to the load carrying capacity was the least at the mid-height compared to the base despite the same effective area of the FRP. The other reason was the reduction of the sliding surface. When a crack formed at the mid-height of the specimen, the sliding surface automatically decreased and this triggered the formation of the sliding surface at the mid-height. Spalling of cover concrete, loss of unconfined core concrete and buckling of longitudinal steel in the lap splice regions were observed at the end of the test at a drift level of 1.26%.

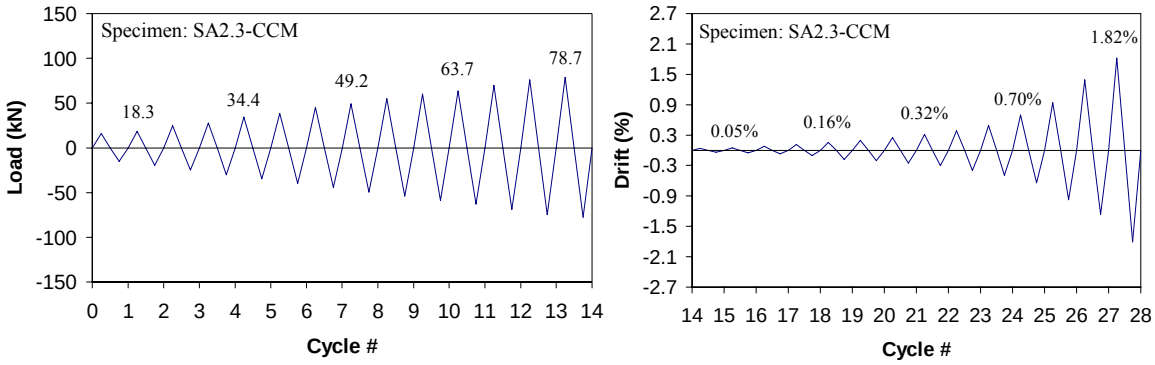

Figure 4.50. Load pattern applied for specimen SA2.3-CCM

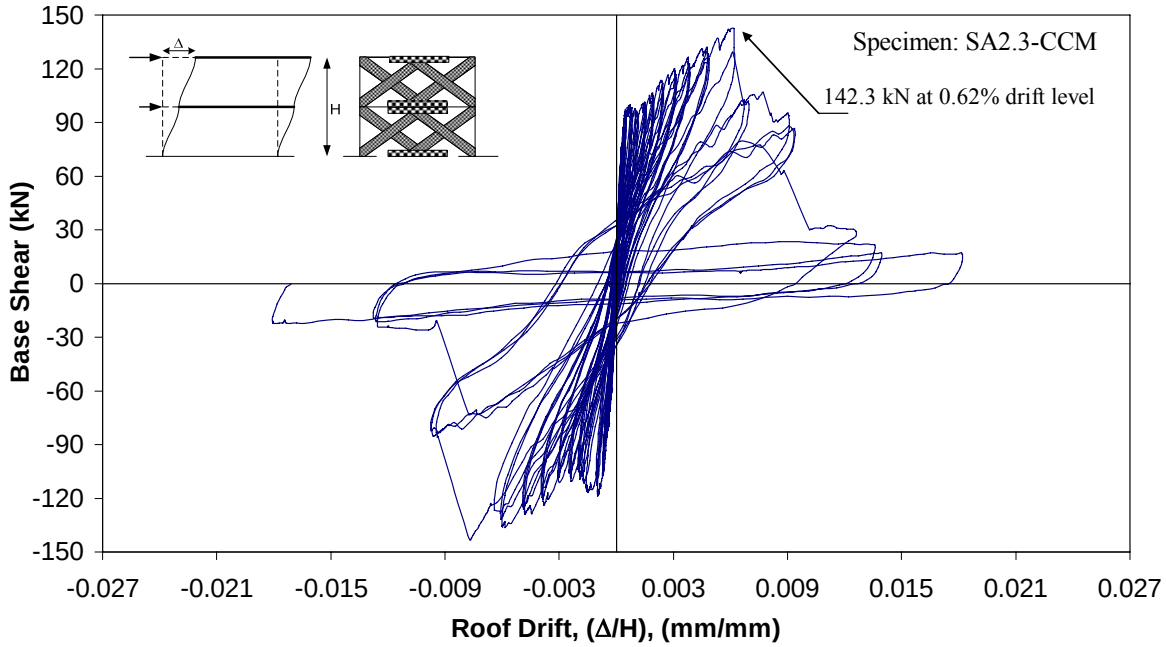

Figure 4.51. Base shear-top drift diagram for specimen SA2.3-CCM

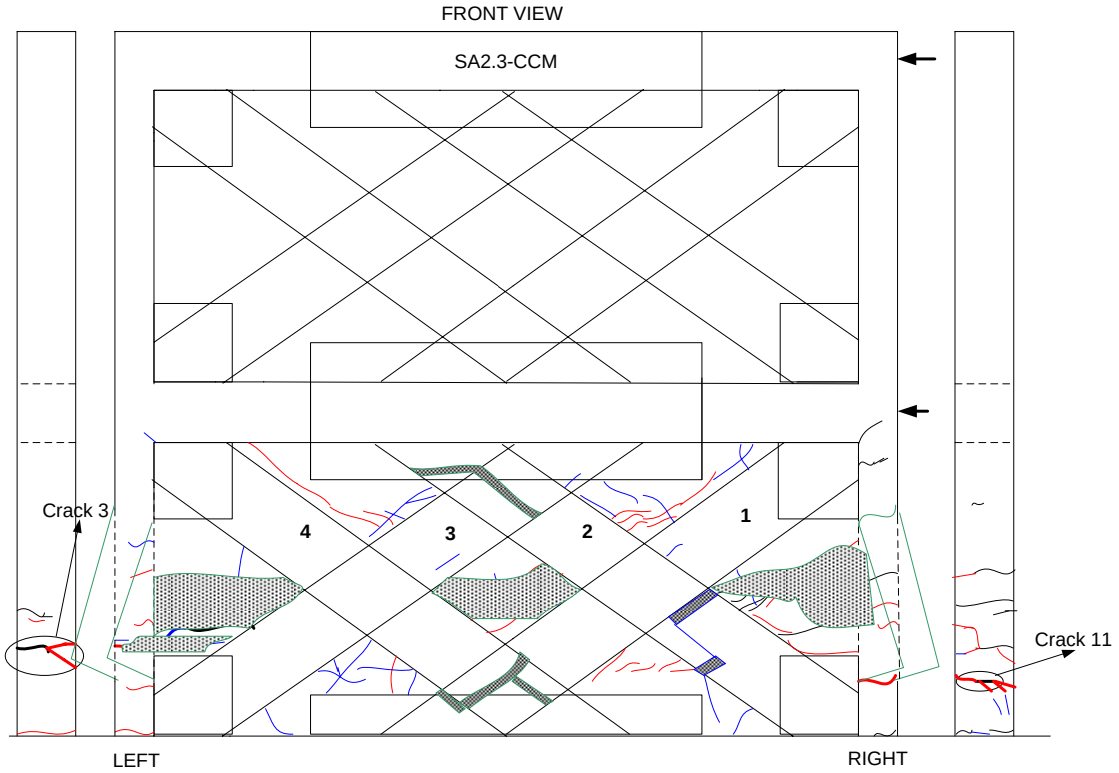

Figure 4.52. Crack distribution at the end of the test for front view

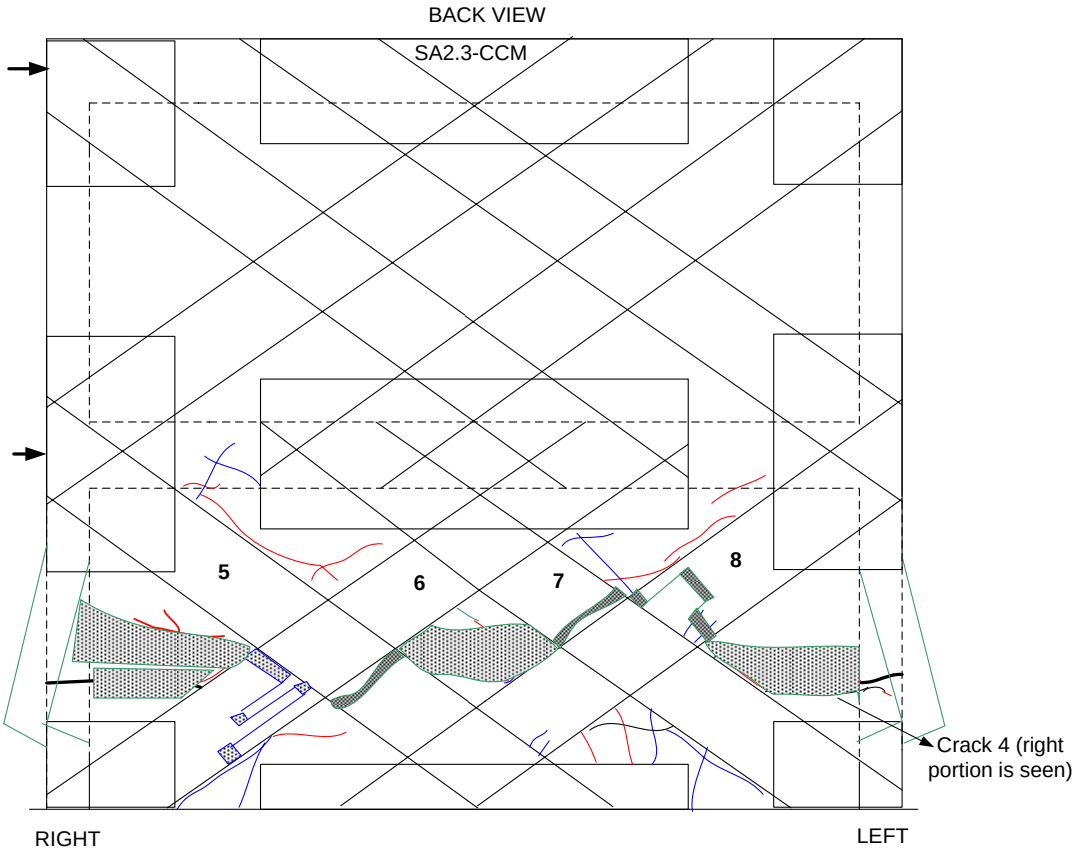

Figure 4.53. Crack distribution at the end of the test for back side of the specimen

Figure 4.54. Close-up of left column at the end of the test

Figure 4.55. Front view of the specimen at the final state

Figure 4.56. A view of the right column

Table 4.8. Maximum values for specimen SA2.3-CCM

Specimen: SA2.3-CCM					
Cycle #	Control Type	Maximum Load P_{max} (kN)	Corresponding Displacement Δ_{max} @ P_{max} (mm)	Minimum Load P_{min} (kN)	Corresponding Displacement Δ_{min} @ P_{min} (mm)
1	LC	15.87	0.04	-14.85	-0.08
2	LC	18.31	0.07	-19.29	-0.09
3	LC	24.74	0.10	-24.48	-0.12
4	LC	27.90	0.11	-30.00	-0.18
5	LC	34.38	0.15	-34.59	-0.21
6	LC	38.34	0.15	-39.78	-0.25
7	LC	45.27	0.20	-44.32	-0.29
8	LC	49.19	0.25	-49.51	-0.34
9	LC	54.96	0.29	-54.01	-0.40
10	LC	60.15	0.36	-58.58	-0.48
11	LC	63.71	0.34	-62.91	-0.52
12	LC	69.72	0.40	-68.83	-0.58
13	LC	76.11	0.47	-74.59	-0.68
14	LC	78.69	0.54	-77.69	-0.71
Specimen: SA12.3-CCM					
Cycle #	Control Type	Maximum Displacement Δ_{max} (mm)	Corresponding Load P_{max} @ Δ_{max} (kN)	Minimum Displacement Δ_{min} (mm)	Corresponding Load P_{min} @ Δ_{min} (kN)
15	DC	0.63	84.20	-0.62	-64.18
16	DC	0.90	93.36	-0.85	-82.41
17	DC	1.41	85.47	-1.14	-96.35
18	DC	1.99	88.81	-1.81	-105.17
19	DC	2.74	95.12	-3.12	-104.55
20	DC	3.42	101.46	-3.48	-102.60
21	DC	4.29	109.38	-4.30	-104.27
22	DC	5.44	113.55	-5.25	-107.12
23	DC	6.67	120.51	-6.83	-115.53
24	DC	8.44	125.92	-8.47	-124.45
25	DC	12.01	97.12	-11.06	-126.02
26	DC	16.19	83.02	-16.82	-81.13
27	DC	24.06	16.13	-21.81	-19.54
28	DC	31.40	15.51	-31.14	-21.25
Note 1: The values given were obtained from the third consecutive cycle of each drift level.					
Note 2: The measurement height was 1724 mm.					
Note 3: LC represents load controlled type of loading.					
Note 4: DC represents displacement controlled type of loading.					

4.9. Specimen SA2.3-CV

Specimen SA2.3-CV with an aspect ratio of 2.3 (l/h=2.3) was strengthened with CFRP overlays which were applied in the form of cross diagonals and vertical strips. The CFRP scheme was the same as specimens SA1.7-S and SA1.0-CV. These CFRP overlays were anchored to the predetermined holes on the surrounding frame by using CFRP anchors. Load controlled and displacement controlled type of loading were applied to specimen SA2.3-CV to simulate seismic action. Loading protocol was given in Figure 4.57. Constant axial load of 22.5 kN (N/N_0=0.09) was applied on each column and kept constant throughout the test. Base shear roof drift diagram is shown in Figure 4.58.

Load controlled type of loading was applied in the first cycle. Maximum applied load and corresponding drift for the forward half cycle was 9.3 kN and 0.0000058 respectively. Load increment of the consecutive cycles was 5 kN. There were no visible cracks in the first eight cycles.

In cycle 9, Maximum applied load and corresponding drift for forward half cycle was about 48.1 kN and 0.025% respectively. First visible crack was on the right column outer face having a length of 8 cm and was 18 cm away from the foundation level. The second one, which was 5cm in length, was on the intersection of the foundation and right column outer face. Both flexural cracks formed in the forward half cycle.

In cycle 11, displacement controlled cycles began. Maximum applied load and corresponding drift were about 57.3 kN and 0.042% for the forward half cycle. In this cycle the crack between first story panel and the first story beam extended to the length of 97 cm. In cycle 12, some of the previous cracks extended and new cracks formed on the right beam-column joint and right column outer face. The shear crack on the joint was about 4 cm in length whereas the flexural crack was long about 5.5 cm, and 14.5 cm away from the foundation level. Maximum applied push load and corresponding drift for this cycle was about 67.5 kN and 0.064% respectively.

In cycle 15, maximum applied load and corresponding drift for the forward half cycle were 80.8 kN and 0.19% respectively. The crack located on the right column outer

face, 14.5 cm away from the foundation level, forked out and extended 10 cm toward the foundation. Protrusion of plaster was also observed on the back of the specimen on the first story beam level. Previous cracks extended. New cracks on the first story masonry panel appeared. A crack with a length of 11 cm between left column outer face and the foundation occurred. Separation with a length of 105 cm between first story panel and the foundation started.

In cycle 17, maximum load and corresponding drift for the forward half cycle were 83.3 kN and 0.28% respectively. No new cracks on the surrounding frame were observed. Diagonal cracks which were parallel to cross FRPs were observed on the first story masonry panel. A crack on the left column outer face which was about 14 cm away from the foundation level extended throughout the front face of the column. Previous cracks were also extended to different lengths, changing from 2 cm to 10 cm. Protrusion was observed on the cross diagonals. Half of the vertical strip, named as 22, which was 13.5 cm away from the right column outer face was broken.

In cycle 18, maximum applied push load and corresponding drift were 89.4 kN and 0.37% respectively. The vertical strip, named as 22, which was partially broken ruptured completely in the forward half cycle as shown in Figure 4.59. However, load carrying capacity tended to increase in the following cycles. Vertical cracks appeared on the first story masonry panel extended until the diagonal FRPs. These cracks were almost perpendicular to cross FRPs. This event illustrated the restraining effects and effectiveness of the cross FRPs. Two flexural cracks with an average length of 3.5 cm appeared 70 cm and 75 cm away from the foundation level on the front of the right column in the forward half cycle.

In cycle 20, maximum applied push load and corresponding drift were 105.2 kN and 0.59% respectively. The vertical strip which was 27.5 cm away from the right column outer face, on the back of the specimen, ruptured in the forward half cycle. A shear-flexural crack on the right column outer face with a length of 5 cm appeared 4.5 cm away from the foundation level. New cracks on the first story masonry panel occurred. At the end of this cycle two vertical strips, 22 and 23, ruptured completely. However, specimen continued to carry the extra load in the following cycle.

In cycle 21, maximum applied load and corresponding drift for the forward and backward half cycles were 111.6 kN (0.83%) and -102.1 kN (-0.68%) respectively. Maximum load for the forward cycles was attained in this cycle. However, load for the backward cycles started to decrease. In the forward half cycle, a significant stiffness change was observed. Cross diagonal, 19, ruptured in tension near to top left flag when the specimen reached the maximum load as indicated in Figure 4.60. After rupturing of this FRP, load dropped drastically. Cross diagonal 24 started to rupture in the backward cycle. When the specimen reached about 102.1 kN, cross diagonals 24 and 18 ruptured completely and sudden load drop was observed as shown in Figure 4.58. These cross diagonals ruptured around the right top flags. At the end of this cycle, all FRP sheets were ruptured except 16.

In the next two cycles, drift levels corresponding maximum loads for the forward half cycles were about 1.26% and 1.68% respectively. After the FRPs were ruptured, heavy damage occurred as shown in Figure 4.61 and test was terminated at the end of the 23rd cycle. Loading type and maximum values for each successive drift level are summarized in Table 4.9. Failure could be attributed to the rupturing of FRPs and capacity exceedance of the columns. Frame columns failed under a combined action of shear, moment and axial forces (Figures 4.62 and 4.63). Rupturing of FRPs transferred all the actions from the FRP strengthened frame to the infilled frame and accelerated cracking and deterioration took place. Buckling of the longitudinal steel on the left column top end, spalling of cover concrete and loss of inadequately confined core concrete which can cause vertical movement implied gravity collapse of the frame after crushing of the infill at the end of the test (Figure 4.62). Separation of the infill from the surrounding frame was observed clearly after rupturing of the FRPs. Formation of horizontal cracks on the masonry panel was the indicator of sliding but this was not seen as predominant on the failure. At the last cycle, pictures and video camera investigations illustrated that the frame and infilled masonry behaviors were not consistent with each other especially after rupturing of FRPs and crushing of masonry around the corner flags. In other words separation was much more notable. Behavior of the specimen showed that axial load failure occurred right after the shear failure of the columns that of which was in good agreement with the literature.

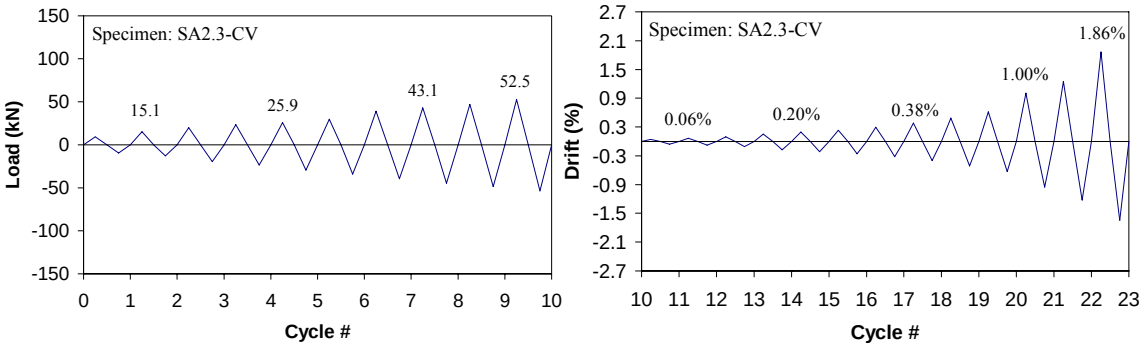

Figure 4.57. Load pattern applied for specimen SA2.3-CV

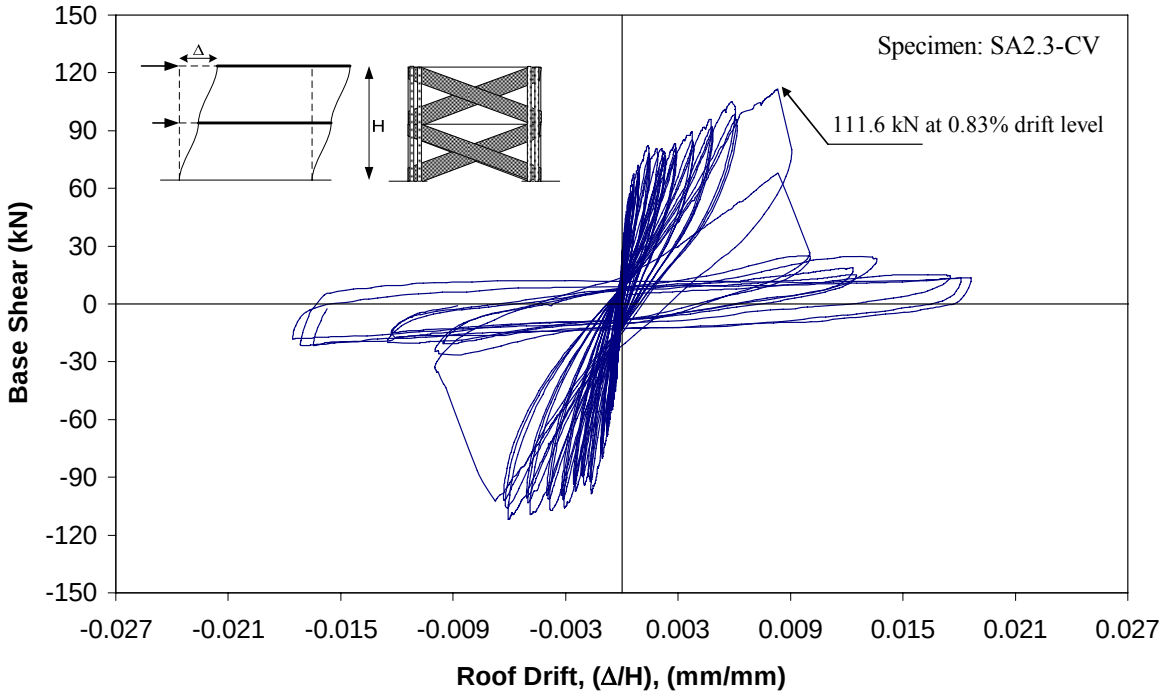

Figure 4.58. Base shear-top drift diagram for specimen SA2.3-CV

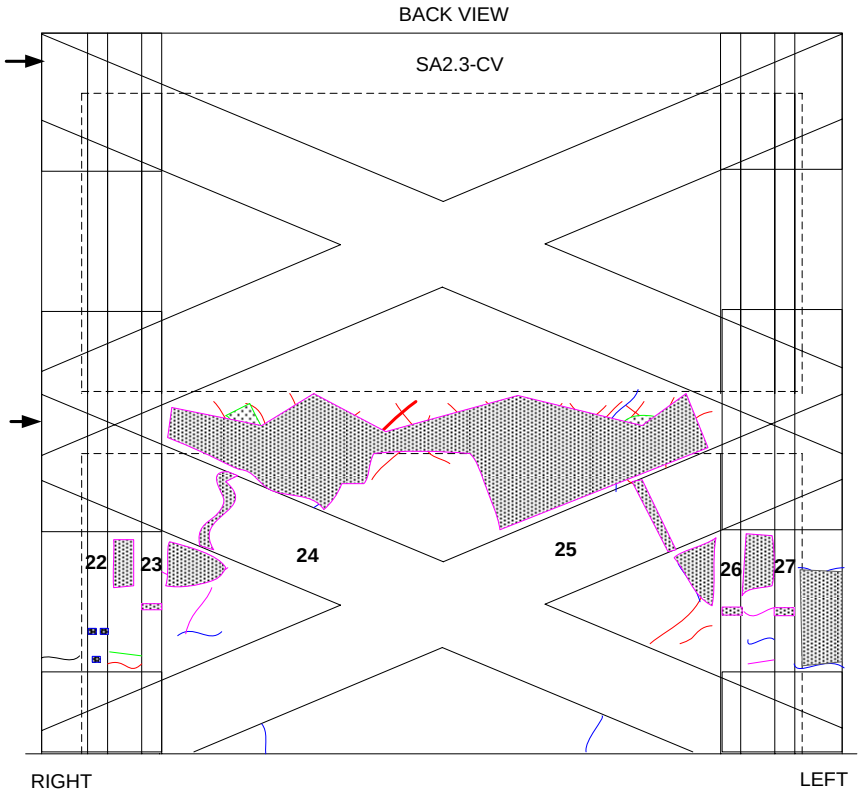

Figure 4.59. Crack distribution at the end of the test for back side of the specimen

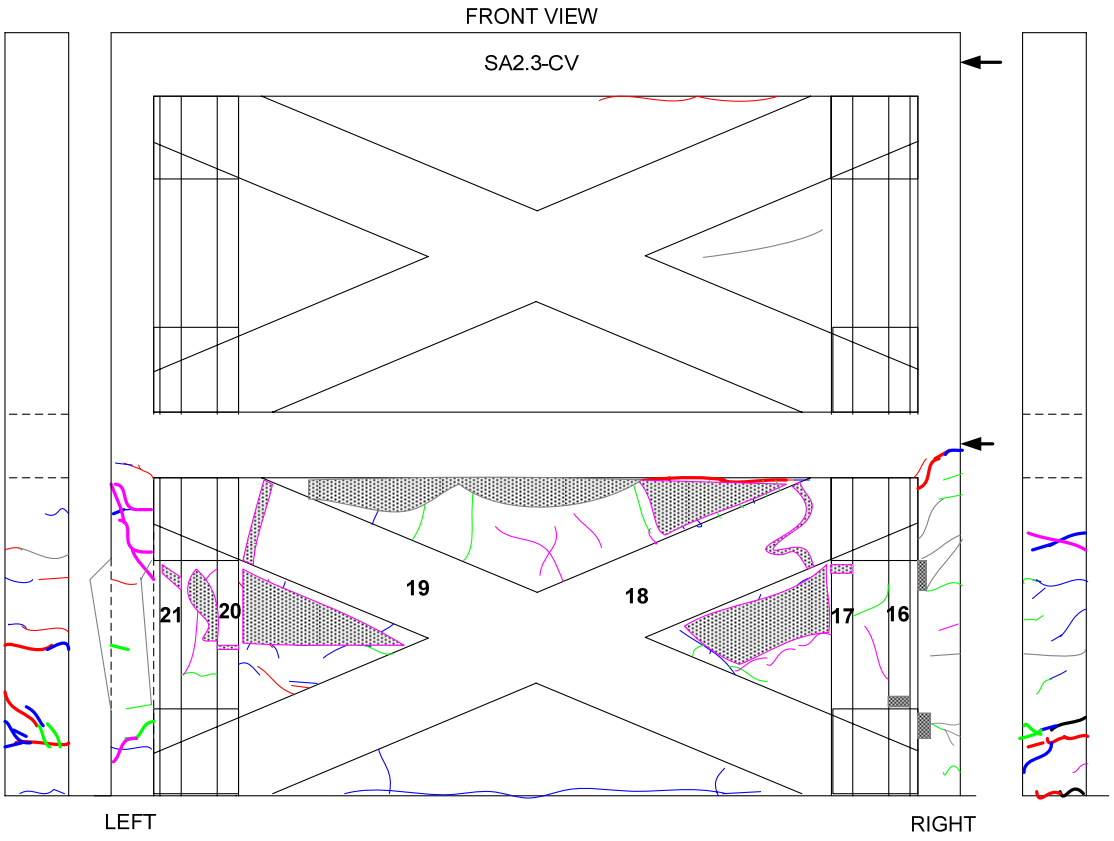

Figure 4.60. Crack distribution at the end of the test for front view

Figure 4.61. Front view of the specimen

Figure 4.62. Close-up of left column top and bottom ends

Figure 4.63. Close-up of right column

Table 4.9. Maximum values for specimen SA2.3-CV

Specimen: SA2.3-CV					
Cycle #	Control Type	Maximum Load P_{max} (kN)	Corresponding Displacement Δ_{max} @ P_{max} (mm)	Minimum Load P_{min} (kN)	Corresponding Displacement Δ_{min} @ P_{min} (mm)
1	LC	9.28	0.01	-9.53	-0.11
2	LC	15.13	0.02	-12.75	-0.14
3	LC	19.72	0.06	-19.54	-0.22
4	LC	23.63	0.03	-23.46	-0.33
5	LC	25.92	0.07	-29.37	-0.38
6	LC	29.83	0.15	-34.26	-0.44
7	LC	38.92	0.25	-39.34	-0.52
8	LC	43.08	0.37	-44.61	-0.63
9	LC	47.01	0.48	-48.64	-0.76
10	LC	52.52	0.62	-53.64	-0.90
Specimen: SA2.3-CV					
Cycle #	Control Type	Maximum Displacement Δ_{max} (mm)	Corresponding Load P_{max} @ Δ_{max} (kN)	Minimum Displacement Δ_{min} (mm)	Corresponding Load P_{min} @ Δ_{min} (kN)
11	DC	0.74	55.32	-1.01	-54.68
12	DC	1.08	60.46	-1.39	-67.17
13	DC	1.61	64.24	-1.93	-77.20
14	DC	2.61	73.96	-3.08	-88.07
15	DC	3.42	66.24	-3.73	-88.81
16	DC	4.04	75.54	-4.46	-93.25
17	DC	5.05	78.68	-5.57	-98.26
18	DC	6.64	80.32	-6.93	-98.03
19	DC	8.41	85.81	-8.81	-99.61
20	DC	10.66	90.03	-10.91	-101.27
21	DC	17.38	24.70	-16.49	-20.27
22	DC	21.65	15.06	-21.18	-14.17
23	DC	32.24	12.93	-28.47	-21.21
Note 1: The values given were obtained from the third consecutive cycle of each drift level.					
Note 2: The measurement height was 1730 mm.					
Note 3: LC represents load controlled type of loading.					
Note 4: DC represents displacement controlled type of loading.					

4.10. Specimen SA2.3-CFM

Specimen SA2.3-CFM had an aspect ratio of 2.3 (l/h=2.3). CFRP overlays were applied in the form of narrow cross diagonals with a width of 8 cm smeared over the infill panels and columns were wrapped horizontally. Moreover beams were also wrapped vertically. These CFRP overlays were anchored to the predetermined locations on the surrounding frame by using CFRP anchors. Load controlled and displacement controlled type of loading were applied to this specimen to simulate seismic action. Loading protocol was given in Figure 4.64. Constant axial load of 27.5 kN (N/N_0=0.10) was applied on each column and kept constant throughout the test. Base shear versus roof drift diagram was given in Figure 4.65. Loading type and maximum values at each successive drift level was listed in Table 4.10.

In the first cycle maximum load and corresponding drift for the forward half cycle were 18.6 kN and 0.000070 respectively. Load controlled type of loading was applied. No visible damage was observed in the first 9 cycles. Displacement controlled type of loading was started in cycle 9 at a load level of 67.1 kN (0.034% drift) for the forward half cycle.

In cycle 10, some protrusion on the left column and right column FRP wraps was observed. Since the specimen was strengthened by means of cross diagonals and wrapping of columns, cracks were not able to be observed on the columns and most of the panels. Maximum load and corresponding drift for the forward half cycle were 82.5 kN and 0.051% respectively.

In cycle 12, the first cracks at the intersections of the left column foundation and right column foundation were observed. Also inclined and horizontal cracks formed on the first story masonry panel. Maximum load and corresponding drift for the forward half cycle were 105.1 kN and 0.099% respectively.

In cycle 13, previous cracks extended and new cracks formed. A new shear crack with a length of 2.5 cm on the right beam-column joint region formed. Maximum load and corresponding drift for the forward half cycle were 118.4 kN and 0.146% respectively.

In cycle 17, cracks at the intersection of the masonry panel and foundation were observed. Crack width of crack 41 reached 2 mm in the backward half cycle as shown in Figure 4.66. Cracks were generally either parallel to FRP cross diagonals which showed the signs of protrusion or horizontal which illustrated the signs of sliding (Figure 4.67). Extensive cracks were observed in this cycle. Maximum load and corresponding drift for the forward half cycle were 128.4 kN and 0.37% respectively.

In cycle 19, debonding of FRPs from the plaster between CFRP anchorages was observed. Previous cracks extended and widened (Figure 4.68). New cracks at different elevations were observed on the masonry. These cracks were generally parallel to the cross diagonals. Wrapping overlay of the left column ruptured at different levels and cross diagonal under that overlay was seen clearly as indicated in Figure 4.69. Moreover separation between right column and foundation started in the forward half cycle. Maximum load and corresponding drift for the forward half cycle were 135.6 kN and 0.55% respectively. Maximum load and corresponding drift for the backward half cycle were -137.3 kN and -0.59% respectively. The specimen reached maximum load in the backward half cycle at this drift level.

In cycle 20, cross diagonals, wraps and flags started to rupture. In the forward cycle, 7^{th} FRP ruptured under the action of axial forces just below the anchorage between 2^{nd} and 7^{th} FRPs. Separation between foundation and right column plus masonry increased and became more noticeable due to rupturing of inclined anchorage which fixed the cross diagonal of G and vertical anchorage which supported the flag behind the right column (Figure 4.70). The middle flag in the front face of the specimen peeled off from the plaster at the right end. The middle flag in the back of the specimen ruptured vertically just next to the wall anchorage. The anchorage that supported 8^{th} cross diagonal on the foundation level started to slip. Some cracks formed on the cross diagonals namely 9, 10, 3, 4 in the fiber direction. Cross diagonals D and C ruptured at elevations of 24 cm and 52 cm respectively. 10^{th} FRP also ruptured completely but 3^{rd} FRP ruptured partially. Load drop was not sudden due to confinement effect of wrapping sheets and even distribution of the cross FRPs. Maximum load and corresponding drift values for the forward half cycle were 136.8 kN and 0.737% respectively.

In cycle 21 all cross diagonals except A, E, F, 5, 6 ruptured. Crushed plaster and hollow clay tiles (HCTs) started to fall down. Sliding started to be seen clearly. In cycle 22, test was terminated. The cross diagonal A ruptured in this cycle.

Failure was due to rupturing of FRPs and shear-sliding which was an undesirable failure mode. Figures 4.71 and 4.72 illustrated the specimen after the test. Some observations during the test and after the test were done as listed below. Buckling of longitudinal re-bars in lap splice region and spalling of cover and unconfined core concrete were recorded which implied sudden loss of gravity load carrying capacity (Figure 4.72). Debonding of FRPs from plaster accumulated especially at the first story mid-height region of the specimen (Figure 4.71). Crushing and spalling of hollow clay tiles around the sliding failure surface occurred. That ties bent 90^0 around column lap splice regions opened indicated the insufficiency bent angle. Shortening of columns took place as much as 4 cm. No conspicuous cracks were noted due to wrapping of the columns throughout the story height. Debonded FRPs buckled in the forward or backward cycles depending on their orientations with respect to horizontal axis. This caused some cracks on the FRPs in the fiber direction and accelerated FRP failure. Insignificant sliding between the FRP and foundation anchorages was also observed as indicated in Figure 4.73. The failure on the columns were at the tips of the lap splices which were 16 cm away from the foundation. However, failure surface on the masonry wall was about 22 cm away from the foundation. In other words, failure surfaces on the masonry and columns were at different elevations. There were several reasons why specimen slided at the location mentioned above. One of them was FRP orientation. Since we applied FRP in the form of cross diagonals, contribution of FRPs to the rocking moment capacity was the least at that certain height compared to the base despite the same effective area of the FRP. The other reason was the reduction of the sliding surface. When a horizontal crack opened at a certain height of the specimen, resulting a decreased contact surface, sliding type of failure was triggered at that specific height. This certain height generally coincided with the height where the cross diagonals met.

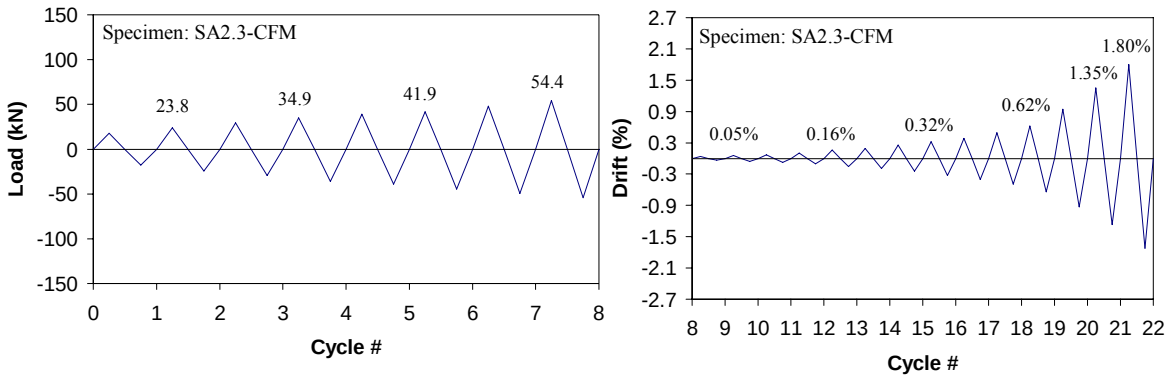

Figure 4.64. Load pattern applied for specimen SA2.3-CFM

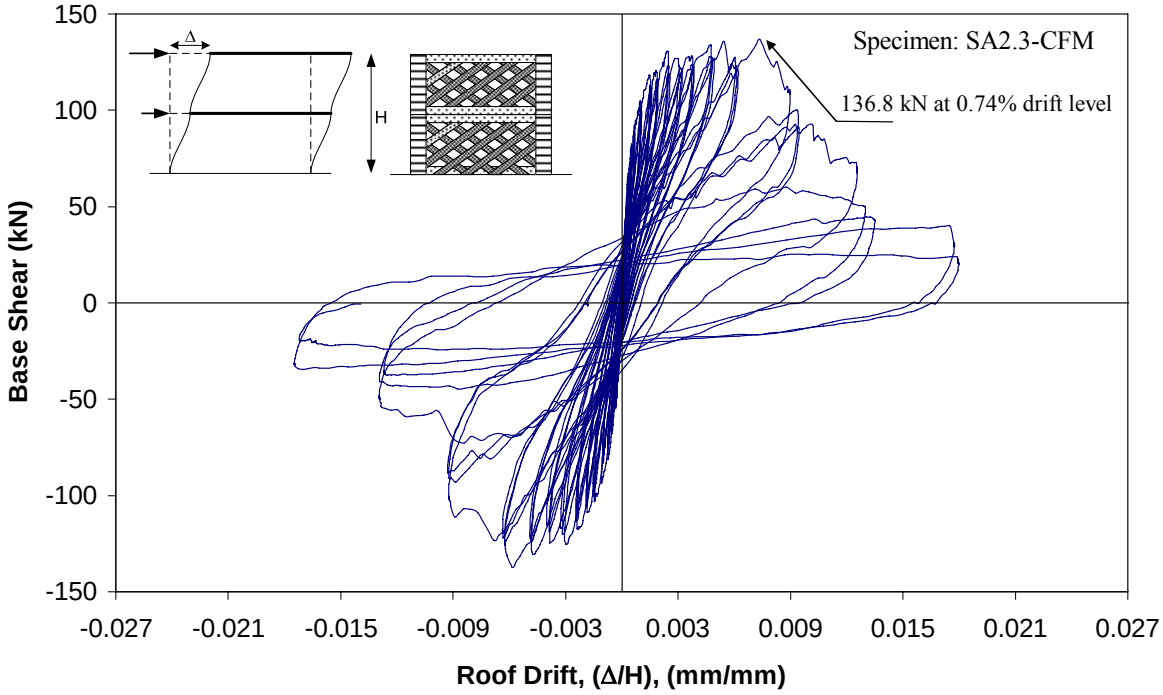

Figure 4.65. Base shear-top drift diagram for specimen SA2.3-CFM

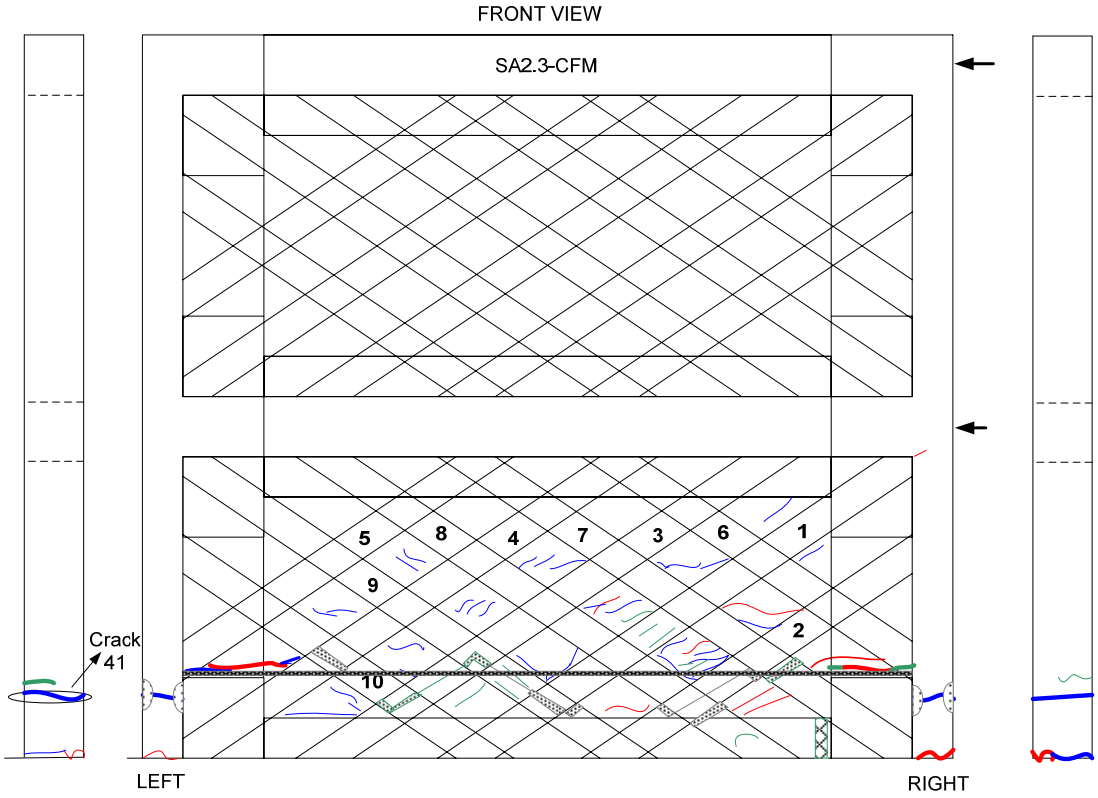

Figure 4.66. Crack distribution at the end of the test for front view

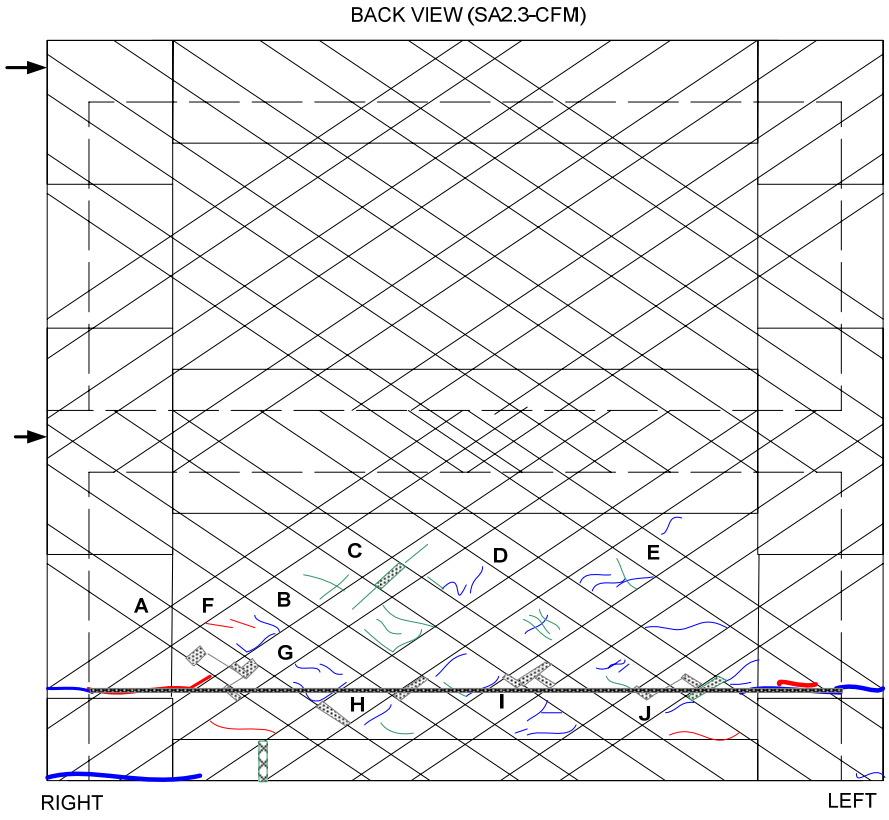

Figure 4.67. Crack distribution at the end of the test for back side of the specimen

Figure 4.68. Close-up of a crack width on the left column outer face

Figure 4.69. Close-up of cross diagonal under the ruptured wrapping overlay

Figure 4.70. Close up of the separation around right column

Figure 4.71. Front view of the specimen after the test

Figure 4.72. Close-up of the left and right columns after the test

Figure 4.73. Close-up of the anchorage sliding

Table 4.10. Maximum values for specimen SA2.3-CFM

Specimen: SA2.3-CFM					
Cycle #	Control Type	Maximum Load P_{max} (kN)	Corresponding Displacement D_{max} @ P_{max} (mm)	Minimum Load P_{min} (kN)	Corresponding Displacement D_{min} @ P_{min} (mm)
1	LC	17.69	0.09	-17.61	-0.13
2	LC	23.82	0.19	-24.44	-0.17
3	LC	29.37	0.19	-29.28	-0.26
4	LC	34.85	0.21	-35.94	-0.36
5	LC	39.08	0.32	-38.94	-0.38
6	LC	41.91	0.31	-44.45	-0.50
7	LC	48.20	0.45	-49.55	-0.50
8	LC	54.42	0.56	-54.22	-0.55
Specimen: SA2.3-CFM					
Cycle #	Control Type	Maximum Displacement D_{max} (mm)	Corresponding Load P_{max} @ D_{max} (kN)	Minimum Displacement D_{min} (mm)	Corresponding Load P_{min} @ D_{min} (kN)
9	DC	0.62	66.62	-0.60	-45.57
10	DC	0.92	75.07	-0.96	-65.80
11	DC	1.18	84.47	-1.29	-75.51
12	DC	1.80	99.49	-1.76	-82.38
13	DC	2.73	110.19	-2.66	-99.46
14	DC	3.30	112.21	-3.30	-101.71
15	DC	4.41	117.11	-4.22	-109.78
16	DC	5.51	119.96	-5.60	-116.91
17	DC	6.62	122.56	-6.88	-112.95
18	DC	8.46	125.40	-8.43	-121.14
19	DC	10.67	120.18	-10.93	-118.10
20	DC	16.21	89.95	-15.94	-87.83
21	DC	23.16	42.74	-21.76	-36.01
22	DC	30.84	20.18	-29.54	-19.38
Note 1: The values given were obtained from the third consecutive cycle of each drift level.					
Note 2: The measurement height was 1716 mm.					
Note 3: LC represents load controlled type of loading.					
Note 4: DC represents displacement controlled type of loading.					

Axial load levels, some material properties, peak loads and corresponding drifts as well as failure modes for each specimen are summarized in Table 4.11.

Table 4.11. Summary of test results

Specimen	f_{ck} (MPa)	f_m (MPa)	N/N_0 (%)	P_{max} (kN)	$(\Delta/h)_{roof}$ @P_{max} (kN)	P_{min} (kN)	$(\Delta/h)_{roof}$ @P_{min} (kN)	Failure Mode
SA1.0	8.0	12.6	14	25.7	0.000988	-23.4	-0.00134	Rocking mechanism Insufficient lap splice length
SA1.0-CV	8.9	5.2	11	58.0	0.00771	-60.0	-0.00719	Tensile failure of columns Rupturing of vertical FRP
SA1.0-C2V	16.9	7.0	9	75.2	0.00694	-71.7	-0.00705	Shear sliding at mid-height
SA1.0-CVL	15.3	7.5	10	60.8	0.00894	-57.1	-0.00899	Shear sliding at midheight
SA1.7-D	13.7	5.2	11	86.2	0.00338	-89.9	-0.00377	Insufficient CFRP anchorage lengths at the foundation level
SA1.7-S	10.2	6.7	10	83.7	0.00591	-86.2	-0.00381	Lap splice failure of column longitudinal bars Shear failure of the right column, Rocking and sliding at the midheight of the panel
SA2.3	11.0	6.5	11	51.0	0.00133	-53.3	-0.00274	Corner crushing and Excessive flexural cracks
SA2.3-CCM	16.0	10.5	10	142.3	0.0062	-143.2	-0.00768	Shear sliding at mid-height Gravity collapse of columns
SA2.3-CV	15.8	7.0	9	111.6	0.0083	-111.8	-0.00605	Capacity exceedance of columns and Rupturing of FRPs
SA2.3-CFM	18.0	6.5	10	136.8	0.00737	-137.3	-0.00585	Shear sliding (22 cm above the foundation) Rupturing of FRPs

5. EVALUATION OF THE TEST RESULTS

5.1. General

In this chapter, the test specimens are evaluated in terms of strength deterioration, stiffness degradation, energy dissipation, and residual displacement and ductility.

5.2. Failure Modes

Strengthening of the specimens with FRP increased the ultimate loads depending mainly on FRP configurations and on the frame aspect ratio. Also, application of FRP changed the failure modes of the infilled specimens depending on the aspect ratio (frame bay length/story height). Stress-strain relation of CFRP is assumed linearly elastic under uniaxial loading. However, FRP showed relatively poor behavior under the combined action of shear and axial tensile forces. That's why high strains that can be obtained from FRP coupon tests could not possibly be obtained during the test of the frame specimens. Analytically and experimentally obtained ultimate loads of the strengthened specimens are compared and listed in Table 5.1. The ratios between calculated and measured capacities are given in the last column of Table 5.1. The formulations developed in this chapter are inspired from the Paulay's approach [2]. As indicated in Table 5.1, capacities can be calculated more accurate for flexural dominant system (smaller aspect ratio) whereas there was scatter for shear dominant systems. However, the calculated values can satisfactorily predict failure loads. In order to better understand and visualize the convergence of the calculated capacities, envelope curves were normalized with respect to calculated capacity loads. For the tested specimens, some combination of the following failure modes can be described:

- Tension failure of the tension column,
- Flexural or shear failure of the columns,
- Sliding shear failure,
- Compression failure of the diagonal strut,
- Overturning mode of failure,

- Anchorage failure of the FRP anchorages, and rupturing of FRP overlays,

Low aspect ratio (l/h_1), and high moment/shear ratio results in tension failure of the tension column which can be identified as an overall flexural type of failure. Tension failure of the tension column can also be considered as a part of the overturning mode of failure. The lateral load capacity of the columns, either flexure or shear is included in the overall shear sliding type of failure of the specimens. Diagonal tensile cracking of the panel generally takes place before the compression failure of the diagonal strut or the flexural or shear failure of the columns. Therefore, such a failure is not stated as one of the failure modes. Local debonding of FRP strips from the substrate surface generally took place right before the complete loss of strength. Hence, this type was also not listed as one of the failure modes as it happened at low load levels compared to the failure load. Rupturing of FRP was not considered as a failure mode since it was already included in the shear sliding and overturning type of failures. Mainly three failure modes out of above listed ones were described as following; the sliding shear failure mode, the compression failure of the diagonal strut mode, and the overturning mode of failure.

At low load levels, the frame and the panel acted together. As deformations increased, infill and frame behaved differently and all of the shear was assumed to be carried by infill panel at this stage due to high infill to frame stiffness ratio. Different behavior tendency, which were shear and flexural modes, resulted in separation between infill and the surrounding frame. An infilled frame could be idealized as diagonally braced pin-jointed frame. As the lateral deformations increased, the response mechanism shifted from a diagonally braced pin jointed frame to a knee-braced frame [2]. Effective height of the column decreased due to the formation of hinges which were about at mid-height and top or bottom of the column. Hinge formation at about mid-height and top or bottom of the columns and imminent shear failure of the columns resulted from the masonry panel which was in contact with the lower left portion of the left column and upper right portion of the right column. Pin jointed frame and knee braced frame with shear sliding at mid-height are shown in Figures 5.1 and 5.2.

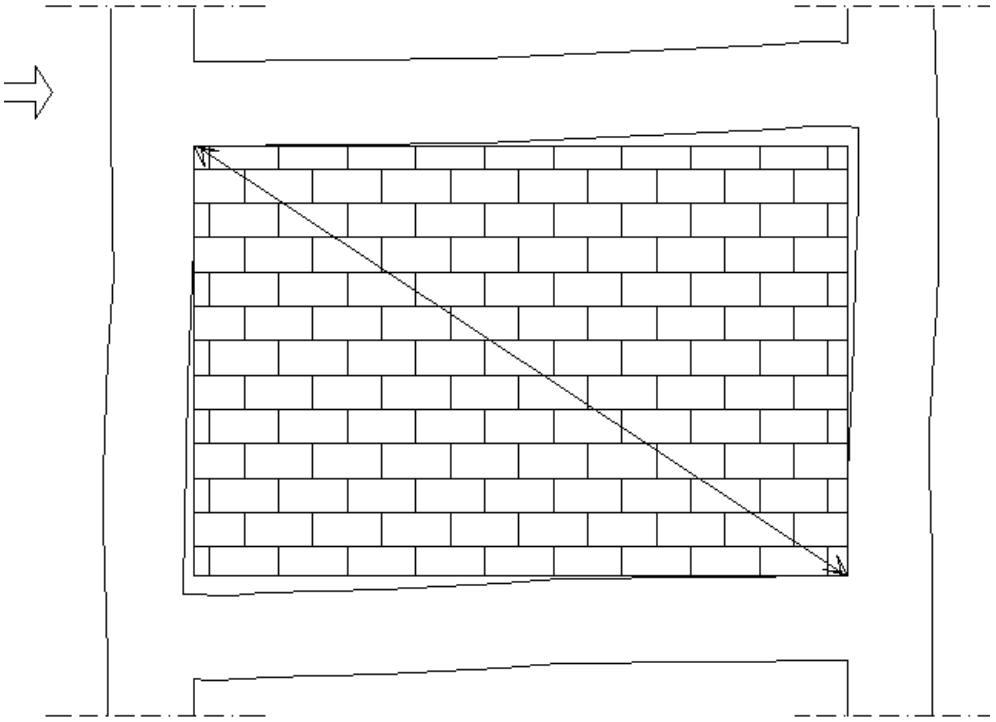

Figure 5.1. Pin jointed frame behavior

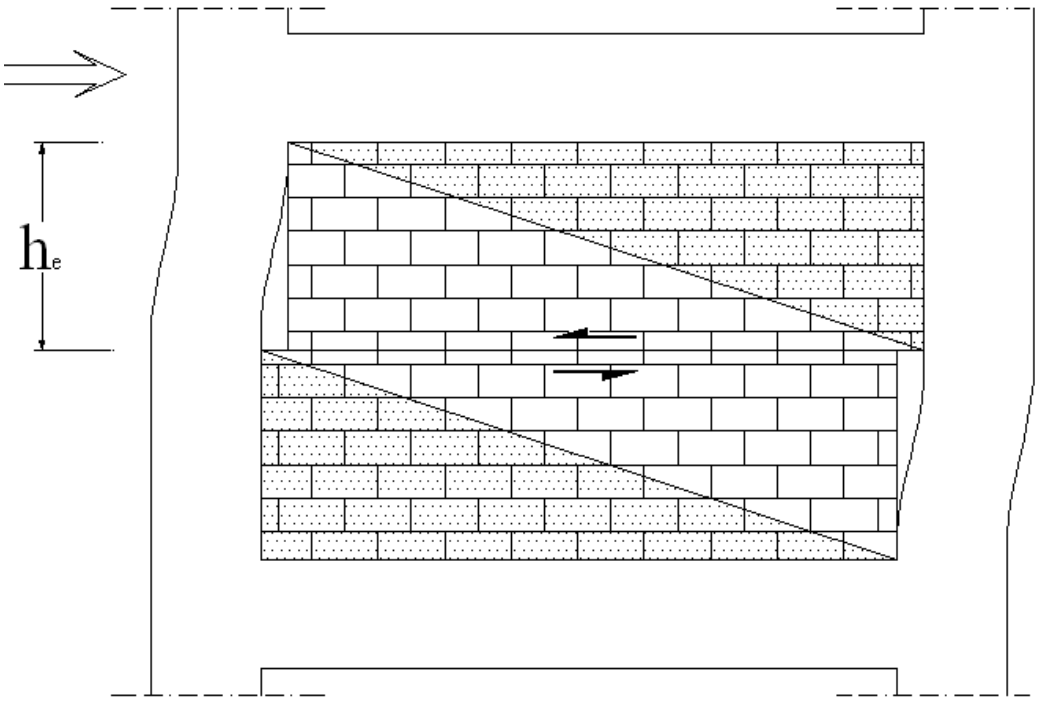

Figure 5.2. Knee braced frame behavior

5.3. Procedure for Capacity Predictions

In the light of the failure modes described above, a procedure is developed to predict the failure modes and capacities of the specimens tested. For the ease of defining the procedure, the specimens are grouped according to their CFRP configuration and discussed in the following sections.

5.3.1. Specimens: SA1.0, SA1.0-CV, SA1.0-C2V, SA2.3, SA2.3-CV, SA1.7-S

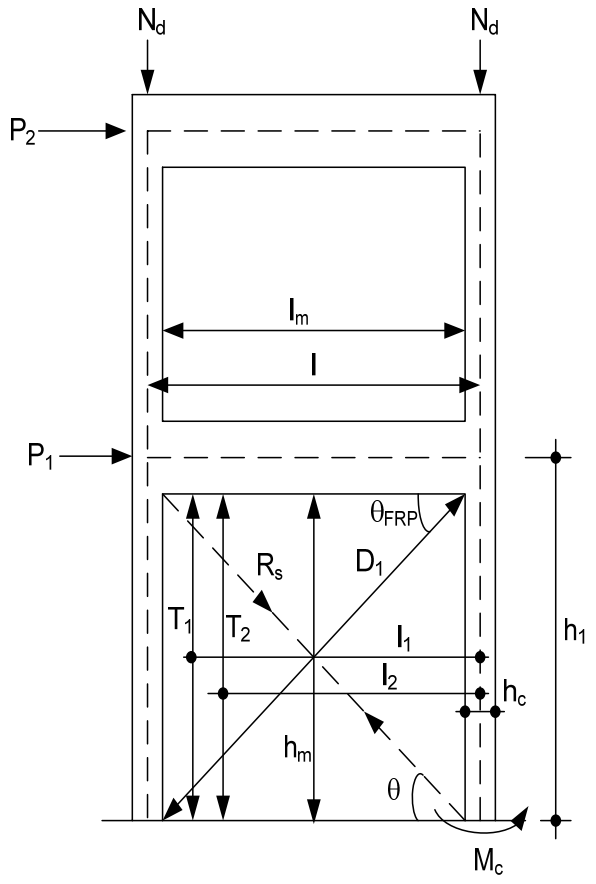

Figure 5.3. Forces and dimensions for the specimens with vertical and diagonal strips on the panel

Shear sliding mode of failure, as described above, is one of the three main failure modes. The following equations are used to predict the shear sliding capacity of the specimens and they are in SI units unless otherwise indicated. The modulus of elasticity of the masonry infill (E_{bm}), inclination of the diagonal strut (θ), the modulus of elasticity of

concrete in the frame (E_c), the maximum stress that can be developed in the rebars of the tension column (f_s) due to the insufficient lap splice length (l_b), and the characteristic tensile strength of concrete (f_{ctk}) are calculated according to Equations 5.1~5.7.

$$E_{bm} = 750 \times f_{bm} \le 20600 \qquad \text{(in accordance with UBC 1997 [93])} \tag{5.1}$$

$$E_p = 5500\sqrt{f_p} \tag{5.2}$$

$$E_{bmp} = E_{bm} \times \frac{t_{bm}}{t_{bm} + 2 \times t_p} + E_p \times \frac{2 \times t_p}{t_{bm} + 2 \times t_p} \tag{5.3}$$

$$\theta = \tan^{-1}\left(\frac{h_{bmp}}{l_{bmp}}\right) \quad (\ \theta \text{ is in radian}) \tag{5.4}$$

$$E_c = 3250\sqrt{f_{ck}} + 14000 \text{ (in accordance with TS500 [94])} \tag{5.5}$$

$$f_s = \frac{l_b}{l_{b0}} \times f_{yk} \qquad \text{where } l_{b0} = 0.67 \times 0.24 \times \phi \times \frac{f_{yk}}{f_{ctk}} \tag{5.6}$$

It should be noted that the constant 0.24 should be 0.12 in case of deformed reinforcing bars.

$$f_{ctk} = 0.35\sqrt{f_{ck}} \quad \text{(in accordance with TS500)} \tag{5.7}$$

The maximum shear force resisted by the panel (V_f) is calculated assuming that the vertical load on the infill panel is zero. The following formulations are used to calculate the V_f. At first, all of the shear is assumed to be taken by infill. The lateral load capacity of the columns, either flexure or shear, is developed at further drift levels.

$$\begin{aligned} V_f &= \tau_{bm} \times l_{bmp} \times t_{bm} + \tau_p \times l_{bmp} \times 2 \times t_p + \mu \times R_s \times \sin\theta \\ &+ 2 \times \mu \times t_{frp-cross} \times b_{frp-cross} \times \sigma_{frp-cross} \times \sin\theta_{FRP} \\ &+ 4 \times \mu \times t_{frp-vertical} \times b_{frp-vertical} \times \sigma_{frp-vertical} \end{aligned} \tag{5.8}$$

The diagonal compression strut force (R_s) shown in Figure 5.3 is a function of the shear friction stresses, inclination of the strut (θ) and the aspect ratio of the frame. The

summation of the horizontal component of R_s and the cross diagonal CFRP can also be assumed equal to the panel shear capacity as given in Equation 5.9.

$$V_f = R_s \times \cos\theta + 2 \times t_{frp-cross} \times b_{frp-cross} \times \sigma_{frp-cross} \times \cos\theta_{FRP} \tag{5.9}$$

By equating the Equations 5.8 and 5.9, R_s can be written as follows;

$$R_s = \frac{1}{\cos\theta - \mu \times \sin\theta} \begin{Bmatrix} \tau_{bm} \times l_{bmp} \times t_{bm} + \tau_p \times l_{bmp} \times 2 \times t_p \\ +2 \times \mu \times t_{frp-cross} \times b_{frp-cross} \times \sigma_{frp-cross} \times \sin\theta_{FRP} \\ +4 \times \mu \times t_{frp-vertical} \times b_{frp-vertical} \times \sigma_{frp-vertical} \\ -2 \times t_{frp-cross} \times b_{frp-cross} \times \sigma_{frp-cross} \times \cos\theta_{FRP} \end{Bmatrix} \tag{5.10}$$

The diagonal tension cracking capacity of concrete columns both in compression ($V_{cr\text{-}compression}$) and in tension ($V_{cr\text{-}tension}$) are given in Equations 5.11 and 5.12 respectively, while the contribution of transverse steel to the shear capacity is given in Equation 5.13.

$$V_{cr-compression} = 0.65 \times f_{ctk} \times b_{column} \times d_{column} \times \left[1 + 0.07 \times \frac{N_d}{b_{column} \times h_{column}} \right] \tag{5.11}$$

$$V_{cr-tension} = 0.65 \times f_{ctk} \times b_{column} \times d_{column} \times \left[1 - 0.3 \times \frac{N_d}{b_{column} \times h_{column}} \right] \tag{5.12}$$

$$V_w = A_{sw} \times f_{ywk} \times \frac{d_{column}}{s} \tag{5.13}$$

The shear capacity of the frame columns are calculated in accordance with Equation 5.14.

$$V_{column} = V_w + 0.8 \times V_{cr} \tag{5.14}$$

When a knee braced frame mechanism takes place imminent to the failure, hinges occur at approximately mid-height and top or bottom of the columns or column shear

failure takes place [2]. In this condition, moment induced shears are calculated as follows. These moment-induced shears included axial load effects due to gravity loads.

$$V_{up} = \frac{M_{p-upper} + M_{p-middle}}{h_{eff}} \quad \text{where } h_{eff} = \frac{h_m}{2} \tag{5.15}$$

$$V_{down} = \frac{M_{p-lower} + M_{p-middle}}{h_{eff}} \tag{5.16}$$

Total shear force carried by concrete columns, $V_{f\text{-column}}$, under the action of moment, shear and axial load can be calculated in accordance with Equation 5.17.

$$V_{f-column} = \min(V_{up},\ V_{colum-tension}) + \min(V_{down},\ V_{column-compression}) \tag{5.17}$$

The sliding shear failure capacity of the infilled frame strengthened with the CFRP overlays can be calculated by adding the shear forces carried by panel and the column as shown in Equation 5.18.

$$V_i = V_f + V_{f-column} \tag{5.18}$$

The second type of failure defined previously is the compression failure of the compression strut, where the compressive strength of the masonry constitutes a failure criterion. Diagonal compression failure force, R_c, is direcly proportional to the compressive strength of the strengthened masonry (f_{bmpF}) and contact length (z_{clm}) between panel and the column.

$$z_{clm} = \frac{\pi}{2}\left(\frac{4 \times E_c \times I_g \times h_{bmp}}{E_{bmp} \times t_{bmp} \times \sin 2\theta}\right)^{\frac{1}{4}} \tag{5.19}$$

$$R_c = \frac{2}{3} \times z_{clm} \times t_{bmp} \times f_{bmpF} \times \sec\theta \tag{5.20}$$

$$f_{bmpF} = \left[f_{bm} \times \frac{t_{bm}}{t_{bm} + 2 \times t_p} + f_p \times \frac{2 \times t_p}{t_{bm} + 2 \times t_p} \right] \times k \tag{5.21}$$

The overturning mode of failure capacity as the last mode of failure defined previously, is calculated in accordance with the Equation 5.22.

$$P = P_1 + P_2 = \frac{1}{\frac{h_1 + 2h_2}{3}} \begin{Bmatrix} N_d \times l + A_s \times f_s \times l + 2 \times b_{FRP-vertical} \times t_{FRP-vertical} \times \sigma_{FRP-vertical} \times l_1 \\ +2 \times b_{FRP-vertical} \times t_{FRP-vertical} \times \sigma_{FRP-vertical} \times l_2 \\ +2 \times b_{FRP-cross} \times t_{FRP-cross} \times \sigma_{FRP-cross} \times \cos\theta_{FRP} \times h_1 + M_c \end{Bmatrix} \tag{5.22}$$

In the above formulations masonry compressive strength was determined by linear regression using the formulation $f_{bm}=0.1063f_m+3.8875$ which was developed from laboratory tests specifically for the mortar and brick quality used. In order to determine the shear strength of the brick masonry, quadlet tests were performed and shear strength is determined by linear regression analysis. In the lights of these experiments shear stress values for mortar and brick were determined for each specimen using Formula 5.23 and 5.24.

$$\tau_{bm} = (0.0133 \times f_m + 1.3783) \times 0.3 \tag{5.23}$$

$$\tau_m = 0.15 \times (f_m \times 0.30) \tag{5.24}$$

$$\tau_p = 0.15 \times (f_p \times 0.30) \tag{5.25}$$

It is assumed that the mortar shear strength is 15% of the mortar compressive strength, and approximately 30% of the panel length is assumed in contact at mid-height when the crack which caused sliding or rocking appears at this level. The above assumptions were found quite prudent considering the test results. The cross diagonals and flags used on the corners of the masonry panels improved the compressive strength of the masonry panel and increased diagonal compression failure load. The following formulation (Equation 5.26) is used to modify the masonry compressive strength improved by FRP. (l/h) defined the aspect ratio and the constant 0.67 was found from the experiments.

$$k = \left[\frac{0.67}{(l/h)} \times \left(\frac{L_{flag} + L_{flag} + \sum W_{cross-diagonals}}{L_{diagonal}} \right) + 1 \right] \tag{5.26}$$

5.3.2. Specimen SA1.0-CVL

The difference between this specimen and the previous ones described above was that the existence of vertical strips on the panel were shifted to the vertical strips around the columns to improve the load transfer mechanism on the column. Thus the above formulations are valid for this specimen as well. The only difference was the calculation of the axial tension capacity increase of the columns due to vertical strips around the columns and exclusion of the effect of vertical strips on shear sliding and overturning mode of failures. This value is calculated by using Equation 5.27. The increased axial tension load capacity of the column directly affects the overturning capacity and influences the shear sliding capacity of the panel.

$$\Delta N_{increase} = L_{FRP-peripheral} \times t_{FRP} \times \varepsilon_{FRP-peripheral} \times E_{FRP} \tag{5.27}$$

5.3.3. Specimen SA2.3-CCM

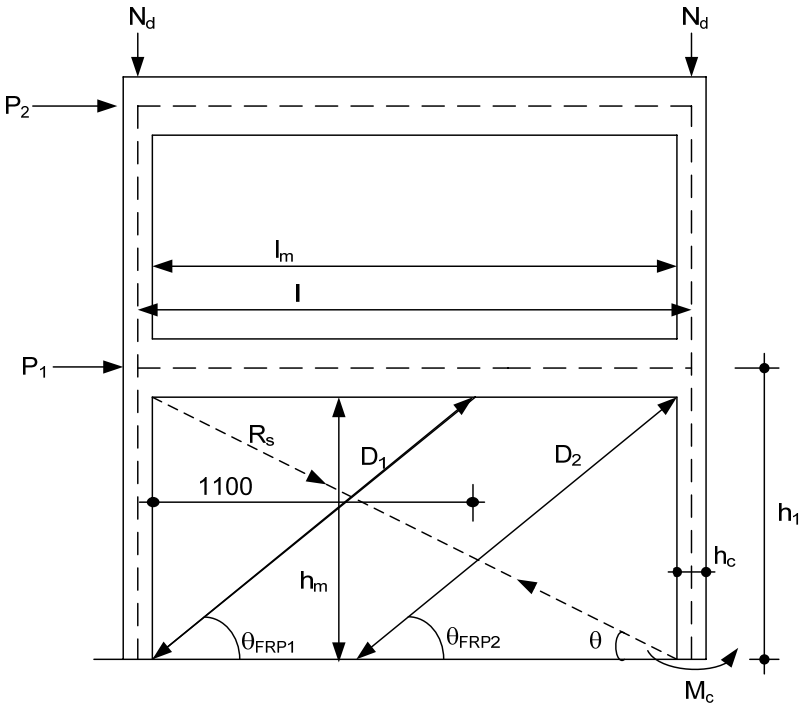

Figure 5.4. Forces and dimensions for the specimens SA2.3-CCM

Depending on the FRP scheme, free body diagram of the specimen changes (Figure 5.4). Thus, maximum shear force which is resisted by the panel and the diagonal compression force should be calculated accordingly. These values should be calculated in accordance with the following formulations.

$$V_f = \tau_{bm} \times l_{bmp} \times t_{bm} + \tau_p \times l_{bmp} \times 2 \times t_p + \mu \times R_s \times \sin\theta + \sum_{i=1}^{2} 2 \times \mu \times t_{frp-i} \times b_{frp-cross-i} \times \sigma_{frp-cross-i} \times \sin\theta_{FRP-i} \quad (5.28)$$

$$V_f = R_s \times \cos\theta + \sum_{i=1}^{2} 2 \times t_{frp-i} \times b_{frp-cross-i} \times \sigma_{frp-cross-i} \times \cos\theta_{FRP-i} \quad (5.29)$$

from Equations 5.28 and 5.29, R_s can be obtained as follows;

$$R_s = \frac{1}{\cos\theta - \mu \times \sin\theta} \left\{ \begin{array}{l} \tau_{bm} \times l_{bmp} \times t_{bm} + \tau_p \times l_{bmp} \times 2 \times t_p \\ + \sum_{i=1}^{2} 2 \times \mu \times t_{frp-i} \times b_{frp-cross-i} \times \sigma_{frp-cross-i} \times \sin\theta_{FRP-i} \\ - \sum_{i=1}^{2} 2 \times t_{frp-i} \times b_{frp-cross-i} \times \sigma_{frp-cross-i} \times \cos\theta_{FRP-i} \end{array} \right\} \quad (5.30)$$

Shear sliding force and diagonal compression force can be calculated using the previous formula. Overturning mode of failure is calculated as follows;

$$P = \frac{1}{\frac{h_1 + 2h_2}{3}} \left\{ \begin{array}{l} N_d \times l + A_s \times f_s \times l + 2 \times b_{FRP-1} \times t_{FRP-1} \times \sigma_{FRP-1} \times \cos\theta_{FRP-1} \times h_1 \\ + 2 \times b_{FRP-1} \times t_{FRP-1} \times \sigma_{FRP-1} \times \sin\theta_{FRP-1} \times (l - 1100 - \frac{h_c}{2} - 110) \\ + 2 \times b_{FRP-2} \times t_{FRP-2} \times \sigma_{FRP-2} \times \cos\theta_{FRP-2} \times h_1 + M_c \end{array} \right\} \quad (5.31)$$

5.3.4. Specimen SA2.3-CFM

Necessary dimensions and forces acting on specimen SA2.3-CFM is illustrated in Figure 5.5.

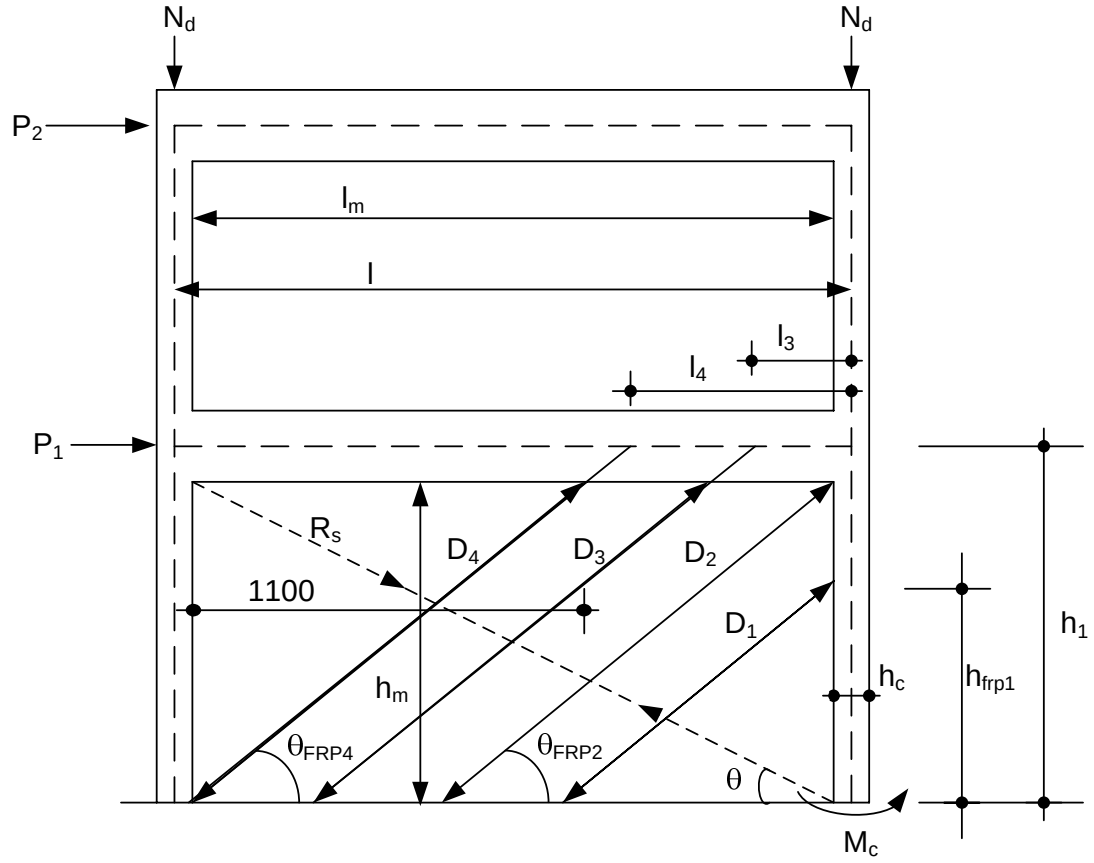

Figure 5.5. Forces and dimensions for the specimens SA2.3-CFM

$$V_f = \tau_{bm} \times l_{bmp} \times t_{bm} + \tau_p \times l_{bmp} \times 2 \times t_p + \mu \times R_s \times \sin\theta + \sum_{i=1}^{4} 2 \times \mu \times t_{frp-i} \times b_{frp-cross-i} \times \sigma_{frp-cross-i} \times \sin\theta_{FRP-i} \quad (5.32)$$

$$V_f = R_s \times \cos\theta + \sum_{i=1}^{4} 2 \times t_{frp-i} \times b_{frp-cross-i} \times \sigma_{frp-cross-i} \times \cos\theta_{FRP-i} \quad (5.33)$$

from Equations 5.32 and 5.33, R_s can be obtained as follows;

$$R_s = \frac{1}{\cos\theta - \mu \times \sin\theta} \left\{ \begin{array}{l} \tau_{bm} \times l_{bmp} \times t_{bm} + \tau_p \times l_{bmp} \times 2 \times t_p \\ + \sum_{i=1}^{4} 2 \times \mu \times t_{frp-i} \times b_{frp-i} \times \sigma_{frp-i} \times \sin\theta_{FRP-i} \\ - \sum_{i=1}^{4} 2 \times t_{frp-i} \times b_{frp-i} \times \sigma_{frp-i} \times \cos\theta_{FRP-i} \end{array} \right\} \quad (5.34)$$

Overturning mode of failure can be calculated by using the Equation 5.35. For the specimens having single bay like SA2.3-CFM, the increase in shear strength due to horizontal wrapping of columns horizontally can be found by using Equation 5.36.

$$P = \frac{1}{\frac{2h_2 + h_1}{3}} \left\{ \begin{array}{l} N_d \times l + A_s \times f_s \times l + M_c \\ +2 \times t_{FRP-1} \times b_{FRP-1} \times \sigma_{FRP-1} \times \cos\theta_{FRP-1} \times h_{FRP-1} \\ +2 \times t_{FRP-2} \times b_{FRP-2} \times \sigma_{FRP-2} \times \cos\theta_{FRP-2} \times h_1 \\ +2 \times t_{FRP-3} \times b_{FRP-3} \times \sigma_{FRP-3} \times (\cos\theta_{FRP-3} \times h_1 + \sin\theta_{FRP-3} \times l_3) \\ +2 \times t_{FRP-4} \times b_{FRP-4} \times \sigma_{FRP-4} \times (\cos\theta_{FRP-4} \times h_1 + \sin\theta_{FRP-4} \times l_4) \end{array} \right\} \quad (5.35)$$

$$V_{shear-wrap} = h_c \times 2 \times 2 \times t_{FRP-wrap} \times \varepsilon_{FRP-wrap} \times E_{FRP} \quad (5.36)$$

Implications of the above formulas for different FRP patterns were illustrated in Appendix B.

5.4. Predicted Capacities

The procedure defined in the previous pages is used to determine the lateral load capacity and the failure mode of the specimens. The results of the model predictions are given in Table 5.1. Predictions on specimens with small aspect ratio show good correlation with the experimental results on the basis of both failure loads and failure modes. On the other hand, failure mode predictions for SA2.3 series specimens scatter. No predictions were made for specimen SA1.7-D, since the anchorage failure was not defined in the proposed procedure. Experimental envelope curves, normalized by the calculated ultimate load values, are given in Figure 5.6, 5.7 and 5.8. As indicated in Figure 5.6, the ratios were very close to the ordinate of 1.0. This was the indicator of the success of the capacity

predictions. However, the same trend was not observed in the case of the aspect ratio of 2.3. The scatter in Figure 5.7 indicated that calculated and predicted values differed more than the specimens with an aspect ratio of 1.0. Since the specimens with an aspect ratio of 2.3 were not flexure dominant systems, the accuracy in the results were not as close as that of specimens with the aspect ratio of 1. Figure 5.8 included only specimen SA1.7-S because failure mode of specimen SA1.7-D was not calculated by using available formulations.

Table 5.1. Capacity results

	EXPERIMENTAL		ANALYTICAL				RATIO
Specimen	P_{max} (kN)	Failure Mode	$P_{overturning}$ (kN)	$P_{shear\ sliding}$ (kN)	R_c (kN)	$P_{diagonal\ compression}$ (R_c*cosθ) (kN)	$P_{exp.}/P_{an.}$
SA1.0	25.7	Rocking mechanism insufficient lap splices	25.3	64.0	169.5	118.2	1.02
SA1.0-CV	58	Tensile failure of columns and rupturing of vertical FRP	59.3	68.2	188.3	131.3	0.98
SA1.0-C2V	75.2	Shear sliding at mid-height	83.1	87.0	217.0	151.3	0.90
SA1.0-CVL	60.8	Shear sliding at mid-height	67.5	64.2	220.7	153.9	0.95
SA1.7-D	86.2	Insufficient CFRP anchorage lengths at the foundation level					
SA1.7-S	83.7	Lap splice failure of column longitudinal bars, rocking and sliding at the mid-height of the panel	83.5	88.5	136.8	118.5	1.00
SA2.3	51	Corner crushing and Excessive flexural cracks	64.3	96.6	113.5	104.8	0.79
SA2.3-CCM	142.3	Shear sliding at mid-height and gravity collapse of columns	145.5	115.2	154.6	142.7	1.24
SA2.3-CV	111.6	Capacity exceedance of columns and Rupturing of FRPs	118.0	108.5	130.2	120.2	1.03
SA2.3-CFM	136.8	Shear sliding (22 cm above the foundation)	132.6	142.4	133.7	123.5	1.11

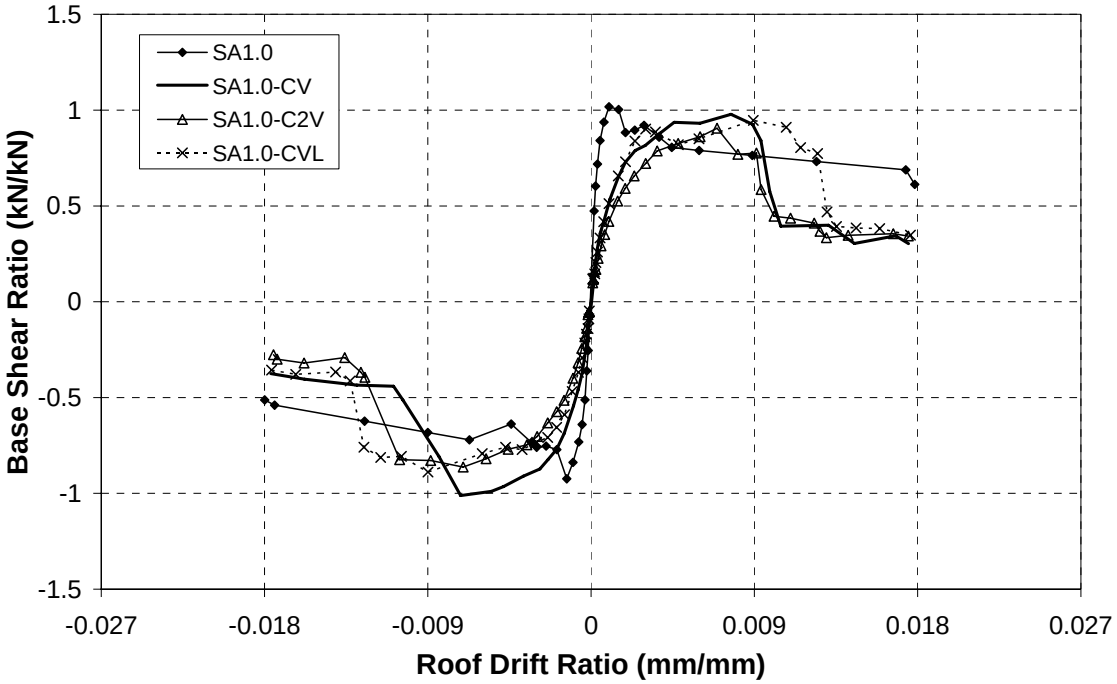

Figure 5.6. Normalized envelopes for specimens with an aspect ratio of 1.0

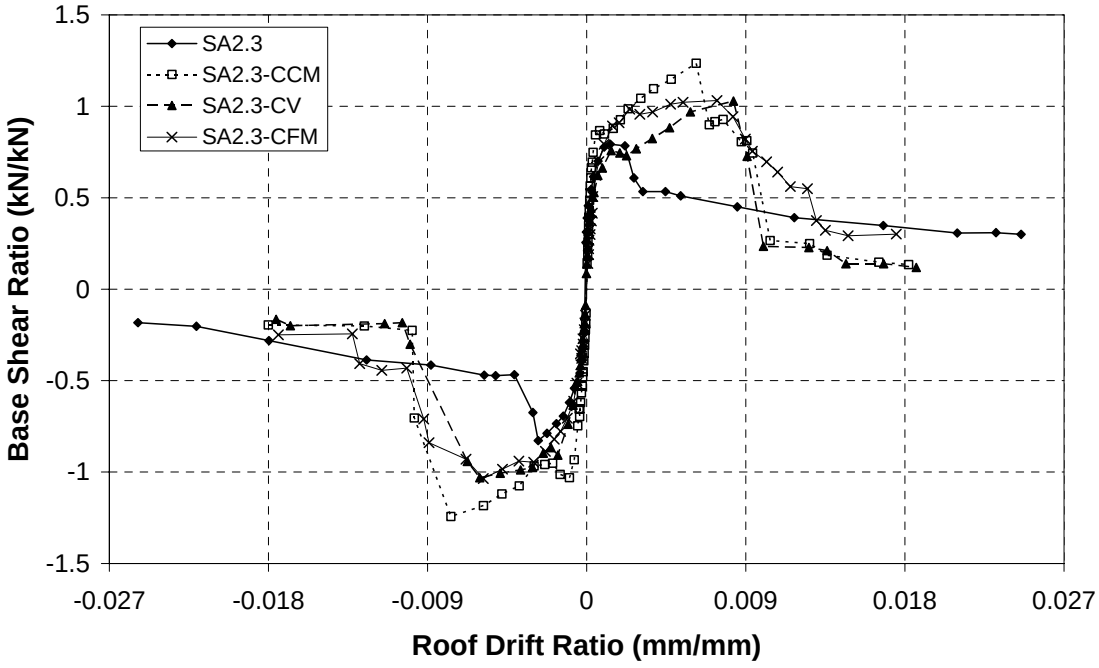

Figure 5.7. Normalized envelopes for specimens with an aspect ratio of 2.3

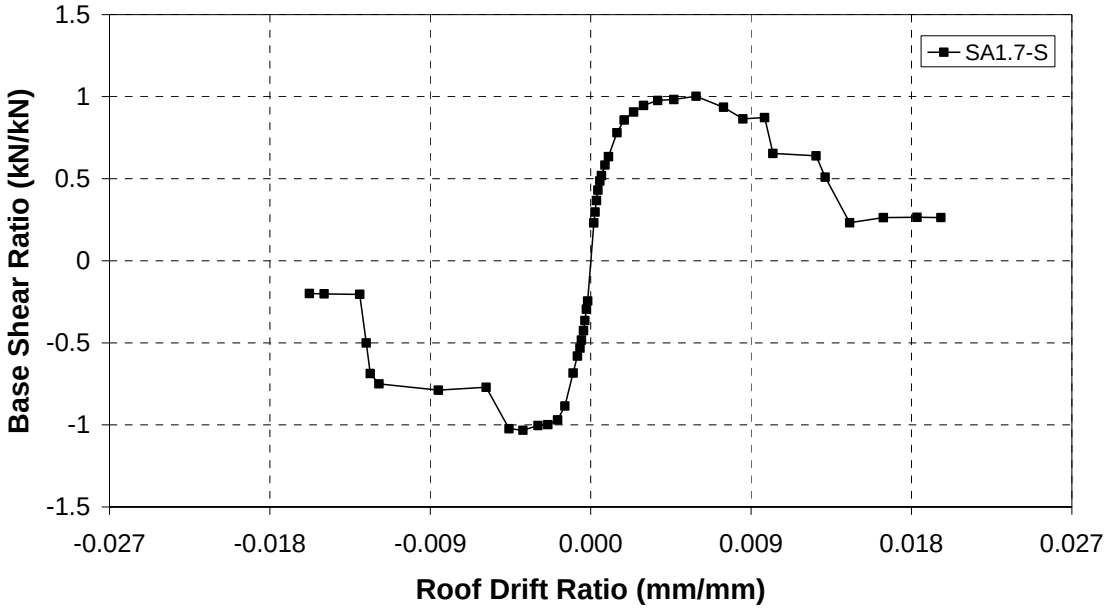

Figure 5.8. Normalized envelope for specimens SA1.7-S

5.5. Response Envelopes

Maximum load values and corresponding drifts for each successive drift levels were used to plot the response envelope curves. Moreover, some intermediate points between these two maximums on the hysteretic curve were also connected in order to better trace the response envelope. In the next pages, base shear versus roof drift ratio envelope curves are presented and cross comparisons are performed.

In Figure 5.9, envelope curves of specimens with aspect ratio of 1.0 are given. The FRP strengthening scheme affected the specimen behavior significantly and provided strength enhancement to the specimens as indicated in Figure 5.9. Doubling the vertical strips on the panel (specimen SA1.0-C2V) increased the ultimate load by approximately 30% with respect to specimen SA1.0-CV which has single vertical strip. However, a slight decrease in roof drift ratio and change in displacement ductility observed. Failure mode shifted from tensile failure of columns and mid-height rocking action (Specimen SA1.0-CV) to shear sliding for SA-C2V. Attracting high forces caused shear failure of the columns due to horizontal sliding of the panel for specimen SA1.0-C2V. Application of vertical strips around columns created partial fixity and improved lap splice deficiency in SA1.0-CVL. Shear sliding type of failure was also observed in specimen SA1.0-CVL.

Residual strengths of SA1.0-CV and SA1.0-CVL were almost the same whereas the residual strength of SA1.0-C2V was slightly higher than the former ones. The behavior of SA1.0-CVL among the FRP strengthened specimens having aspect ratio of 1.0 might be preferable for earthquake prone areas due to so-called ductility obtained. However, failure mode of this specimen was undesirable.

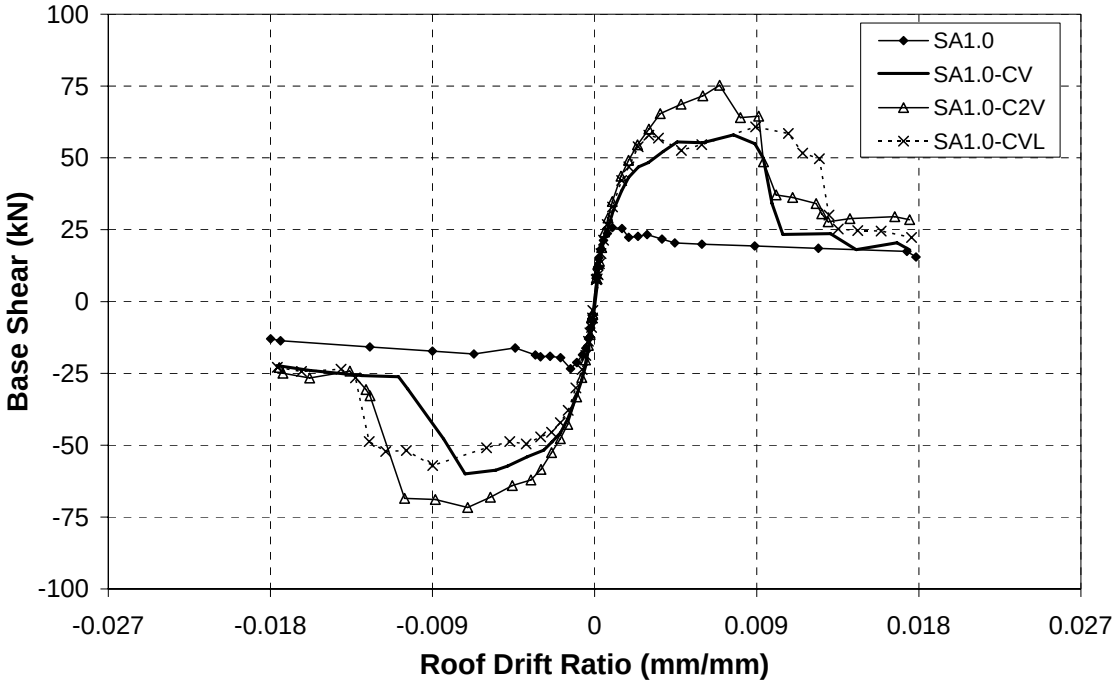

Figure 5.9. Response envelopes of the specimens having aspect ratio of 1.0

Load versus roof drift envelope curves of specimens having aspect ratio of 1.7 were plotted in Figure 5.10. The behavior of these specimens was similar until the 0.0025 roof drift ratio. After this point the specimen behavior started to deviate. Although the strengthening scheme and aspect ratios were the same, the ultimate loads were different due to different FRP material properties and anchorage details. The post peak behavior was significantly affected by the failure mode. Load decrease of SA1.7-S was more sudden due to rupturing of FRPs whereas it was smoother for SA1.7-D due to bond loss between the FRP anchors and foundation beam. Using this strengthening scheme for this aspect ratio, 41% strength enhancement was attained when specimen SA1.7-S and specimen U2 [71] of a previous study were compared.

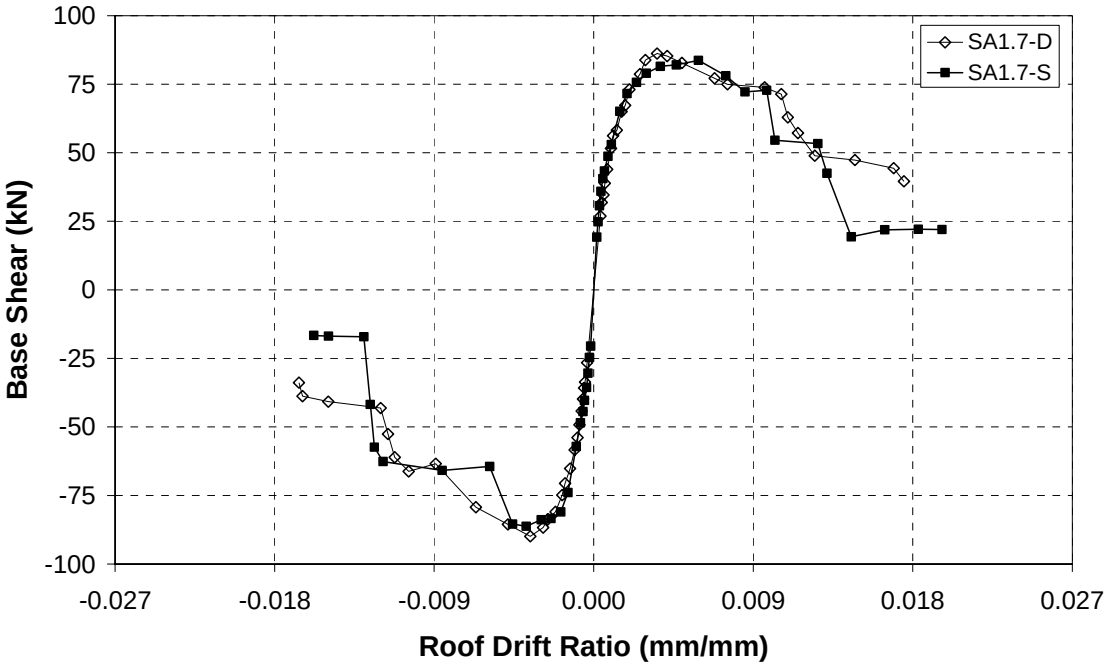

Figure 5.10. Response envelopes of the specimens having aspect ratio of 1.7

Base shear versus roof drift ratio envelope curves for specimens with aspect ratio of 2.3 are presented in Figure 5.11. It may be necessary to reiterate that SA2.3-CV had cross diagonals and vertical strips on the panel. The cross diagonals doubled, shortened, and vertical strips removed in case of SA2.3-CCM. Although the strengthening scheme was different for these specimens, we can visualize the effect of cross diagonals in Figure 5.11. Evaluation of SA2.3-CV revealed that the effect of vertical strips on the load carrying capacity for the aspect ratio of 2.3 was insignificant because specimen SA2.3-CV carried extra load after two vertical strips around right column failed. Doubling the cross diagonals increased its load bearing capacity about 27% and decreased ultimate roof drift ratio about 34% as compared to specimen SA2.3-CV. The behavior of SA2.3-CFM differed from the former ones. The post yield stiffness of the specimen SA2.3-CFM was smaller than the former strengthened specimens in this group. However, drift corresponding to peak load was smaller than that of SA2.3-CV and greater than that of SA2.3-CCM. The smoother behavior after yielding could be attributed to the presence of column confinement overlays and finely distributed FRP diagonals.

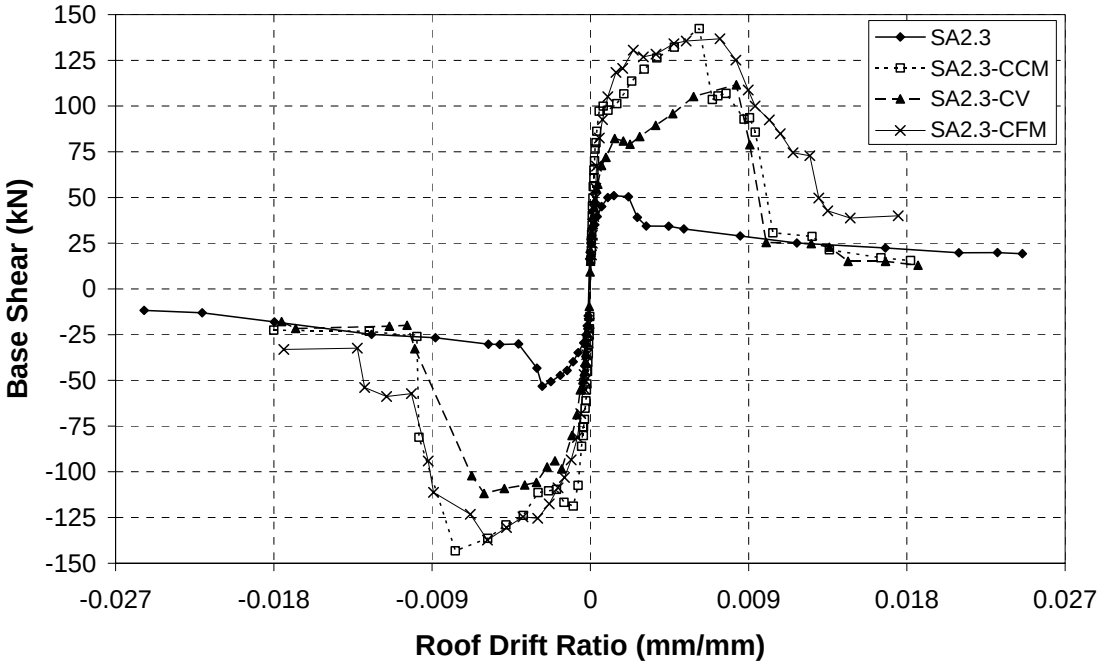

Figure 5.11. Response envelopes of the specimens having aspect ratio of 2.3

5.6. Different Envelope Curve Definitions

The procedure to trace the envelope curves used in this dissertation was previously described. However, FEMA 356 [95], pre-standard and commentary for the seismic rehabilitation of buildings, proposes an alternative way to determine the response envelope curves. According to FEMA 356, idealized load deformation curve should be presented in a single quadrant. It is proposed by FEMA 356 that the envelope curve should be obtained by combining the intersection points of the first cycle for the i^{th} deformation step and second cycle for the $(i-1)^{th}$ deformation step for all deformation levels. By using FEMA 356 procedure envelope curves of two strengthened specimens having different aspect ratios are plotted and compared to the ones used in this dissertation. As indicated in Figures 5.12, 5.13, 5.14 and 5.15, there are some differences between envelopes used in this dissertation and the ones proposed by FEMA. The envelope curves started to differ especially after yielding. For specimen SA1.0-CV, the envelope curve was unable to determine the maximum load and the corresponding displacement (Figure 5.12). In addition, after the maximum load the slope of the envelope curve was quite different than

the one experimentally obtained (Figure 5.14). Moreover, the FEMA procedure results in underestimations in the ultimate deformation capacity of the specimens.

Figures 5.13 and 5.15 illustrate the behavior of SA1.7-S. The envelope curves started to differ after the yielding like SA1.0-CV. Although the ultimate load was not estimated correctly, the displacement corresponding to this ultimate load was almost equal to the displacement value in the envelope used in this dissertation. After the peak load, the behavior was not traced appropriately due to mainly rupturing of FRPs.

The comparison of these envelope curves and hysteretic behavior showed that the approach proposed by FEMA 356 may not be appropriate to determine envelope curve for the FRP strengthened infilled frames due to brittle nature of strengthening material. The author believes that this approach should be checked and evaluated by using further test results.

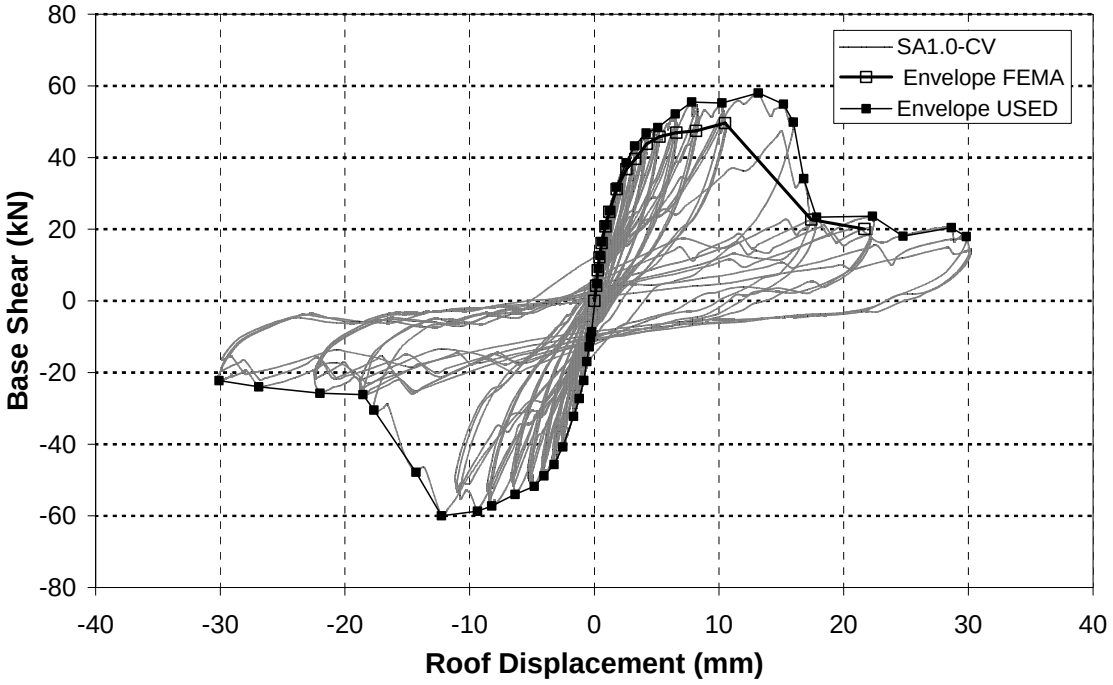

Figure 5.12. Comparison of the envelope and hysteretic loops for SA1.0-CV

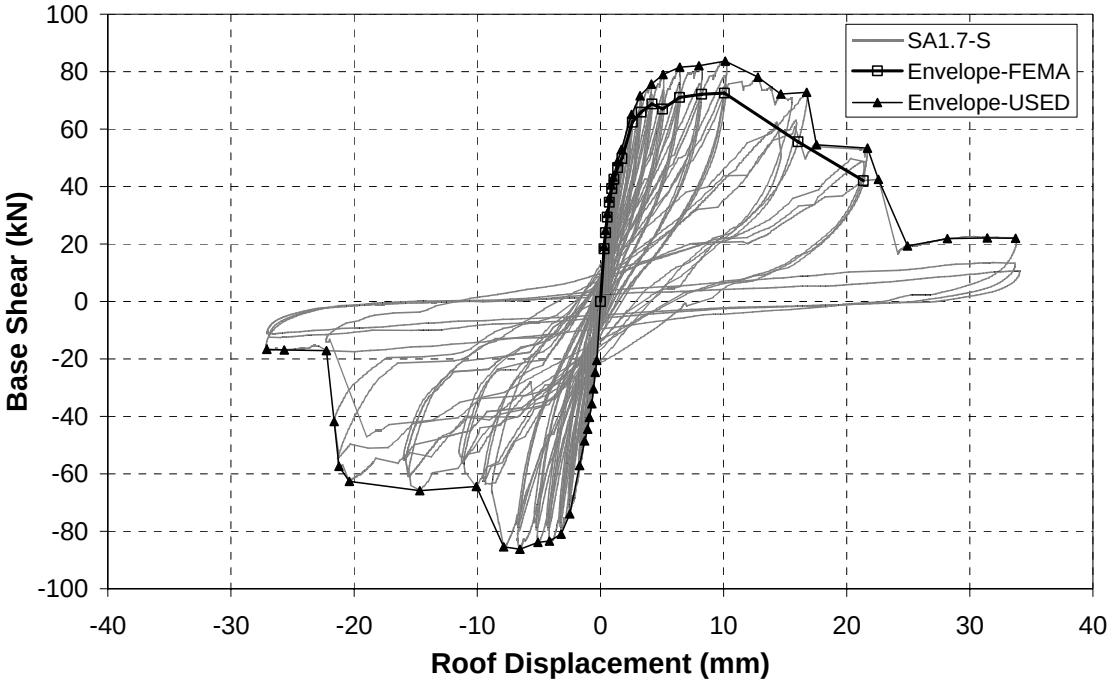

Figure 5.13. Comparison of the envelope and hysteretic loops for SA1.7-S

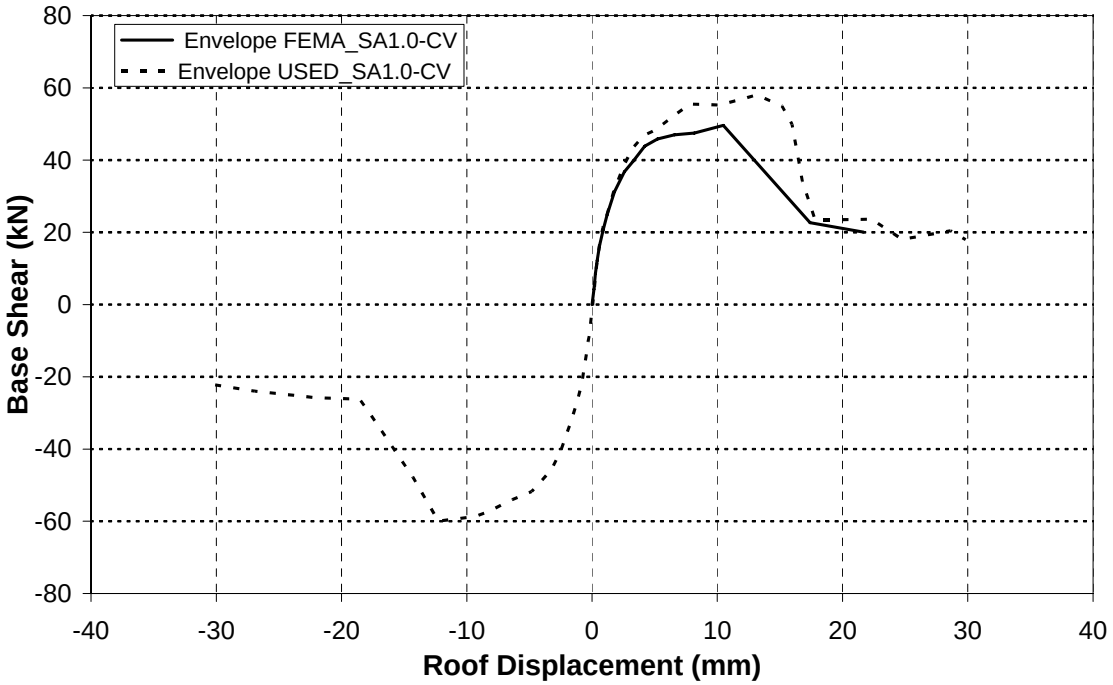

Figure 5.14. Envelope proposed by FEMA for SA1.0-CV

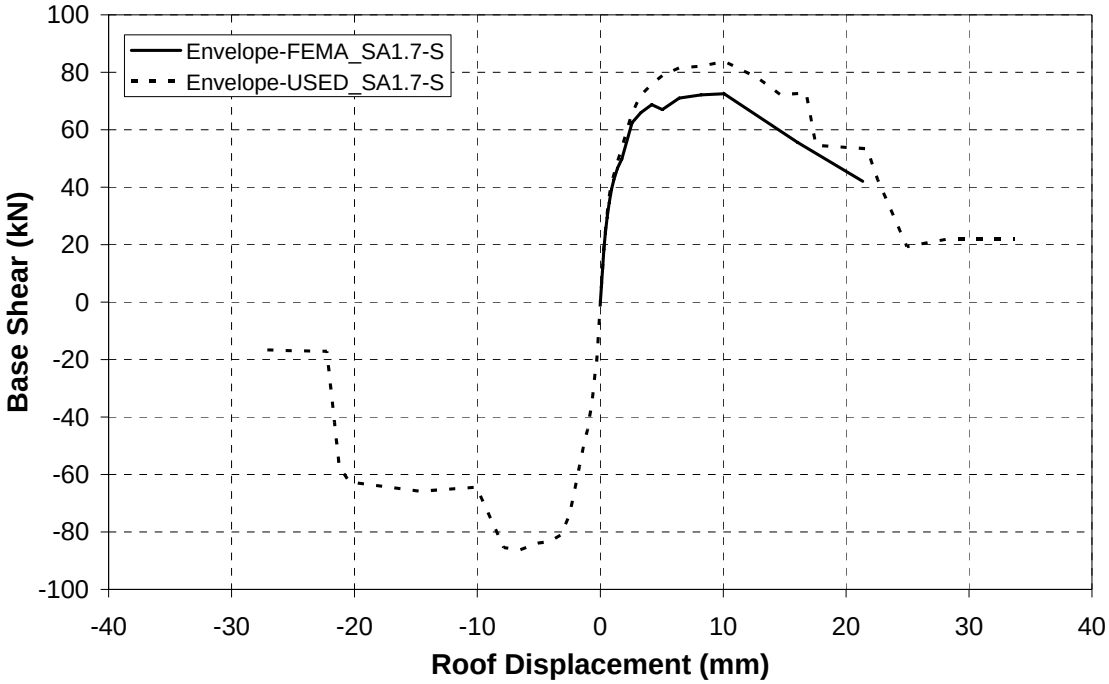

Figure 5.15. Envelope proposed by FEMA for SA1.7-S

5.7. Displacement Ductility

Detailing for ductility considerations is a very important phenomenon. Under severe earthquake conditions, detailing and ductility becomes extremely important. The tested specimens were inappropriately detailed to simulate the real inadequate structures. Ductility can be defined as capability to undergo large inelastic deformations without significant loss of strength. Ductility observed in infilled specimens was different than the one in reinforced concrete frames without infill. Therefore, the given ductility values will be mainly used to compare the effectiveness of the strengthening scheme and the aspect ratio effect on the specimen behavior. Moreover, displacement ductilities obtained in this section are more meaningful with the energy dissipation capacities in describing the behavior of the infilled and FRP strengthened frames.

Ductility depends on many factors such as number of longitudinal bars, diameter of bars for the same area of steel, detailing, confinement, material characteristics, and configuration of lateral reinforcement (tie and stirrups) [96]. There are various deformation ductility values such as displacement ductility, curvature ductility, strain and rotation

ductility [2]. These ductility values are related to each other but curvature ductility is greater than displacement ductility [97]. In other words, local ductility and overall ductility values differ greatly. Once the plastic hinge developed, demand at that section or region would be greater than that of the structure. That's why local and overall ductilities were different. Only if some of the constituent materials are ductile, can ductility be defined. Concrete, masonry infill, and FRP are brittle materials unlike reinforcing steel. The first two materials were generally used to carry compression stresses, and the latter ones were used to carry tensile stresses. In order to undergo large inelastic deformations induced by seismic forces and to dissipate energy, the above mentioned materials should be carefully used, detailed, and required ductility should be supplied.

Hakam [98] used two methods to determine displacement ductility of the specimens. The first one calculates ductility as the ratio between maximum displacement corresponding to 75% of the maximum load in the descending branch and displacement corresponding to 75% of the maximum load in the ascending branch. This method was suggested to be appropriate for the infilled frames whose load capacities were quite greater than the ones of bare frames and load deformation curves had obvious ascending and descending branches. The second method was described as modified method. It is stated that this method did not produce a truly-representative values. However, it was found useful to show the changes in initial stiffness and to evaluate the influence of the infill. These methods were used for the masonry infilled steel frames of the Hakam's study, but none of them were found appropriate for the specimens tested here. Moreover, it is believed that the maximum displacement value corresponding to 25% decrease in ultimate load was out of the failure range given in the literature [97], [99], [100].

The procedure used in this study is defined as follows. Presenting a bilinear relation makes the ductility calculations easier. However, there is not any strict method to define this bilinear relation. It is very important to find yield and ultimate deformations for the structures showing nonlinear load deformation behavior. As explained by Park [99] some load deformation diagrams did not have a well defined yield point depending on the materials used. Nonlinear behavior of the materials, and yielding in different parts starting at different levels were some of the reasons [99]. The accepted methods of finding maximum displacement are a 20% decrease ([99] and [100]) or a 15% decrease [97] or the

point corresponding to first fracture or buckling of an element [99]. The first linear line which passes through the origin should also pass from the first yield point or 60%-80% of the maximum load ([1] and [99]). Although the coefficient of 0.75 was used for concrete bridge columns [100] and the coefficient of 0.7 was proposed for the resistance of the masonry wall constructed in a construction system, 65% of the maximum load gave satisfactory results in this study. Also 15 % loss of strength was used to find the maximum displacement of the infilled frames. Moreover, the principal of the equality of the areas under the bilinear curve and response envelope was employed to find yield point. Ductility (μ) was calculated as the ratio of the ultimate deformation to the yield deformation described in Figure 5.16.

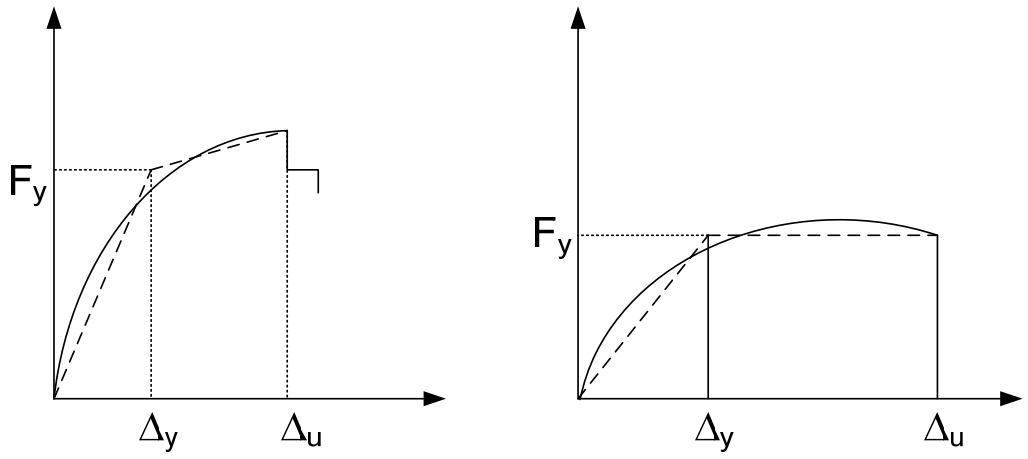

Figure 5.16. Ductility Description

Based on the above explanations the ductility values for the test specimens were calculated and listed in Table 5.2. As indicated, strengthening with CFRP overlays affected the ductility significantly depending on the aspect ratio. Displacement ductility of the FRP strengthened specimens with an aspect ratio of 2.3 was greater than that of the infilled specimen in the same group. However the same trend could not be observed among the specimens with an aspect ratio of 1.0. Among the strengthened specimens with an aspect ratio of 1.0, specimen SA1.0-CVL had the highest energy dissipation and the highest ductility when the bilinear ultimate displacement was attained. This meant that the strengthening scheme in this group would be more appropriate for earthquake prone areas for the frames having aspect ratio of 1.0. In other words, continuity in the vertical

reinforcement was better achieved and detailing deficiencies were better eliminated. Increasing of vertical FRP cross sectional area adversely affected ductility of the specimen SA1.0-C2V. However, SA1.0-C2V reached maximum load carrying capacity among the specimens having aspect ratio of 1.0. Energy dissipation capacity was less than SA1.0-CV and SA1.0-CVL when ultimate displacements of the bilinear curves were attained. Since it is known that the ductility is important to dissipate energy imposed by seismic forces, the specimen SA1.0-CVL may be more appropriate for the cases where the ductility and energy dissipation need to be utilized. In such cases, force reduction factors should be kept minimal.

Table 5.2. Displacement Ductility

Specimen	Yield Drift (Δ/h)	Ultimate Drift (Δ/h)	Displacement Ductility (μ)	Structural Behavior Factor (R)
SA1.0	0.000476	0.003704	7.8	3.8
SA1.0-CV	0.001877	0.007683	4.1	2.7
SA1.0-C2V	0.002475	0.006981	2.8	2.2
SA1.0-CVL	0.001960	0.010802	5.5	3.2
SA1.7-D	0.001359	0.003572	2.6	2.1
SA1.7-S	0.001491	0.005901	4.0	2.6
SA2.3	0.000416	0.002566	6.2	3.4
SA2.3-CCM	0.000483	0.006198	12.8	5.0
SA2.3-CV	0.001100	0.008340	7.6	3.8
SA2.3-CFM	0.000864	0.007371	8.5	4.0

Premature failure of the specimen SA1.7-D affected its displacement ductility as well as energy dissipation characteristics when ultimate displacement of the bilinear curve was attained. Although the strengthening schemes of SA1.7-D and SA1.7-S were the same, the obtained displacement ductility differed greatly. One reason was the FRP used for these specimens obtained from different sources. As a result their thickness values were different. Another reason was that the premature failure of SA1.7-D due to inadequate FRP anchor depth prevented development of displacement ductility.

Interesting results were obtained when displacement ductilities of the specimens with an aspect ratio of 2.3 were compared. The first one was that displacement ductility of all the strengthened specimens in this group was greater than the infilled specimen SA2.3. Another interesting result was that the highest ductility was obtained from the specimen SA2.3-CCM. This may be due to the difference in initial stiffness, and the cross sectional area of effectively used FRP on the wall (linked panel to the foundation). This result might cause misleading results if evaluated alone. When the response envelopes and bilinear curves were evaluated, the difference in yield loads appeared clearly. Specimen SA2.3-CFM had a higher yield load and smoother behavior at the post yield region. Moreover, load drop of specimen SA2.3-CFM was more gradual as compared to specimen SA2.3-CCM. Cumulative dissipated energy of specimen SA2.3-CFM was almost 25% higher than that of SA2.3-CCM when the ultimate displacements of the bilinear curves were attained. It could be attributed to the confinement effect of FRP on the columns. It may be necessary to reiterate that evaluation of displacement ductility alone was not enough. Energy dissipation should also be taken into account during the evaluation as well as stiffness consideration. Moreover, aspect ratio was very important parameter to be taken into account prior to any evaluation or application.

The comparison of the specimens having the same strengthening scheme yielded interesting results. SA1.0-CV, SA1.7-S, and SA2.3-CV possessed the same strengthening scheme with different aspect ratios. As the ductilities of the first two specimens were almost the same, ductility of SA2.3-CV was almost two times greater than the previous ones. Energy dissipation capacities of these specimens increased as the aspect ratio increased. Hence aspect ratio affected displacement ductility, and energy dissipation capacity significantly; especially for the extreme cases (SA1.0-CV and SA2.3-CV).

Structural behavior factor, R, can be defined considering natural period of the structure under consideration. If the natural period of the structure was greater than that corresponding to peak elastic spectral response, T_m, maximum displacements of elastic and inelastic systems would be similar and equal displacement principle would be valid for such system as illustrated in Figure 5.17. If the natural period of the structure was equal to or smaller than the peak elastic spectral response period, the maximum displacement could not be equal. However the areas under elastic and inelastic systems could be equated for

many structures; this is also called the equal-energy principle (Figure 5.17). The status of these two principles was unwarranted. If period of the structure was close to zero, or in the limit case zero, force reduction factors could not be used and the structure must resist the peak ground acceleration. This behavior was called equal-acceleration principle and was theoretically warranted [2]. The formulations for the long period structures (the equal displacement principle), and short period structures (the equal energy principle) can be derived by using the Figure 5.17. Structural behavior factor must be 1 for zero period structures (the equal acceleration structures). Newmark and Hall [101] defined natural period ranges for long period structures, short period structures and zero period structures as given in Equations 5.37, 5.38, and 5.39 respectively.

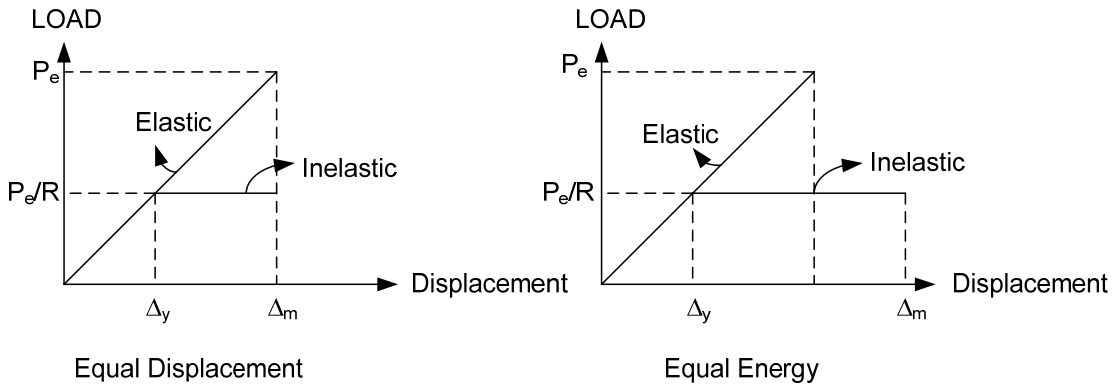

Figure 5.17. Structural Behavior Factor

$$R = \mu \qquad \text{if } T \geq 0.5 \text{ sec} \tag{5.37}$$

$$R = \sqrt{(2 \times \mu - 1)} \qquad \text{if } 0.1 < T < 0.5 \text{ sec} \tag{5.38}$$

$$R = 1 \qquad \text{if } T < 0.03 \text{ sec} \tag{5.39}$$

Displacement ductility values were found in accordance with equal energy principle illustrated in Figure 5.17. Inelastic structure was idealized by using bilinear curve having the same initial elastic stiffness of the elastic system. By using the formulation proposed for short period structures (Equation 5.38), structural behavior factors for each specimen were calculated and illustrated in Table 5.2. According to this Table, structural behavior factor decreased for the strengthened specimens having aspect ratio of 1.0 with respect to

the unstrengthened specimen SA1.0. On the other hand, specimens with aspect ratio of 2.3 yielded increasing ductilities when strengthened with respect to the unstrengthened specimen SA2.3. In other words, strengthening of specimens having aspect ratio of 1.0 increased the strength supply and decreased ductility supply of the system. However, strength and ductility supply of the specimens with an aspect ratio of 2.3 increased with FRP strengthening. This observations and findings about ductility must be investigated further. However, a structural behavior factor for SA1.0 series strengthened specimens may be taken as 2.0; while 3.0 will be more appropriate for SA2.3 series strengthened specimens regardless of the strengthening scheme.

5.8. Stiffness

Different stiffness descriptions, such as secant stiffness, effective stiffness, and peak to peak stiffness, exist in defining the lateral load response of members and systems. Secant stiffness among these can be defined as the ratio of the load to the corresponding displacement at a given drift level [102], while the stiffness at cracking can be defined as the effective stiffness [102]. In this study, the peak to peak stiffness is used. The peak to peak stiffness can be defined as the slope of the line which connects the two peak displacements in one load cycle as given in Equation 5.40.

$$K_{peaktopeak} = \frac{\left|P@\Delta^{+}_{\max}\right| + \left|P@\Delta^{-}_{\min}\right|}{\left|\Delta^{+}_{\max}\right| + \left|\Delta^{-}_{\min}\right|} \tag{5.40}$$

As the terms in the numerator are the loads corresponding to maximum and minimum deformations, the terms in the denominator are maximum and minimum displacement at that specified load cycle. Stiffness calculations were done at each consecutive cycle using the experimental load displacement loops. Peak to peak stiffness values were normalized against that stiffness value at 0.02% drift ratio. At the initial stages of the loading stiffness values were considerably high due to the composite action of the frame, wall, and FRP. At higher displacement amplitudes stiffness degradation took place due to several reasons such as nonlinear deformations, formation of cracks (flexural and shear), slip of the reinforcement, debonding of FRP from the plaster or brick shell, and re-bar bond deterioration.

The following figures illustrate the change in peak to peak stiffness with respect to the roof drift ratio and the cumulative drift ratio. Cumulative drift was calculated by adding the forward cycle drift ratios obtained at each consecutive cycle. In other words, cumulative drift ratio at the n^{th} cycle is the summation of n forward cycle drift ratios. Stiffness values were normalized against the stiffness at 0.02% roof drift ratio. The specimens underwent 3 cycles at each drift level. The stiffness values presented herein corresponds to the third cycle's peak to peak stiffness. The diagrams are presented for the three aspect ratios.

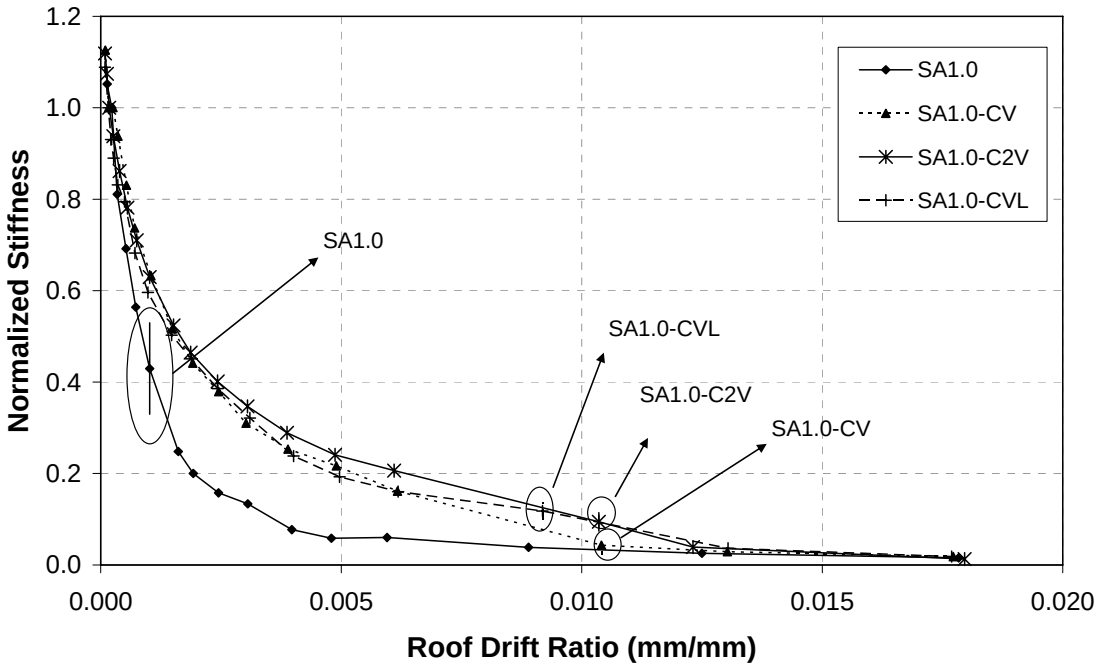

Figure 5.18. Normalized stiffness-roof drift ratio for specimens with an aspect ratio (A.R.) of 1

As indicated in Figure 5.18, the infilled specimen SA1.0 established the lower bound for the stiffness degradation diagram. Encircled points represented the third cycle stiffness values at which the maximum load was attained in the first cycle of that drift level. All the strengthened specimens faced serious stiffness degradation when peak load was reached except specimen SA1.0. Figure 5.19 and Figure 5.20 were drawn for the specimens with an aspect ratio of 1.7 and 2.3 respectively. When peak load was attained, normalized stiffness was approximately 0.32 for the specimen SA1.7-D. This is a high value for a strengthened specimen. The reason for this was probably due to the failure mode of this specimen. The

failure was due to FRP anchorage separation at the foundation level. Early failure of this specimen was seen in Figure 5.19 clearly.

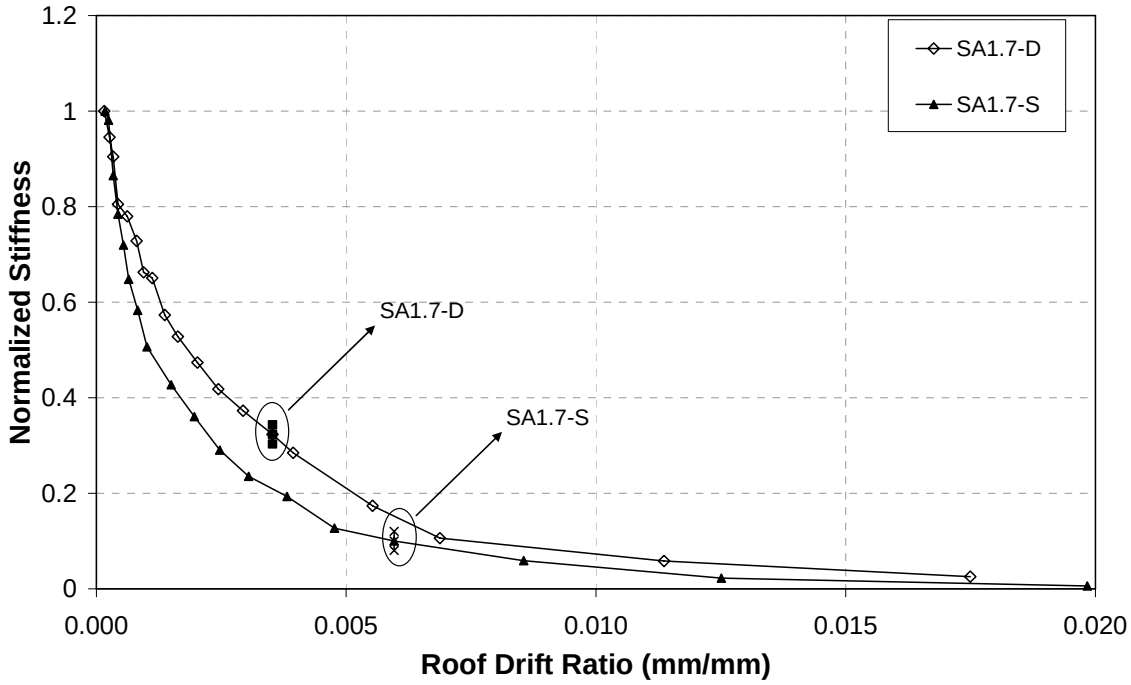

Figure 5.19. Normalized stiffness-roof drift ratio for specimens with an aspect ratio of 1.7

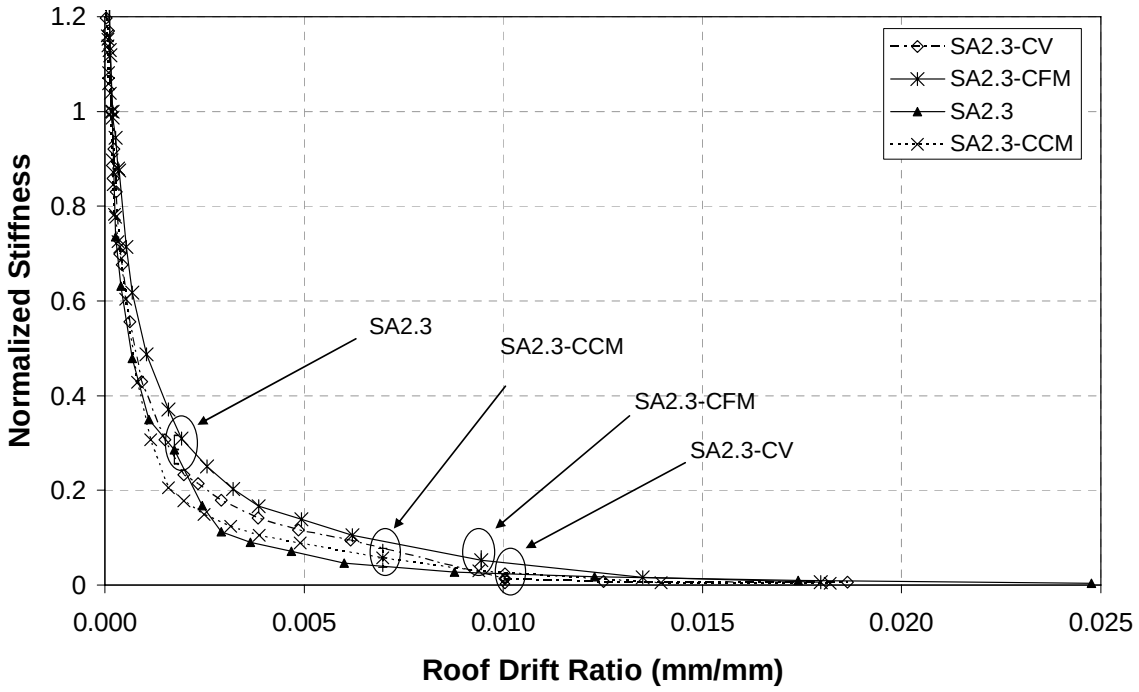

Figure 5.20. Normalized stiffness-roof drift ratio for specimens with an aspect ratio of 2.3

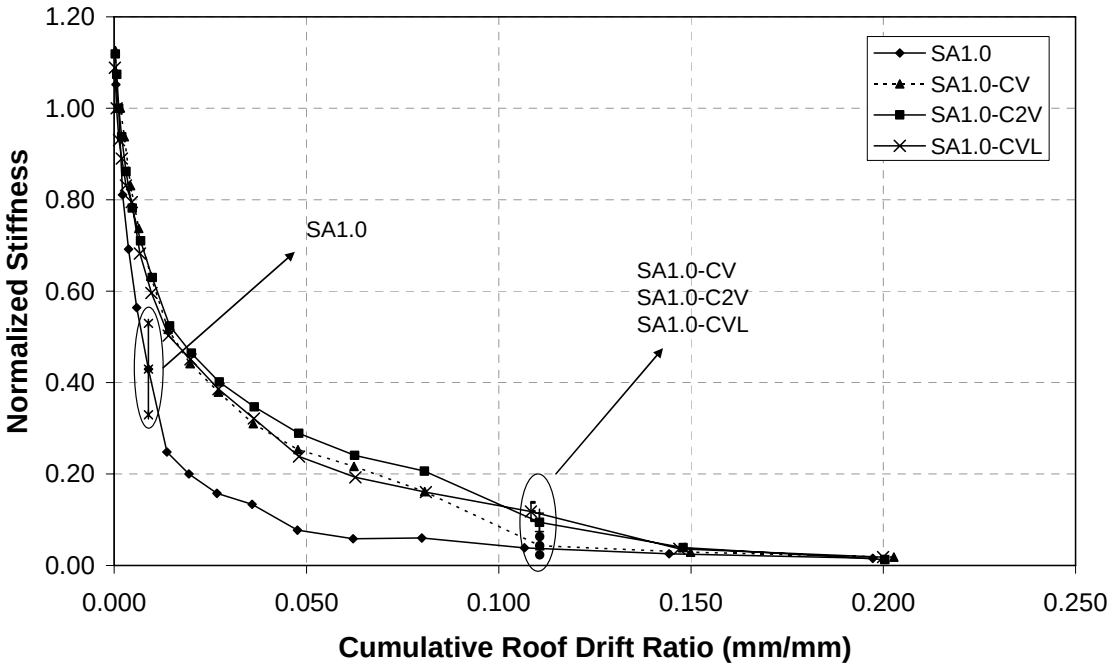

Figure 5.21. Normalized stiffness-cumulative drift ratio for specimens with an A.R. of 1.0

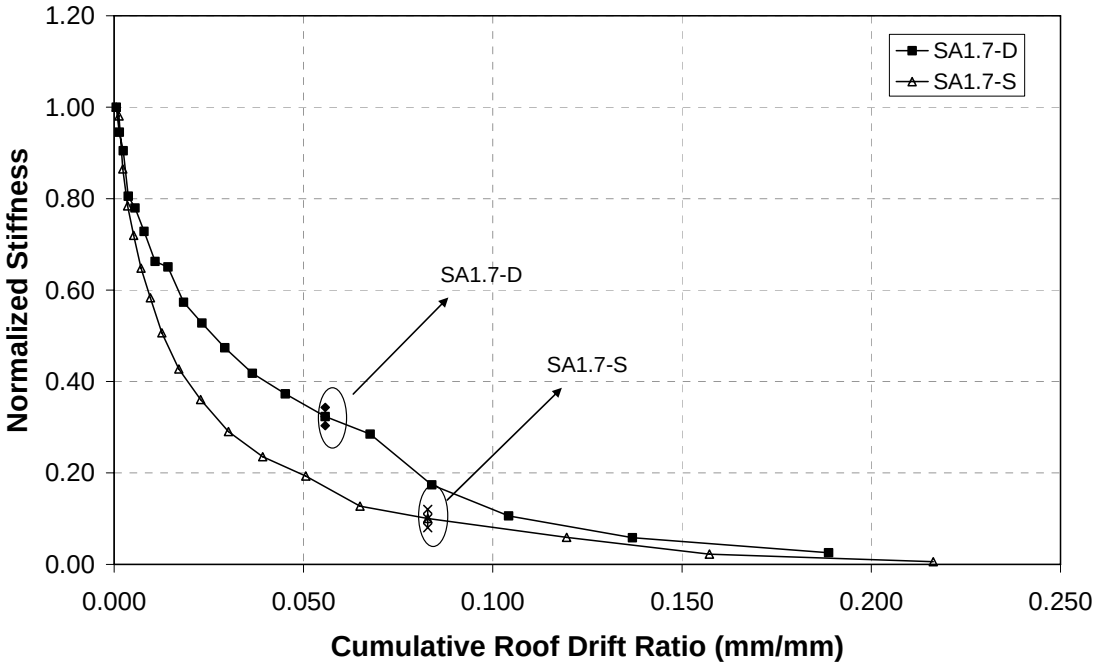

Figure 5.22. Normalized stiffness-cumulative drift ratio for specimens with an A.R. of 1.7

Although specimen SA2.3-CFM established the upper bound for the stiffness degradation for specimens having an aspect ratio of 2.3, the stiffness degradation for specimens with an aspect ratio of 2.3 was similar. Normalized stiffness values for the strengthened specimens with aspect ratio of 1.0 and 2.3 at a drift ratio of 0.005 are respectively 0.20 and 0.10 as indicated in Figures 5.18 and 5.20. This shows that the bigger the aspect ratio was the faster the stiffness degradation takes place. Moreover, normalized stiffness-cumulative drift ratio graphs (Figures 5.21, 5.22 and 5.23) revealed that the cumulative drift ratios when maximum load was attained were almost the same for the specimens with an aspect ratio (A.R.) of 1.0. This cumulative drift ratio was about 0.11 for the strengthened specimens having aspect ratio of 1.0. The same trend was not observed for the other aspect ratio groups. In other words, cumulative roof drift ratio values scattered around the value of 0.10.

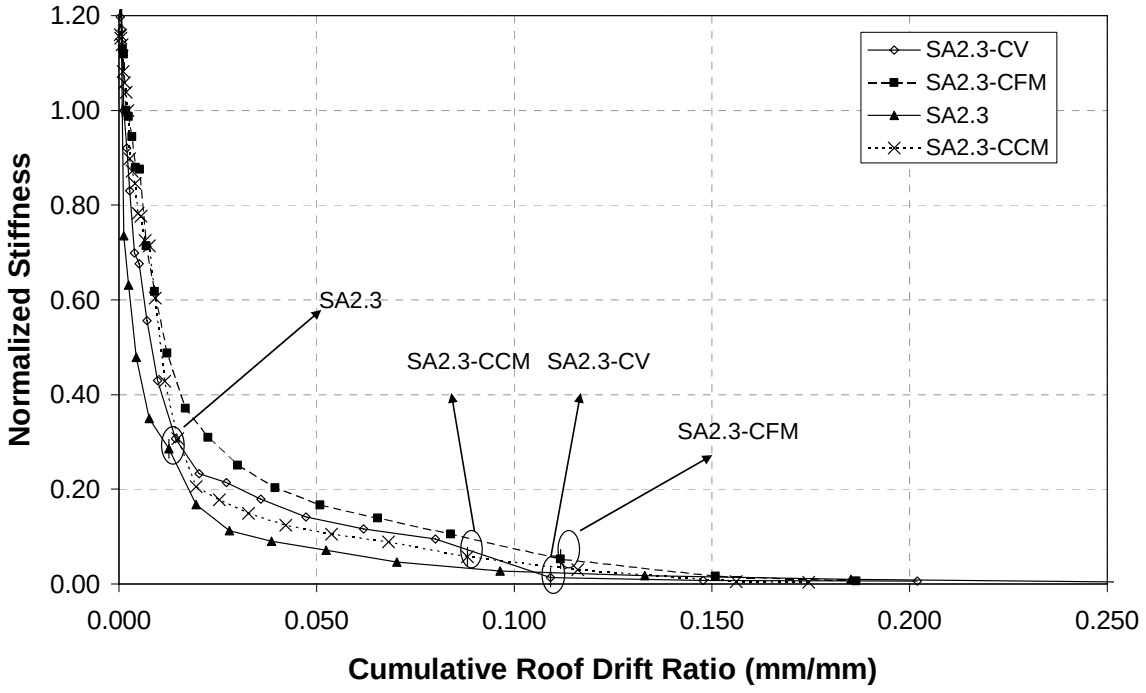

Figure 5.23. Normalized stiffness-cumulative drift ratio for specimens with an A.R. of 2.3

Initial stiffness, stiffness at peak load, first cracking load and drifts were summarized in Table 5.3. As indicated in Table 5.3, 40% of the initial stiffness of specimen SA1.0 left when the maximum load was attained. However, it was 10% for the specimen SA2.3. This comparison in Table 5.3 took place considering maximum stiffness at the first cycle

whereas the Figures 5.18~5.23 were drawn considering the third cycle of each displacement amplitude.

5.9. Energy Dissipation

Loading history strongly affects the energy dissipation characteristics, especially in the nonlinear range [50, 43, 70, and 103]. However it was not possible to use the same loading protocol for all the specimens. Depending on the aspect ratio of the specimens, their behavior shifted from flexural dominant behavior to a shear dominant one as specimens from SA1.0 to SA2.3. This was the reason to compare the energy dissipation characteristics in 3 different groups, considering the aspect ratios. Cumulative energy and cumulative drift ratios were used for the cross comparison of the three aspect ratios. Energy dissipation was investigated in terms of cumulative values and dissipated energy at each successive story drift ratio.

Dissipated energy is defined as the area enclosed within the load-deformation loops. Input energy was defined as the work of the actuator to deform the specimen up to the predefined displacement amplitude [102]. The work done by axial loads and friction forces were ignored to calculate the input energy. The definitions given for the input and dissipated energy is described in Figure 5.24.

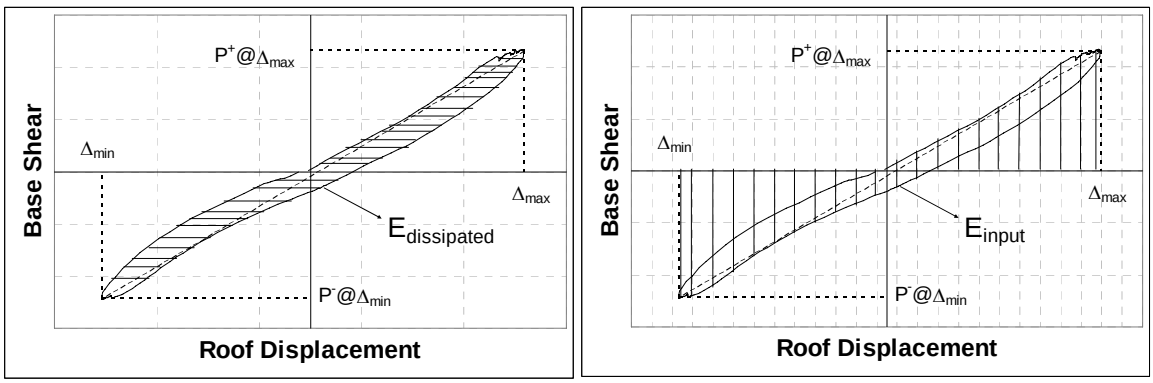

Figure 5.24. Dissipated Energy and Input Energy in One Loading Cycle

Table 5.3. Summary of stiffness values

Specimen	First Cracking Load (kN)	Maximum drift at the cycle in which the first crack was observed		$K_{initial}$	$K_{initial}$ @3rd cycle	K@0.02%	Kinitial /K@0.02%	K@ peak load cycle		K@peak load/$K_{initial}$	K@peak load/$K_{initial}$	K@peak load /K@0.02%
	Observed	Forward Half Cycle (mm/mm)	Backward Half Cycle (mm/mm)	(kN/mm)	(kN/mm)	(kN/mm)		After peak load	At peak load	After peak load	At peak load	At peak load
SA1.0	25.7	0.00100	-0.00100	34.20	29.93	28.45	1.20	13.42	13.77	0.39	0.40	0.48
SA1.0-CV	21.2	0.00052	-0.00050	31.64	31.64	28.10	1.13	2.39	4.64	0.08	0.15	0.17
SA1.0-C2V	34.8	0.00100	-0.00100	35.63	34.22	30.58	1.16	3.67	6.13	0.10	0.17	0.20
SA-CVL	26.8	0.00071	-0.00070	31.25	31.25	28.71	1.09	3.65	3.83	0.12	0.12	0.13
SA1.7-D	31.9	0.00028	-0.00067	41.48	41.48	41.48	1.00	14.61	15.69	0.35	0.38	0.38
SA1.7-S	36	0.00043	-0.00042	64.79	58.60	58.60	1.11	6.48	7.33	0.10	0.11	0.13
SA2.3	25	0.00004	-0.00026	165.05	165.05	45.29	3.64	13.79	16.48	0.08	0.10	0.36
SA2.3-CCM	49.7	0.00015	-0.00019	203.98	203.98	166.22	1.23	12.43	13.44	0.06	0.07	0.08
SA2.3-CV	48.1	0.00027	-0.00043	171.14	167.75	92.87	1.84	3.38	8.21	0.02	0.05	0.09
SA2.3-CFM	105.1	0.00101	-0.00109	136.01	136.01	104.97	1.30	6.64	10.68	0.05	0.08	0.10

Energy dissipation takes place in several ways. Yielding of reinforcement, cracking of concrete and masonry, crushing of concrete and masonry corners, sliding, and bond failure may be listed as the piers of the energy dissipation. Although FRP influenced the energy dissipation characteristics, it did not have any contribution by itself. During the beam tests on the FRP-strengthened beams done previously, the same effect was also observed [104].

Cumulative dissipated energy and cumulative roof drift ratio graphs are given in Figure 5.25~5.27 for three different aspect ratios. As indicated in Figure 5.25, cumulative dissipated energy values of the specimens having A.R. of 1.0 were almost the same until the cumulative drift ratio of 0.027. The same trend is valid for the specimens with an aspect ratio of 2.3 at the same cumulative drift ratio as shown in Figure 5.27. Even though there was a slight difference in the cumulative dissipated energy values of the specimens with aspect ratio of 1.7 (Figure 5.26), the same trend took place and it can be calculated that cumulative dissipated energy values, if compared for each aspect ratio distinctly, were almost the same until the cumulative drift level of 0.027. After the cumulative drift level of 0.027 was attained, the dissipated energy started to deviate for the strengthened and non strengthened infilled frames. At the cumulative drift level of 0.1, strengthened specimens with A.R. of 1.0 dissipated almost as much as 2 times energy as infilled specimen SA1.0. Strengthened specimens having A.R. of 2.3 dissipated less than 2 times energy that the companion unstrengthened specimen dissipated in this group. When the ultimate drift ratios described in Table 5.2 were attained, cumulative drift ratios differed slightly. In other words, it can be said that energy loss due to change in drift ratio was almost equal to the energy gain due to increase in ultimate load.

Although the strengthening schemes and failure modes of the specimens having aspect ratio of 1.0 were different, very good agreement was traced considering cumulative dissipated energy as indicated in Figure 5.25. This also showed that lap splice deficiency, the main deficiency in this group which affected behavior significantly, was successfully quenched.

The highest cumulative dissipated energy among the specimens with the aspect ratio of 2.3 was dissipated by SA2.3-CFM. It can be attributed to the better load transfer

mechanisms constructed via FRP cross diagonals and increased shear capacity of columns via wrapped FRP around columns. Although the area of cross diagonals on the masonry panel used to strengthen the specimens SA2.3-CCM and SA2.3-CFM was the same, energy dissipation capacity of SA2.3-CFM at peak load was almost 60% higher than that of SA2.3-CCM.

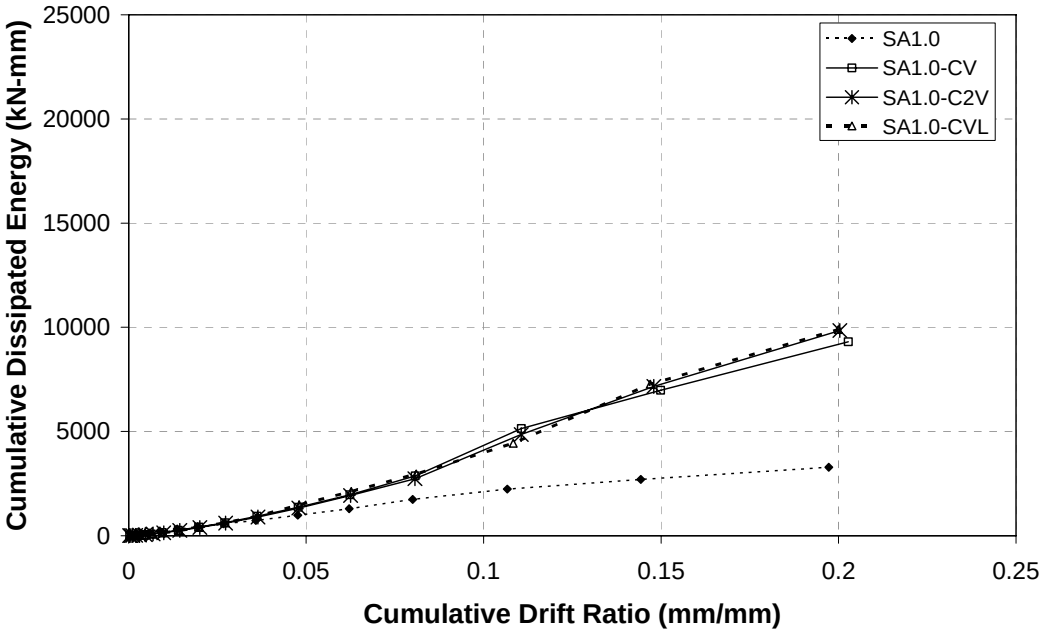

Figure 5.25. Cum. dis. energy vs cum. drift ratio for the specimens with A.R. of 1.0

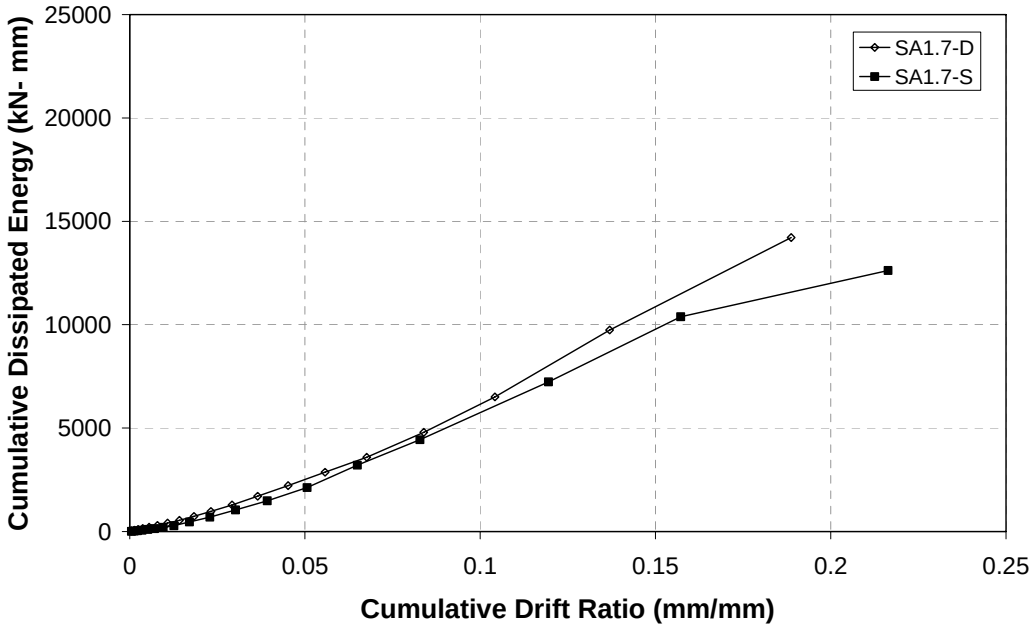

Figure 5.26. Cum. dis. energy vs cumulative drift ratio for the specimens with A.R. of 1.7

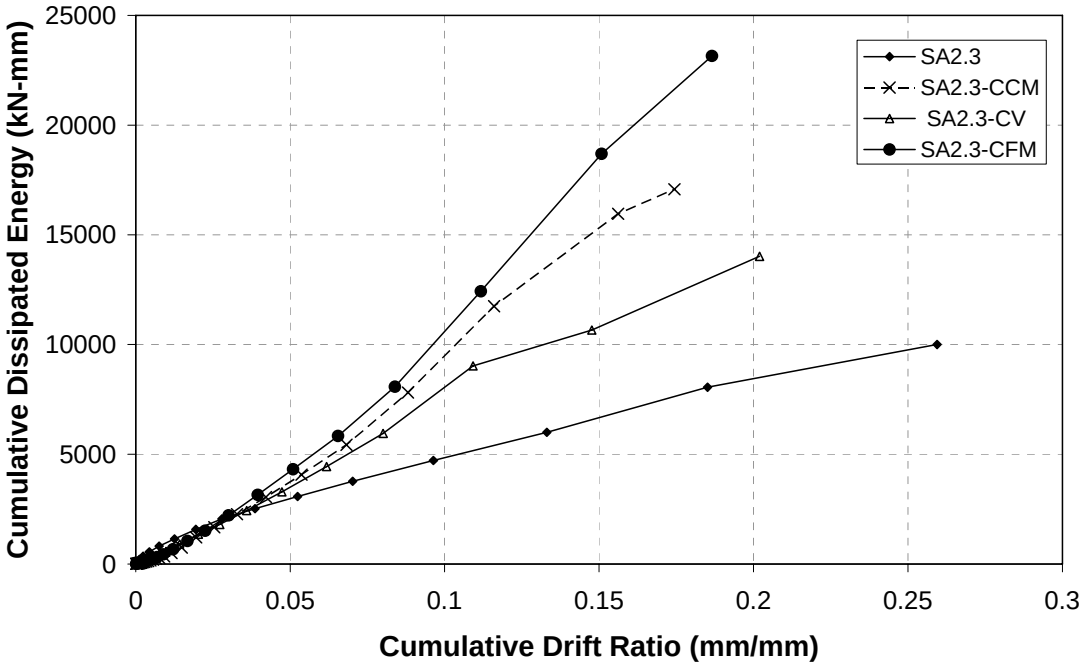

Figure 5.27. Cumulative dissipated energy vs cumulative drift ratio for the specimens with A.R. of 2.3

The ratio of dissipated energy to input energy per drift level was calculated and drawn with respect to roof drift ratio for each specimen. The area enclosed by each loop at a specific drift level was described as the dissipated energy. As shown in Figure 5.28, the ratio tended to decrease in the first several cycles. During the test, no damage was observed in these cycles. The system was in the elastic range. Once the cracks occurred, energy dissipation mechanisms activated and input energy dissipated by the system started to increase. This trend was much clearer for the strengthened specimens. When the strengthened specimens with an aspect ratio of 1.0 reached their peak loads, SA1.0-CV dissipated almost 80% of the input energy at that drift level as indicated in Figure 5.28 (0.01mm/mm).

The specimens with an aspect ratio of 1.7 showed different dissipation characteristics due to early failure of the SA1.7-D. As indicated in Figure 5.29, at the last cycles the rate of dissipated energy tended to decrease for the specimen SA1.7-D unlike SA1.7-S. However after the peak load cycle, both specimens' energy dissipation decreased slightly. While the specimen SA1.7-D dissipated 42% of the input energy at peak load, SA1.7-S dissipated 49% of the input energy at peak load level.

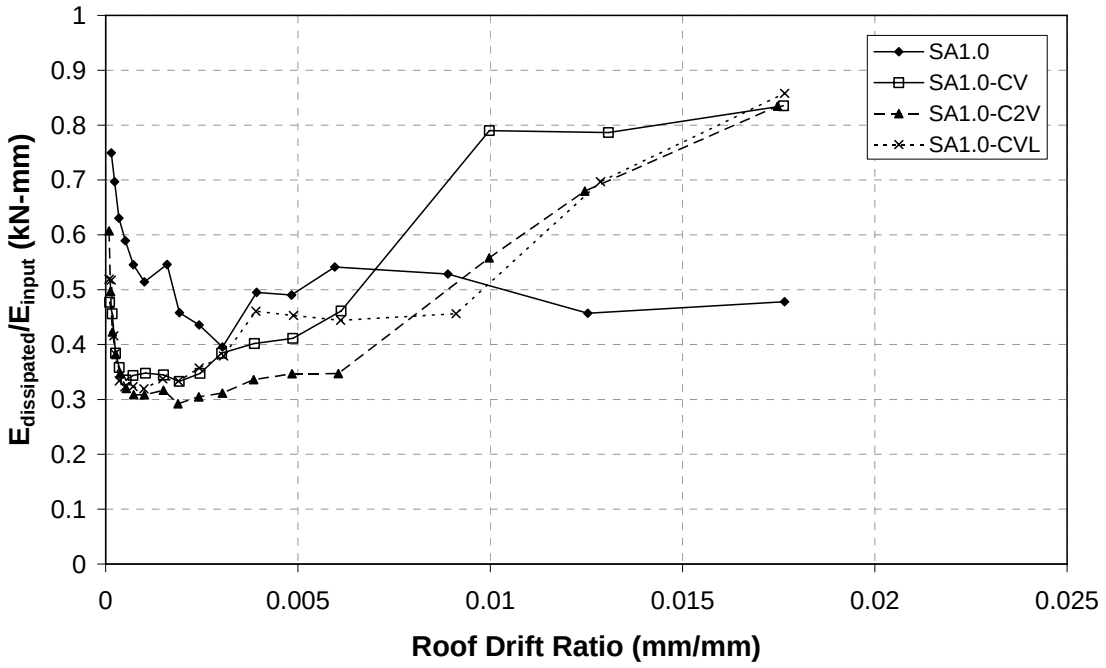

Figure 5.28. The ratio between dissipated and input energy at each drift level for specimens with A.R. of 1.0

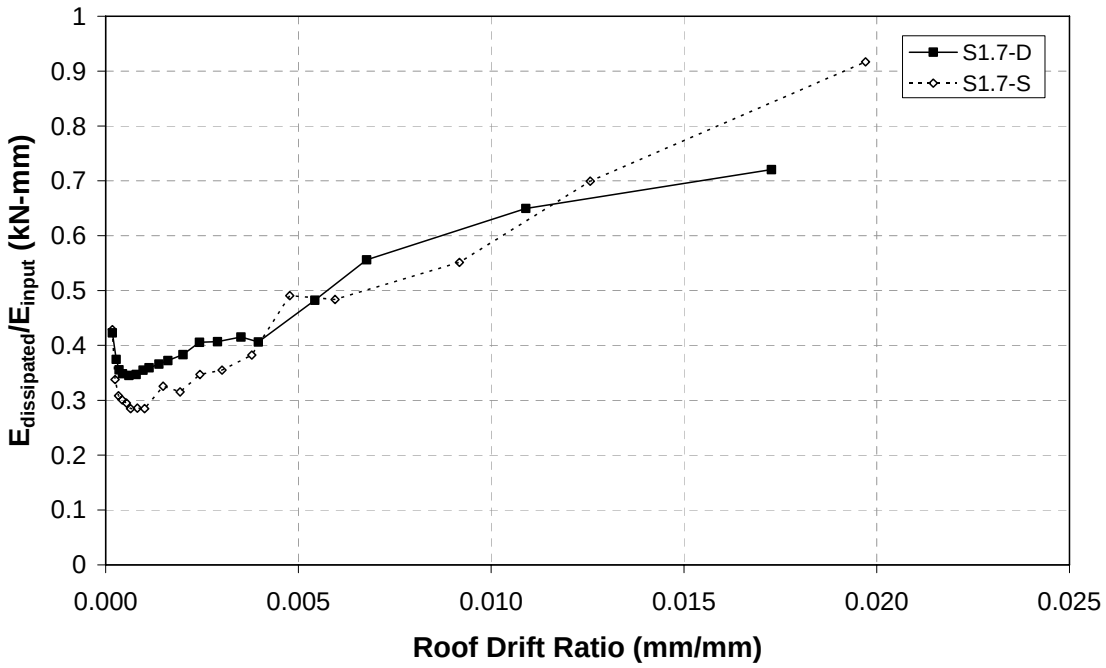

Figure 5.29. The ratio between dissipated and input energy at each drift level for specimens with A.R. of 1.7

As indicated in Figure 5.30, the dissipated energy ratio tended to decrease during the load controlled type of loading. One explanation is that the specimen behaved mostly elastic during these load controlled cycles, as the increase in displacement for each load increment was very little compared to the previous cycle.

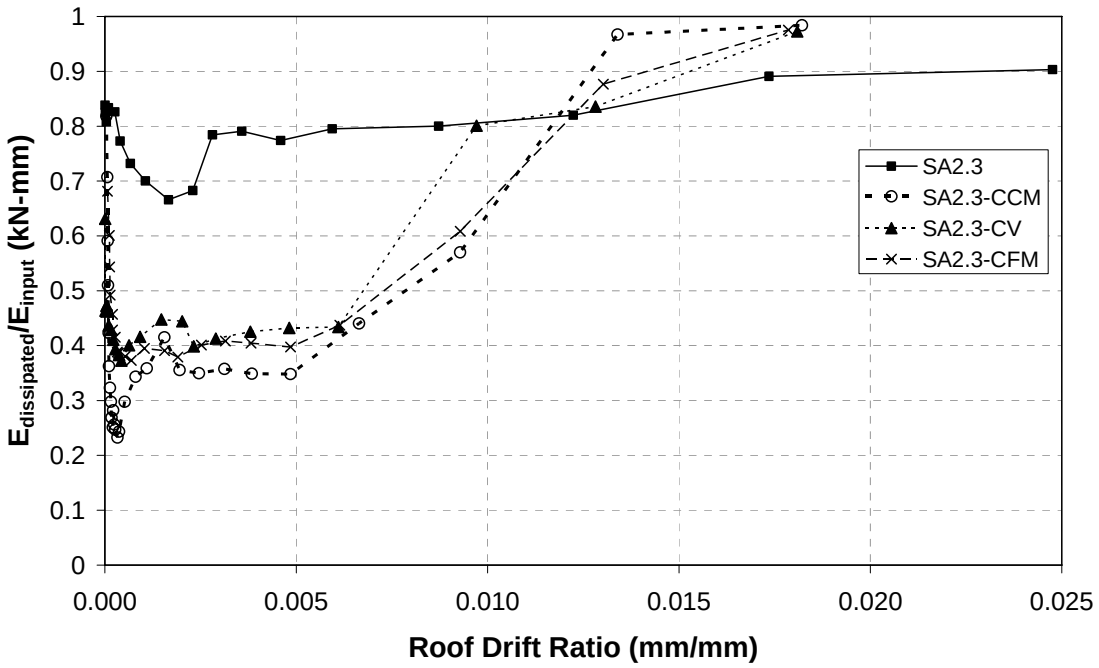

Figure 5.30. The ratio between dissipated and input energy at each drift level for specimens with A.R. of 2.3

Figures 5.31, 5.32, and 5.33 illustrate the general trend for all the specimens tested in this study. As indicated, SA2.3 was the closest specimen to the y=x line. This line showed that all of the input energy dissipated by the given system. SA1.0 was also very close to this line. All the strengthened specimens tended to deviate from the y=x line. SA2.3-CCM established the upper bound for this diagram. This graph showed how aspect ratio and strengthening scheme influenced the energy dissipation capacity under reversed cyclic loading. SB2.3-CCM was the most rigid (the highest initial stiffness) and had the most input energy for the same cumulative dissipated energy among the strengthened specimens. The highest energy dissipation was achieved by SA2.3-CFM due to the evenly distributed FRP cross diagonal sheets and wrapping of columns with FRP overlays. However, SA1.0-CV dissipated 62% of the input energy which was the highest dissipation amount.

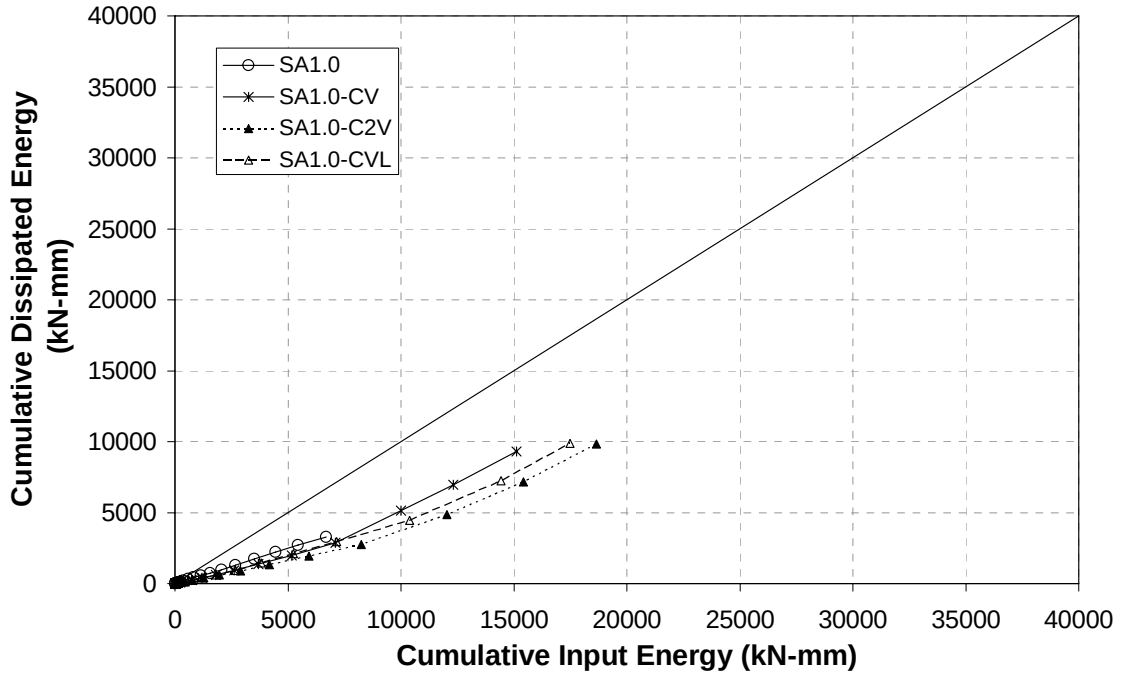

Figure 5.31. Cumulative dissipated energy vs. cumulative input energy for specimens with an Aspect Ratio of 1.0

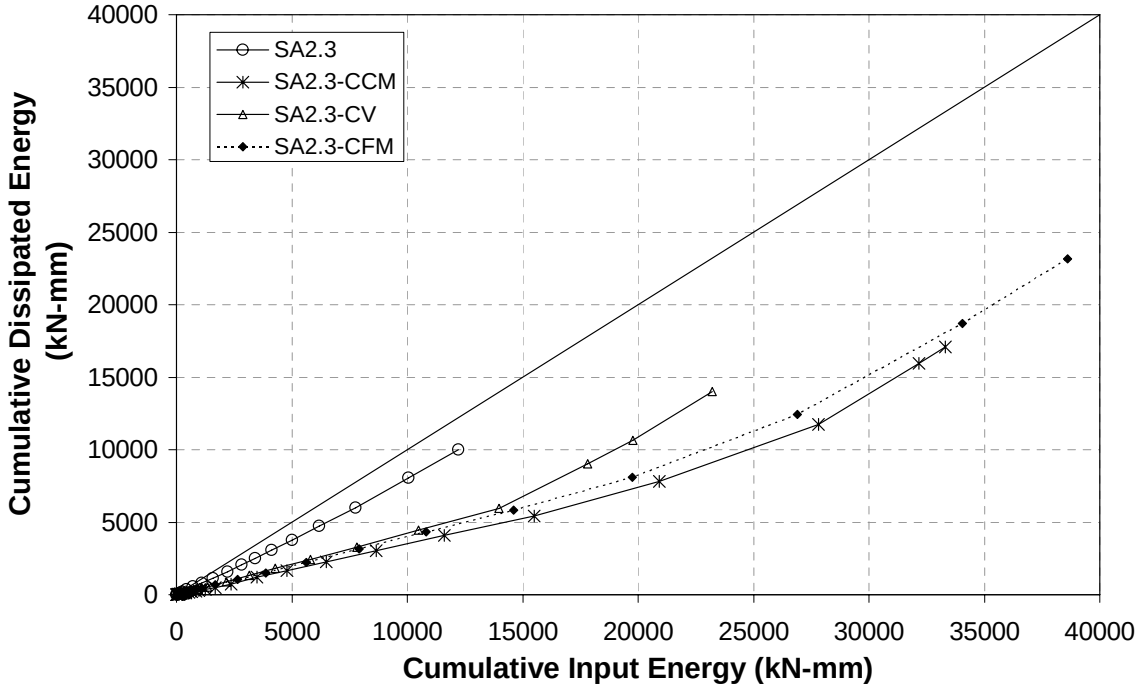

Figure 5.32. Cumulative dissipated energy vs. cumulative input energy for specimens with an Aspect Ratio of 2.3

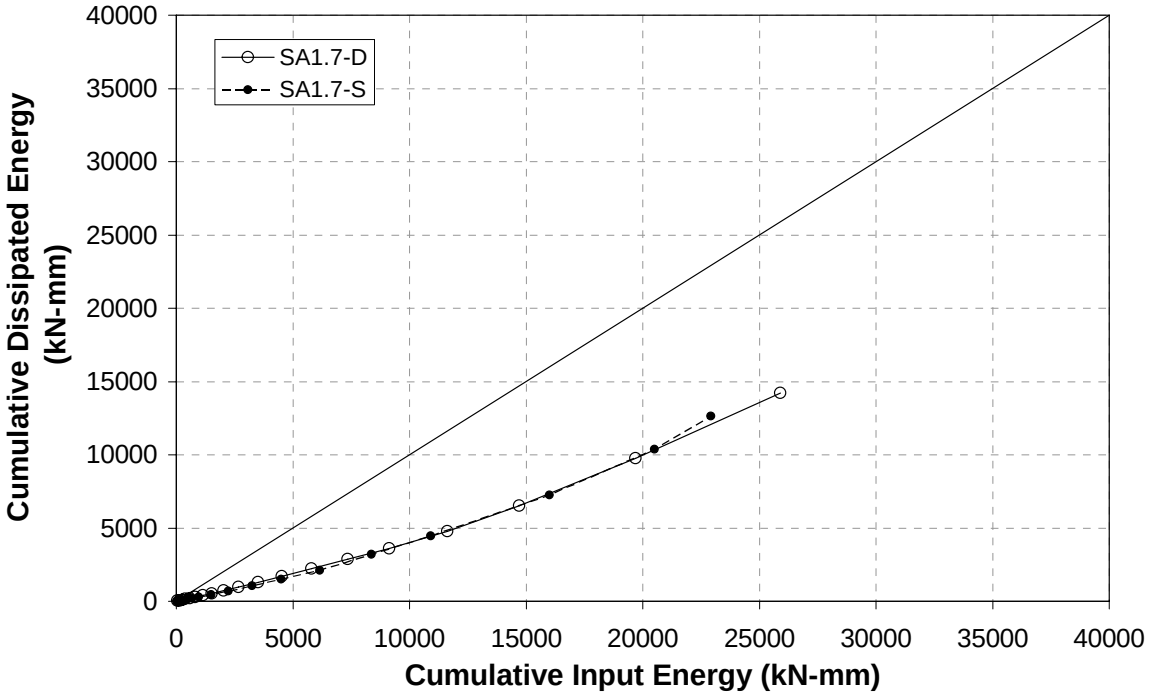

Figure 5.33. Cumulative dissipated energy vs. cumulative input energy for specimens with an Aspect Ratio of 1.7

5.10. Equivalent Damping Ratio

One of the most important parameters in earthquake engineering is the energy dissipation, and the equivalent damping ratio is directly related to the energy dissipation of the system. There are several definitions of the equivalent viscous damping. The detailed information is given in reference [105], and the most widely used definition is given in Equation 5.41 [105]. In this formula E_D represents the energy dissipated in one loading cycle in the actual structure as E_S is the strain energy defined as the triangular areas between stiffness line and x axis.

$$\zeta_{eq} = \frac{1}{2\pi}\frac{E_D}{E_S} \tag{5.41}$$

Equivalent damping ratio is discussed in the following paragraphs considering the three different diagrams drawn for each aspect ratio. Equivalent damping ratio values stand for that of the third cycle of each successive drift ratio. Cumulative drift ratios are the sum of the all drift ratios obtained from the sets of three cycles. The stiffness values in the

diagrams correspond to the third cycle value, same as in the case of equivalent damping ratio. Moreover the ratio of dissipated energy at the 1st and 3rd cycles was also illustrated for each aspect ratio.

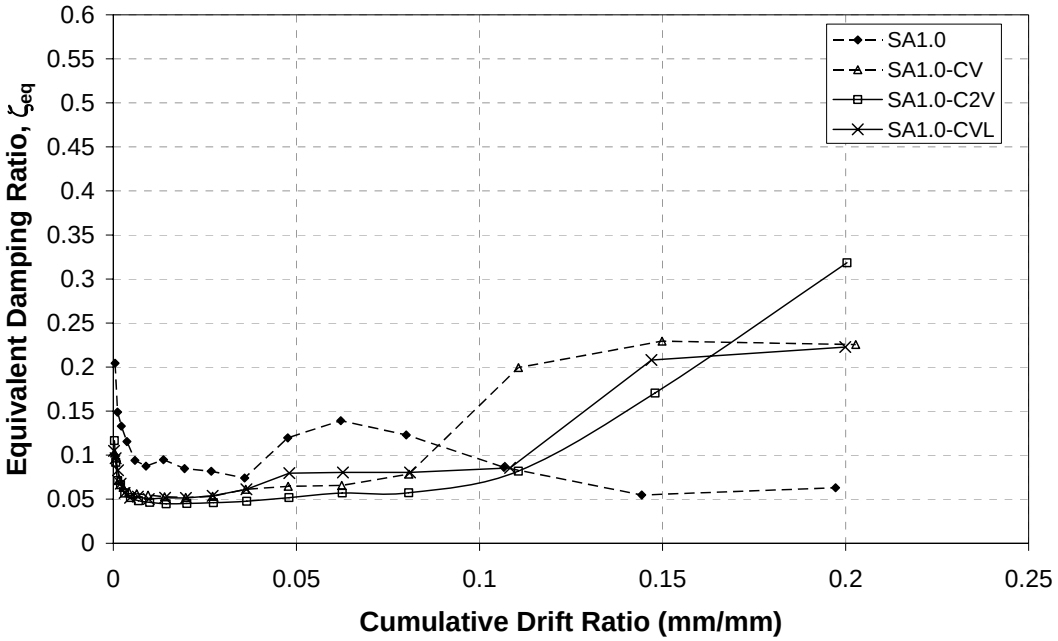

Figure 5.34. Equivalent damping ratio vs. cumulative drift ratio for A.R. 1.0

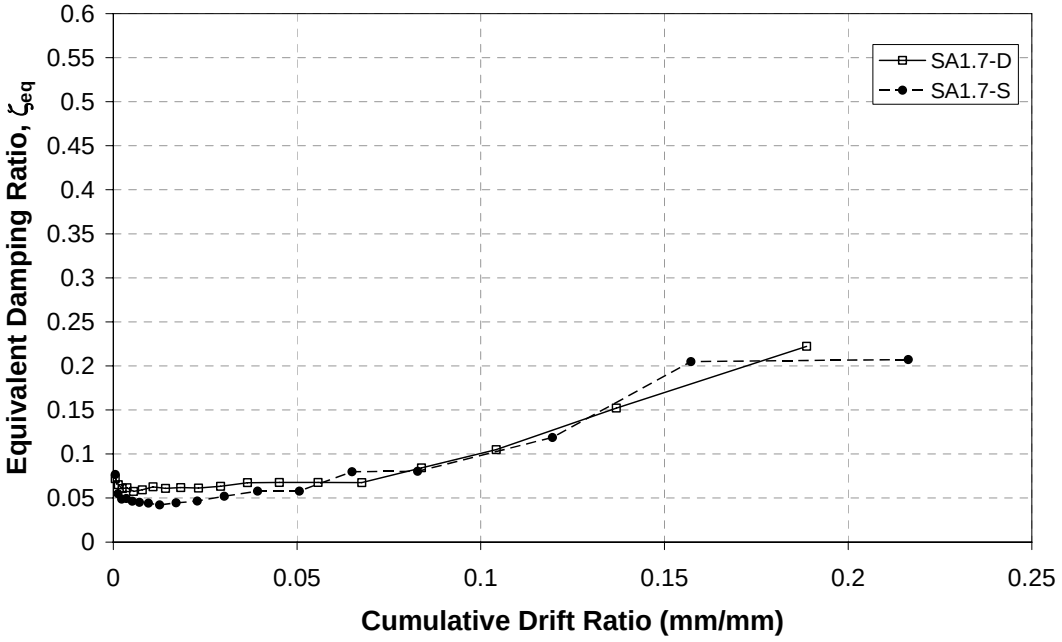

Figure 5.35. Equivalent damping ratio vs. cumulative drift ratio for A.R. 1.7

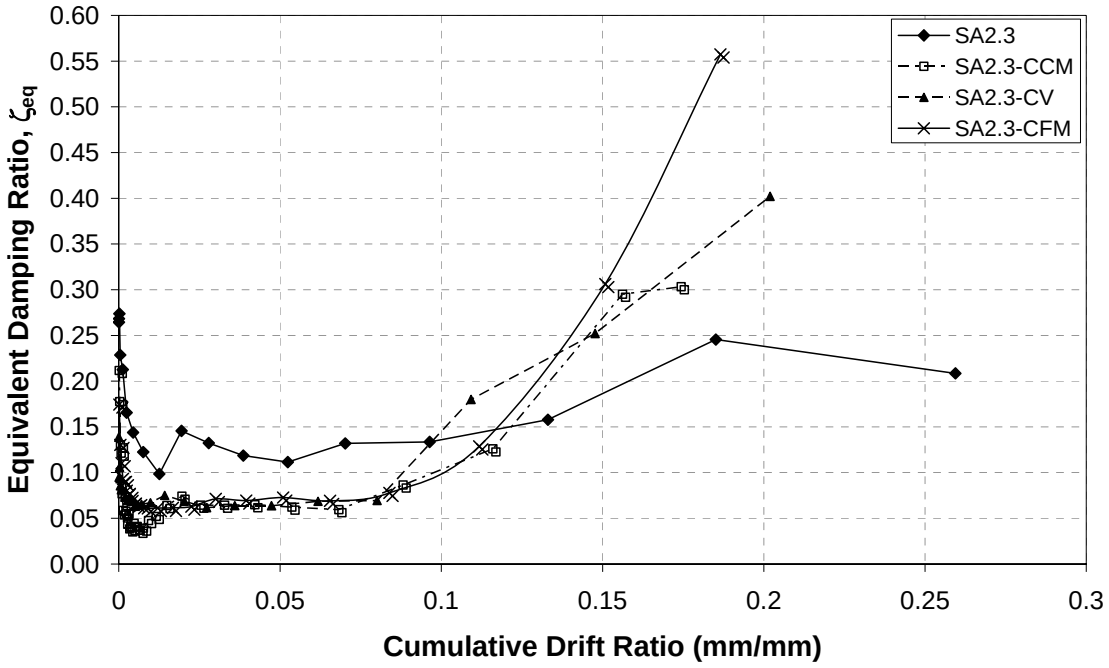

Figure 5.36. Equivalent damping ratio vs. cumulative drift ratio for A.R. 2.3

Figure 5.34, 5.35, and 5.36 illustrate the changes in equivalent damping ratios of the third cycles of each set with respect to cumulative drift ratios. For the strengthened specimens with an aspect ratio of 1.0, the equivalent damping ratio experienced a sudden drop then stabilized at approximately 0.05 until the cumulative drift level of 0.027. After this point it deviated from the value of 0.05. When the strengthened specimens reached peak loads, SA1.0-CV had the highest equivalent damping ratio of 0.20 among the specimens with an aspect ratio of 1.0. Strengthening scheme played an important role for equivalent damping ratio as indicated in Figure 5.34. Sudden drop in equivalent damping ratio was not observed in the specimens having A.R. of 1.7. As indicated in Figure 5.35, equivalent damping ratio was stabilized around 0.05 until the cumulative drift level reached 0.05 . It tended to increase after the cumulative drift ratio of 0.05 especially after the peak load. Specimens with an aspect ratio of 2.3 experienced sudden drop in equivalent damping ratio as indicated in Figure 5.36. However this drop was in the small drift ratio range. Equivalent damping ratio of the strengthened specimens in this group stabilized about 0.065 between cumulative drift ratios of 0.017 and 0.068.

Figure 5.37, 5.38, and 5.39 illustrate the changes in the equivalent damping ratio with respect to the stiffness values of the third cycles of each drift ratio level. As indicated

in Figure 5.37 specimens having aspect ratio of 1.0 showed a very good convergence while stiffness was degraded. Equivalent damping ratio for this group converged to 0.05 in the large range of stiffness degradation. However, the equivalent damping ratio was inclined to rise after 75%-80% stiffness degradation, especially for the strengthened specimens with an aspect ratio of 1.0. As indicated in Figure 5.38, equivalent damping ratio stabilized around 0.05 for the large range of stiffness degradation. Equivalent damping ratio tended to increase after a stiffness degradation of about 68% for SA1.7-S and of about 76% for SA1.7-D. As shown in Figure 5.39, the strengthened specimens experienced better convergence than the infilled specimens. However, the scatter in the specimens with aspect ratio of 2.3 was greater than the other two groups. This can be attributed to the effect of the infill's aspect ratio on the behavior. As explained before, changes in aspect ratio influenced the behavior appreciably from the flexural dominance into the shear dominance.

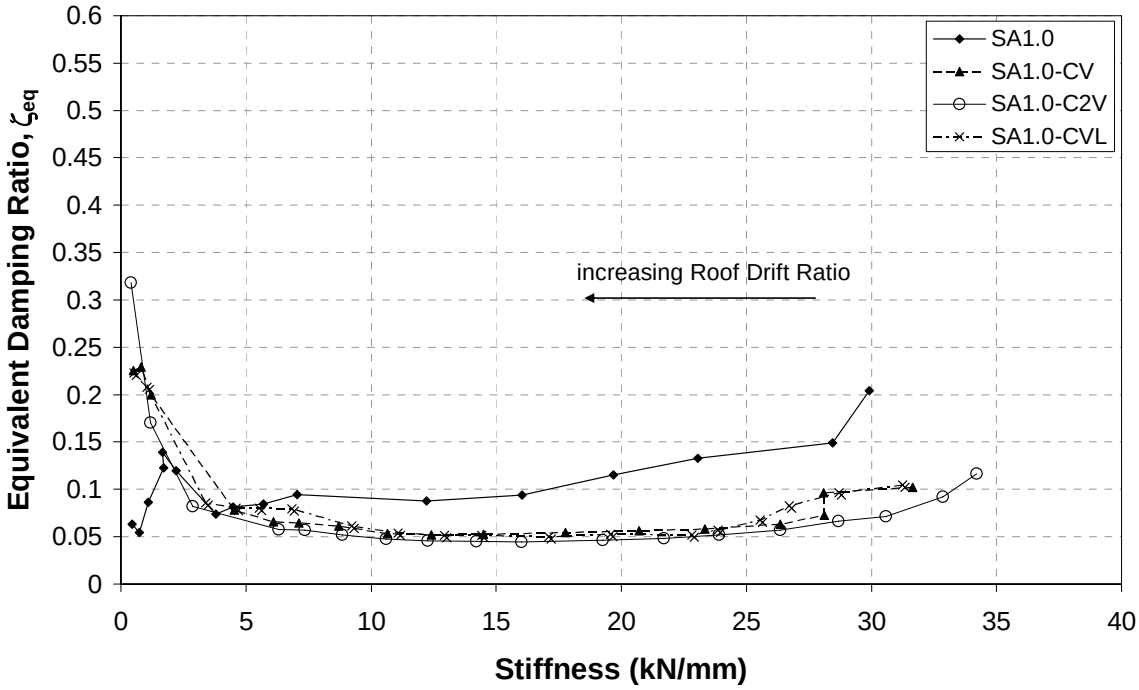

Figure 5.37. Equivalent damping ratio vs. stiffness for A.R. 1.0

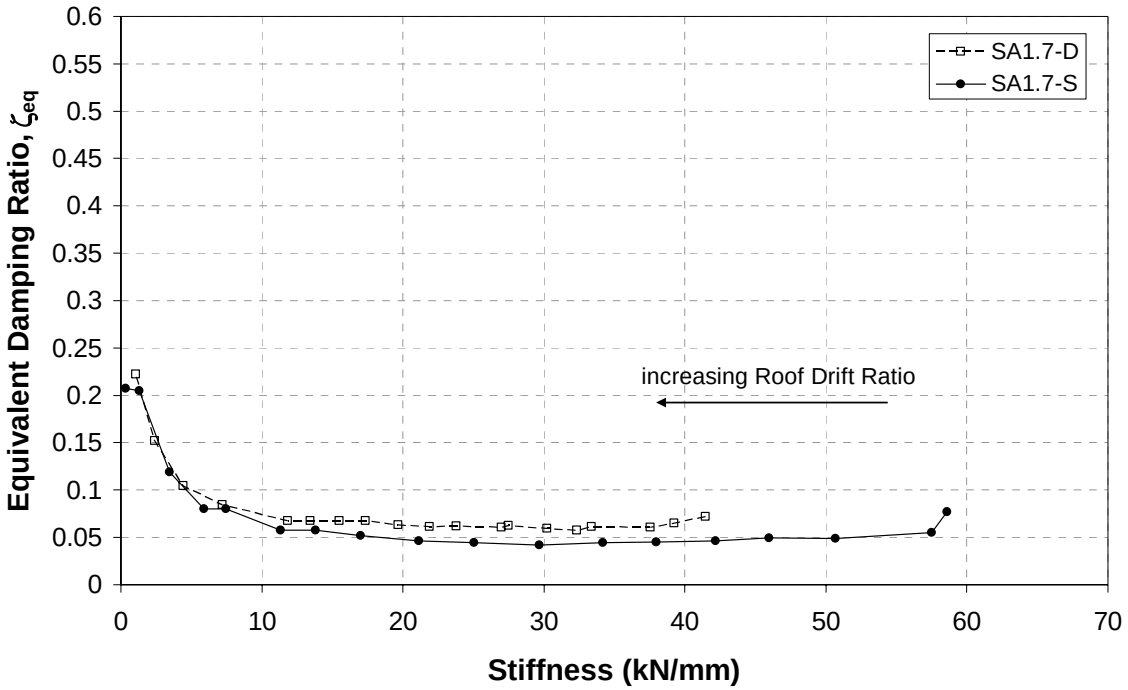

Figure 5.38. Equivalent damping ratio vs. stiffness for A.R. 1.7

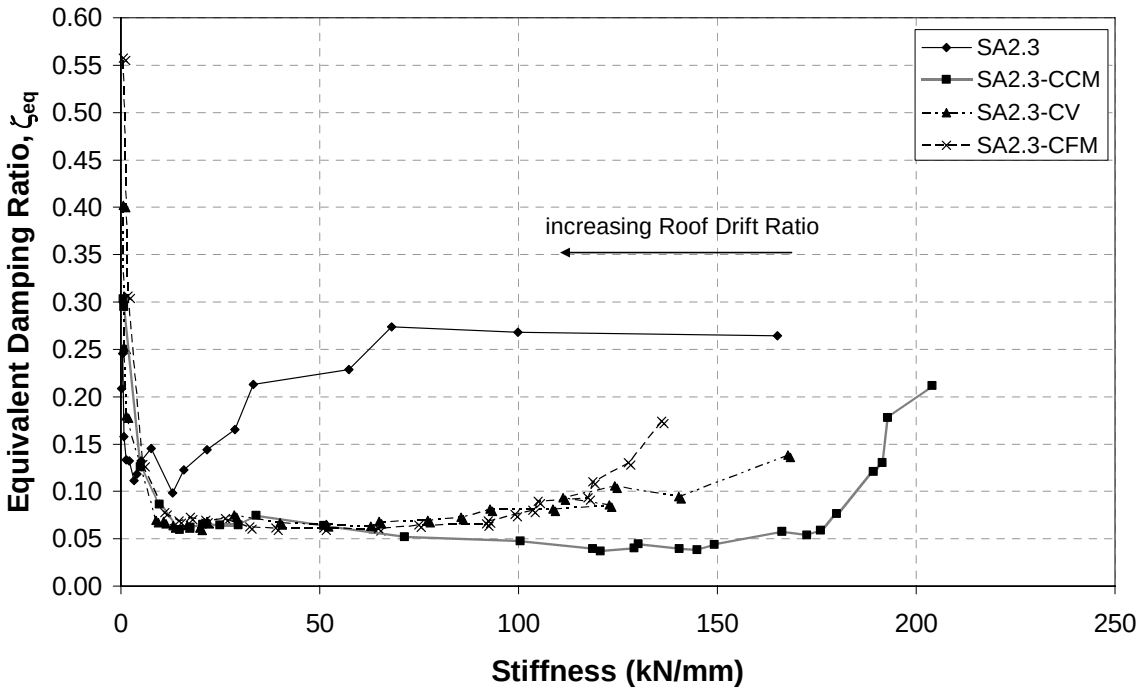

Figure 5.39. Equivalent damping ratio vs. stiffness for A.R. 2.3

The Figures 5.40, 5.41, and 5.42 investigate the dissipated energy ratios between the first and the third cycles. The ratio and corresponding cumulative drift ratios are given in these diagrams considering aspect ratios of the frames. As indicated in Figure 5.40, dissipated energy at the first cycles was inclined to be greater than the third cycle. This ratio reached 2.2 for the case of SA1.0-C2V at the peak load corresponding to the 0.11 cumulative drift ratio. As expected, SA1.0 reached maximum load level at earlier cumulative drift ratio. The strengthening scheme influenced dissipated energy ratios between first and third cycles, especially after the peak load. As the ratio decreased for the specimens SA1.0-CV and SA1.0-C2V after the peak load, it increased for SA1.0-CVL. Dissipated energy ratios between 1st and 3rd cycles were in the range of 1.14 and 1.52 as shown in Figure 5.41. Even though strengthening schemes were the same, premature failure of the specimen SA1.7-D led to the dissipation of less energy in the first cycles. Scattering in the specimens with an aspect ratio of 2.3 was higher than the rest, as shown in Figure 5.42. The energy dissipation ratio reached 3.9 for SA2.3-CV. The dissipated energy ratio was mainly in the range of 1-1.5 before the peak load was attained. In the strengthened specimens, when the peak load was reached or in the following cycles, the ratio was much more greater than 1. This can be attributed to the failure modes, strengthening scheme and formation of energy dissipation mechanisms. For example rupturing of FRP caused less energy dissipation in the successive cycles. These strong deviations from unity for specimen SA2.3-CV is because of the failure started in the first cycle and severely developed in the second cycle of that specified drift level.

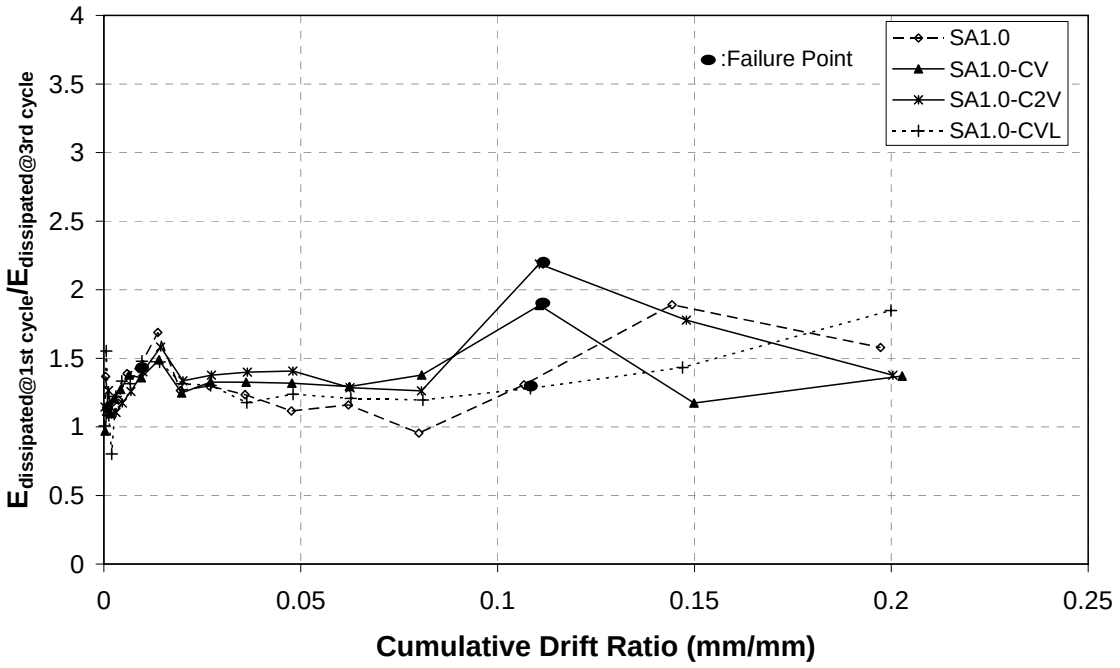

Figure 5.40. Dissipated energy ratio vs. cumulative drift ratio for A.R. 1.0

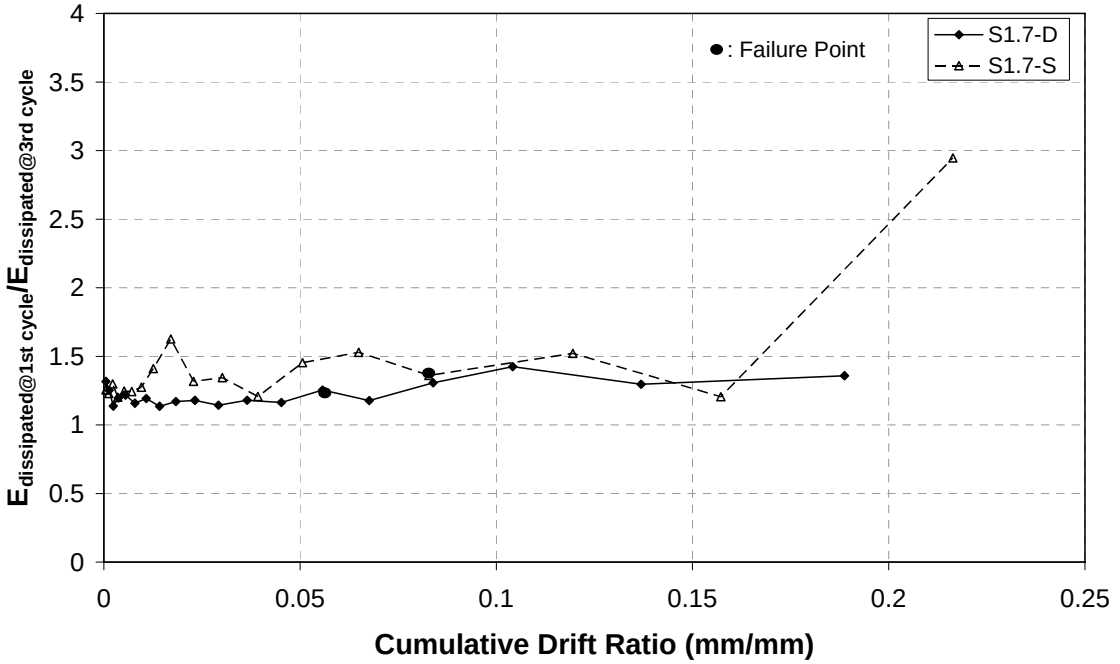

Figure 5.41. Dissipated energy ratio vs. cumulative drift ratio for A.R. 1.7

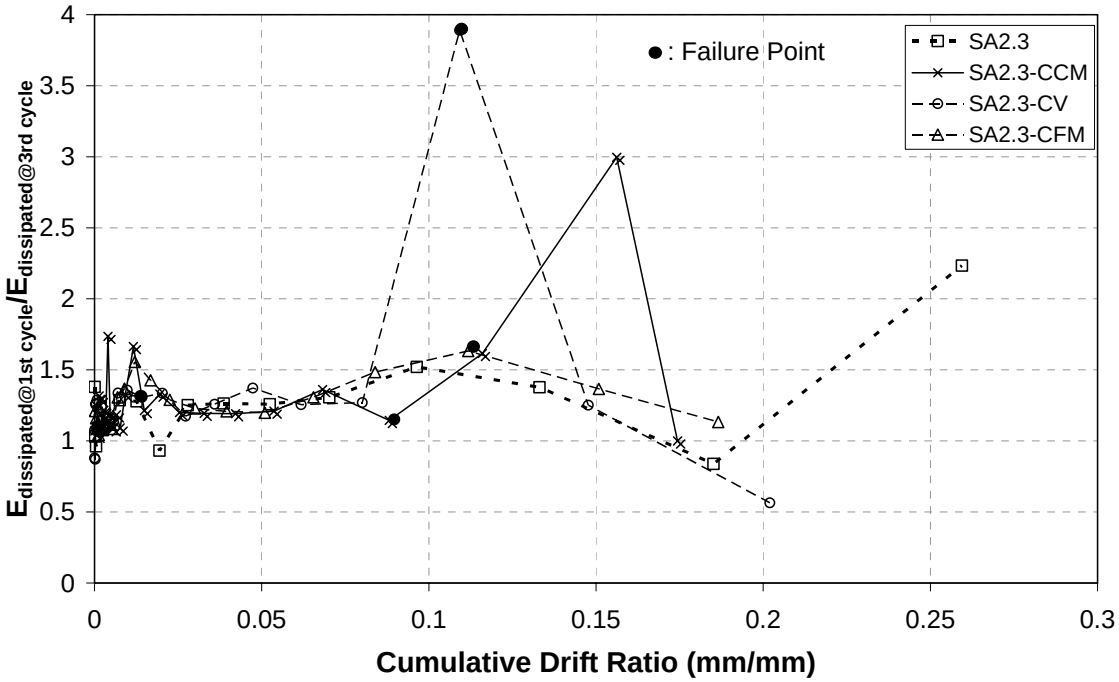

Figure 5.42. Dissipated energy ratio vs. cumulative drift ratio for A.R. 2.3

5.11. Residual Displacement Ratio

Residual displacement is a measure of the plastic deformation that the specimen undergoes. Residual displacement ratio is one of the indicators showing the damage accumulation behavior of the specimen. Stiffness and strength degradation along with the residual displacements are affected from the same reasons. Some of the reasons for the residual displacement are the formation of cracks (on the masonry or surrounding frame), yielding of steel, bond deterioration (either in concrete and steel or concrete and FRP), FRP failures (debonding, peeling off, rupturing), nonlinear deformations, and failures in the masonry and the surrounding frame (crushing of the masonry corners, sliding, interaction of the masonry panel and surrounding frame). Residual displacement ratio can be defined as the ratio between the residual displacement and the positive maximum displacement in each cycle. Residual displacement ratios at the third cycles are drawn with respect to the corresponding roof drift ratios.

Figures 5.43, 5.44, and 5.45 depicted changes in residual displacement ratio considering the aspect ratios. As SA1.0-CV established upper bound for the specimens

having aspect ratio of 1.0, there was no such similarity in the other groups. As indicated in Figure 5.43 residual displacement ratios were inclined to be less than 0.1 up to the roof drift level of 0.01 except the specimen SA1.0-CV. The difference between SA1.0-CV and SA1.0-C2V showed that doubling vertical strips on the masonry panel significantly affected the behavior and decreased residual displacement ratios leading to more linear behavior.

Changes in residual displacement ratio with respect to roof drift ratio for the specimen with an aspect ratio of 1.7 is shown in Figure 5.44. As soon as peak load was attained, residual displacement ratios increased in SA1.7-S. The same trend was not observed in the specimen SA1.7-D. When peak load was reached, the ratio tended to increase but then it decreased until 0.1. In other words, a stabilized behavior was not observed considering this specimen. Anchorage failure didn't lead to significant plastic deformations as observed in SA1.7-S.

Figure 5.45 illustrates the residual displacement ratio trend for the specimens with an aspect ratio of 2.3. Fluctuation in small drift levels was quite high. This can be due to some imperfections of the measuring devices. The highest residual displacement ratio was attained in this group. In other words, most damage was given to the specimens in this group.

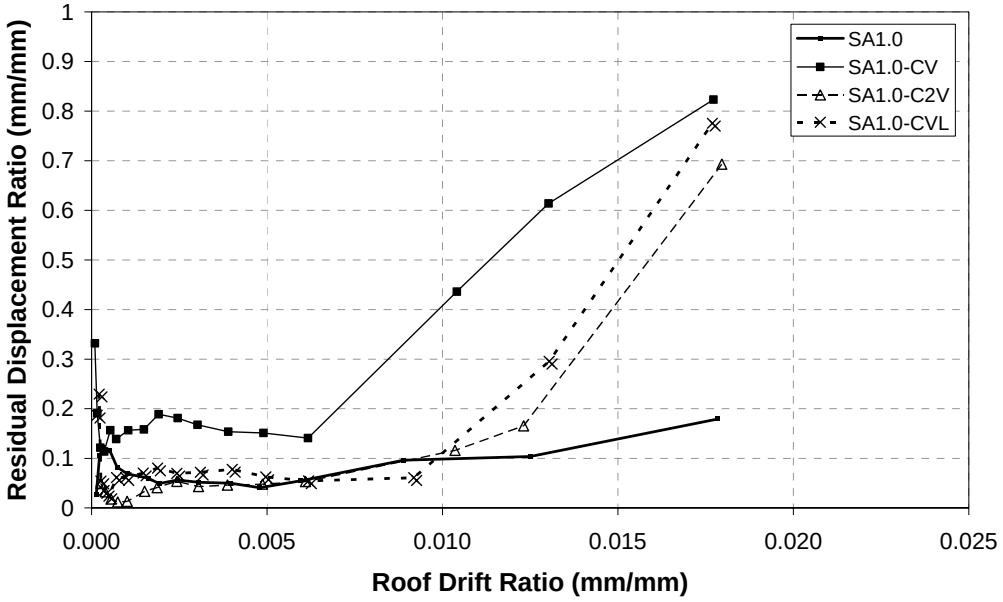

Figure 5.43. Residual displacement ratio vs. roof drift ratio for A.R. 1.0

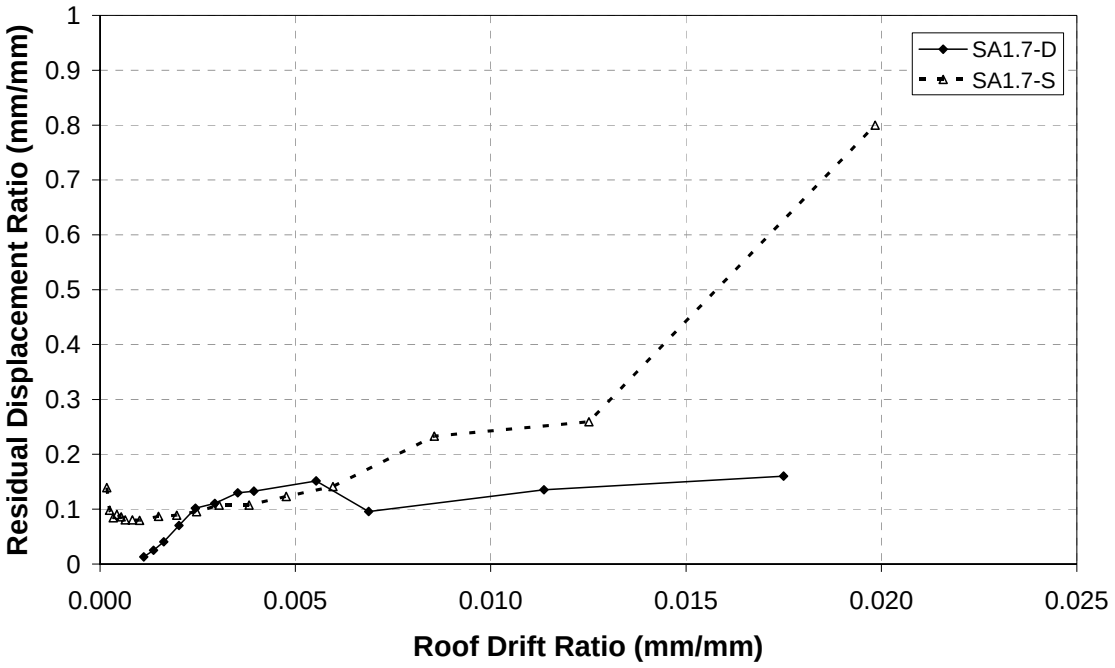

Figure 5.44. Residual displacement ratio vs. roof drift ratio for A.R. 1.7

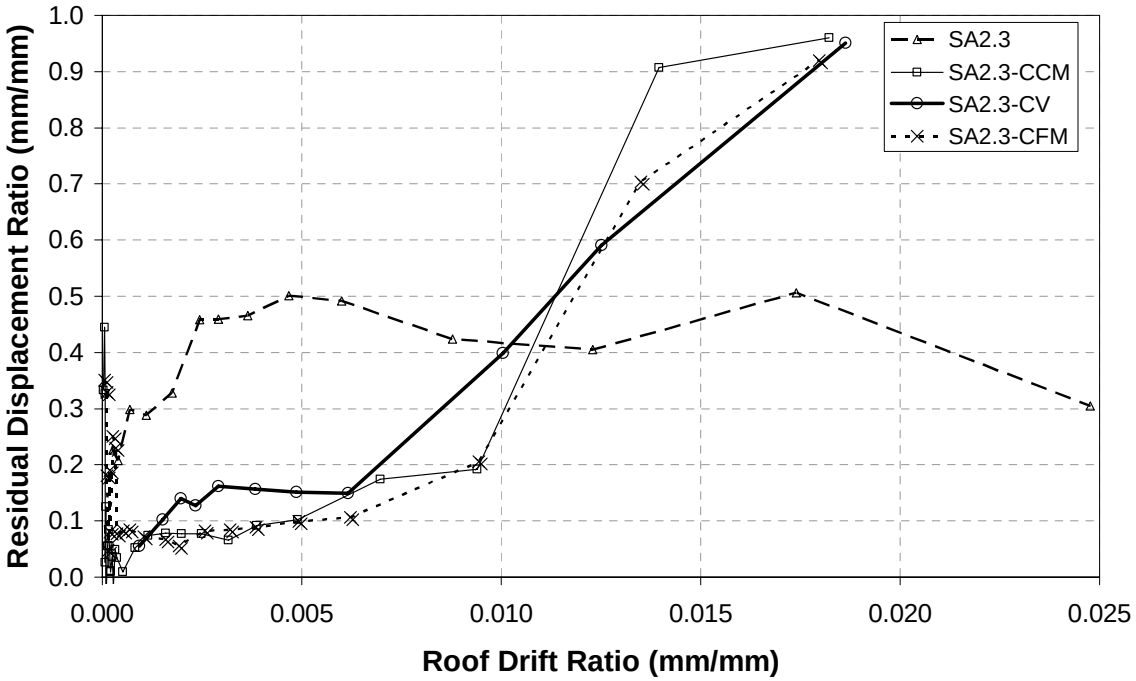

Figure 5.45. Residual displacement ratio vs. roof drift ratio for A.R. 2.3

5.12. Shear Deformations

Shear distortion angles or shear strains were calculated in accordance with the references [90] and [91]. Shear deformations measured by using two dialgages in X configurations were uncorrected deformations (Equation 3.2). In other words, the influence of flexural deformations was neglected. This meant that center of rotation and geometric center of the element were the same [90]. Each of the figures given in Appendix-C was constructed by using the Equations 3.3 and 3.4. As indicated, both models generally yielded almost the same results. Dashed lines in the figures showed the drift ratio of that story. As indicated in Figures C.1 and C.2, contribution of the shear deformation to the roof displacement is negligible due to failure mode of the specimen. Tension failure of the first story columns at the lower ends resulted in the appearance of inadequate lap splice problem and the specimen toppled as a rigid body. Figures C.3~C.8 illustrated that the contribution of shear displacement to the overall displacement was minimal. High shear distortion angles were the indicator of the accumulated damage into the 1^{st} story. Figures C.9~C.12 belonged to the specimens with aspect ratio of 1.7. Since the failure mode of the specimen SA1.7-D was due to inadequate depth of CFRP anchors at the foundation levels, shear distortion angles at the 1^{st} story were relatively small compared to the specimen SA1.7-S. Moreover the slight damage in the second story of specimens SA1.7-S and SA1.7-D explained higher shear distortion angle values as compared to those of the specimens with aspect ratio of 1.0. Figures C.13~C.20 illustrated the diagrams of the specimens with aspect ratio of 2.3. First story shear distortion angles were measured by using two couples of dialgages. In the first couple a square was constructed whereas the second couple was located near to the corners of the panel in a way to construct a rectangle. The diagrams showed that the Equations 3.3 and 3.4 differ slightly in the case of the 45^0 placement of dialgages. Moreover the reliability of first couple dialgages (45^0) was less than the second couple because the first couple covered smaller area.

6. ANALYTICAL STUDY

Construction of RC frames precedes the construction of masonry infills. Masonry infills can either be treated as structural elements or non-structural elements depending on the presence of the isolation gaps between the wall and the frame. Gaps in infilled structures between the frame and the panel have some disadvantages. For example, stability problems may arise due to inappropriate support conditions [2]. In addition, the extra mass provided by infills will increase the demand of the earthquake but this mass will not be used as a supply source for earthquake resistant design.

Masonry infills can be constructed as a part of the lateral load carrying system. In such a case, a gap between frame and panel is not allowed. This study focused on the case in which masonry walls are built tightly inside the surrounding frame. In current practice, masonry infills are not taken into account in design and analysis procedures which is not always conservative. To reiterate, infills influenced the dynamic behavior of the structure significantly. Stiffening effects of the infill decreased the natural period of vibration of the structure and this may result in an increase in the demand of the earthquake. Infills also increase strength of the structure. The importance of frame-wall interaction increases, especially in high seismic regions. For example, damage to the structural members would be limited if the failure of the infill took place at low shear forces because infill dissipates energy and limits the displacements [1]. If the failure of the infills occurs at high shear forces, frame members suffer from high shear forces, for which they are not designed [1]. The latter case shows that ignoring the use of infills in design is sometimes unconservative. Reserved strength of the structure could not be used due to ignoring of the infills, especially in low to moderate seismic regions. Torsional irregularities created by infills and short column effects due to distribution of forces in the frame members of the structure can create design problems. As a result, ignoring infills is not always beneficial and can result in unsafe or expensive designs.

Infill panels are often ignored in the design and analysis procedures because of high uncertainty due to non-homogenous, inelastic and anisotropic nature of the masonry, lack of an accepted approach on the models of masonry panels, and different failure modes [1

and 106]. Bonding FRP to the infill substrate to strengthen the infilled frame helps to decrease the uncertainty in behavior and results in a more reliable infill behavior.

In general, there are two approaches to model the infilled frames: the macro modeling based on equivalent strut concept and the micro modeling based on finite element methods. Both methods have advantages and disadvantages. Local effects such as cracking, frame wall interaction and failure modes, sliding and separation, failure load and displacements can easily be predicted by using finite element methods [107 and 53]. However, micro-modeling analysis is time consuming due to the large number of parameters considered in the analysis. It is also a sophisticated technique, and may not be suitable for using in engineering offices. Macro modeling, however, is relatively easy, fast, and efficient. Moreover, it is not as complicated as the micro-modeling. Macro-modeling may be an appropriate tool to predict the global behavior in terms of ductility, energy dissipation, and failure load levels [108]. However, macro-models may not predict the failure modes and may not simulate the frame-wall interaction. One of the objectives of this part of the dissertation is to develop an easy and reliable model and verify the analytical results with the experimental ones. Equivalent strut concept will be used for the modeling of infilled frames (macro-modeling), and some information about equivalent strut concept and equivalent strut width will be given in the following pages.

6.1. Equivalent Diagonal Strut Concept

Polyakov introduced the first equivalent diagonal strut concept based on the experiments on infilled frames [111]. Later, Holmes [17] used pin jointed equivalent diagonal struts to model infilled frames and proposed a constant strut width of one third of the diagonal length with the same thickness of the panel. Smith and Carter [23] compiled previous research and proposed theoretical relations for stiffness and equivalent strut width. Those relations were taken as bases for the subsequent researches. The assumptions used in the calculations of Smith and Carter [23] were as follows. Infills were non-integral and behaved as diagonal strut between loaded corners upon application of the lateral load. Tension failure in the windward columns, shear failure in the frame members, and various infill failures such as crushing or shear along the mortar plane in case of brick infill were among the defined failure modes. Smith and Carter [23] stated that equivalent strut width

is a function of diagonal load on the panel, material properties of the infill, panel dimensions, and length of contact. Moreover, contact length along the beam and panel interface was taken as one half of the span length because variation in the beam stiffness did not influence the behavior significantly, whereas the column stiffness did. Assuming triangular stress distribution along with the frame and loaded corners of the panel and by using beam on elastic foundation theory, Smith and Carter [23] proposed Equation 6.1 and presented equivalent strut width graphically. Dhanasekar and Page [54] stated that infill to frame relative stiffness parameter and the strength of the infill were inversely proportional.

$$\frac{\alpha}{h}=\frac{\pi}{2\lambda h} \qquad \text{where} \qquad \lambda=\sqrt[4]{\frac{E_{in}\times t_{in}\times \sin 2\theta}{4\times E_c\times I_c\times h_{in}}} \tag{6.1}$$

λh : non-dimensional parameter (infill-to-frame relative stiffness parameter)

E_{in} : modulus of elasticity of the masonry panel

t_{in} :thickness of the masonry panel

θ : the angle of the masonry panel diagonal with respect to the horizontal axis

E_c : modulus of elasticity of the column

I_c :moment of inertia of the column

h_{in} : height of the masonry panel

h : height of the story between centerlines of the beams

α : contact length along the infill panel and column

Based on previous research, small scale, and full scale tests, Mainstone [27] proposed empirical equations for equivalent strut width with the same thickness of the masonry panel prior to cracking and prior to crushing strength as a function of infill to frame relative stiffness. Equation 6.2 is given for brick infills prior to cracking with non-dimensional parameter (λh) less than 5. Some of the variables were described in Figure 6.1.

$$w=0.175*D*(\lambda h)^{-0.4} \tag{6.2}$$

w: effective width of the masonry panel prior to cracking

D: diagonal length of the masonry panel

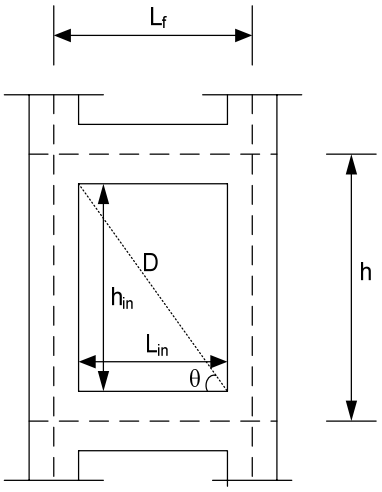

Figure 6.1. Dimensional variables of infill and frame

Klingner et al. [30 and 109] stated that effective strut width was generally in the range of one third to one eighth of the diagonal length of the masonry panel. They used the first nonlinear diagonal strut model including a strength degradation parameter and utilized Equation 6.2 to find the equivalent strut width.

Some provisions such as FEMA 356 [95], TDY'07 [7] and some other researchers [30, 109 and 110] used Equation 6.2 to determine the initial stiffness of the masonry panel. However, equivalent strut thickness may differ from that of the masonry panel depending on the infill type and materials used for strengthening if the infill was strengthened. Equivalent strut thickness for solid un-reinforced masonry infill was taken as the same as the masonry infill thickness in FEMA 356 [95]. The thickness of the equivalent strut of strengthened infilled frames by shotcrete or FRP was the same as the strengthened wall in TDY'07 (even for hollow clay tiles). However equivalent strut thickness of the strengthened infills with prefabricated panels was the same as the prefabricated panel itself [7]. Equivalent strut thickness was important in order to calculate the initial stiffness of the masonry panel. Klingner et al. [30] used the masonry panel thickness as the equivalent strut thickness even though they used hollow core blocks in their experiments. Al-Chaar et al. [110] proposed an analytical method for FRP strengthened infilled frames and utilized an effective net thickness excluding hollow cores. Al Chaar et al. [110] modified effective

strut width depending on the presence of opening, infill damage and FRP overlays as given in Equation 6.3. Like Klingner et al. [30 and 109], Al-Chaar et al. [110] did not consider the change in the strut area under increasing diagonal loads in their proposed method.

$$a_{\text{mod}} = a \times (R_1)_i \times (R_2)_i \times \xi_1 \tag{6.3}$$

a_{mod} : modified equivalent strut width

a : effective strut width calculated in accordance with Equation 6.2

$(R_1)_i$, $(R_2)_i$: reduction factors due to presence of openings and existing infill damage respectively

ξ_1 : strength increase factor due to presence of FRP overlays

Hendry [112] proposed Equation 6.4 based on the analogy of a beam on an elastic foundation. Assumed triangular stress distribution along the width of the equivalent strut is converted into a uniform stress distribution by using that semi-emprical equation [112]. Based on the study of Hendry, Drysdale et al. [113] proposed vertical and horizontal contact lengths as given in the Equations 6.5 and 6.6 and used Equation 6.4 to determine the equivalent strut width. Later, those formulations were used by Hakam [98]. The contact lengths were illustrated in Figure 6.2. Since the contact lengths on the lower right and upper left corners of the equivalent strut were symmetrical, the lower right corner was not illustrated in Figure 6.2.

$$w = \frac{1}{2}\sqrt{\alpha_h{}^2 + \alpha_L^2} \tag{6.4}$$

$$\alpha_h = \frac{\pi}{2\lambda_h} = \frac{\pi}{2}\sqrt[4]{\frac{4 \times E_c \times I_c \times h_{in}}{E_{in} \times t_{in} \times \sin 2\theta}} \tag{6.5}$$

$$\alpha_L = \frac{\pi}{\lambda_L} = \pi\sqrt[4]{\frac{4 \times E_b \times I_b \times L_{in}}{E_{in} \times t_{in} \times \sin 2\theta}} \tag{6.6}$$

α_h : vertical contact length between the column and the masonry panel

α_L : horizontal contact length along the beam-panel interface

w : effective strut width

E_cI_c : flexural rigidity of the column

E_bI_b : flexural rigidity of the beam

h_{in}, L_{in}, t_{in} : height, length and thickness of the masonry infill panel

θ : the angle between diagonal of the panel and horizontal axis

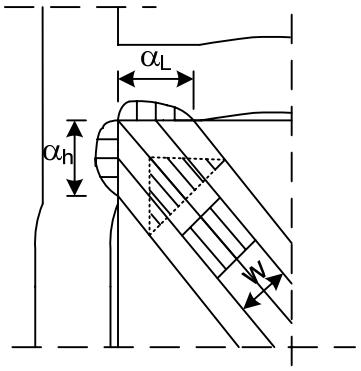

Figure 6.2. Horizontal and vertical contact lengths (Adopted from Drysdale et al. [113])

On the basis of previous research and the Mainstone's formulation, Dawe and Seah [114] proposed a relation for the equivalent strut width as given in Equation 6.7. The variables in Equation 6.7 are given in Equations 6.8 and 6.9. The strut area was the product of the thickness of the panel and equivalent strut width.

$$w = \frac{\pi}{1.5\lambda_h}\cos\theta + \frac{\pi}{1.5\lambda_L}\sin\theta \tag{6.7}$$

$$\lambda_h = \sqrt[4]{\frac{E_{in} \times t_{in} \times \sin 2\theta}{4 \times E_c \times I_c \times h_{in}}} \tag{6.8}$$

$$\lambda_L = \sqrt[4]{\frac{E_{in} \times t_{in} \times \sin 2\theta}{4 \times E_b \times I_b \times L_{in}}} \tag{6.9}$$

θ : slope of the diagonal strut

Durrani and Luo [115] proposed Equation 6.10 to determine the equivalent strut width. Later that formulation was used by Perera [116] and Combescure [117]. The finite element test results were used to obtain the empirical equations 6.10, 6.11, and 6.12. The strut area was the product of the thickness of the masonry panel and equivalent strut width given in Equation 6.10. The variables in these equations are shown in Figure 6.1.

$$w_{eff} = \gamma \times \sqrt{L_{in}^2 + h_{in}^2} \times \sin 2\theta \tag{6.10}$$

$$\gamma = 0.32\sqrt{\sin 2\theta}\left[\frac{h^4 \times E_{in} \times t_{in}}{m \times E_c \times I_c \times h_{in}}\right]^{-0.1} \tag{6.11}$$

$$m = 6 \times \left[1 + \frac{6}{\pi}\arctan\left(\frac{E_b I_b h}{E_c I_c L_f}\right)\right] \tag{6.12}$$

$$\theta = \arctan\left(\frac{h_{in}}{L_{in}}\right) \tag{6.13}$$

Paulay et al. proposed a constant effective strut width as one fourth of the diagonal length of the masonry panel regardless of member properties [2]. Like Paulay et al. [2], Buonopane et al. [118] recommended a constant strut width in the range of one sixth to one fourth of the infill diagonal length for both infill panels with and without openings. Flanagan et al. [45] stated that strut area exhibited nonlinear characteristics and proposed a piecewise linear equivalent strut which was similar to Smith and Carter Equations. Flanagan et al. [45] declared that the proposed equation, (Equation 6.14), can predict the stiffness of infilled frames at various limit states. The indicator of limit states, C, varied depending on infill type and frame type. For example, C can be taken as 8 for concrete frames with concrete masonry infill in case of severe infill damages. In Table 6.1, the value of 8 for C was used in the calculations. Flanagan et al. [45] limited effective strut width, w, to $0.20h_{in}/\cos\theta$ especially for frames with very stiff columns. λ is given in Equation 6.15.

$$A = \frac{\pi t}{C\lambda \cos\theta} \tag{6.14}$$

$$\lambda = \sqrt[4]{\frac{E_{in} \times t_{in} \times \sin 2\theta}{4 \times E_c \times I_c \times h_{in}}} \tag{6.15}$$

t : thickness of the masonry infill

C : empirical constant (indicator of the limit states)

θ : slope of the diagonal strut

Saneinejad and Hobbs [119] proposed an equivalent strut model including inelastic and nonlinear material properties. The developed method which was based on nonlinear FEM and previous experiments also included interface shear forces. In the proposed strut model contact lengths were limited to the 40% of the related infill dimension as given in Equations 6.17 and 6.18. Contact stresses were derived from Tresca hexagonal yield criterion. The strut area and contact length formulae were given in Equations 6.16, 6.17 and 6.18 respectively. Saneinejad et al. [119] stated that infill and frame dimensions can roughly be taken as the same for analytical purposes (i.e. h_{in}=h and L_{in}=L_f). Madan et al. used the same equations to develop a macro-model including a smooth hysteretic model [58].

$$A_d = \frac{(1-\alpha_c)\alpha_c ht \dfrac{\sigma_c}{f_c} + \alpha_b lt \dfrac{\tau_b}{f_c}}{\cos\theta} \le 0.5 \frac{th_{in} \dfrac{f_a}{f_c}}{\cos\theta} \tag{6.16}$$

$$\alpha_c h = \sqrt{\frac{2M_{pj} + 2\beta_c M_{pc}}{\sigma_c t}} \le 0.4 h_{in} \tag{6.17}$$

$$\alpha_b L_f = \sqrt{\frac{2M_{pj} + 2\beta_b M_{pb}}{\sigma_b t}} \le 0.4 L_{in} \tag{6.18}$$

θ: the angle between loaded diagonal and horizontal axis

Later El-Dakhakhni et al. [59] used the above equations with some simplifications. Based on the assumption that infill in the loaded corners region has been plastified near the

failure, upper bound values (β_0, σ_{c0} and σ_{b0}) for β_c, β_b, σ_c and σ_b can be used in the above equations. The upper bound of reduction factors, β_0, for frame intermediate bending moments was suggested as 0.2. It is a fact that the second and fourth power of a number smaller than 1 can be negligible in a square root. In addition, the coefficient of friction, μ, is small and can be negligible based on the parametric study performed by Flanagan et al. [45]. Thus upper bound values for nominal contact stresses would be equal to the compressive strength of the infill. Based on those explanations, El-Dakhakhni et al. proposed Equation 6.19 to calculate effective compressive strut area. Later that equation was used by Binici et al. [120].

$$A = \frac{(1-\alpha_c)\alpha_c h_{in} t}{\cos\theta} \qquad where \qquad \alpha_c h_{in} = \sqrt{\frac{2(M_{pj} + 0.2M_{pc})}{t f_{bmp}}} \leq 0.4 h_{in} \tag{6.19}$$

M_{pj}=min (M_{pb}; M_{pc})

M_{pj} : minimum plastic moment capacity of column or beam

f_{bmp} : compressive strength of infill

t : thickness of the infill

$\alpha_c h_{in}$: contact length along the column

h_{in} : height of the infill

θ : the angle between loaded diagonal of the infill and horizontal axis (i.e. arctan(h_{in}/L_{in}))

Determining the equivalent strut width is important to figure out the initial stiffness of the compression strut. Initial stiffness of the equivalent strut (K_0) is given in Equation 6.20. In this equation w_{strut} and D represent the width of the compression strut and diagonal length of the masonry panel respectively.

$$K_0 = \frac{w_{strut} \times t_{in} \times E_{in}}{D} \tag{6.20}$$

Table 6.1 illustrates the equivalent width and the calculated initial stiffness values for the specimens tested in this study. Equivalent widths were stated in terms of diagonal

length of the specimens in order to make comparison easier. As indicated in this table, effective widths calculated by using formulae of El-Dakhakhni [59] and Flanagan [45] were almost the same. It might be due to the fact that the effective widths were calculated by using the upper bound values of C, β, and contact stresses and the assumptions such as full plastification of the infill. The formulation suggested by FEMA 356 was irrelevant in regards to the aspect ratio unlike the others presented in Table 6.1. To reiterate, the Drysdale et al. [113] formulation which was based on Hendry's study, was for elastic analysis of infilled frames whereas the formulation of Saneinejad which established a basis for the study of El-Dakhakhni et al. [59] was for plastic analysis of infilled frames. The strut width values calculated by the formulae proposed by Paulay et al. [2] and Durrani et al. [115] yielded similar results, especially for the specimens with an aspect ratio of 1.0. Dawe et al. [114] formulation overestimated effective widths. Further explanation about effective width and stiffness values will be given in the subsequent parts.

Table 6.1. Effective width values of test specimens

Specimens	**SA1.0**	**SA1.0-CV**	**SA1.0-C2V**	**SA1.0-CVL**	**SA1.7-S**	**SA2.3**	**SA2.3-CCM**	**SA2.3-CV**	**SA2.3-CFM**
Diagonal Length (D), mm	1046.6	1046.6	1046.6	1046.6	1500.8	1950.0	1950.0	1950.0	1950.0
(w/D) FEMA 356	0.10	0.10	0.10	0.10	0.10	0.10	0.10	0.11	0.11
(w/D) Flanagan et al.	0.10	0.11	0.11	0.11	0.06	0.05	0.05	0.05	0.05
(w/D) Drysdale et al.	0.42	0.46	0.45	0.45	0.36	0.32	0.32	0.33	0.33
(w/D) Dawe et al.	0.65	0.70	0.70	0.69	0.49	0.38	0.38	0.39	0.39
(w/D) Paulay et al.	0.25	0.25	0.25	0.25	0.25	0.25	0.25	0.25	0.25
(w/D) Durrani et al.	**0.21**	**0.22**	**0.22**	**0.22**	**0.17**	**0.13**	**0.13**	**0.13**	**0.13**
(w/D) El-Dakhakhni et al.	0.09	0.11	0.11	0.13	0.05	0.04	0.04	0.04	0.05
Initial Stiffness kN/mm (cal.)*	128.2	145.0	173.0	176.3	120.5	64.5	84.0	71.8	76.0
Initial Stiffness kN/mm (cal.)**	59.5	67.3	80.3	81.9	71.2	52.8	68.7	58.7	62.1
Note 1:* Durrani et al. formulae were used									
Note 2:** FEMA356 formulae were used									

6.2. Analytical Modeling

The infilled frames were modeled in the light of the observed behavior and test results. Since the behavior of infilled frames was highly nonlinear, nonlinear analysis should be performed to predict the behavior of the specimens. Cracking and crushing, debonding of FRP, rupturing of FRP, slip of rebars, opening and closing of the cracks were some of the reasons of nonlinear behavior of the infilled frames. Diagonal strut concept was utilized to facilitate modeling of the test specimens because this technique is simple, practical, and time-saving. However this technique does not permit to study local effects such as infill-frame interface.

In nonlinear static procedure, modeling of the infill panel is vital to obtain a reasonable solution. Determining the material properties and the cross sectional area of the equivalent strut is very important. In the literature, some researchers such as Flanagan et al. [45] used variable strut area as a function of limit states as illustrated in Equation 6.14. Some researchers such as Hakam [98] and El-Dakhakhni et al. [59] used varying material properties (nonlinear stress-strain relationship and an instantaneous modulus of elasticity). Moreover the modulus of elasticity of the equivalent strut can be determined from either compression tests of masonry prisms normal to the bed joints or a combination of the compression tests of masonry prisms normal and parallel to the bed joints. Hakam [98] and Binici et al. [121] used the former approach whereas El-Dakhakhni et al. [59] used the latter approach which was based on the assumption of the orthotropic infill.

Hakam [98] stated that considering masonry infill surrounded by steel frame as an orthotropic material was a good approximation if the observed failure modes were generally corner crushing and diagonal compression. Moreover, Hakam [98] declared that the same approximation may not be valid for the infilled frames with very weak infills or high aspect ratios (l/h) because of the possible shear sliding failure [98].

In this study, uniaxial compression tests of masonry prisms normal to the bed joints were used to determine the material properties and a constant cross sectional area of the equivalent strut were utilized. Equivalent strut area used in this study was based on the Equations 6.10-6.12. The multi-linear strut model was used to model the equivalent strut.

Plastic hinges were placed on the surrounding reinforced concrete frame in order to account for nonlinear actions in the frame members. In the subsequent parts the frame and strut models will be explained in detail.

6.2.1. Modeling of Frame Members

Plastic hinges played an important role in modeling frame members. Plastic hinges were placed on critical parts of the members where nonlinear behavior was expected. Experiments showed that plastic hinges for inelastic flexural actions should generally be located at the end of the members. Unlike an ordinary hinge, deformations or rotations of a plastic hinge increase under a constant moment or an increasing moment. Due to redistribution, formation of a plastic hinge does not necessarily lead to the collapse of the system. When the number of plastic hinges is sufficient to develop a collapse mechanism, the system fails. Nonlinear deformations are developed along a certain length which is called plastic hinge length. Plastic hinge length for inelastic flexural actions was a function of many parameters such as the amount of longitudinal steel, the diameter of re-bars, and anchorage conditions. There are several assumptions for this length. TDY'07 [7], ATC 40 and ACI 318-99 stated that plastic hinge length for the frame members can be taken as half of the cross section dimension perpendicular to the axis of bending. Priestley et al. [122] proposed Equation 6.21 for bridge columns.

$$l_p = 0.08L + 0.022 f_y d_{bl} \geq 0.044 f_y d_{bl} \tag{6.21}$$

L : the distance between critical section of plastic hinge and point of contraflexure

d_{bl} : diameter of longitudinal re-bars

f_y : yield strength of longitudinal re-bars

In this study, three types of plastic hinges were used to model the RC frames on the basis of observed failure modes. SAP2000 v10 [123] was used for macro-modeling. The plastic hinge types used in the modeling were M3, P, and V hinges. Although the explanation of plastic hinge is not appropriate for P and V hinges, the terminology accepted in the program was utilized in this chapter. M3 hinge was used to take into account inelastic flexural deformations on the frame members. The moment versus

normalized curvature (normalized with respect to the yield curvature) behavior of the M3 plastic hinge is described in Figure 6.3. The values corresponding to the labels A, B, C, D, and E for the M3 and V2 plastic hinges as well as P plastic hinge will be given in section 6.4 for each specimen. As indicated in Figure 6.3, plastic deformation (curvature) of the member is zero for moments which are smaller than the yield moment of the section, since the member behaves linear-elastically between A and B. Plastic deformations take place after point B. The positive slope between B and C describes strain hardening portion of the moment-curvature relation. The capacity drops to zero at point E.

P hinges are also used in the column members of the frame to represent possible axial deformation on the column members. In addition, V hinges are used to take into account shear deformations in the frame members (beams and columns). The stress versus plastic strain of the V and P hinges are shown in Figures 6.3 and 6.4 respectively. As indicated in Figure 6.3, the strength degradation of the V hinge is not gradual as is the case for the M3 plastic hinge since shear failure is more sudden and brittle. Test results of the control specimens (SA1.0 and SA2.3) showed that using a relatively gradual degradation is more appropriate for P hinge. In order to get the best correlation between experimental and analytical results, the degradation on the tension side is empirically calibrated as a function of the aspect ratio. As can be noticed from Figures 6.3 and 6.4, stress-strain relationships were used to represent the behavior of the frame members under axial and shear forces.

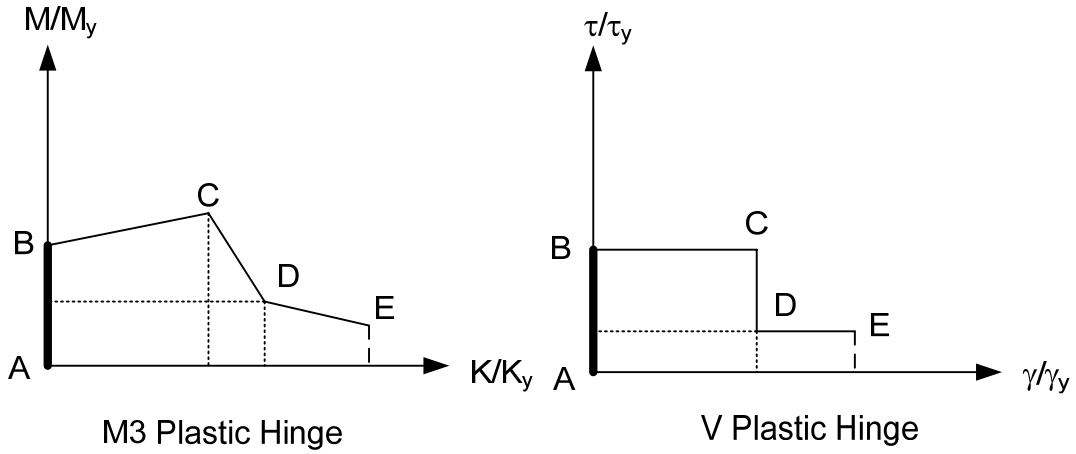

Figure 6.3. Relationships used for M3 (moment-curvature) and V (stress-strain) plastic hinges on the frame members

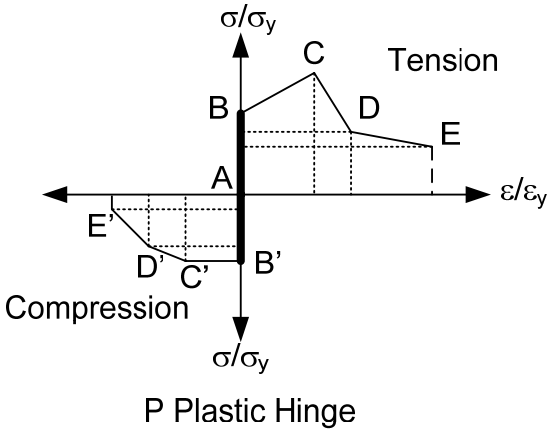

Figure 6.4. Behavior of P plastic hinge used on the column members

Frame members were modeled as elastic members with cracked flexural rigidity which was the initial slope of the bilinear moment curvature diagrams. Plastic hinges were used to impose nonlinear behavior on the structural model. In order to determine the moment–curvature diagram for beam and column members, two programs were used XTRACT [124] and moment curvature program proposed by Ersoy [97]. Both programs yielded similar results. The program proposed by Ersoy [97] was used due to its simplicity. Figures 6.5 and 6.6 illustrate the moment-curvature diagrams obtained from both sectional programs and bi-linearization of the moment-curvature curve for specimen SA2.3-CCM. The same diagrams were developed for each beam and column of each specimen. A modified Kent and Park stress-strain relationship for confined concrete, and a Kent and Park model with a linear descending portion ending at a strain level of 0.004 for unconfined concrete were implemented in the sectional analysis program. Three-linear stress-strain curve was used for steel including strain hardening portion. Concrete in tension was also modeled in the form of a bilinear stress-strain curve to consider the effect of tension stiffening.

Since the axial load on the columns was kept constant throughout the test, M3 hinges were placed at the end of frame members (as opposed to P-M interaction hinges) to account for inelastic flexural deformations which generally occur at the end of the members. Moment-curvature relationships were used to calibrate these plastic hinges.

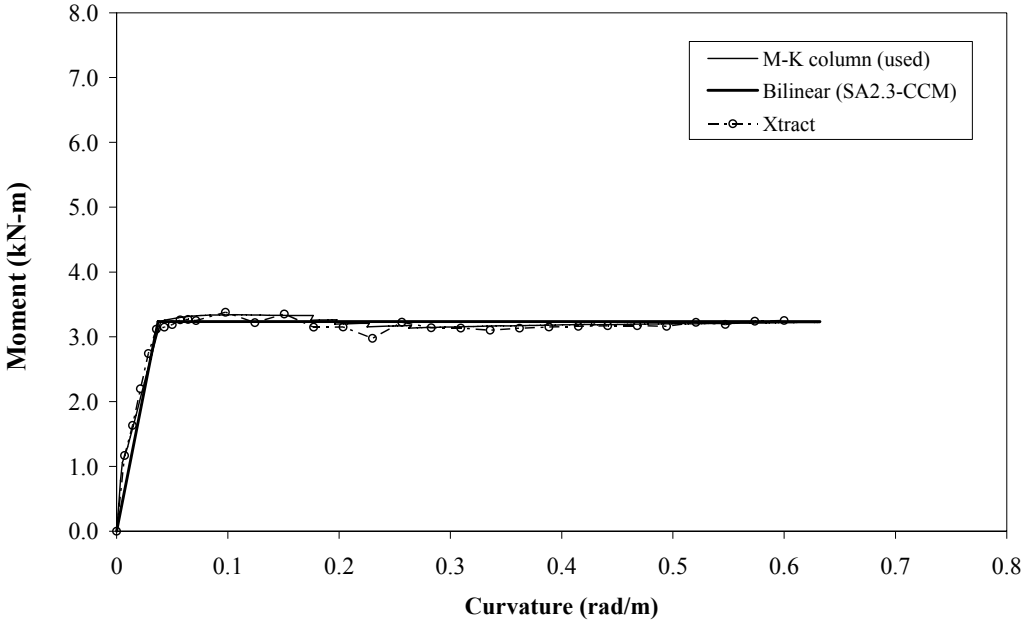

Figure 6.5. Moment Curvature Diagram of the column of specimen SA2.3-CCM

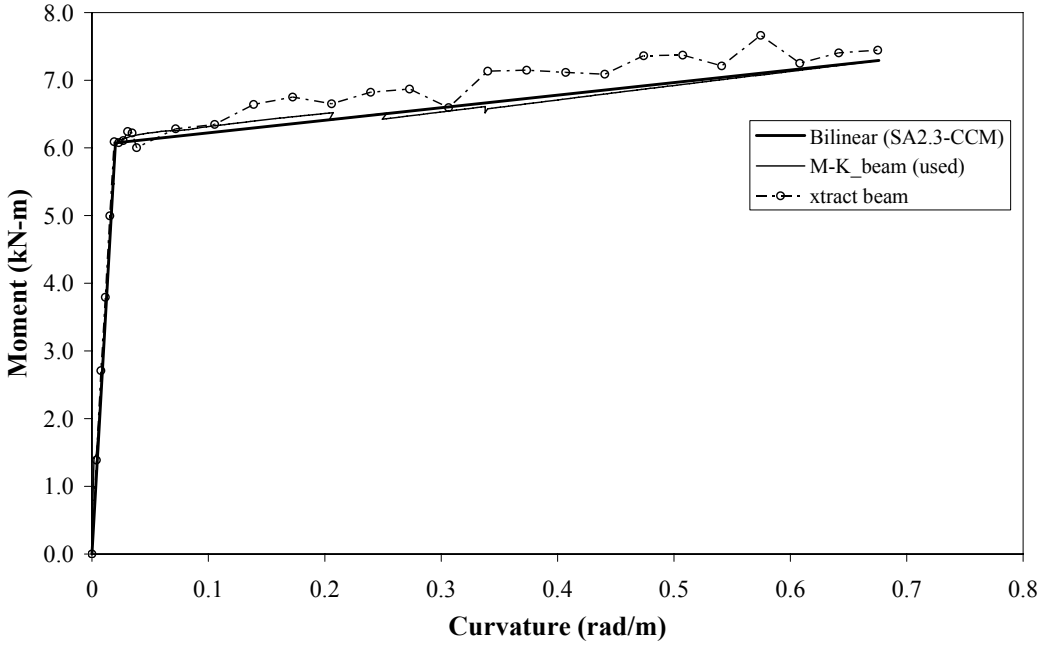

Figure 6.6. Moment Curvature Diagram of the beam of specimen SA2.3-CCM

The plastic hinge length for columns and beams were 50 mm and 75 mm respectively for this plastic hinge type. Presence of inadequate lap splices at the floor levels caused a decrease in the yield moment of the plastic hinges located at the bottom of the columns. Also presence of inadequate lap splices adversely influences curvature ductility. To

account for this fact in the model, curvature ductility at the onset of strength degradation (point C of M3 hinge in Figure 6.3) is assumed to be half of that of the curvature ductility for a column without the lap splice. After attaining ultimate curvature, the moment values decreased gradually.

The V2 shear hinge was defined to account for probable shear failures of the frame members due to poor concrete quality and low transverse steel ratio. A stress-strain relationship was used to define the V2 hinge as shown in Figure 6.3. Since the shear failure is sudden and brittle, a minimal ductility is considered as explained in section 6.4 for each specimen. These hinges were placed at the mid-span of the beams or between M3 and P hinge on the columns. However it should be highlighted that the location is not important for this hinge. Yield stress and yield strain values were determined in accordance with Equation 6.22. Plastic hinge length of this type of plastic hinges was assumed as clear height or length of the frame members. As indicated in Equation 6.22, the effect of transverse reinforcement is not included in the shear capacity calculations because of poorly detailing, and large spacing of the transverse reinforcement (almost equal or very close to the effective depth of the members). Accordingly, a lower bound of the shear capacity excluding the transverse reinforcement is taken into account.

$$\sigma_y = 0.65\, f_{ctk} \;;\; \varepsilon_y = \frac{f_{ctk}}{E_c} \tag{6.22}$$

f_{ctk} : characteristic tensile strength of concrete

E_c : modulus of elasticity of concrete

f_{ck} : characteristic compressive strength of concrete

Observations showed that tension failure of columns (as well as flexural failure) can also occur due to inadequate lap splices under lateral loading. In order to account for this behavior, a P hinge was assigned at the mid-height of the columns. Again, the location of the P hinge is irrelevant, as the axial load is constant along the entire height of a column. Observations showed that presence of FRP on the masonry wall improved the tensile capacity of the columns, or rather, decreased the tensile stress demand on the columns since part of the tension is resisted by the FRP on the masonry infill. In modeling, this

behavior was considered as an equivalent increase in the tensile capacity of the columns. The increase in the capacity highly depended on the orientation of FRP and the number of the layers. Tensile capacity formulation used for each different FRP configuration was given in Equation 6. 23. The capacity loss was found to be related to the aspect ratio (AR) of the frames as indicated in Figure 6.7. P hinge was introduced into the frame members in terms of stress-strain relation and plastic hinge length was taken as the clear height of the columns. The representative diagram is illustrated in Figure 6.7. The descending part of the compression side was gradual and ending at a strain level of 0.012 as can be noticed in Figure 6.4.

$$\sigma_{\max} = \frac{f_s A_s}{A_g} + \frac{\sigma_v A_v}{A_g} + n\frac{\sigma_c A_c}{A_g}\sin\theta_{FRP} \tag{6.23}$$

σ_{max} : ultimate tensile capacity of the tension column

f_s : maximum stress developed at the lap splice region of the column in tension

A_s : the cross sectional area of longitudinal re-bars of the column in tension

A_g : the gross sectional area of the column considered

A_v : the cross sectional area of the effective vertical strips on the infill panel (A_v=0 for SA1.0-CVL)

A_c : the cross sectional area of the effective cross diagonal FRPs on the infill panel

θ_{FRP} : inclination of the cross diagonal FRP with respect to horizontal axis (See Figure B.2)

n : the number of cross diagonals on the infill panel extending from foundation level or bottom beam to the surrounding frame members (n=2 for SA2.3-CCM and 4 for SA2.3-CFM)

In the mathematical model, the upper and lower ends of the frame members were assigned rigid end zones (REZ). However REZs were not assigned the lower ends of the first story columns. In other words, joints are not modeled because flexural deformations observed in the joints were very small compared to the flexural deformations of the frame members.

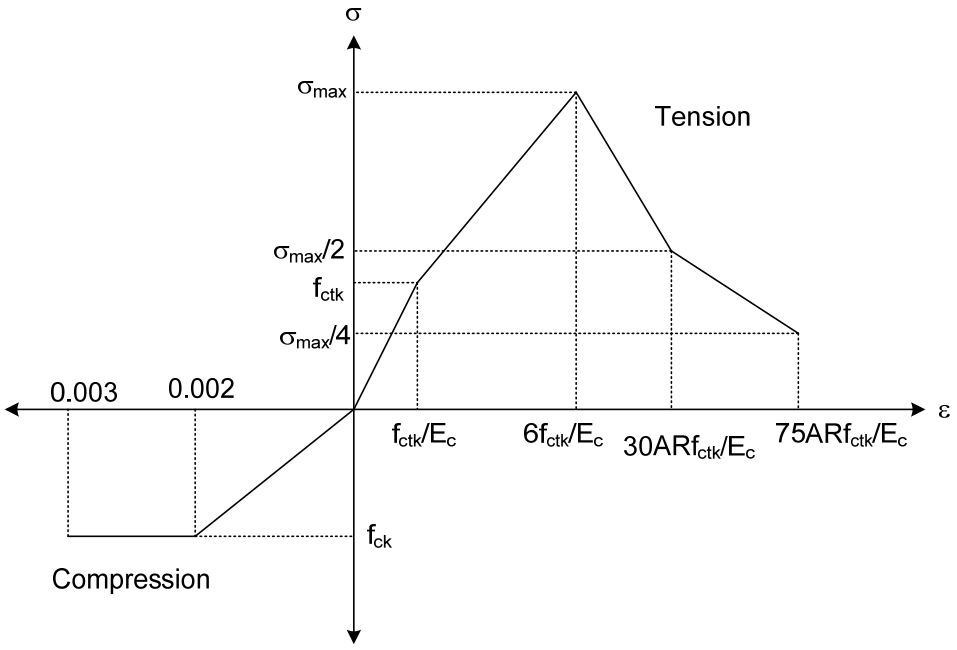

Figure 6.7. Description of tension-compression hinge for the columns (P hinge)

6.2.2. Modeling of Infill Strut

In the literature, there are several infill models. These models were based on either horizontal load-horizontal displacements or axial force-axial deformations. Based on the available models in the literature and the experimental results from this study, a new model for modeling the FRP-strengthened infill panel was proposed. In order to explain the development of the new model, it may be necessary to explain some of the available models in the literature briefly. Fardis and Panagiotakis related the shear force on the masonry infill and lateral displacement of the infill in 1994 [125]. In their model, the effect of FRP was not considered. Multi-linear strut behavior was modeled at four stages as shown in Figure 6.8. As indicated in Equation 6.24, the initial stiffness was obtained by using elastic shear modulus of the infill and the geometry of the infill panel. The cracked stiffness was calculated by using an equivalent strut width. In the numerical model, equivalent diagonal compressive strut concept was used for the application of that infill model.

$$k_0 = \frac{G_w t_w l_w}{h_w} \; ; \; \alpha k_0 = \frac{E_w t_w a}{d} \cos^2\theta \; ; \; V_{cr} = f_{ws} t_w l_w \; ; \; V_{max} = 1.3 V_{cr} \qquad (6.24)$$

G_w : shear modulus obtained from diagonal compressive tests

f_{ws} : shear strength obtained from diagonal compressive tests

l_w : length of the wall

h_w : height of the wall

a : equivalent strut width calculated by using Mainstone's Equation

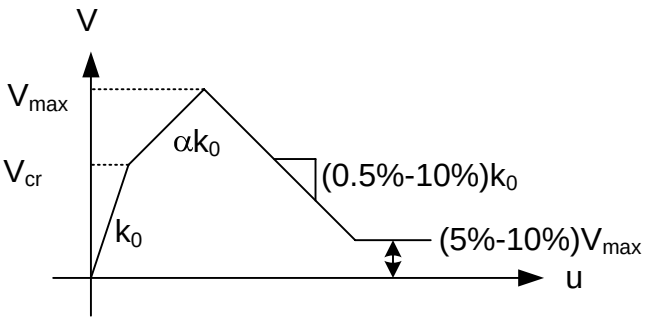

Figure 6.8. Lateral Force-lateral displacement relationship of the infill wall (As recommended by Fardis and Panagiotakis)

Mostafaei and Kabeyasawa [126] proposed a macro-model based on the model proposed by Madan et al. [58]. In that model, the lateral force and lateral displacement relationship of infill panels were established. The model can be implemented into the system by using horizontal and diagonal springs. It is shown that both spring models yielded almost the same response for the same infilled frame. Masonry compression strain at maximum compression stress was assumed as 0.0018. Residual strength was 30% of the maximum lateral force. The details of the model can be found elsewhere [126].

Perera [116] proposed a new infill model and related axial force and axial shortening of the inelastic spring element by introducing a damage variable. Equation 6.10 was used to find the equivalent strut width and initial stiffness prior to cracking.

Al-Chaar et al. proposed an infill model for FRP strengthened infilled frames [110]. They used Mainstone's formulation to find the strut width and the initial stiffness. The net thickness of the infill panel was used as the thickness of the strut. Al-Chaar et al. [110] proposed some stiffness and strength increase factors based on the experiments depending on the number of FRP layers and orientation of the overlays. The capacity of the strut was

the minimum of the crushing strength and the shear strength of the infill in the direction of the strut. The elasto-plastic relation between axial force of the infill and lateral deformation of the infill was defined to determine the behavior of the equivalent strut. In that model, a bilinear pushover curve was obtained and corrected to attain realistic stiffness and displacements to be agreeable with their test results. Al-Chaar et al. [110] used an eccentric equivalent strut to model the infill and extended rigid end offsets (REOs) to a certain distance in order to decrease the flexibility of the mathematical model resulting from the confinement effect provided by the strut to the frame members. Al-Chaar et al. [110] placed plastic hinges where nonlinearities were expected. The locations were generally at the end of frame members and at the middle region of equivalent strut.

El-Dakhakhni [127] proposed a macro model for concrete masonry infilled steel frames failing in corner crushing (CC) mode based on the equivalent compression strut concept. The model does not include shear sliding failure. He used a piecewise linear strut model and three struts. El-Dakhakhni [127] stated that masonry can be assumed as orthotropic because of the minimum shear-compression interaction developed in case of CC failure mode. Based on the assumption of orthotropic behavior of masonry, the material properties in the direction of the strut were determined and the axial stress-axial strain relationship was established. In the model, the effective width of the strut was determined in accordance with Equation 6.19 and kept constant throughout the analysis. The relation between axial stress and axial strain was shown in Figure 6.9. The formulations are given in Equations 6.25 and 6.26. Axial load and displacement values can easily be obtained by multiplying stresses with the area and strains with the length of the strut.

$$f'_{m-\theta} = \frac{E_\theta}{\alpha} \; ; \mathrm{E_p} = 0.5E_\theta \text{ (monotonic loading)}; \mathrm{E_p} = 0.25E_\theta \text{ (cyclic loading)} \qquad (6.25)$$

$$\varepsilon_l = \begin{Bmatrix} \varepsilon_p + 0.002 \text{ for monotonic loading} \\ \varepsilon_p + 0.003 \text{ for cyclic loading} \end{Bmatrix} ; \mathrm{E_d} = \begin{Bmatrix} -0.25E_\theta \text{ for monotonic loading} \\ -0.10E_\theta \text{ for cyclic loading} \end{Bmatrix} \qquad (6.26)$$

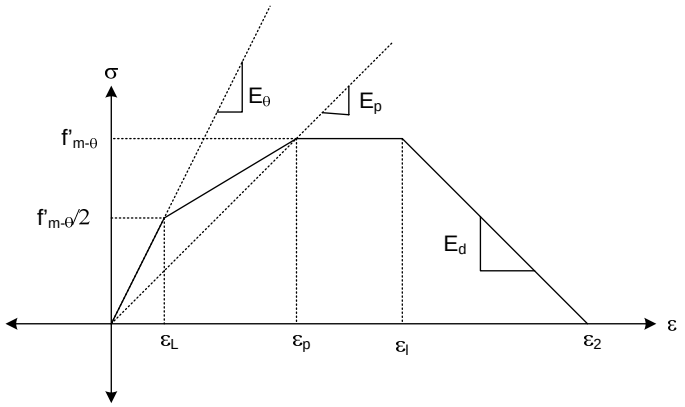

Figure 6.9. Infill model proposed by El-Dakhakhni [127]

On the basis of the observations made in the experimental study, a novel, simple, and practical model was proposed by the author as a function of the aspect ratio effect. In order to better understand this model, some of the previous models were explained briefly in section 6.2.2. In order to develop this model, geometry, material properties, and the effective area of the strut should be determined. Moreover, failure modes of the infill wall should be predicted.

There are various formulations to calculate effective width of the equivalent strut based on empirical, semi-emprical, or finite element approaches [2, 45, 110, and 115]. Some of them were listed in section 6.1. In this study, two formulations which were Durrani et al. [115] and FEMA 356 [95] were compared because the other approaches yielded similar results with these two formulations as indicated in Table 6.1. The nonlinear analyses performed by using these two approaches showed that the formulations which were proposed by Durrani et al. [115] represented the experimental base shear versus roof drift ratio curves better. Thus, it was decided to use the formulations of Durrani et al. [115] to develop the infill wall model. The related diagrams will be presented in the following sections.

Equations 6.10-6.12 were used to calculate the effective width of the diagonal compression strut. This strut width was used to calculate both the elastic stiffness of the masonry panel and the ultimate capacity of the infilled frames. The same approach was also used in the literature by the reference [110]. Based on the rule of mixture, modulus of elasticity and compressive strength of plastered masonry infill were calculated as

illustrated in Chapter 5. To reiterate, compressive strength of the brick prisms were obtained from the prism tests subjected to compression normal to the bed joint and parallel to the cores. Experimental results confirmed that presence of FRP on the infill panel generally improved the behavior in terms of stiffness and strength. In the literature, depending on many factors such as age of the specimens and strength of the mortar, 25%-45% strength increase was reported for FRP strengthened (single sided $0^0/90^0$) brick prism compression tests normal to the bed joint [128]. Test results of this study proved that presence of FRP increased first cracking load. In other words, FRP delayed the cracking of the specimens. Presence of anchorages played an important role to delay cracking. Moreover orientation of FRP, aspect ratio of the infilled frames, the type of infill and FRP and the number of layers affected the first cracking load of the infill panels strengthened with FRP. Based on these observations, modulus of elasticity of the strengthened infills was modified. The modification factor was a function of the frame's aspect ratio and calculated by using Equation 5.26. The modified modulus of elasticity was calculated in accordance with Equation 6.27. There are various approaches to determine the thickness of the equivalent strut. For example, Hakam [98] used the gross thickness of the panel whereas Al-Chaar [110] used the net thickness of the infill panel. In this study gross thickness of the infill wall was used because gross area based material properties were used. Although the strut area decreased as the lateral loads increased [23, 45, 59 and 98], the cross sectional area of the equivalent strut which was the product of the strut width and strut thickness was kept constant throughout the analysis. Equation 6.28 can be used to calculate the equivalent strut area. The constant k is calculated according to Equation 5.26.

$$E_{bmpF} = E_{bmp} \times k \tag{6.27}$$

$$A_{strut} = w_{strut} \times t_{strut} \tag{6.28}$$

A piecewise linear stress-strain relationship was implemented to model the equivalent strut. The same approach was also used by several researchers in the literature [98, 127 and 121]. Once the stress-strain relation was established, axial load-axial deformation relation can easily be derived by multiplying strains and stresses with the initial length of the strut and initial area of the strut respectively. The proposed σ–ε

relation for axial stress-axial strain of the infill wall strengthened with FRP overlays is shown in Figure 6.10.

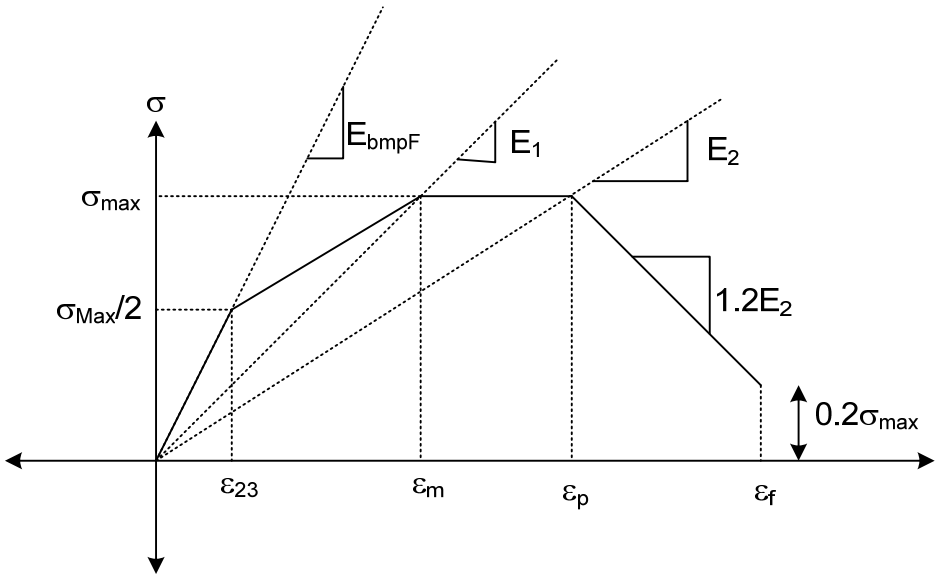

Figure 6.10. Proposed axial stress-axial strain model of the equivalent strut

As indicated in Figure 6.10, initial stiffness can be calculated by using Equation 6.27. Modification factor (k) for the unretrofitted specimens was 1. The most important issue was to calculate the capacity of the equivalent strut. Failure mode becomes very important to calculate the capacity of the equivalent strut. The possible in-plane failure modes based on site observations and experimental studies were; sliding-shear failure, corner crushing due to high stress concentrations at the loaded corners, diagonal tension, diagonal compression [59]. In addition to these failure modes, frame failure modes such as flexural, tensile due to increasing axial forces as a result of truss action, or shear failure modes should also be evaluated to determine overall capacity of the infilled frames. Section 6.2.1 gives the detailed information about frame failures. Experimental failure modes including FRP failures such as anchorage failure, debonding and rupturing of FRPs were explained in Chapter 4 and 5. Among the four failure modes, diagonal tensile cracking can be considered as a serviceability limit state instead of a failure mode because the system continued to carry extra lateral loads. Diagonal cracking occurred due to the principle tensile strains which surpassed cracking strain of the infill panel and started in the center of the infill panel [129]. Diagonal compression failure occurred due to the out of plane

behavior of the infill. It is hard to see this failure mode for infill panels with typical slenderness and height to thickness ratio [59]. As a result, there are mainly two failure modes for infill panels under in plane horizontal forces. Shear-sliding failure load and corner crushing failure load can be calculated in accordance with the equations given in Chapter 5. These equations included the effect of FRP. The minimum value of the maximum shear force resisted by the infill panel in the strut direction ($V_f/\cos\theta$) and diagonal compression failure load (R_c) of the strut established the capacity of the strut as illustrated in Equation 6.29.

$$R_{strut} = \min\begin{Bmatrix} V_f / \cos\theta_{strut} \\ R_c \end{Bmatrix} \tag{6.29}$$

It is a commonly acknowledged fact that there is an interaction between shear and axial compression in the walls. A Mohr-Coulomb type of relation existed between shear strength and axial compression for un-reinforced masonry panels as expressed in Equation 6.30. This equation is valid to a certain axial compression stress prior to cracking. As illustrated in Equation 6.30, initial shear stress is a function of adhesion between the masonry units and mortar increased by a frictional component. Paulay et al. assumed that the frictional component of the Equation 6.30 can be ignored because gravity loads were transferred by bounding frames due to the interface gaps between the infill panel and the frame along the top edge resulting from some problems such as lack of tight construction between panel and frame, shrinkage of the wall and vertical enlargement of the tension column [2]. FEMA 356 also ignored the frictional component in Equation 6.30 and considered only cohesive bond strength excluding shear-friction contribution provided by the compressive strut action. This caused quite conservative infill shear strength values. However, Al-Chaar et al. stated that the product of 20% of the normal stress and the coefficient of friction might be included in the resisting mechanism and added to the bond shear strength [110].

$$\tau = \tau_0 + \mu\sigma_c \tag{6.30}$$

τ_0 : shear stress at zero pre-compression

μ : apparent coefficient of friction along the bed joint

σ_c : vertical compressive stress

Buonopane et al. stated that lateral strength of un-reinforced masonry infill was highly sensitive to the coefficient of friction and recommended the lower bound value of 0.3 for infill shear-friction models which was used to explain strut action [118]. To reiterate, the coefficient of friction was a function of materials used in the masonry wall. Paulay et al. [2] also proposed the value of 0.3 for the coefficient of friction. In this study, based on the previous research, the coefficient of friction of 0.3 was used to calculate the capacity of the equivalent strut given in Equation 6.29.

Apart from ultimate stress, it was necessary to determine the strain corresponding to this stress. Ultimate stress can be calculated by using Equation 6.31. As indicated, ultimate stress was a function of aspect ratio of the frame (L_f/h). The coefficients used in Equation 6.31 were calibrated from the tests. Test results showed that the aspect ratio (AR) influenced the behavior and failure mode considerably. In addition to that, aspect ratio changed the crushing force of the infill panel. These observations showed that it may be possible to state the first crushing strain (ε_0) as a function of the aspect ratio of the frame in an unstrengthened state. The proposed formulation for ε_0 is given in Equation 6.33.

$$\sigma_{\max} = (0.7 + 0.3AR)R_{strut} / A_{strut} \tag{6.31}$$

$$\varepsilon_m = \frac{k\varepsilon_0}{AR} \tag{6.32}$$

$$\varepsilon_0 = 0.0024 \times \ln(\mathrm{AR}) + 0.0011 \tag{6.33}$$

$$\varepsilon_p = 4\varepsilon_m \frac{AR}{(1.4AR - 0.4)} \tag{6.34}$$

In the literature, the ratio between cracking stress and maximum stress was in the range of 0.50 and 0.77 [127 and 125]. Paulay et al. stated that the separation between infill wall and reinforced concrete frame took place at 50%-70% of the ideal lateral shear capacity of the infill wall [2]. Based on those recommendations and observed behavior of

the test specimens, cracking stress was assumed to be half of the maximum stress. The cracking strain can be easily calculated by using the cracking stress and initial modulus of elasticity of the infill panel as shown in Equation 6.35.

$$\varepsilon_{23} = \frac{\sigma_{\max} / 2}{E_{bmpF}} \tag{6.35}$$

In the literature, it was reported that application of FRP to the failure surface of masonry prisms provided pseudo-ductility because FRP kept the cracked specimens together [128]. However Hanoglu [70] stated that void ratio and brittle nature of hollow clay tiles inversely affected ductility of the FRP strengthened masonry. Some researchers proposed a constant value for the length of the horizontal plateau of the axial stress-axial strain diagram of the infill. Based on previous research and the parametric study done in this dissertation, a post peak strain value (ε_p) was proposed as a function of aspect ratio as illustrated in Equation 6.34. If there is no strengthening, the post peak strain (ε_p) and the first crushing strain (ε_m) would be equal to each other. The points defining the stress-strain curves for each specimen will be given in the following sections. It is obvious that the post peak strains of the retrofitted specimens were greater than 0.0045 which was assumed to be the ultimate strain at which FRP could resist, because the failure of the retrofitted infilled frame was triggered by FRP failures such as rupturing, anchorage failure or debonding. This value was obtained from the experiments. Post peak behavior of the infill strut was calibrated by using test results. The negative slope of the curve was suggested as $1.2*E_2$. Although this negative slope was recommended as a function of the initial slope in the literature, it was suggested as a function of the secant modulus of elasticity at post peak strain. When the stress decreased to 20% of the ultimate stress, failure strain of the compression strut was assumed to be reached.

The equivalent strut was modeled as a single strut between two loaded diagonal of the infilled frame. The nonlinearities took place at P hinge which was defined in the middle of the strut. The plastic hinge length of the compression-only spring was the diagonal length of the strut. The compression-only member was released at both ends (M3 release) to allow only axial loads on the member.

6.3. Nonlinear Static Analysis Procedure (Pushover Analysis)

Pushover analysis was carried out for each specimen in order to determine the capacity and the global behavior of the specimens. Pushover analysis is a useful tool for performance based design. In this procedure, the constant vertical loads were first applied followed by the application of lateral loads. Proportional lateral loads were applied in the form of the inverted triangle in accordance with the experimental test set-up. Nonlinear behavior was assured by using plastic hinges. SAP2000 V10 was used to determine performance of the specimens. Application of vertical loads was load controlled unlike the lateral loads. Failure loads and envelope curves of the specimens under increasing horizontal loads were determined. Stress-strain curves and moment curvature relations were used to define the backbone of the plastic hinges which included 5 points (A, B, C, D, and E) as shown in Figures 6.3 and 6.4. User defined nonlinear plastic hinges were used to obtain pushover curves. Cracked section stiffness values determined from the moment curvature relationship were used for the frame members. Rigid end offsets with a rigid zone factor of 1 were defined at the beam-column joint regions to raise the stiffness of the joints.

In order to determine the accuracy of the frame model, the envelope curve obtained by using the pushover analysis was compared to the one obtained experimentally done by Akguzel [71] and after some modifications on the M3 plastic hinges, satisfactory results were obtained. M3 plastic hinges incorporating the effect of lap splices on the column members were used to model the bare frame tested by Akguzel [71]. The comparison between test and model was satisfactory. Then, the infill model was incorporated into the RC frame model by connecting two loaded corners.

The mathematical model is illustrated in Figure 6.11. Rigid end zones are shown with thick lines at the end of the frame members. Equivalent strut which was used to define the infill panel was released at both ends in order to exclude moment effects. In the model, it is assumed that all the plastic deformations are concentrated at the plastic hinges. In other words, lumped plasticity is incorporated. Outside of the plastic hinges, the members are modeled as linear elastic elements.

When an adequate number of plastic hinges develops, a collapse mechanism forms. In the framed structures, failure mechanisms can be grouped as column sway mechanism (soft story failure) which is undesirable, beam sway mechanism and combined mechanism. Strong beam-weak column framed systems which are often seen in Turkey generally lead to story sway mechanisms. In infilled frames, failure modes are various as described before such as corner crushing, shear sliding, diagonal compression and frame failure modes. The formation sequence and location of the plastic hinges determine the type of the sway mechanism.

To model the specimens, it is necessary to assign some properties of the structure to the structural elements such as cross-sections, material properties, hinge properties and loads. To reiterate, proportional lateral loads are increased as the vertical loads are kept constant. Vertical loads were applied prior to the application of lateral loads and the solution for the vertical loads is first obtained. Nonlinearities are given to the structure by using nonlinear hinges (P, V2, M3) as explained before. Base shear versus roof drift envelop curves are developed and compared with the experimental results. Moreover, the sequence of hinge formation can also give some information about the global behavior of the structure such as failure mode, and sway mechanism.

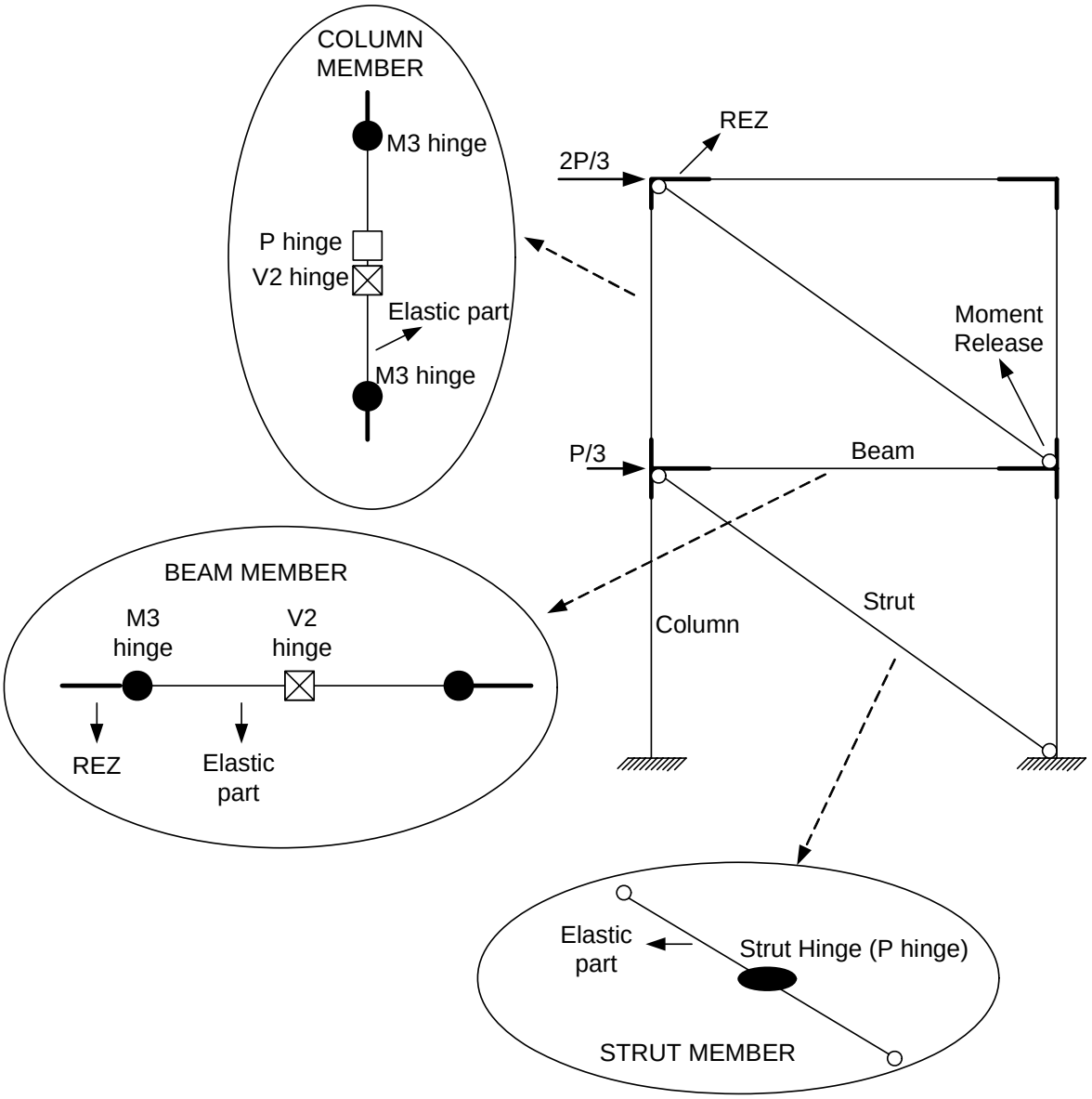

Figure 6.11. Mathematical model of the infilled frames

6.3.1. Comparison of The Capacity Predictions of Masonry Infills

Two methods were used to compare the capacity of the equivalent strut. The first method was proposed by Al-Chaar et al [110]. The second method was based on the proposed formulations given in this chapter. The second method takes into account the effects of the aspect ratio, strengthening scheme and the material properties. As indicated in Table 6.2, the difference between these two methods was clear for the specimens with aspect ratio of 1.0, even though the aspect ratio of the tests performed by Al-Chaar was

about 1.0. One of the reasons for such a difference was the coefficients used in the Al-Chaar method. Stiffness and strength increase factors were derived based on the infill walls which were strengthened on one face only. In this study, FRP was applied on both faces of the infill wall and anchored to the infill wall and the surrounding frame. The second reason might be the cross sectional area and the type of the FRP. As indicated in Table 6.2, the infill capacity ratio of the specimens SA1.7-S and SA2.3-CCM were about 1.0. The ratio between the cross sectional area of the FRP and the length of the infill of these specimens with respect to both methods was comparable. Another reason might be the masonry infill shear strength formulation was based on the cohesive bond of the bed joints and did not include shear-friction contribution provided by the equivalent strut. This effect is much clearer for the un-strengthened infilled frames. In addition, the force in the strut direction depended also on the strut inclination. Since the inclination of the strut was smaller in the Al-Chaar method, the forces in the strut direction tended to be smaller. As can be seen in Table 6.2, proposed method was more appropriate for the procedure for capacity predictions given in Chapter 5.

Table 6.2. Comparison of the equivalent strut forces

Specimens	$\mathbf{R_{strut\text{-}Al\text{-}Chaar}}$	$\mathbf{R_{strut\text{-}Proposed}}$	**Ratio**
SA1.0	37.01	63.70	1.7
SA1.0-CV	44.52	68.74	1.5
SA1.0-C2V	48.18	89.74	1.9
SA1.0-CVL	42.69	57.17	1.3
SA1.7-S	74.00	77.60	1.0
SA2.3	66.53	80.94	1.2
SA2.3-CCM	98.41	98.75	1.0
SA2.3-CV	99.12	91.49	0.9
SA2.3-CFM	94.53	88.59	0.9

6.4. Predicting the Nonlinear Response

The experimental and analytical base shear-roof drift ratio graphs of the specimens were drawn in Figures 6.12-6.20. In order to better understand the envelope curves, the initial stiffness, secant stiffness at peak load, and the areas under the envelope curves were compared. The envelope curves obtained analytically were based on the width calculations

used by Durrani et al. [115] since these width calculations represented the global behavior of the specimens better. The effect of the effective width on the global behavior of the specimens will be discussed in section 6.5.

6.4.1. Specimen SA1.0

The failure mode of specimen SA1.0 was tension failure of the columns at the floor level due to the inadequate lap splices. The numerical simulation produced the same failure mode and the capacity of the specimen was well-predicted. Nonlinear hinge properties used for pushover analysis are submitted in Table 6.3. After the peak load, the behavior could not be predicted accurately as indicated in Figure 6.12 indicating that the parameters selected to represent the post peak load deformation behavior (points D and E in Figure 6.4) are not very suitable for this specimen. The analytically obtained initial stiffness and secant stiffness at the peak load of the specimen SA1.0 were 26.4 kN/mm and 17.6 kN/mm respectively. The areas under experimental and numerical envelope curves were 0.177 kNmm/mm and 0.112 kNmm/mm. The experimental values corresponding to the residual strength of the specimens were not used to calculate area under the envelope curve. Initial stiffness and stiffness at peak load of the experimentally obtained envelope curve were 34.2 kN/mm and 13.77 kN/mm respectively. The calculation of these values was given in Chapter 5. To reiterate, these values were obtained by using positive and negative peaks of the same cycle. The behavior up to the peak load was satisfactorily reproduced by using pushover analysis.

Table 6.3. Nonlinear hinge properties of specimen SA1.0

SPECIMEN: SA1.0	*A*	*B [B']*	*C [C']*	*D [D']*	*E [E']*	*Yield Values*
Column (M3 @ bottom) (Type: Moment-Curvature) (Units: kN,mm)	(0;0)	(0;1)	(20.5;1)	(41;0.85)	(82;0.3)	(1.58E-5;1040)
Column (M3 @ top) (Type: Moment-Curvature) (Units: kN,mm)	(0;0)	(0;1)	(41.3;1.09)	(82;0.85)	(164;0.3)	(4.40E-5;2898)
Beam (M3) (Type: Moment-Curvature) (Units: kN,mm)	(0;0)	(0;1)	(35.2;1.31)	(70;0.65)	(140;0.3)	(2.70E-5;6020)
Column P hinge (Type: Stress-Strain) (Units: kN,mm)	(0;0)	(0;1) [0;-1]	(6;1.67) [-1.5;-1]	(30;0.84) [-2.5;-0.75]	(75;0.42) [-6;-0.25]	(4.30E-5;9.9E-4) [-0.002;-0.008]
Column V2 hinge (Type: Stress-Strain) (Units: kN,mm)	(0;0)	(0;1)	(1.5;1.0)	(1.5;0.2)	(2;0.2)	(4.30E-5;6.4E-4)
Beam V2 hinge (Type: Stress-Strain) (Units: kN,mm)	(0;0)	(0;1)	(1.5;1.0)	(1.5;0.2)	(2;0.2)	(4.30E-5;6.4E-4)
Strut P hinge (Type: Stress-Strain) (Units: kN,mm)	(0;0)	(0;1)	(4.6;2)	(4.6;2)	(7.7;0.4)	(2.4E-4;0.00165)

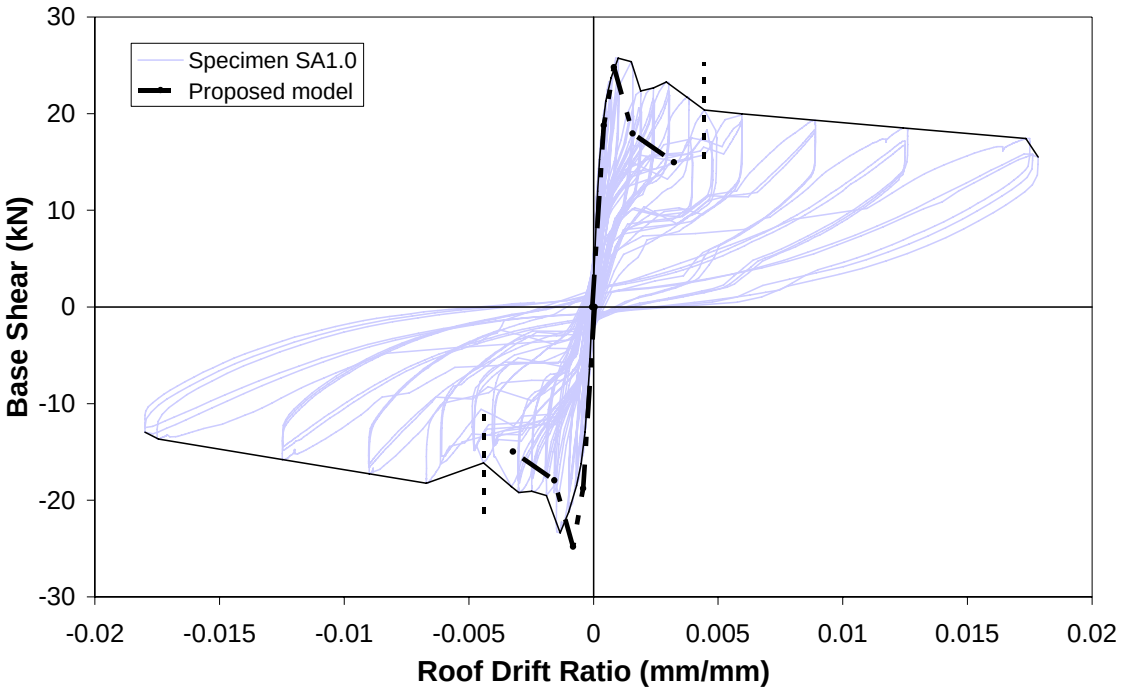

Figure 6.12 Base shear versus roof drift diagram for specimen SA1.0

6.4.2. Specimen SA1.0-CV

Tensile failure of the columns and rupturing of vertical FRPs resulted in failure of the specimen. Rupturing of FRP caused severe strength degradation and the pre-peak and post-peak behavior was satisfactorily obtained. The similarity between backbone curve of the test specimen and nonlinear model of the equivalent strut was due to the fact that strengthened infill properties governed the failure mode. Failure of the strut resulted in sudden strength degradation as shown in Figure 6.13. Thus, depending on the aspect ratio, strengthening of the infilled frame with FRP shifted failure mode and failure load as well as the behavior of the specimen as illustrated in Figures 6.12 and 6.13. Nonlinear hinge properties of specimen SA1.0-CV used for pushover analysis are submitted in Table 6.4. When experimental and analytical envelopes were compared, the first cracking loads were quite close to each other. The first cracking load was observed as 21.2 kN. In the model, the first stiffness change occurred at a load level of 17.7 kN. However this stiffness change was not significant. The significant stiffness change was at a load level of 25.7 kN. The ratio between analytical and experimental first cracking loads was 0.84. The model slightly underestimated the first cracking load. Initial stiffness and stiffness at peak load of the analytically obtained envelope curve were 28.7 kN/mm and 4.6 kN/mm respectively. The experimentally obtained values were 31.64 kN/mm and 4.64 kN/mm respectively. As indicated, initial stiffness and stiffness at peak load can be represented by the accepted width values satisfactorily. To reiterate, experimental stiffness values covered the cyclic effects unlike the analytical calculations. That might be one of the reasons for the differences between analytical and experimental values. The area under the experimentally and analytically obtained envelope curves were 0.996 kNmm/mm and 0.980 kNmm/mm respectively. These numbers were an indicator for the dissipated energy. It should be kept in mind that these numbers were obtained from base shear-roof drift ratio graphs. Thus they did not represent dissipated energy but they showed dissipated energies relative to each other. The results of this specimen showed that pushover analysis and proposed model can satisfactorily predict the behavior including post peak strength degradation.

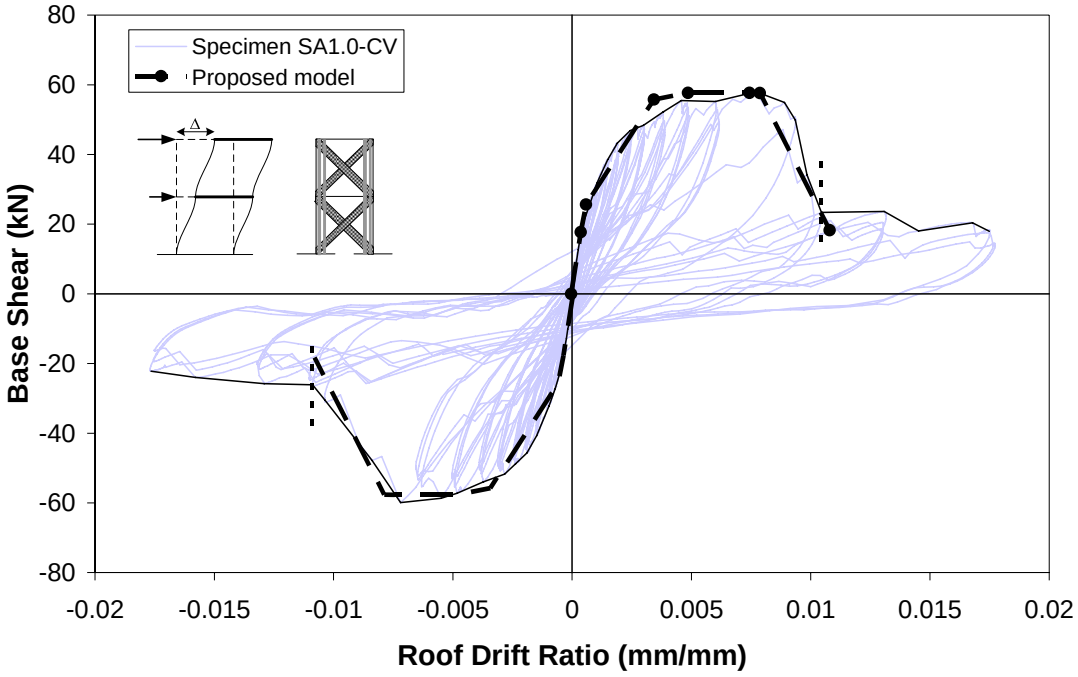

Figure 6.13 Base shear versus roof drift diagram for specimen SA1.0-CV

Table 6.4. Nonlinear hinge properties of specimen SA1.0-CV

SPECIMEN: SA1.0-CV	*A*	*B [B']*	*C [C']*	*D [D']*	*E [E']*	*Yield Values*
Column (M3 @ bottom) (Type: Moment-Curvature) (Units: kN,mm)	(0;0)	(0;1)	(15;1)	(30;0.85)	(60;0.3)	(1.74E-5;1176)
Column (M3 @ top) (Type: Moment-Curvature) (Units: kN,mm)	(0;0)	(0;1)	(20;1)	(40;0.85)	(80;0.3)	(3.17E-5;2150)
Beam (M3) (Type: Moment-Curvature) (Units: kN,mm)	(0;0)	(0;1)	(41.5;1.3)	(83;0.65)	(160;0.3)	(2.20E-5;5930)
Column P hinge (Type: Stress-Strain) (Units: kN,mm)	(0;0)	(0;1) [0;-1]	(6;5.87) [-1.5;-1]	(30;2.94) [-2.5;-0.75]	(75;1.47) [-6;-0.25]	(4.4E-5;1.04E-3) [-0.002;-0.0089]
Column V2 hinge (Type: Stress-Strain) (Units: kN,mm)	(0;0)	(0;1)	(1.5;1.0)	(1.5;0.2)	(2;0.2)	(4.40E-5;6.8E-4)
Beam V2 hinge (Type: Stress-Strain) (Units: kN,mm)	(0;0)	(0;1)	(1.5;1.0)	(1.5;0.2)	(2;0.2)	(4.40E-5;6.8E-4)
Strut P hinge (Type: Stress-Strain) (Units: kN,mm)	(0;0)	(0;1)	(7.2;2)	(28.9;2)	(48.2;0.4)	(2.3E-4;1.73E-3)

6.4.3. Specimen SA1.0-C2V

Experimental failure mode of this specimen was in the form of shear sliding at mid-height. Strut behavior governed the behavior of the specimen in the model. Thus the failure mode of the model was the same as the test specimen. To reiterate, the capacity of the equivalent strut was calculated based on the failure modes described in the previous chapter. Nonlinear hinge properties of specimen SA1.0-C2V used for pushover analysis are submitted in Table 6.5. The failure loads of the model and test were almost the same. Thus the proposed model was able to predict the capacity of the specimen SA1.0-C2V. Figure 6.14 depicted both experimental and analytical base shear roof drift ratio graphs. Initial stiffness and stiffness at peak load of the model were 34.40 kN/mm and 7.95 kN/mm respectively. Those values for the test were 35.63 kN/mm and 6.13 kN/mm. The stiffness values of the proposed model and test were comparable. The areas under the envelope curves of the model and test were 1.29 kNmm/mm and 1.43 kNmm/mm respectively. The ratio was 0.90. One of the reasons for the difference might be the behavior of the specimen after peak load. The model did not include partial rupture of the FRPs. This behavior increased the dissipated energy. Moreover, the last point on the envelope of the test specimen which was shown as thin dashed lines in Figure 6.14 was selected so that the residual load was stabilized. Due to the material models, the strength loss was sudden in the model. In contrary, the specimen exhibited more energy in the post failure zone. The first cracking load of the test was 34.8 kN. The significant stiffness change of the model occurred at a load level of 33.5 kN. These two values were quite close to each other. In the model, however, the first hinge formation occurred at a load level of 26.9 kN. The ratio between the first cracking loads was 0.77 when the value of 26.9 kN was accepted as the first cracking load of the model.

Table 6.5. Nonlinear hinge properties of specimen SA1.0-C2V

SPECIMEN: SA1.0-C2V	*A*	*B [B']*	*C [C']*	*D [D']*	*E [E']*	*Yield Values*
Column (M3 @ bottom) (Type: Moment-Curvature) (Units: kN,mm)	(0;0)	(0;1)	(8.5;1)	(17;0.85)	(34;0.3)	(1.9E-5;1680)
Column (M3 @ top) (Type: Moment-Curvature) (Units: kN,mm)	(0;0)	(0;1)	(17;1)	(34;0.85)	(68;0.3)	(3.67E-5;3240)
Beam (M3) (Type: Moment-Curvature) (Units: kN,mm)	(0;0)	(0;1)	(32.2;1.19)	(64;0.60)	(128;0.3)	(2.0E-5;6080)
Column P hinge (Type: Stress-Strain) (Units: kN,mm)	(0;0)	(0;1) [0;-1]	(6;5.97) [-1.5;-1]	(30;3) [-2.5;-0.75]	(75;1.5) [-6;-0.25]	(5.3E-5;1.44E-3) [-0.002;-0.0169]
Column V2 hinge (Type: Stress-Strain) (Units: kN,mm)	(0;0)	(0;1)	(1.5;1.0)	(1.5;0.2)	(2;0.2)	(5.30E-5;9.4E-4)
Beam V2 hinge (Type: Stress-Strain) (Units: kN,mm)	(0;0)	(0;1)	(1.5;1.0)	(1.5;0.2)	(2;0.2)	(5.30E-5;9.4E-4)
Strut P hinge (Type: Stress-Strain) (Units: kN,mm)	(0;0)	(0;1)	(6.6;2)	(26.4;2)	(44;0.4)	(2.5E-4;0.00219)

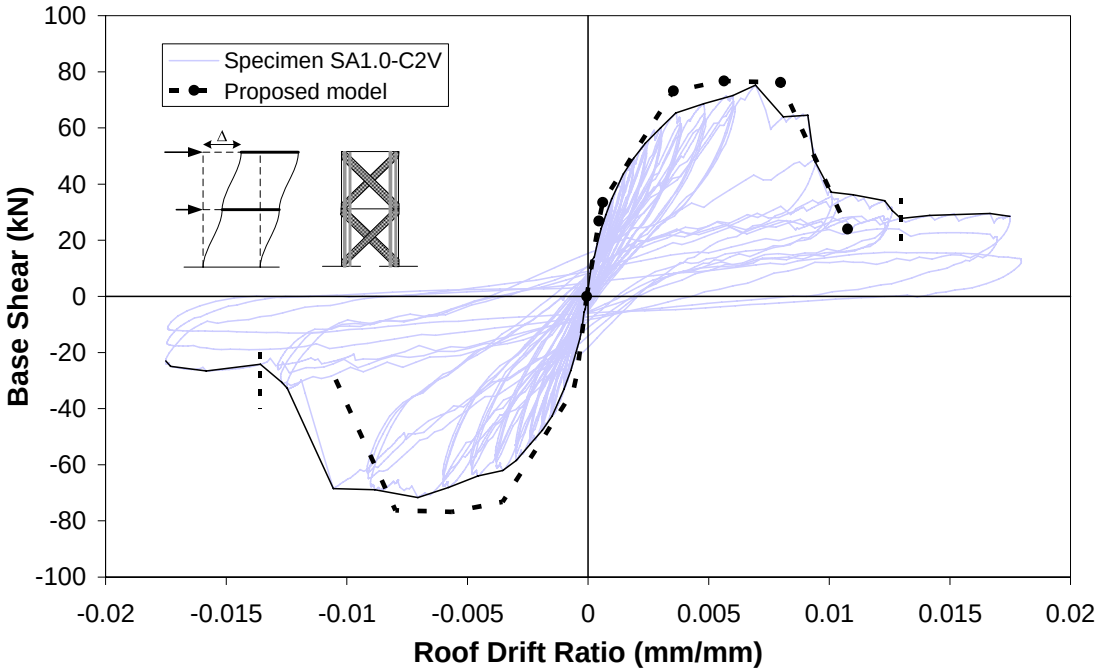

Figure 6.14. Base shear versus roof drift diagram for specimen SA1.0-C2V

6.4.4. Specimen SA1.0-CVL

Base shear versus roof drift ratio graphs of the model and test of specimen SA1.0-CVL are shown in Figure 6.15. The peak loads of the model and the test were 55.3 kN and 60.8 kN respectively. The model predicted failure mode as shear sliding type of failure which was observed failure mode. Nonlinear hinge properties of specimen SA1.0-CVL used for pushover analysis are submitted in Table 6.6. The first cracking load of the model and the test were 21.2 kN and 26.8 kN respectively. The ratio was 0.79. The initial stiffness and stiffness at peak load of the model were 35.65 kN/mm and 4.36 kN/mm respectively whereas those values for the test specimen were 31.25 kN/mm and 3.83 kN/mm. The model overestimated the stiffness values. In addition, the lateral displacement capacity of the model was also smaller than that of the test as illustrated in Figure 6.15. The areas under envelope curves of the model and test were 0.92 kNmm/mm and 1.31 kNmm/mm respectively. The pseudo-ductility was not obtained by the model successfully. It may be due to the fact that the model did not consider local effects and the failure was sudden following the failure of the equivalent strut. In other words the proposed model did not consider partial rupturing of the FRPs observed in the test.

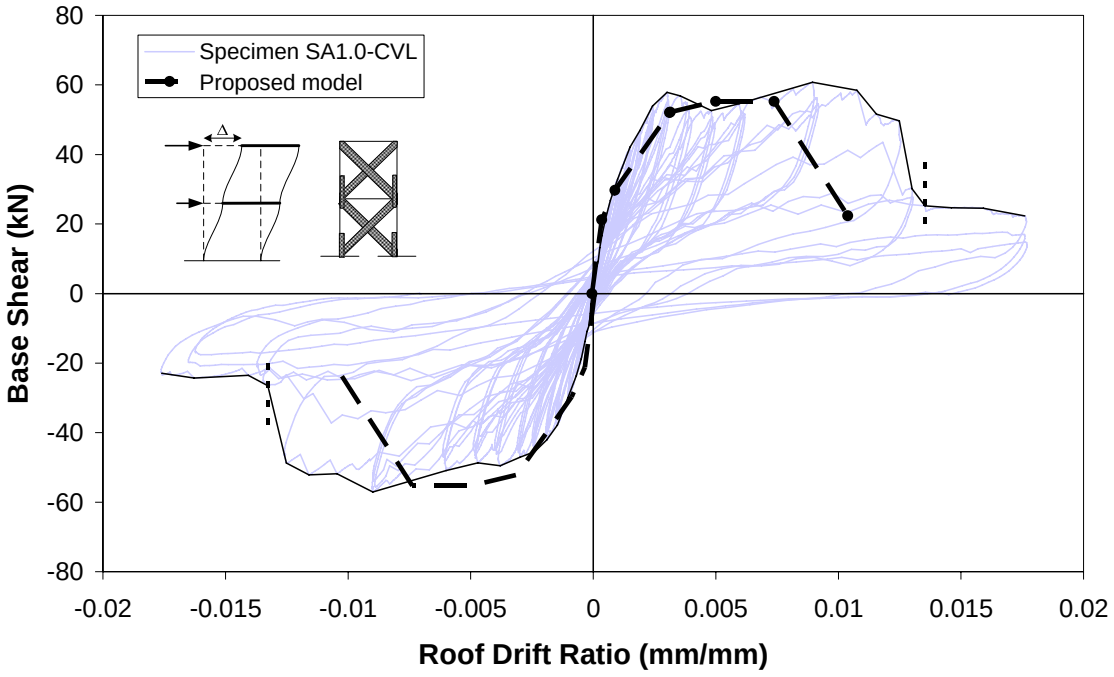

Figure 6.15. Base shear versus roof drift diagram for specimen SA1.0-CVL

Table 6.6. Nonlinear hinge properties of specimen SA1.0-CVL

SPECIMEN: SA1.0-CVL	*A*	*B [B']*	*C [C']*	*D [D']*	*E [E']*	*Yield Values*
Column (M3 @ bottom) (Type: Moment-Curvature) (Units: kN,mm)	(0;0)	(0;1)	(8.6;1)	(17;0.85)	(34;0.3)	(2.81E-5;2390)
Column (M3 @ top) (Type: Moment-Curvature) (Units: kN,mm)	(0;0)	(0;1)	(17.3;1)	(35;0.85)	(70;0.3)	(3.75E-5;3190)
Beam (M3) (Type: Moment-Curvature) (Units: kN,mm)	(0;0)	(0;1)	(16.3;1.06)	(32;0.53)	(64;0.3)	(2.07E-5;6190)
Column P hinge (Type: Stress-Strain) (Units: kN,mm)	(0;0)	(0;1) [0;-1]	(6;4.4) [-1.5;-1]	(30;2.2) [-2.5;-0.75]	(75;1.1) [-6;-0.25]	(5.1E-5;1.37E-3) [-0.002;-0.0153]
Column V2 hinge (Type: Stress-Strain) (Units: kN,mm)	(0;0)	(0;1)	(1.5;1.0)	(1.5;0.2)	(2;0.2)	(5.1E-5;8.9E-4)
Beam V2 hinge (Type: Stress-Strain) (Units: kN,mm)	(0;0)	(0;1)	(1.5;1.0)	(1.5;0.2)	(2;0.2)	(5.1E-5;8.9E-4)
Strut P hinge (Type: Stress-Strain) (Units: kN,mm)	(0;0)	(0;1)	(10.6;2)	(42.2;2)	(70.4;0.4)	(1.5E-4;0.00140)

6.4.5. Specimen SA1.7-S

The failure of this specimen was due to rocking and sliding at the mid-height and shear and tensile failure of the columns. Thus a mixed failure was observed. In the model, failure of the strut and flexural hinging at the column bottoms were noticed. The comparison of the model and test envelope curves was shown in Figure 6.16. The thin dashed lines represented the last points of the experimental envelope curves to calculate the area under the backbone curve. The model predicted the capacity of the specimen satisfactorily. Nonlinear hinge properties of specimen SA1.7-S used for pushover analysis are submitted in Table 6.7. Initial stiffness and stiffness at the peak load of the model were 36.29 kN/mm and 8.63 kN/mm respectively whereas those values for the test specimen were 64.79 kN/mm and 7.33 kN/mm. The areas under the backbone curves of the model and test were 1.34 kNmm/mm and 1.80 kNmm/mm respectively. First cracking load of the model and test were 31.6 kN and 36 kN respectively. Stiffness change between first and

second steps was quite different than that between the second and third steps because the first hinging occurred on the frame whereas the third hinging occurred on the strut. This fact was indicative of how the retrofitted infill affected the behavior of the FRP strengthened masonry infilled RC frames.

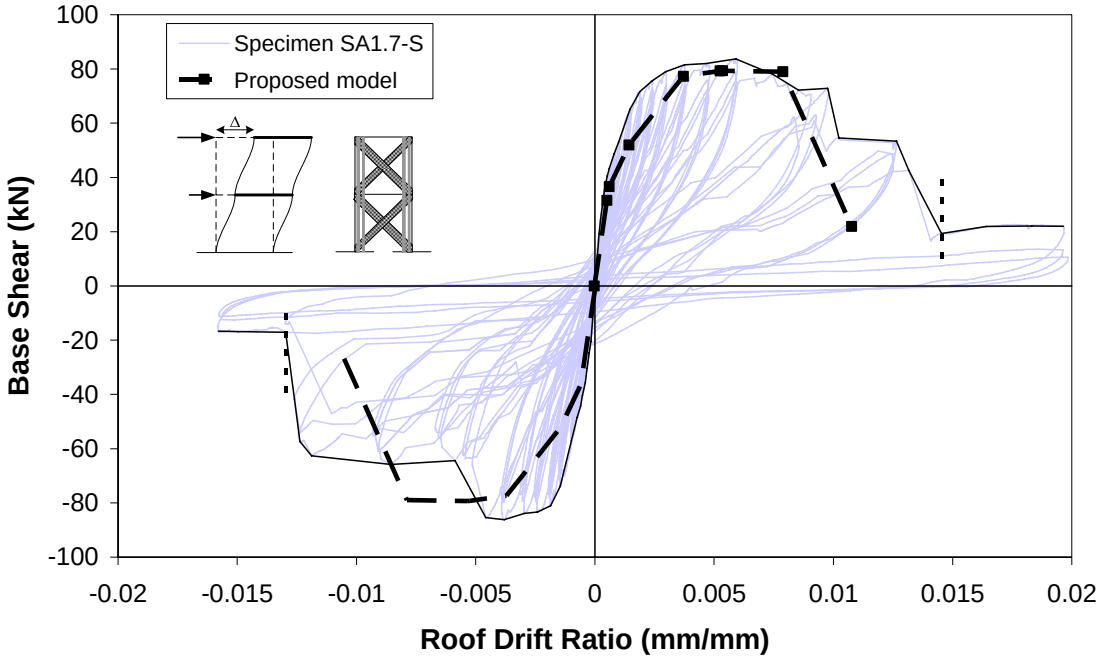

Figure 6.16. Base shear versus roof drift diagram for specimen SA1.7-S

Table 6.7. Nonlinear hinge properties of specimen SA1.7-S

SPECIMEN: SA1.7-S	*A*	*B [B']*	*C [C']*	*D [D']*	*E [E']*	*Yield Values*
Column (M3 @ bottom) (Type: Moment-Curvature) (Units: kN,mm)	(0;0)	(0;1)	(10;1)	(20;0.85)	(40;0.3)	(1.6E-5;1160)
Column (M3 @ top) (Type: Moment-Curvature) (Units: kN,mm)	(0;0)	(0;1)	(12;1)	(24;0.85)	(48;0.3)	(3.16E-5;2260)
Beam (M3) (Type: Moment-Curvature) (Units: kN,mm)	(0;0)	(0;1)	(40;1.3)	(80;0.65)	(160;0.3)	(2.25E-5;5970)
Column P hinge (Type: Stress-Strain) (Units: kN,mm)	(0;0)	(0;1) [0;-1]	(6;4.86) [-1.5;-1]	(51;2.33) [-2.5;-0.75]	(128;1.15) [-6;-0.25]	(4.6E-5;1.12E-3) [-0.002;-0.0102]
Column V2 hinge (Type: Stress-Strain) (Units: kN,mm)	(0;0)	(0;1)	(1.5;1.0)	(1.5;0.2)	(2;0.2)	(4.60E-5;7.3E-4)
Beam V2 hinge (Type: Stress-Strain) (Units: kN,mm)	(0;0)	(0;1)	(1.5;1.0)	(1.5;0.2)	(2;0.2)	(4.60E-5;7.3E-4)
Strut P hinge (Type: Stress-Strain) (Units: kN,mm)	(0;0)	(0;1)	(6.4;2)	(21.8;2)	(36.4;0.4)	(2.6E-4;0.00177)

6.4.6. Specimen SA2.3

Figure 6.17 shows the base shear versus roof drift ratio graphs of the model and test. Nonlinear hinge properties of specimen SA2.3 used for pushover analysis are submitted in Table 6.8. The test specimen suffered from corner crushing and excessive flexural cracks. The failure mode of the model was tensile failure of the column followed by flexural hinging indicating excessive flexural cracks. Peak load of the specimen which was 51 kN was overestimated by the model. Initial stiffness and stiffness at peak load for the model were 28.3 kN/mm and 22.2 kN/mm respectively whereas the corresponding stiffness values for the test specimen were 165.05 kN/mm and 16.48 kN/mm respectively. The reason why initial and secant stiffness values were not attained might be the failure mode. The areas under the envelope curves for the model and the test were 0.351 kNmm/mm and 0.306 kNmm/mm respectively. The difference was mainly due to the fact that the peak load was not attained. First cracking load was overestimated for this specimen which might be due to the failure mode of the model.

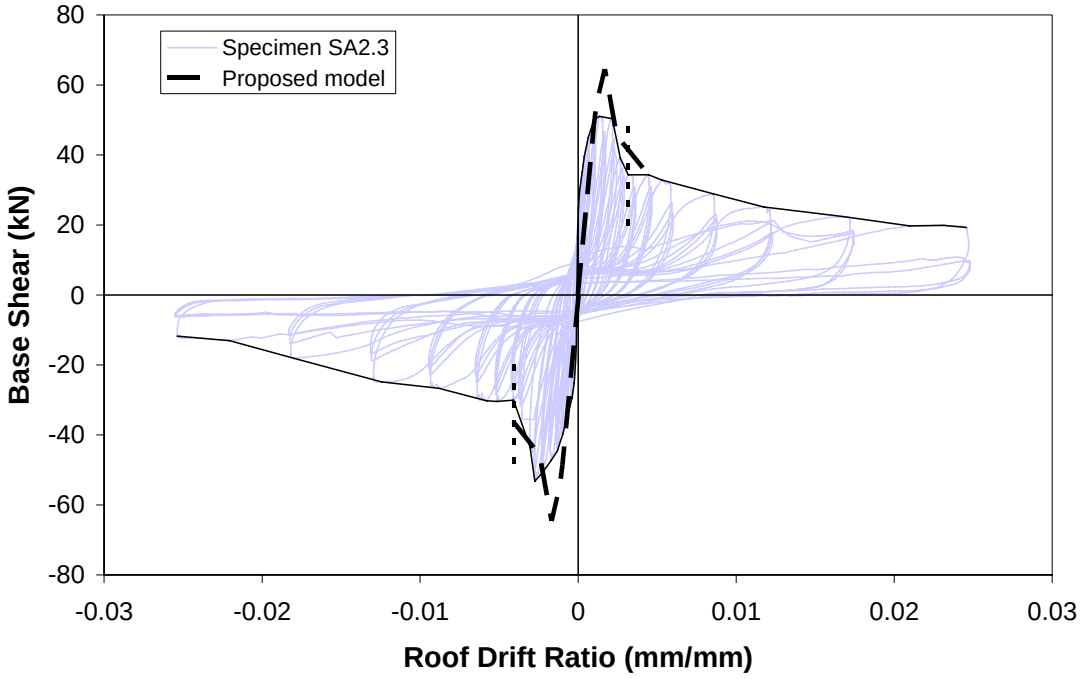

Figure 6.17. Base shear versus roof drift diagram for specimen SA2.3

Table 6.8. Nonlinear hinge properties of specimen SA2.3

SPECIMEN: SA2.3	*A*	*B [B']*	*C [C']*	*D [D']*	*E [E']*	*Yield Values*
Column (M3 @ bottom) (Type: Moment-Curvature) (Units: kN,mm)	(0;0)	(0;1)	(10.2;1)	(20;0.85)	(40;0.3)	(1.69E-5;1260)
Column (M3 @ top) (Type: Moment-Curvature) (Units: kN,mm)	(0;0)	(0;1)	(20.4;1)	(40;0.85)	(80;0.3)	(4.05E-5;3020)
Beam (M3) (Type: Moment-Curvature) (Units: kN,mm)	(0;0)	(0;1)	(41.4;1.3)	(82;0.65)	(164;0.3)	(2.17E-5;5950)
Column P hinge (Type: Stress-Strain) (Units: kN,mm)	(0;0)	(0;1) [0;-1]	(6;1.66) [-1.5;-1]	(69;0.83) [-2.5;-0.75]	(173;0.41) [-6;-0.25]	(4.7E-5;1.16E-3) [-0.002;-0.011]
Column V2 hinge (Type: Stress-Strain) (Units: kN,mm)	(0;0)	(0;1)	(1.5;1.0)	(1.5;0.2)	(2;0.2)	(4.7E-5;7.5E-4)
Beam V2 hinge (Type: Stress-Strain) (Units: kN,mm)	(0;0)	(0;1)	(1.5;1.0)	(1.5;0.2)	(2;0.2)	(4.7E-5;7.5E-4)
Strut P hinge (Type: Stress-Strain) (Units: kN,mm)	(0;0)	(0;1)	(3;2)	(3;2)	(5;0.4)	(4.5E-4;0.00254)

6.4.7. Specimen SA2.3-CCM

Shear sliding type of failure was observed in the test as explained in chapter 4. The model captured this failure mode as well as failure load satisfactorily. Base shear versus roof drift diagram of specimen SA2.3-CCM is shown in Figure 6.18. Nonlinear hinge properties of specimen SA2.3-CCM used for pushover analysis are submitted in Table 6.9. Initial stiffness and secant stiffness at the peak load for the model were 36.0 kN/mm and 11.5 kN/mm respectively whereas initial stiffness and stiffness at peak load of the experimentally obtained envelop curve were calculated as 204 kN/mm and 13.4 kN/mm respectively. The model was unable to predict the initial stiffness satisfactorily. Stiffness at peak load of the model was close to that of the test. The areas under envelope curves for the model and test were 2.50 kNmm/mm and 2.27 kNmm/mm. The ratio was about 1.1. First cracking load of the model and test were 60.8 kN and 49.7 kN respectively. The model for this specimen was satisfactory for the quick evaluation process considering the capacity and post peak degradation.

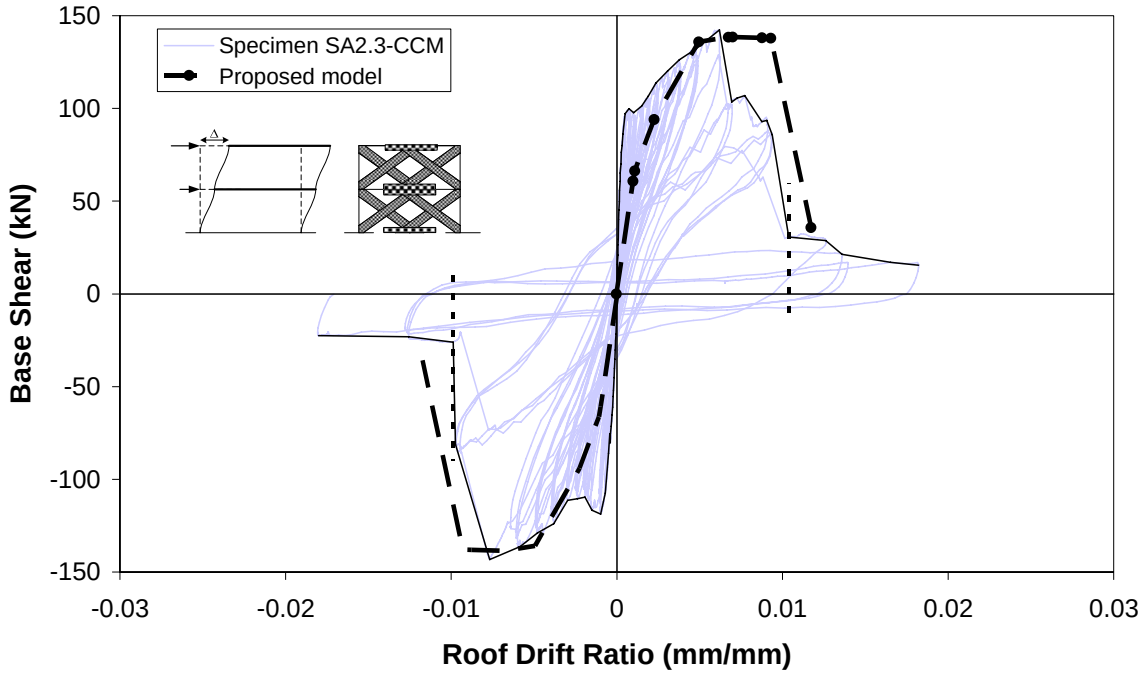

Figure 6.18. Base shear versus roof drift diagram for specimen SA2.3-CCM

Table 6.9. Nonlinear hinge properties of specimen SA2.3-CCM

SPECIMEN: SA2.3-CCM	*A*	*B [B']*	*C [C']*	*D [D']*	*E [E']*	*Yield Values*
Column (M3 @ bottom) (Type: Moment-Curvature) (Units: kN,mm)	(0;0)	(0;1)	(8.5;1)	(17;0.85)	(34;0.3)	(1.86E-5;1620)
Column (M3 @ top) (Type: Moment-Curvature) (Units: kN,mm)	(0;0)	(0;1)	(16;1)	(32;0.85)	(64;0.3)	(3.6E-5;3180)
Beam (M3) (Type: Moment-Curvature) (Units: kN,mm)	(0;0)	(0;1)	(33.5;1.2)	(67;0.6)	(134;0.3)	(2.02E-5;6070)
Column P hinge (Type: Stress-Strain) (Units: kN,mm)	(0;0)	(0;1) [0;-1]	(6;4.55) [-1.5;-1]	(69;2.25) [-2.5;-0.75]	(173;1.12) [-6;-0.25]	(5.2E-5;1.4E-3) [-0.002;-0.016]
Column V2 hinge (Type: Stress-Strain) (Units: kN,mm)	(0;0)	(0;1)	(1.5;1.0)	(1.5;0.2)	(2;0.2)	(5.2E-5;9.1E-4)
Beam V2 hinge (Type: Stress-Strain) (Units: kN,mm)	(0;0)	(0;1)	(1.5;1.0)	(1.5;0.2)	(2;0.2)	(5.2E-5;9.1E-4)
Strut P hinge (Type: Stress-Strain) (Units: kN,mm)	(0;0)	(0;1)	(3.7;2)	(11.9;2)	(19.9;0.4)	(4.2E-4;0.00316)

6.4.8. Specimen SA2.3-CV

In the test, rupturing of FRPs on the masonry infill panel caused severe strength degradation and shell loss of the masonry as well as gravity collapse of the column in the extreme case. The model predicted failure mode as shear sliding and excessive rotations of the columns. The model overestimated peak load 16% as shown in Figure 6.19. Nonlinear hinge properties of specimen SA2.3-CV used for pushover analysis are submitted in Table 6.10. Initial and secant stiffness values for the model were 31.4 kN/mm and 10.5 kN/mm respectively. However, the initial and secant stiffness values for the test were 171.14 kN/mm and 8. 21 kN/mm respectively. Unlike the initial stiffness, stiffness at peak load was captured satisfactorily. First cracking loads for the model and test were 58.6 kN and 48.1 kN respectively. The ratio was 1.22. The areas under envelope curves for the model and test were 2.23 kNmm/mm and 1.75 kNmm/mm respectively. The difference was mainly due to overestimation of the peak load.

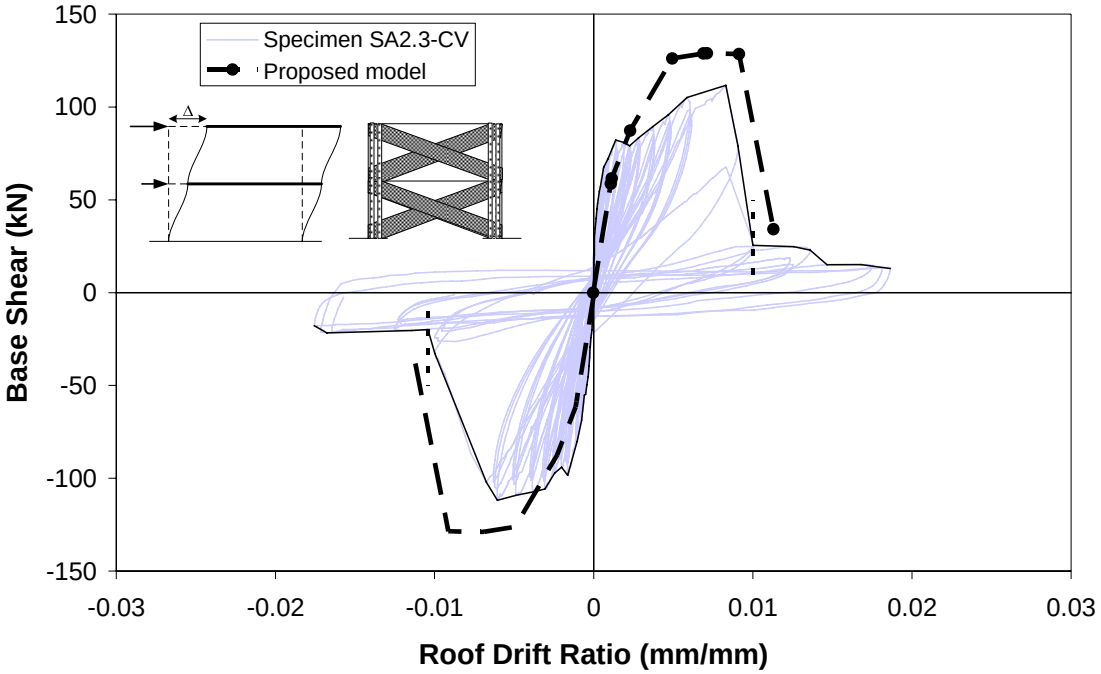

Figure 6.19. Base shear versus roof drift diagram for specimen SA2.3-CV

Table 6.10. Nonlinear hinge properties of specimen SA2.3-CV

SPECIMEN: SA2.3-CV	*A*	*B [B']*	*C [C']*	*D [D']*	*E [E']*	*Yield Values*
Column (M3 @ bottom) (Type: Moment-Curvature) (Units: kN,mm)	(0;0)	(0;1)	(9;1)	(18;0.85)	(36;0.3)	(1.86E-5;1590)
Column (M3 @ top) (Type: Moment-Curvature) (Units: kN,mm)	(0;0)	(0;1)	(17.6;1)	(35;0.85)	(70;0.3)	(3.7E-5;3170)
Beam (M3) (Type: Moment-Curvature) (Units: kN,mm)	(0;0)	(0;1)	(33.7;1.2)	(67;0.6)	(134;0.3)	(2.02E-5;6060)
Column P hinge (Type: Stress-Strain) (Units: kN,mm)	(0;0)	(0;1) [0;-1]	(6;3.95) [-1.5;-1]	(69;1.98) [-2.5;-0.75]	(173;0.99) [-6;-0.25]	(5.2E-5;1.39E-3) [-0.002;-0.0158]
Column V2 hinge (Type: Stress-Strain) (Units: kN,mm)	(0;0)	(0;1)	(1.5;1.0)	(1.5;0.2)	(2;0.2)	(5.2E-5;9.0E-4)
Beam V2 hinge (Type: Stress-Strain) (Units: kN,mm)	(0;0)	(0;1)	(1.5;1.0)	(1.5;0.2)	(2;0.2)	(5.2E-5;9.0E-4)
Strut P hinge (Type: Stress-Strain) (Units: kN,mm)	(0;0)	(0;1)	(3.3;2)	(10.7;2)	(17.9;0.4)	(4.5E-4;0.00288)

6.4.9. Specimen SA2.3-CFM

Shear sliding type of failure was observed in both model and test. The thin dashed lines in Figure 6.20 represented the last points to calculate the areas under backbone curve of the test. The difference between predicted and observed peak loads was about 8%. Nonlinear hinge properties of specimen SA2.3-CFM used for pushover analysis are submitted in Table 6.11. The areas under the envelope curves for the model and test were 2.31 kNmm/mm and 2.75 kNmm/mm respectively. The difference was approximately 16%. Initial stiffness and stiffness at the peak load of the model were 33.4 kN/mm and 10.6 kN/mm respectively. However the test specimen revealed 136 kN/mm for the initial stiffness and 10.7 kN/mm for the secant stiffness. As indicated secant stiffness was captured unlike the initial stiffness. Due to the strengthening pattern the first cracking loads of the model and test were quite different. The difference was about 45%.

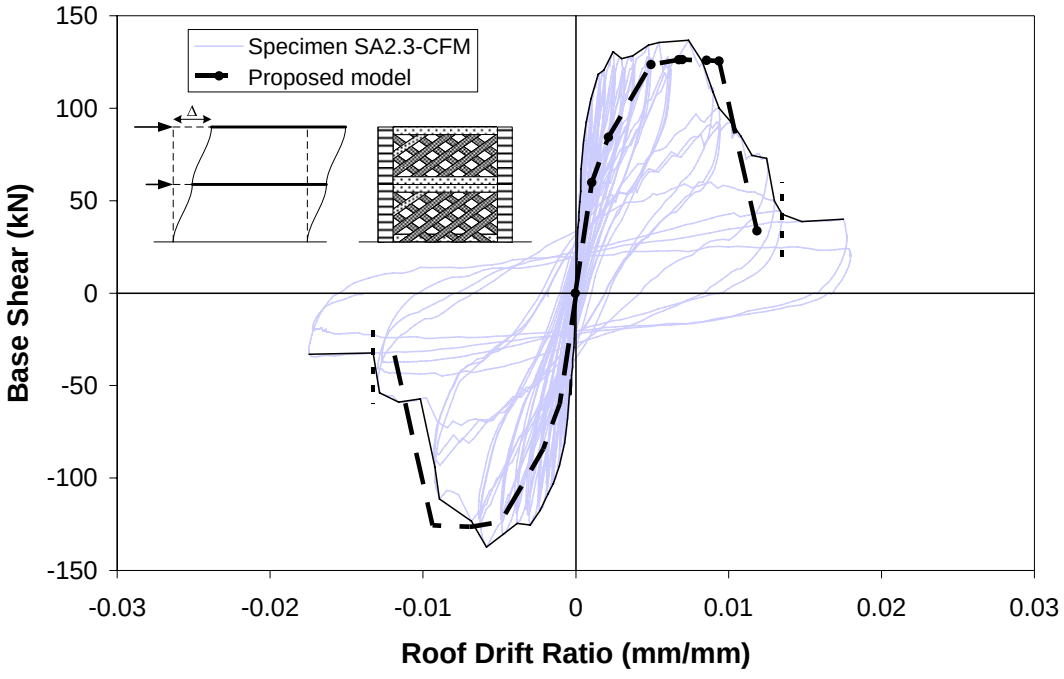

Figure 6.20. Base shear versus roof drift diagram for specimen SA2.3-CFM

Table 6.11. Nonlinear hinge properties of specimen SA2.3-CFM

SPECIMEN: SA2.3-CFM	A	B [B']	C [C']	D [D']	E [E']	Yield Values
Column (M3 @ bottom) (Type: Moment-Curvature) (Units: kN,mm)	(0;0)	(0;1)	(8.1;1)	(16.2;0.85)	(32.4;0.3)	(1.9E-5;1780)
Column (M3 @ top) (Type: Moment-Curvature) (Units: kN,mm)	(0;0)	(0;1)	(16.3;1)	(32;0.85)	(64;0.3)	(3.6E-5;3360)
Beam (M3) (Type: Moment-Curvature) (Units: kN,mm)	(0;0)	(0;1)	(31;1.17)	(62;0.58)	(124;0.29)	(2.0E-5;6110)
Column P hinge (Type: Stress-Strain) (Units: kN,mm)	(0;0)	(0;1) [0;-1]	(6;3.85) [-1.5;-1]	(69;1.92) [-2.5;-0.75]	(173;0.96) [-6;-0.25]	(5.3E-5;1.48E-3) [-0.002;-0.018]
Column V2 hinge (Type: Stress-Strain) (Units: kN,mm)	(0;0)	(0;1)	(1.5;1.0)	(1.5;0.2)	(2;0.2)	(5.3E-5;9.6E-4)
Beam V2 hinge (Type: Stress-Strain) (Units: kN,mm)	(0;0)	(0;1)	(1.5;1.0)	(1.5;0.2)	(2;0.2)	(5.3E-5;9.6E-4)
Strut P hinge (Type: Stress-Strain) (Units: kN,mm)	(0;0)	(0;1)	(3.7;2)	(12;2)	(20;0.4)	(4.2E-4;0.00273)

6.5. The Effect of Effective Width on the Global Behavior of the Specimens

Two different effective width values are used to determine the pushover curves of the specimens and illustrated in Figures 6.21-6.29 for each specimen. Experimentally obtained backbone curve of each specimen was also given in these figures. The first effective width calculation was based on the equations given by Durrani et al. [115] and the second approach was based on the width calculations proposed by FEMA 356 [95]. As can be seen in Figures 6.21-6.29, a decrease in the effective width tends to decrease the initial stiffness, and secant stiffness at peak load. However the change in the effective width did not influence the capacity significantly. Since the stresses and strains in the equivalent strut are inversely proportional to the area of the strut, cracking strains (ε_{23}) and the corresponding stresses change as the strut area changes. Nonetheless, the first crushing strains were defined as a function of the aspect ratio. Thus, the change in the strut area in the specified range did not affect the performance of the strut in regards to the capacity of the

specimens. In addition full capacity of the strut could not be used for the specimens whose failure modes are governed by the deficiencies of RC frames. Thus in the numerical model the change in the strut area also did not change the capacity of the specimens failed due to the deficiencies in the surrounding frame. Post peak crushing strain and ultimate strain influenced negative slope in the numerical model. In the model the increase in the strut area resulted in a decrease in the slope because the relevant strain values were defined as a function of the aspect ratio. These strains were the same as the stresses decrease.

As explained above, the formulations which were used for the equivalent strut width proposed by FEMA 356 underestimated the initial stiffness and the secant stiffness at peak load for all the specimens. For example, the initial stiffness and stiffness at peak load values for the specimen SA1.0 were 14.7 kN/mm and 11.8 kN/mm respectively if FEMA 356 approach was used. As illustrated in Figure 6.21, the stiffness values calculated by using formulations recommended by Durrani et al. [115] better predicted the experimental values. However, secant stiffness at peak load was very close to the initial stiffness calculated by FEMA 356. As indicated in Figure 6.23, initial and secant stiffness values of the model incorporating the FEMA 356 approach were 19.36 kN/mm and 7.43 kN/mm. These values clearly differed from the test values of specimen SA1.0-C2V. Like the specimens with an aspect ratio of 1.0, the performance of the other specimens was also poorer when FEMA 356 strut width was used.

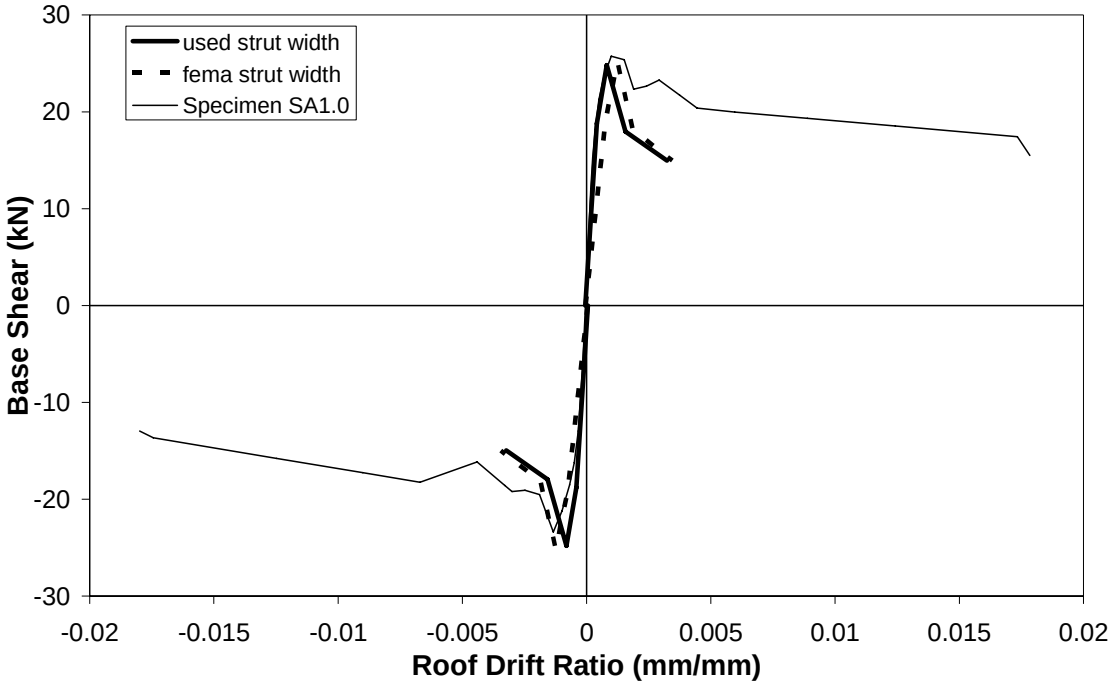

Figure 6.21. Analytically obtained base shear-roof drift diagrams for specimen SA1.0

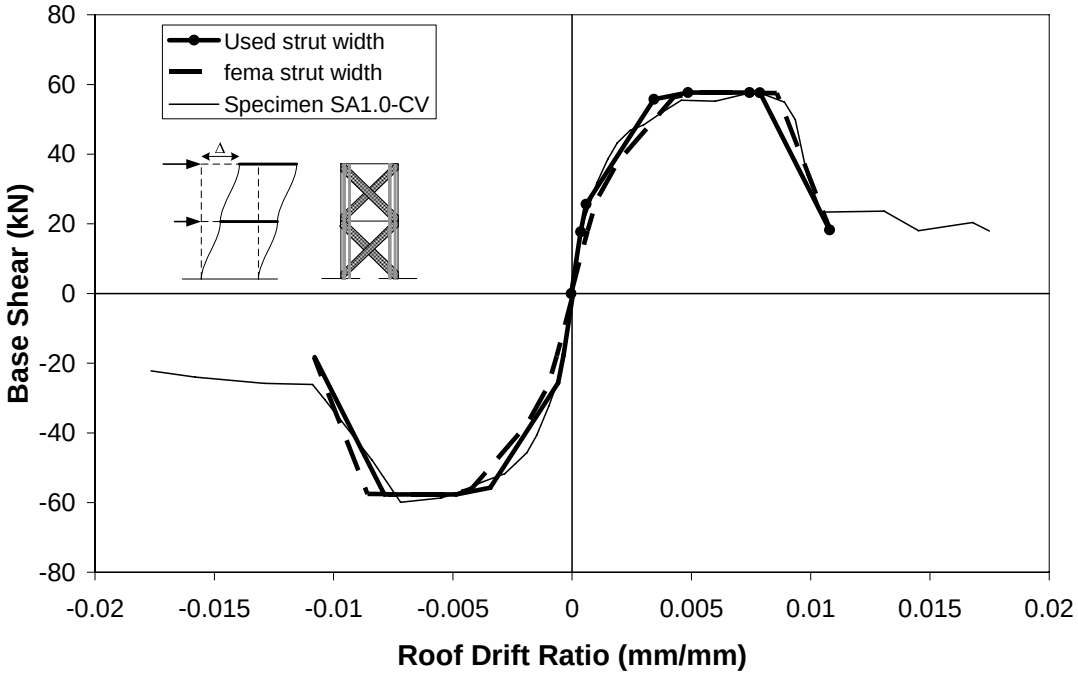

Figure 6.22. Analytically obtained envelope curves for specimen SA1.0-CV

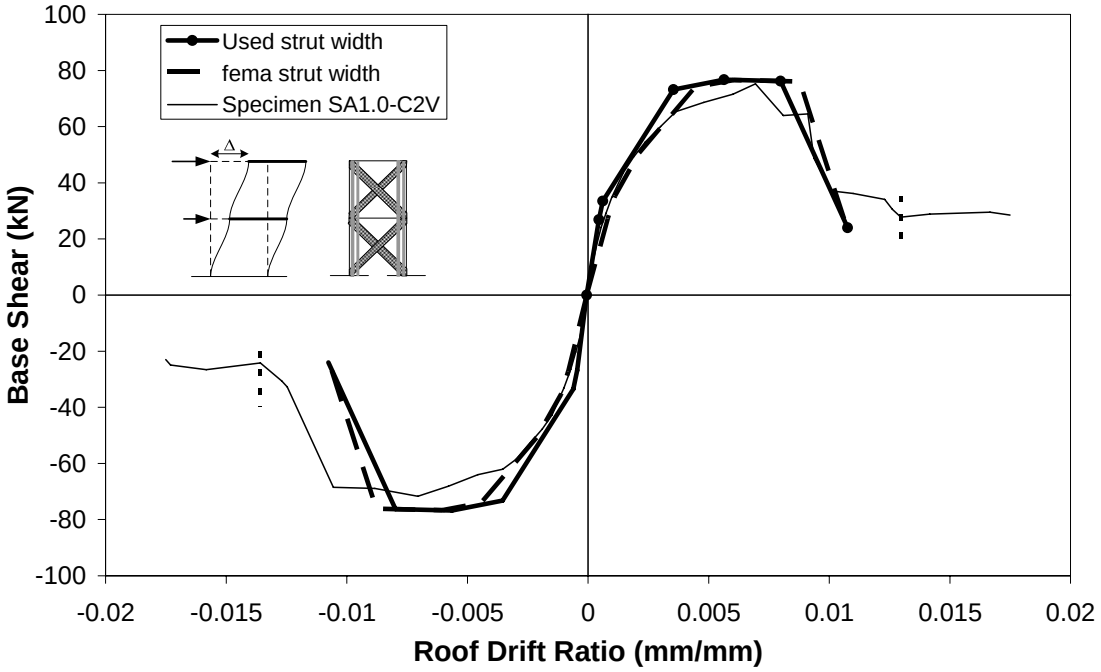

Figure 6.23. Analytically obtained envelope curves for specimen SA1.0-C2V

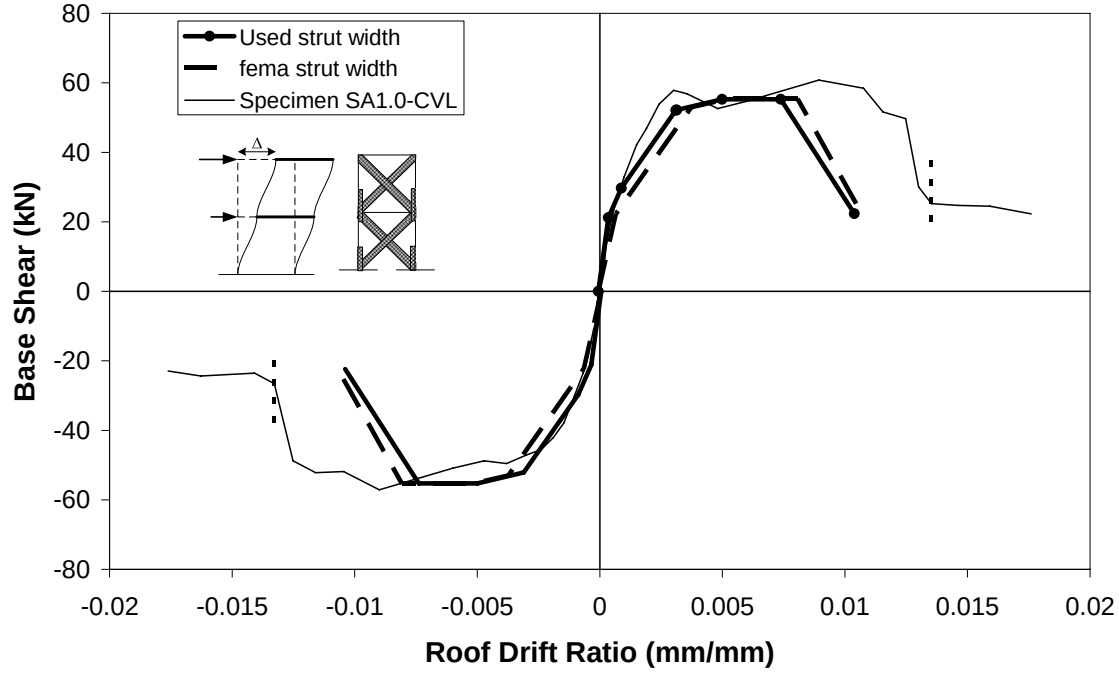

Figure 6.24. Analytically obtained envelope curves for specimen SA1.0-CVL

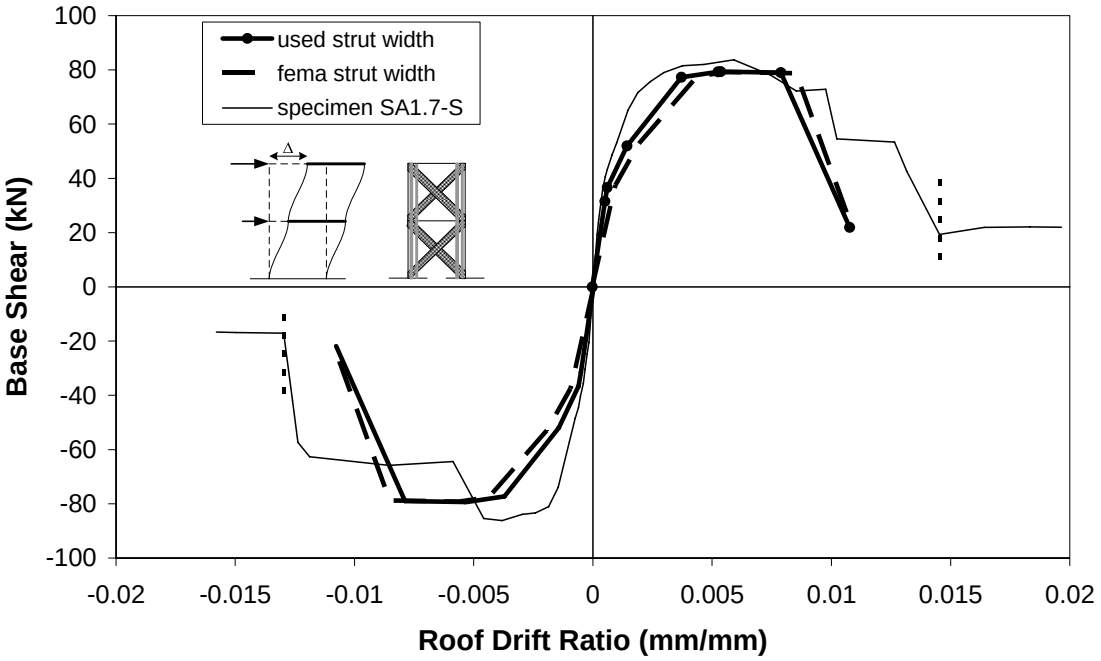

Figure 6.25. Analytically obtained envelope curves for specimen SA1.7-S

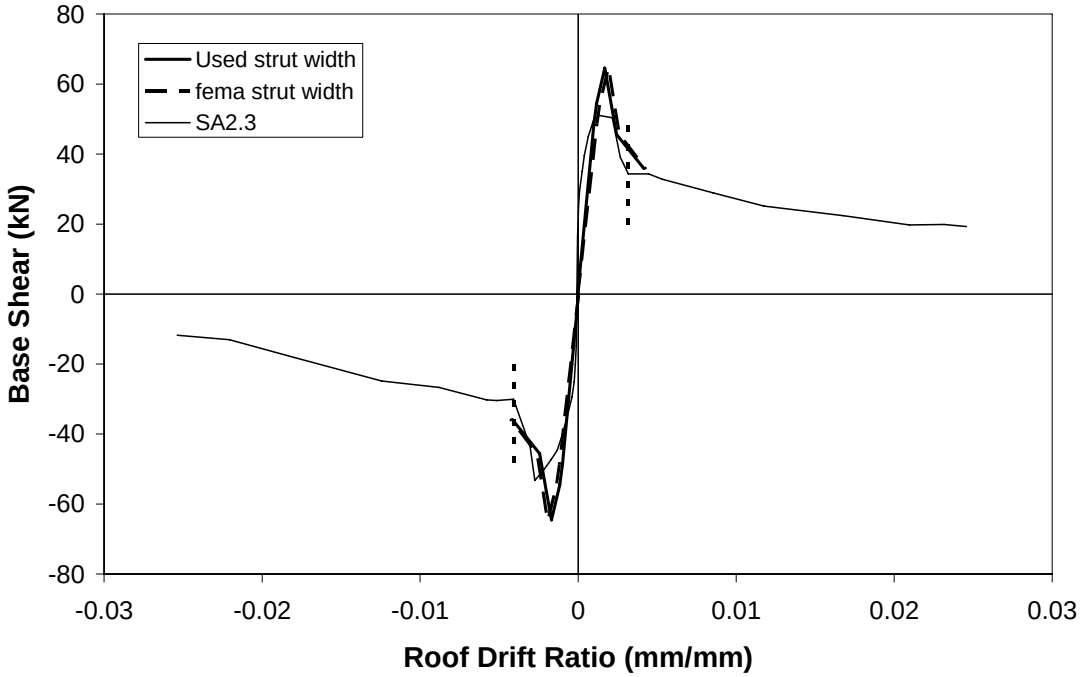

Figure 6.26. Analytically obtained envelope curves for specimen SA2.3

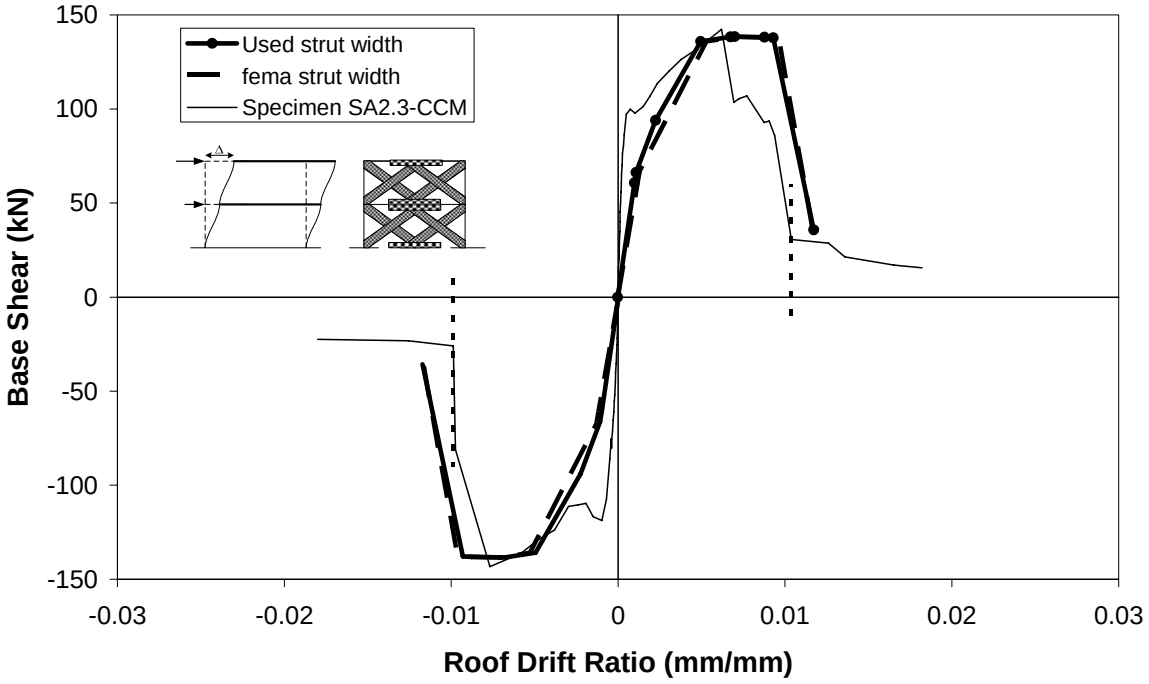

Figure 6.27. Analytically obtained envelope curves for specimen SA2.3-CCM

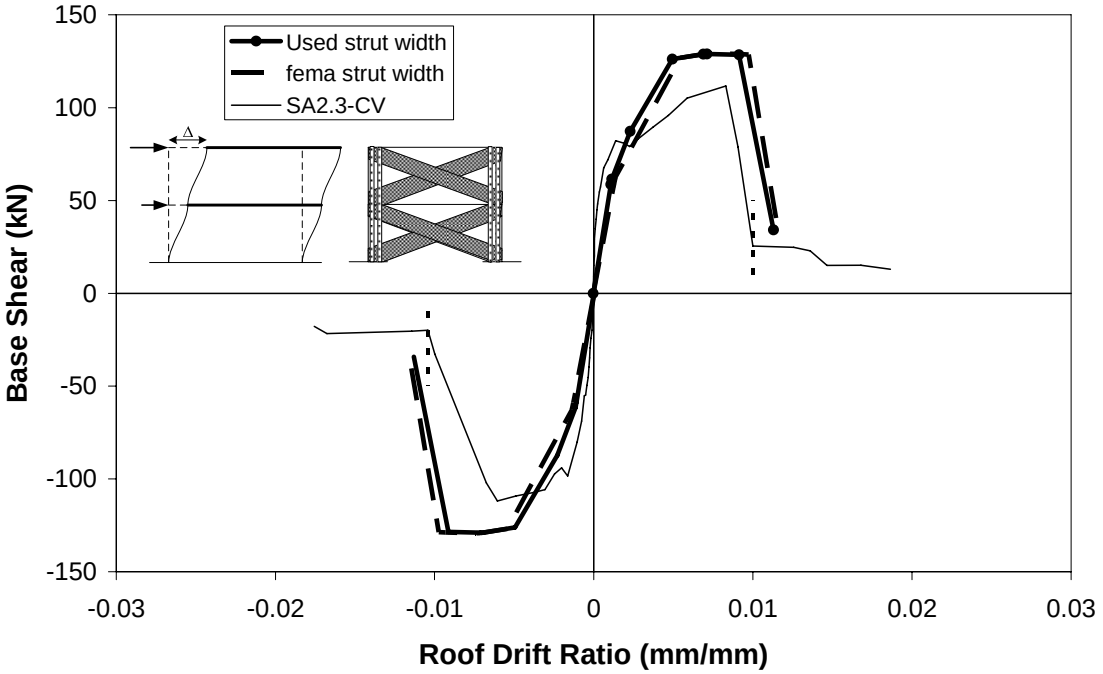

Figure 6.28. Analytically obtained envelope curves for specimen SA2.3-CV

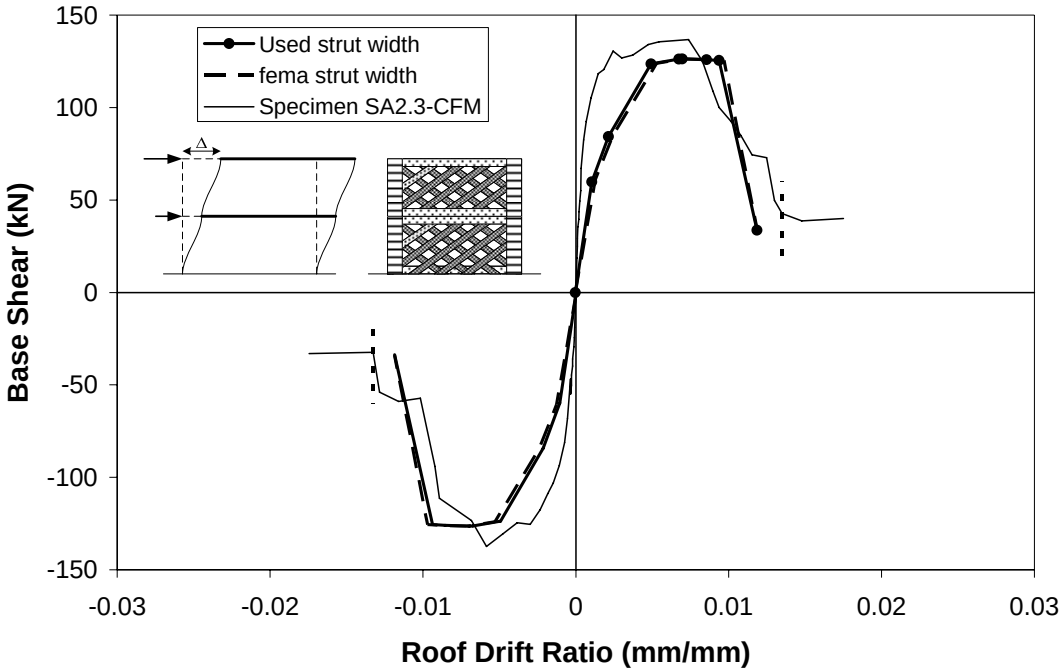

Figure 6.29. Analytically obtained envelope curves for specimen SA2.3-CFM

6.6. Cost Analysis

CFRP surface areas for each specimen were calculated and presented in Table 6.12. Last column of this table represents the ratio of the CFRP surface area to the total wall area. As indicated in this table, specimens with an aspect ratio of 1.0 yielded the highest ratios among the three specimen groups because hole pattern of the specimens was similar while the surface area varied. The lowest ratio was obtained by specimen SA2.3-CV due to the CFRP configuration.

14% increase in the area of the CFRP resulted in 30% increase in the load carrying capacity when specimens SA1.0-CV and SA1.0-C2V were compared. The same tendency was observed for the specimen SA1.0-CVL. When specimens SA2.3-CV and SA2.3-CCM were compared, it was observed that 64% increase in the CFRP surface area resulted in approximately 28% increase in the load carrying capacity. However, the load carrying capacity increased approximately 23% when specimens SA2.3-CV and SA2.3-CFM were compared. The observations showed that the increase in CFRP area increased the load carrying capacity but this increase was nonlinear for the specimens with an aspect ratio of 1.0. In addition, comparison of the specimens with an aspect ratio of 2.3 revealed that not

only CFRP surface area but also CFRP orientation should be evaluated together to better understand the performance of the specimens. Specimen SA2.3-CFM did not yield the highest load carrying capacity although it had the highest ratio among the specimens with an aspect ratio of 2.3.

Table 6.12. Cost analysis of each specimen

Specimen	$A_{FRP\text{-}total}$ (cm^2)	$A_{wall\text{-}total}$ (cm^2)	Ratio
	1	2	(1)/(2)
SA1.0	0	27690	0.00
SA1.0-CV	68024	27690	2.46
SA1.0-C2V	77664	27690	2.80
SA1.0-CVL	69708	27690	2.52
SA1.7-D	73368	46500	1.58
SA1.7-S	75960	46500	1.63
SA2.3	0	63000	0.00
SA2.3-CCM	138328	63000	2.20
SA2.3-CV	84296	63000	1.34
SA2.3-CFM	155830	63000	2.47

6.7. Summary

In this chapter, an easy, fast and time saving macro modeling based on equivalent strut concept was proposed and test results are tried to be replicated. For the infill panel, an equivalent strut was used with P plastic hinge located in the middle of the strut. P plastic hinge was modeled in a multi-linear fashion. The proposed semi-emprical model is sensitive to the aspect ratio (l/h) of the structure. The strut was released at both ends. Equivalent strut also include the effect of FRP overlays for the strengthened infill panels. Two main failure modes are described for the infill panels namely shear sliding and corner crushing.

The frame elements were modeled by using moment, shear and axial plastic hinges described previously. User defined hinge properties were used to match experimental and

analytical results. User defined hinge properties can better simulate the properties of the existing structures than the default hinge properties in the program because default hinge properties are more appropriate for code compliant systems. Test results showed that a gradual decrease in moment and axial hinges are more appropriate. While a gradual decrease in moment hinges (M3) is used, a sudden decrease is incorporated in shear hinges (V2) because shear failure is more sudden and brittle. Tension failure of specimen SA1.0 was predicted by the model effectively whereas failure mode of specimen SA2.3 was not predicted successfully. For the strengthened specimens, strengthened infill properties governed the behavior. The model predicted failure loads satisfactorily. However the sensitivity of the energy dissipation changes depending on the aspect ratio. The specimens with aspect ratio of 1.0 underestimate the energy dissipation whereas those with aspect ratio of 2.3 overestimate. Specimens SA1.0-CV, SA1.0-C2V, and SA2.3-CCM exhibited the best performance considering the energy dissipation.

Two types of effective width values were used in the modeling of the infill. The results of the pushover analysis showed that the effective width is important to determine the stiffness values. Stiffness decreases as the effective width decreases. However the capacity of the specimens does not seem to be sensitive to the effective width variations in regards to the investigated range.

It is very important to determine material properties correctly to improve the accuracy of the model. The model can be improved by including cyclic response of the infill because some local effects such as frame-wall interaction and pinching behavior might be incorporated in the model by using cyclic models. Observations made during the tests showed that most of the specimens generally suffered from the soft story mechanism which is undesirable failure mode. This is also observed in the numerical study.

7. SUMMARY, CONCLUSIONS, AND RECOMMENDATIONS

7.1 Summary

Strengthening of existing vulnerable buildings to an impending earthquake is of great importance in Turkey. There are various methods to increase the supply of the buildings, which could be divided mainly into two categories: member strengthening (jacketing of columns and beams…etc.), and system strengthening (adding of shear walls, steel bracing, or seismic isolators…etc.). If the number of members to be strengthened is limited, the former method can be used to improve the overall performance. However, the latter is more appropriate if the number of members to be strengthened is excessive or the structure suffers from inadequate lateral stiffness resulting excessive deformations. Although the above techniques are effective, they mostly require the evacuation of the dwellers. Presence of large building stock in Turkey, which is vulnerable to an imminent earthquake, entails fast, relatively easier and feasible alternative methods. Application of CFRP materials onto the infilled frames is considered as an alternative strengthening method for the low to mid-rise buildings. In this method, CFRP is adhered to the infill surface by using an appropriate adhesive and anchored to the surrounding frame with CFRP anchors.

This study investigates the effects of various aspect ratios on the behavior of CFRP-strengthened infilled RC frames. One-third scale, single bay and two story HCT brick infilled RC frames with different aspect ratios (1.0, 1.7, and 2.3) were tested under reversed cyclic quasi-static loading. Two specimens out of ten were control specimens. Eight specimens were strengthened with CFRP overlays in different configurations. The CFRP materials were applied on both sides of the specimens. All RC frames had the same deficiencies commonly seen in Turkish practice. Test results are mainly evaluated considering stiffness, strength, and energy dissipation characteristics of the specimens.

A semi-empirical macro model by using equivalent diagonal strut concept for masonry infill panel (with or without FRP) is proposed and calibrated with the test results. The infill panel is replaced with the compression-only strut in the mathematical model. Multi-linear stress-strain relationship is used for the strut model. The model is sensitive to

the aspect ratio which is defines as the ratio between the frame bay width and the story height. The proposed model generally predicted the global behavior of the specimens satisfactorily.

CFRP surface areas for each specimen are also calculated and compared with each other. The comparison of the test results and cost analysis indicated that the structural performance of the specimens, CFRP orientation, and geometric properties of the specimens (i.e. aspect ratio) are strongly related to each other as expected. However, the relation is nonlinear.

7.2. Conclusions Based on the Test Results and the Analytical Study

The following conclusions can be drawn based on the test results and comparisons between the test results and analytical study. These results are limited to the work conducted in this dissertation. Thus, it may mislead to generalize these results without further experimental and analytical studies.

1. Frame geometry (aspect ratio), existing deficiencies, and material properties influence the failure modes significantly. Failure mode of specimen SA1.0 was tension failure of the columns at the floor level due to the inadequate lap splices whereas the failure mode of specimen SA2.3 was due to the excessive flexural cracks following the crushing of the infill panel at the corners.

2. Damage is mostly accumulated in the first story due to the test set-up used.

3. CFRP overlays applied on the masonry infill panel can be satisfactorily anchored to the reinforced concrete frames even the ones with a concrete strength as low as 8 MPa. However, the anchor depth is important to get the highest efficiency. Specimen SA1.7-D failed mainly due inadequate anchorage length (approximately 6 cm to 8cm) at the foundation level. The depth of CFRP anchors for the rest of the strengthened specimens increased up to 15 cm at the foundation level in order to eliminate the premature anchorage failure. The contact length of 7 cm between cross diagonals and CFRP anchors at the foundation level seems to be appropriate even

though inferior local rupturing of some CFRP anchors and some insignificant sliding signs between cross diagonals and CFRP anchors were observed at the foundation level of specimen SA2.3-CFM.

4. Strengthening of brick infilled RC structures with CFRP overlays emerges as an alternative strengthening method. However, the efficiency and effectiveness of this method is directly related to workmanship. In practice, experienced engineers and workers should be assigned during the application process. Surface preparation, preparation of the anchor holes, alignment of the fibers of the CFRP overlays in the desired direction, depth of the anchor holes are some of the important points that should be taken into account during the application.

5. FRP orientation and decreasing of the sliding surface due to the formation of the cracks at the mid-height portion of the infill wall were some of the reasons of the sliding at the mid-height region observed in specimens SA1.0-CVL, and SA2.3-CCM. However, sliding of specimen SA2.3-CFM took place 22 cm away from the foundation beam mainly due to the FRP orientation because cross diagonal FRP overlays on the masonry wall were evenly distributed and intersected approximately at that specific height.

6. When the test results of SA2.3-CV, SA1.0-CV, and SA1.7-S are compared, it can be concluded that presence of vertical strips on the masonry infill is much more effective for the smaller aspect ratios (frame bay length/ frame story height). Rupturing of one vertical strip of the specimen SA1.0-CV caused approximately 10% drop in the load carrying capacity. Rupturing of three vertical strips and a small portion of one of the cross diagonal FRPs of specimen SA1.7-S resulted in approximately 25% decrease in the load carrying capacity whereas rupturing of two vertical strips of specimen SA2.3-CV did not affect the specimen's load carrying capacity and the specimen SA2.3-CV carried further load in the next cycle.

7. Axial load failure, which resulted in vertical movement of the specimen, occurred right after the shear failure of the columns in the extreme case as could be seen in SA1.0-C2V, and SA2.3-CV. Besides, all the strengthened specimens with an aspect

ratio of 2.3 exhibited vertical movement in the extreme cases, which implied sudden loss of gravity load carrying capacity.

8. Test results of specimen SA1.0-C2V revealed that a sudden decrease in load carrying capacity due to rupturing of vertical strips in a first half cycle might not be repeated in the other half cycle of one full cycle. In other words, brittle behavior in push cycle might shift into a so-called ductile behavior in pull cycle of the same cycle. This behavior occurs due to several reasons such as sliding resulting in deterioration of fibers. Rupturing of FRP overlays in the forward half cycles let the specimen slide more freely. Thus, the effective FRP overlays in the other direction which are subjected to axial forces also subject to an increasing shear forces. FRP fibers are not as effective in shear as in axial forces. Thus, deterioration of the fibers of the overlays due to sliding cause a so-called ductile behavior without significant loss of strength because of the rupturing of vertical FRP strips. In addition, test results of specimen SA1.7-S showed that the rupturing of vertical strips in different cycles (i.e. 14 and 16) also resulted in a so-called ductility in one of the half cycles (forward one). In other words, the so-called ductility was mainly due to the rupturing of vertical strips even in different cycles.

9. CFRP diagonal overlays controlled the crack widths on the infill wall and caused an increase in the number of the cracks. Due to the restraining effects of CFRP overlays, the effect of the infill wall on the strength of the specimens was significant. However, the failure of FRPs results in sudden losses in the load carrying capacity and the frame itself can not pick up such a capacity loss since it is not designed for such load levels.

10. Evaluation of test results revealed that a drift level of 0.30% is important in terms of tensile strength of columns. At this drift level, plastic hinging on the columns is about to be formed and horizontal cracks start to encircle the columns especially in specimen SA1.0-CV.

11. Strengthening with CFRP overlays improved the lateral load carrying capacity of the specimens. The increase for specimens with aspect ratios of 1.0 and 2.3 is

approximately up to 3 fold as compared to the control specimen of each group (SA1.0 for specimens with the aspect ratio of 1.0 and SA2.3 for specimens with the aspect ratio of 2.3). Besides, the strengthening scheme limits the increase in lateral load carrying capacity.

12. Capacity predictions are within the reasonable range (10%) for specimens with an aspect ratio of 1.0 whereas they scatter (24%) for specimens with an aspect ratio of 2.3 due to mixed failure modes. Although 24% is high, this scatter can be in an acceptable range when the shear dominant behavior is considered. Besides, the proposed procedure satisfactorily predicts the failure modes of SA1.0 series specimens whereas the failure mode correlations of specimens with an aspect ratio of 2.3 are not as successful as those of specimens with an aspect ratio of 1.0.

13. The procedure given in FEMA 356 to draw backbone curves underestimates the envelope curves used in this dissertation. The deviation is much more pronounced after yielding considering specimens SA1.0-CV and SA1.7-S.

14. Test results of strengthened specimens in the SA1.0 series and SA2.3 series showed that the rate of stiffness degradation increases as the aspect ratio increases. The average values of the third cycle normalized stiffness values of the strengthened specimens with aspect ratio of 1.0 and 2.3 at a drift ratio of 0.005 are about 0.20 and 0.10 respectively.

15. FRP overlays improve the strength of the system remarkably without adding considerable mass. On the other hand, FRP overlays cause increase in earthquake demand according to the frame aspect ratio. For smaller aspect ratios (SA1.0 series) change in stiffness values with FRP application is negligible. However, change in stiffness in specimens with bigger aspect ratios (SA2.3 series) is more pronounced, with an average value of 25% when the initial peak-to-peak values are used. The change in stiffness, when peak-to-peak stiffness at a drift level of 0.02% was used, was approximately 10% for smaller aspect ratios and 270% for bigger aspect ratios.

16. Cumulative dissipated energy values between the un-strengthened specimen and the counterpart strengthened ones start to deviate after reaching a cumulative drift ratio of 2.7%, regardless of the aspect ratio. This deviation is high for SA2.3 series of specimens as compared to the SA1.0 series of specimens. Moreover, the deviation among the strengthened SA1.0 specimens beyond the 2.7% cumulative drift ratio was minimal, while considerable deviation was observed for SA2.3 series with changing CFRP layout.

17. Aspect ratio and strengthening scheme affect the residual displacements significantly. Residual displacement ratios of SA1.0 series specimens tend to be less than 0.1 at a roof drift ratio of 0.005. However, the residual displacement ratios double for SA2.3 series specimens.

18. Test results showed that energy dissipation in the first cycle is generally greater than that of the third cycle for the same drift magnitude before and after the peak load regardless of the aspect ratio and the FRP scheme. This ratio, at the peak load level, is between 1 and 2.5 for changing CFRP schemes among SA1.0 series specimens, while the same ratio is between 1 and 4 among SA2.3 series specimens. This can be attributed to the aspect ratio, failure modes, strengthening scheme, and formation of energy dissipation mechanisms such as opening and closing of cracks.

19. Infill panel (with or without FRP overlays) is modeled by using a multi-linear stress-strain relation incorporating equivalent diagonal strut concept. The proposed semi-empirical model replaces the FRP strengthened infill wall with a pin connected equivalent strut and is sensitive to the aspect ratio of the infilled frames. The semi-empirical model is proposed to represent the experimental envelope curves depending on the experimental test set-up. The specimens were tested under quasi-static reversed cyclic loading whereas the mathematical model was developed for monotonic loading.

20. The proposed model predicted failure loads of the specimens in an acceptable range.

21. A parametric study investigating the effects of effective width variations on the nonlinear behavior of the specimens showed that initial stiffness decreases as the effective width decreases but the capacity of the specimens does not seem to be sensitive to the effective width variations.

7.3. Overall Conclusions

- Presence of the flag FRP configuration at the corners of the masonry infill panel impeded the crushing significantly.

- Doubling vertical strips increases load carrying capacity nonlinearly but further test should be conducted to confirm this conclusion.

- The test results showed that FRP orientation and strengthening scheme influence the behavior as well as the failure mode significantly as expected.

- Presence of FRP affected the energy dissipation characteristics of the specimens but it did not have any contribution by itself. The fact is that FRP prevents HCTs from flaking and keeps them together, hence increasing the possibility of sliding which is one of the ways of the energy dissipation.

- The similarities in cumulative energy dissipation curves of SA1.0 series specimens show that the lap splice deficiency, which is the main deficiency, can be eliminated by incorporating vertical strips in the strengthening scheme successfully. However, cross diagonal configurations excluding vertical strips and including wrapped FRPs around columns perform better for larger aspect ratios (SA2.3 series specimens) considering dissipated energies.

- Strengthening of infilled frames with CFRP overlays do not influence the initial stiffness considerably. While stiffness enhancement is quite limited for larger aspect ratios (i.e. SA2.3 group specimens), it is insignificant for smaller aspect ratios (i.e. SA1.0 group specimens).

7.4. Recommendations for Future Studies

- Full scale tests should be performed to highlight the size effects on the behavior and ensure the reliability of the scaled tests.

- In addition to cyclic quasi-static tests, pseudo-dynamic and shake table tests should also be performed for the strengthened infilled frames.

- Long term behavior of FRP composites should also be investigated carefully. The research on the non-flammable, ductile adhesives should be developed.

- Damaged infilled frames should also be rehabilitated and tested.

APPENDIX A: LOCATION OF THE SENSORS

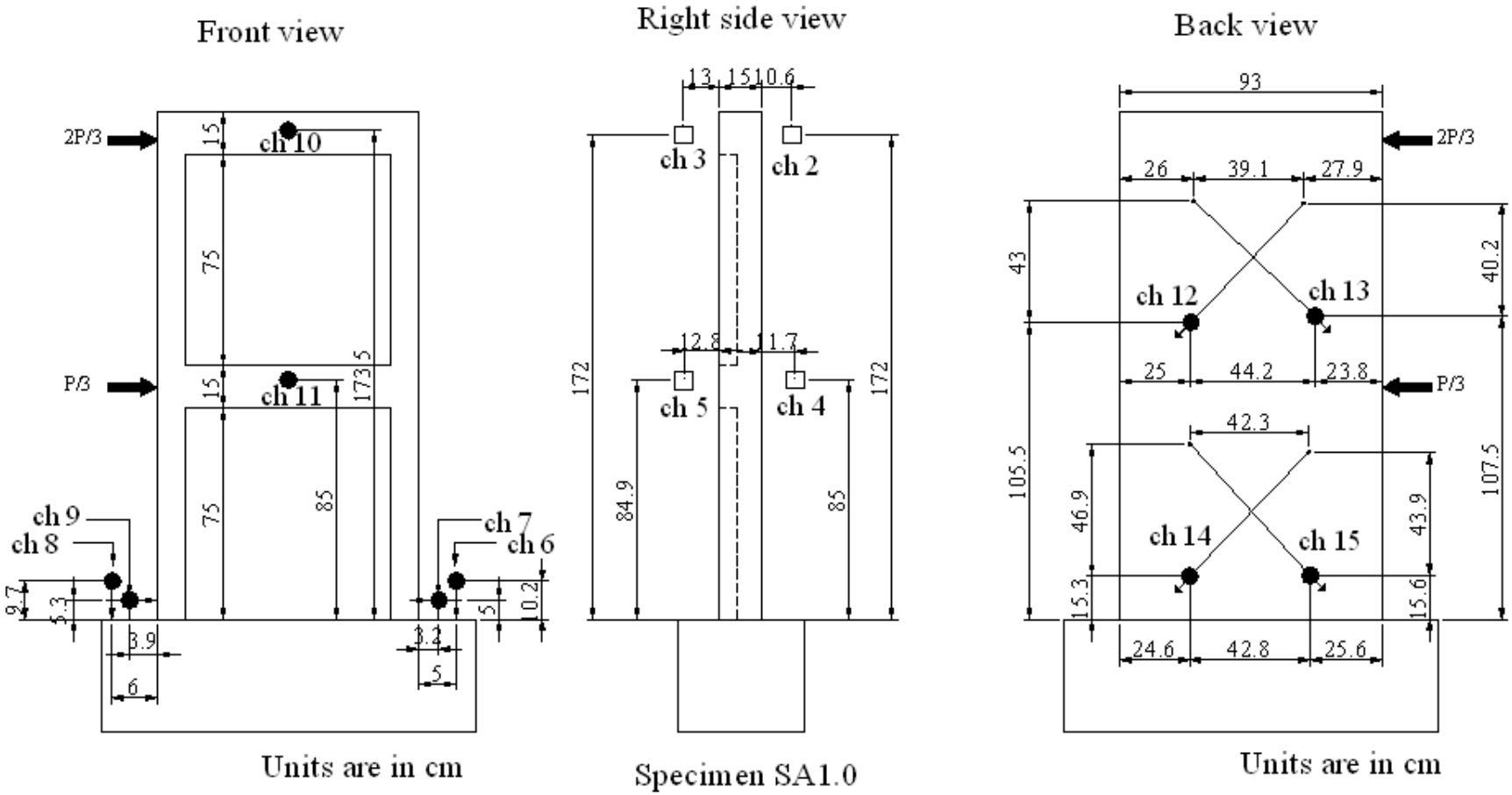

Figure A.1. Position of measuring sensors of specimen SA1.0

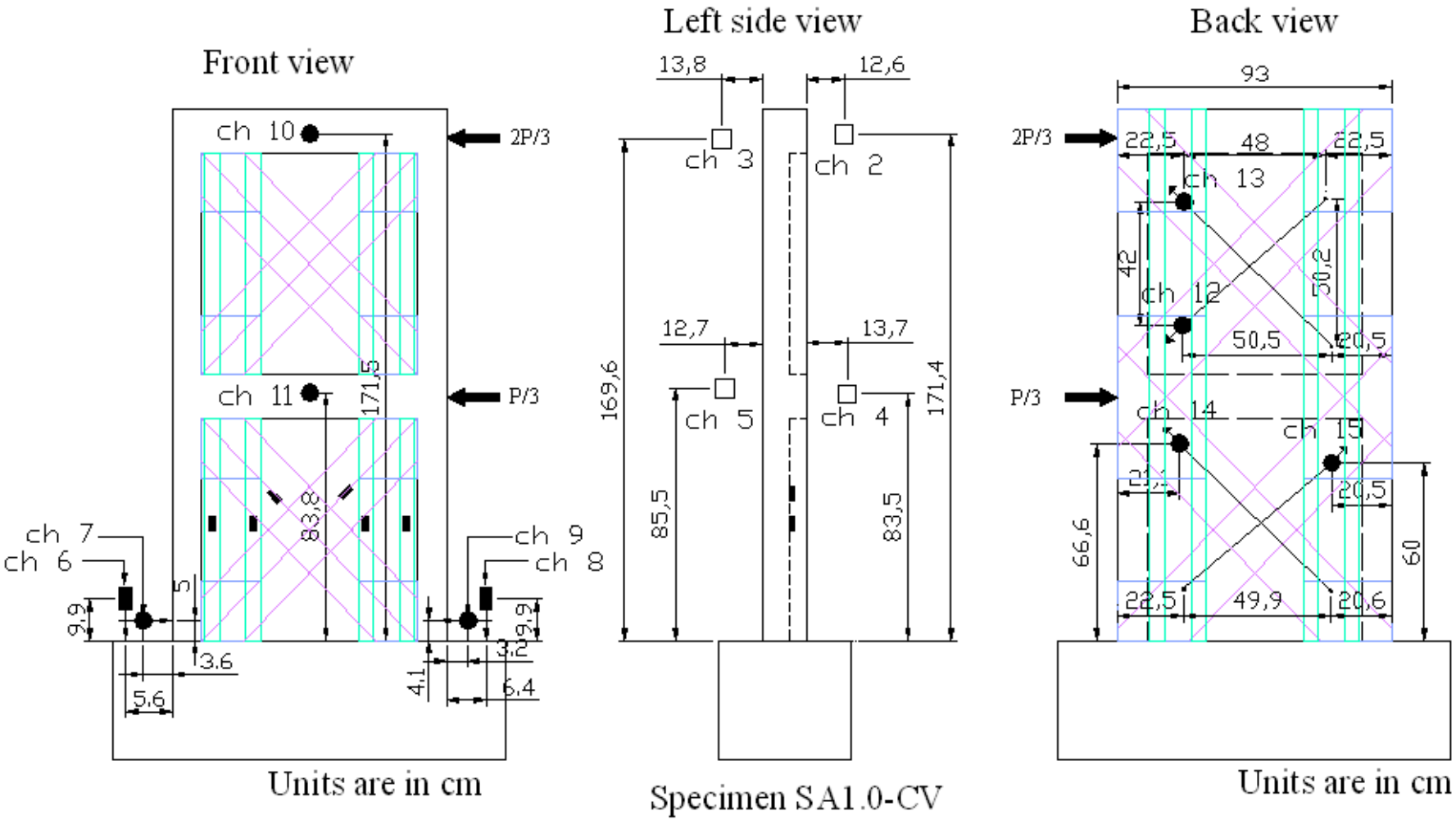

Figure A.2. Position of measuring sensors of specimen SA1.0-CV

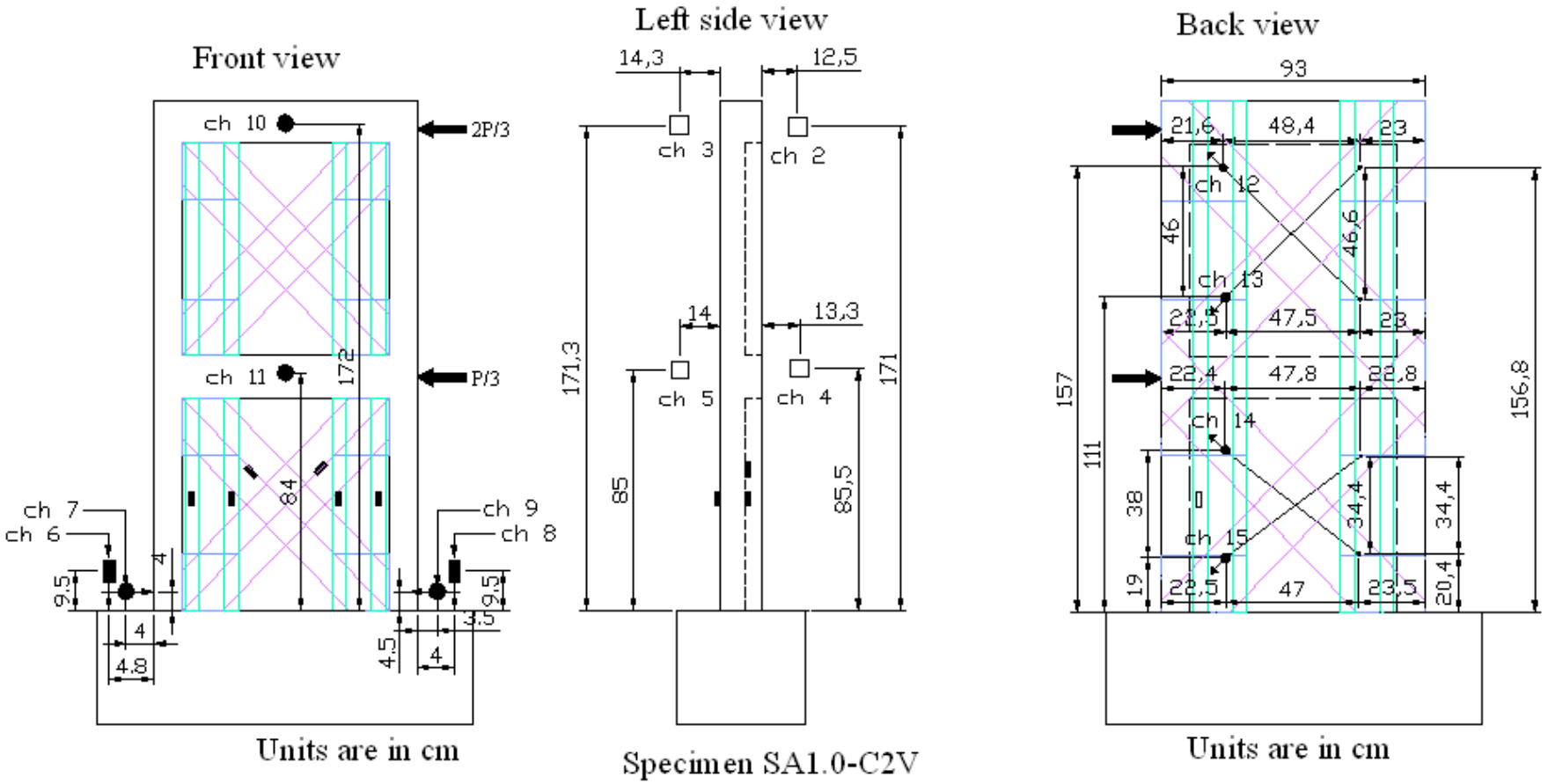

Figure A.3. Position of measuring sensors of specimen SA1.0-C2V

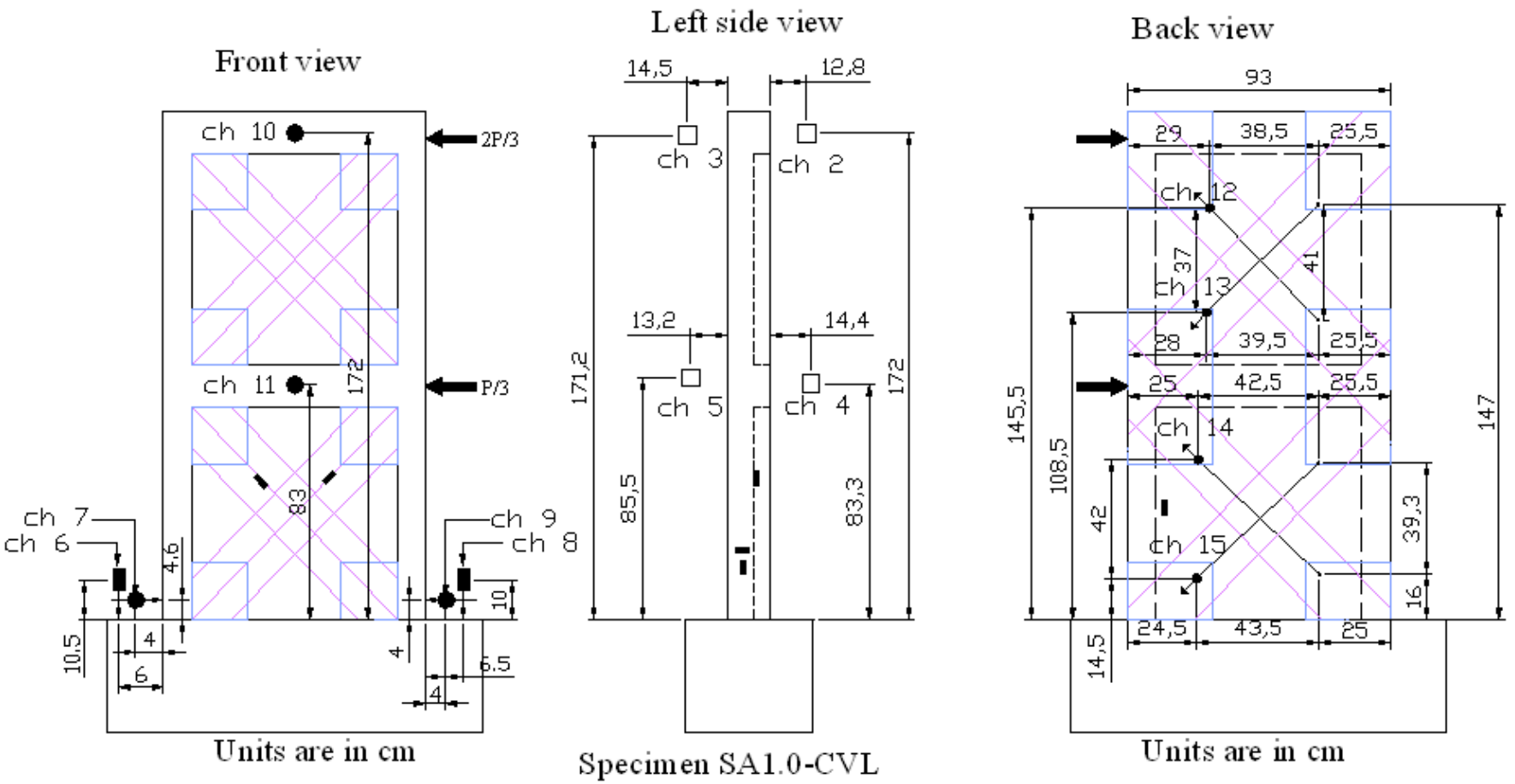

Figure A.4. Position of measuring sensors of specimen SA1.0-CVL

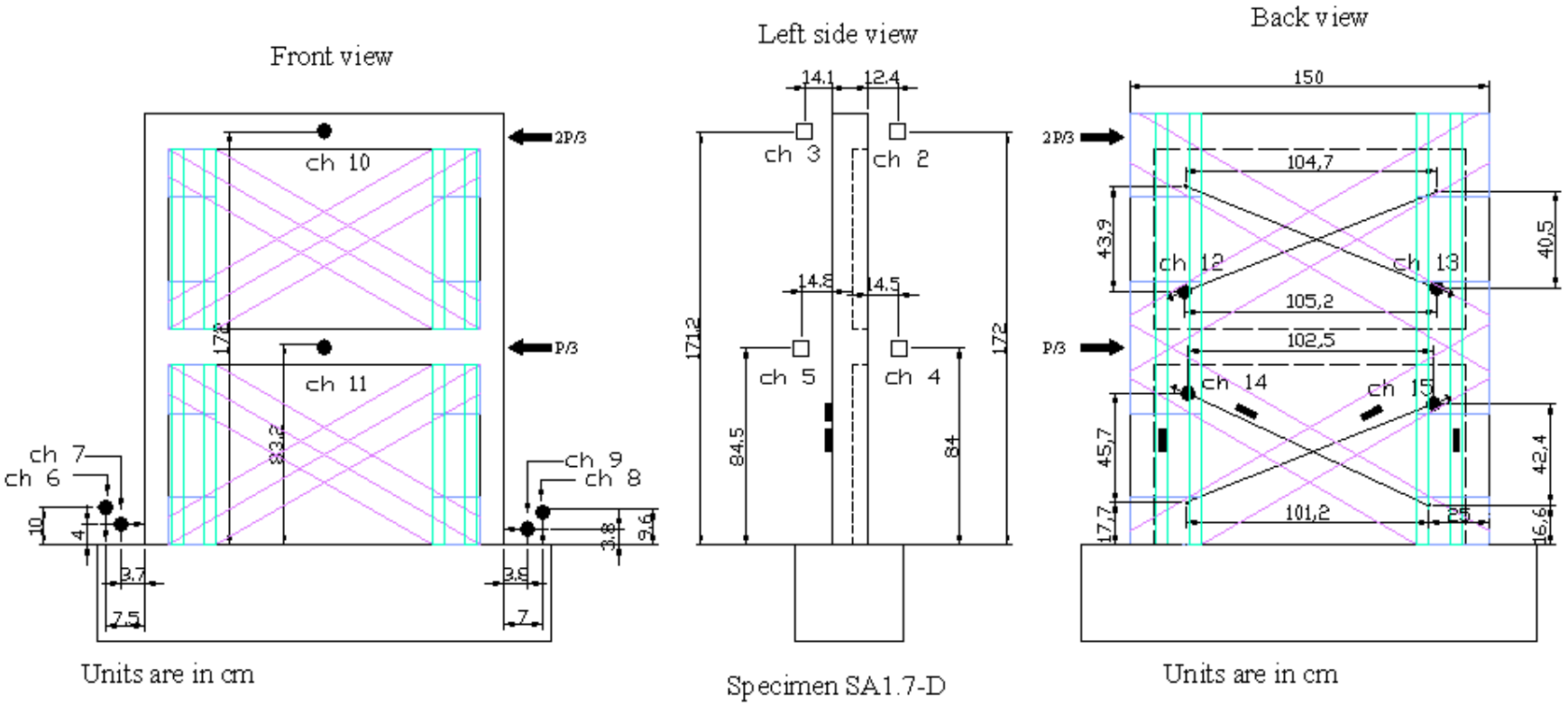

Figure A.5. Position of measuring sensors of specimen SA1.7-D

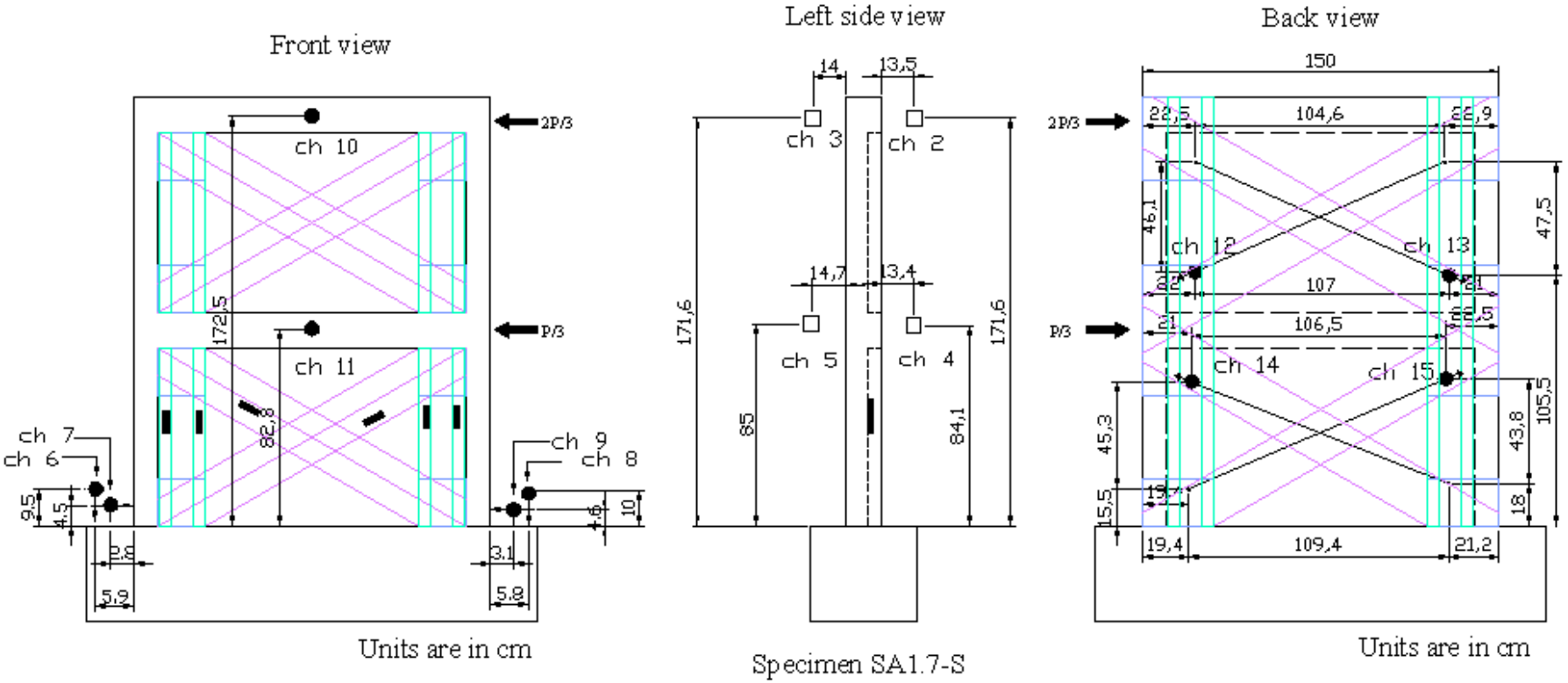

Figure A.6. Position of measuring sensors of specimen SA1.7-S

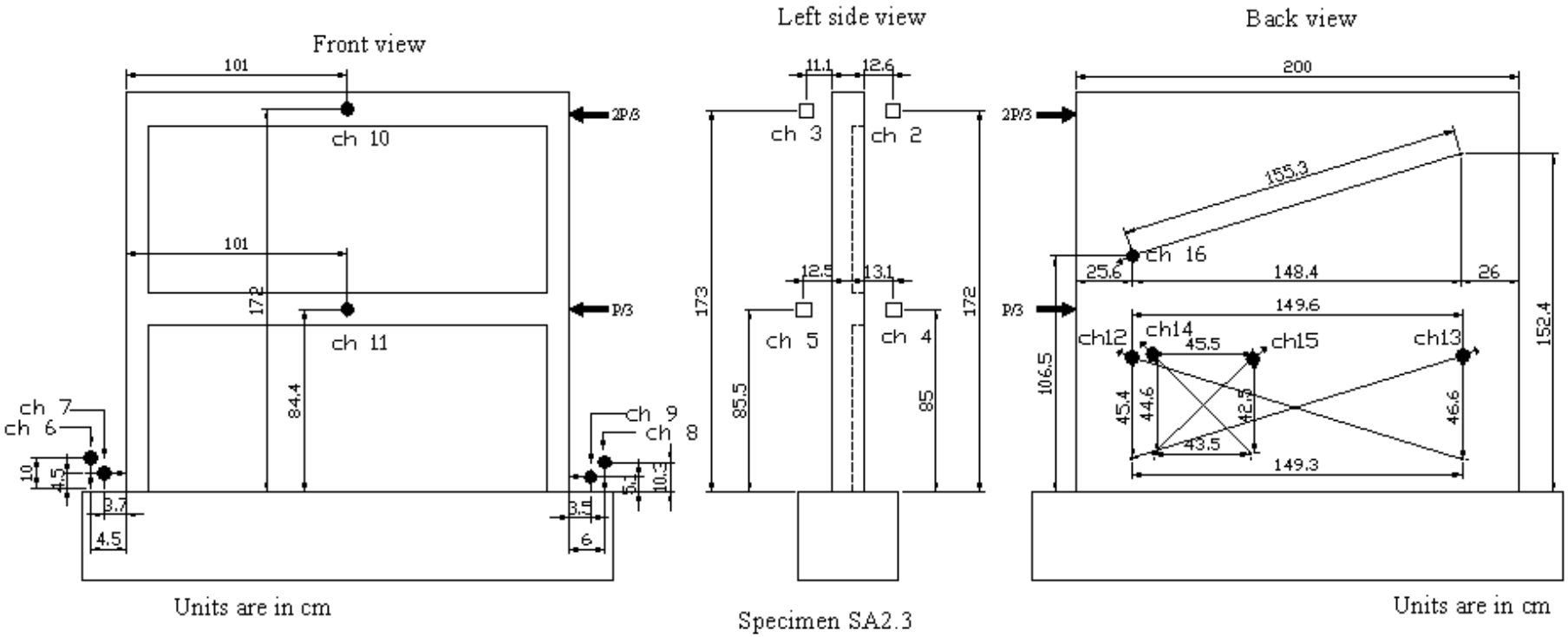

Figure A.7. Position of measuring sensors of specimen SA2.3

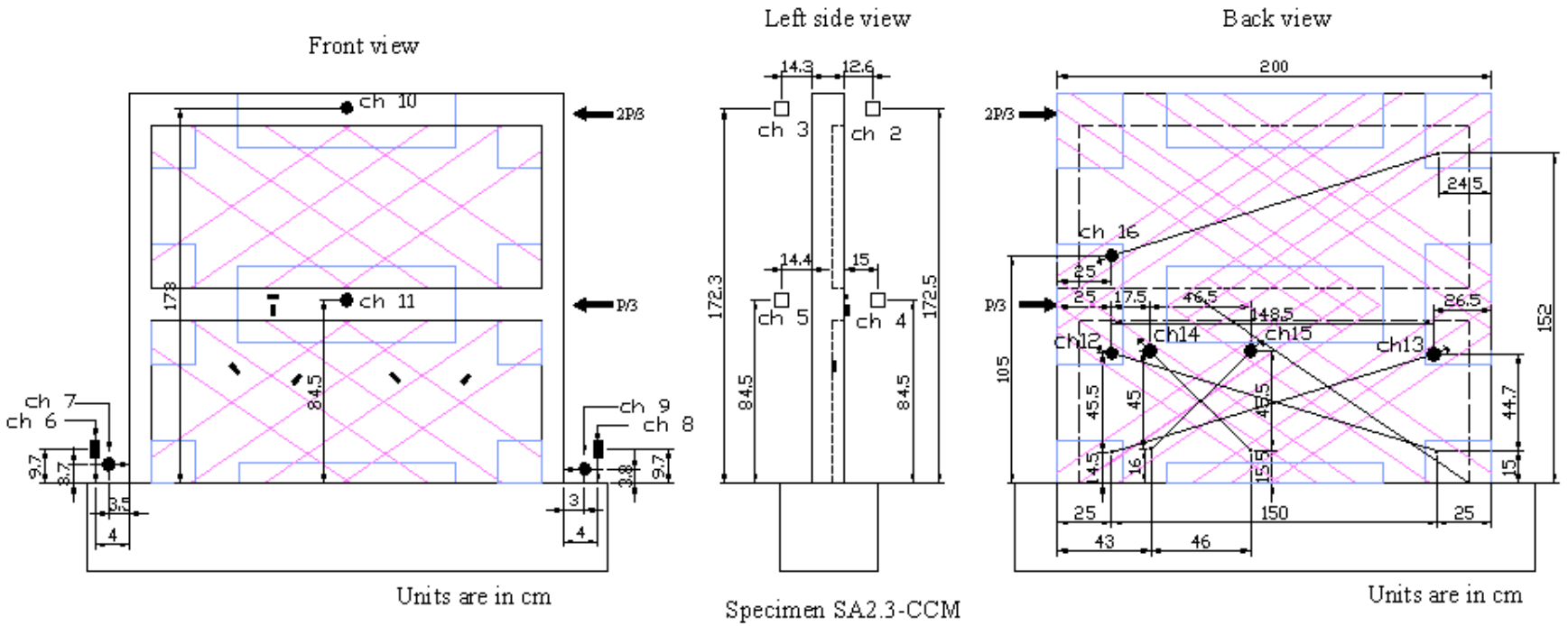

Figure A.8. Position of measuring sensors of specimen SA2.3-CCM

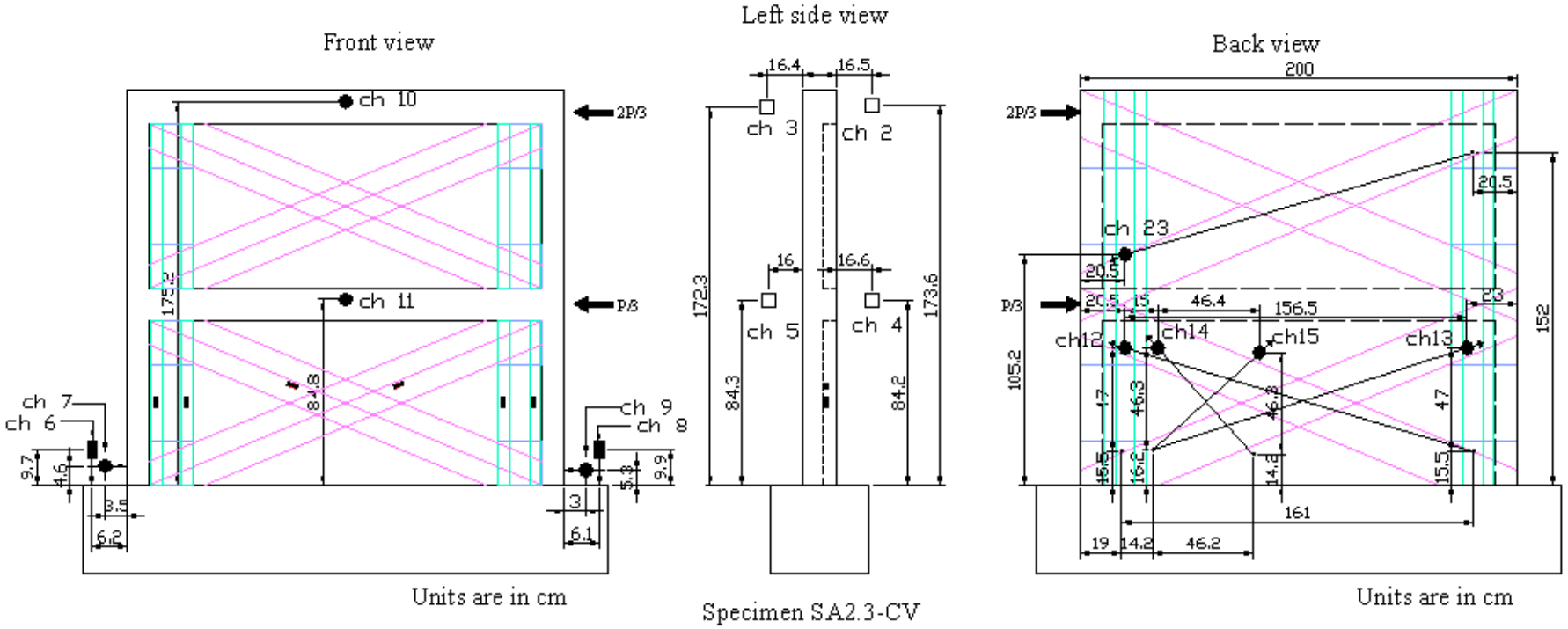

Figure A.9. Position of measuring sensors of specimen SA2.3-CV

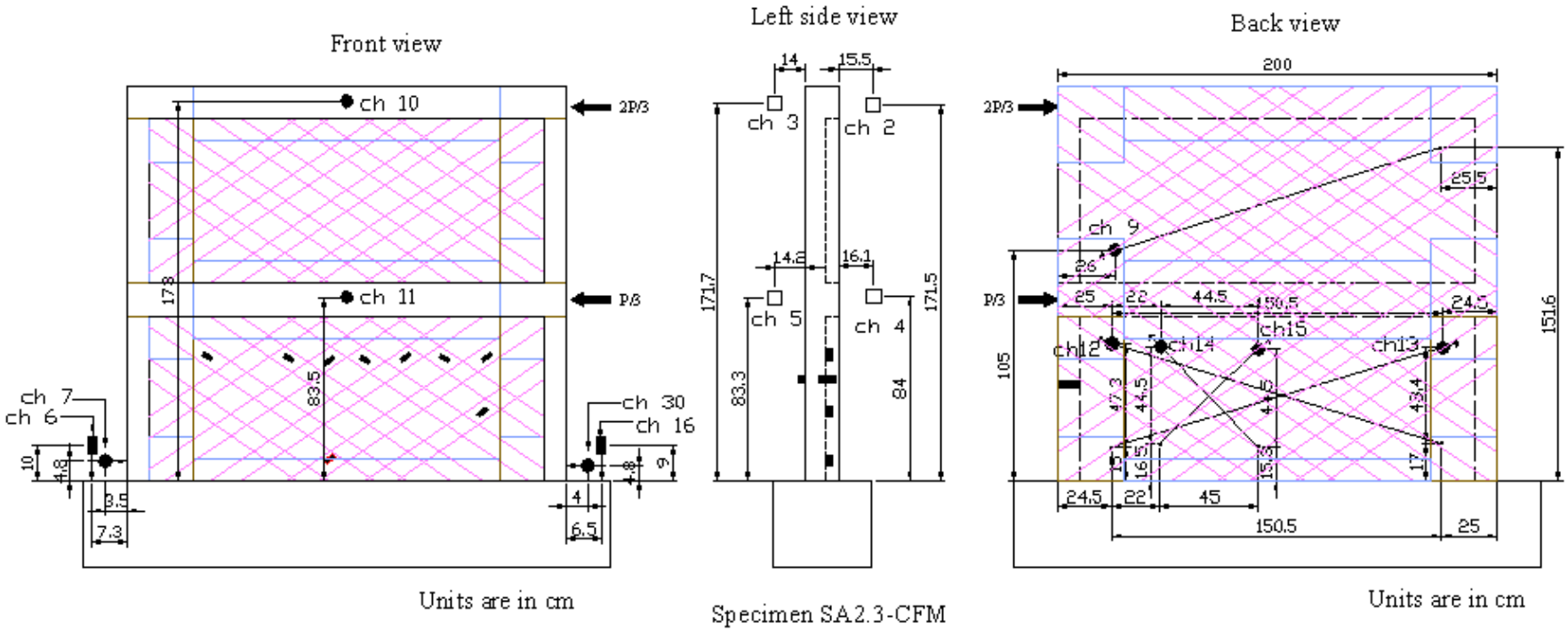

Figure A.10. Position of measuring sensors of specimen SA2.3-CFM

APPENDIX B: EXAMPLES OF THE CAPACITY CALCULATIONS

B.1. Capacity Calculation of Specimen SA1.0-CV

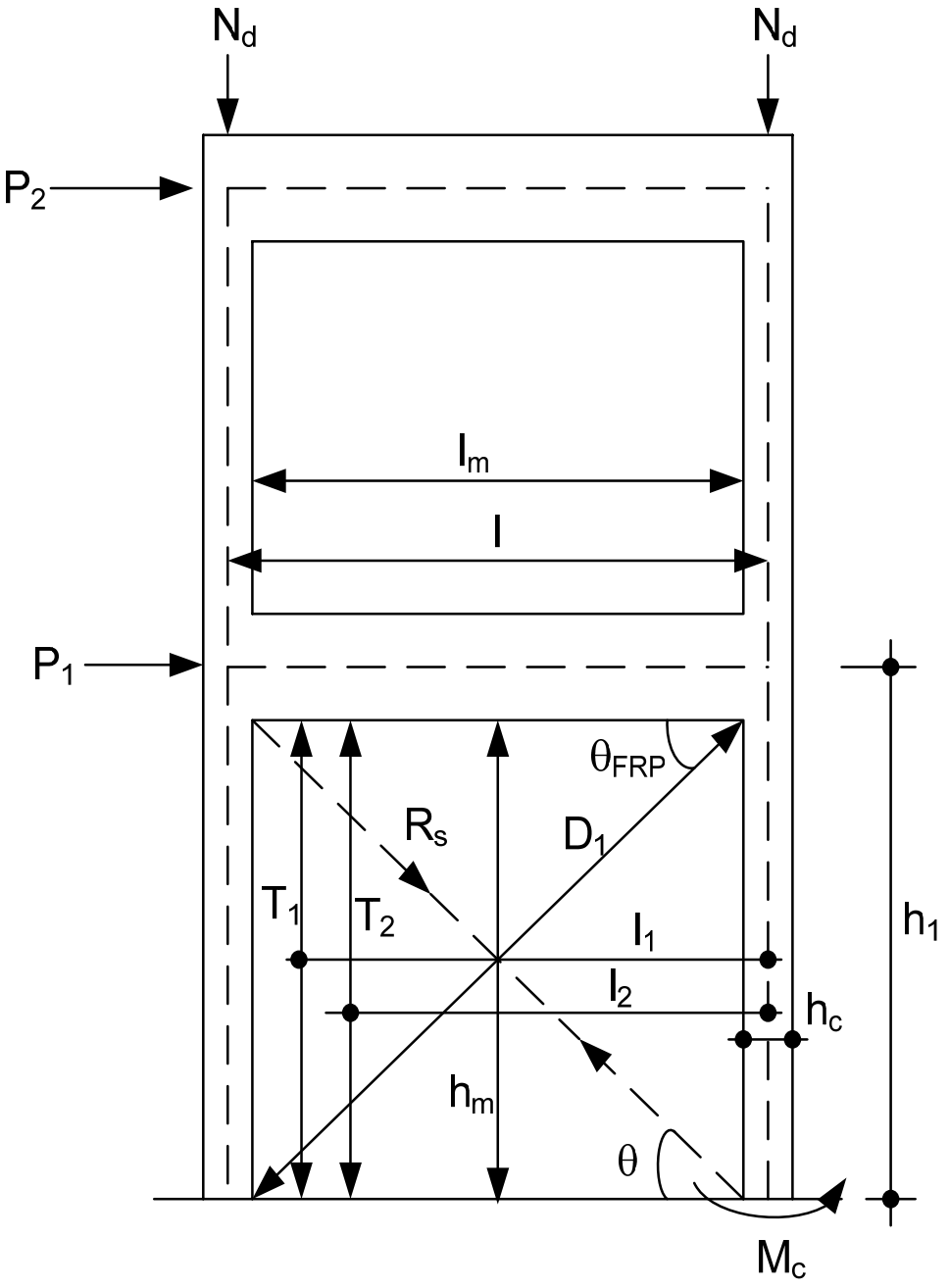

Figure B.1. Variables of Specimen SA1.0-CV

Table B.1. Mechanical and geometric properties of specimen SA1.0-CV

Geometric Properties (SA1.0-CV)		**Mechanical Properties (SA1.0-CV)**			
Infill		**Masonry, Steel, Concrete**		**Cross FRP**	
		E_{bmp} (Mpa)	5130		
l_m (mm)	730	f_{bmp} (Mpa)	4.6		
h_m (mm)	750	f_m (Mpa)	5.2	ε_{FRP}	0.0045
d_m (mm)	1046.6	μ	0.3	E_{FRP} (Mpa)	230000
θ_strut (rad)	0.799	τ_{bm} (Mpa)	0.43	t_{FRP} (mm)	0.13
Frame		τ_p (Mpa)	0.23	b_{wFRP} (mm)	200
		E_c (Mpa)	23696	θ_{FRP}(rad)	0.799
l (mm)	830	I_g (mm^4)	12500000		
h_1 (mm)	825	E_s (Mpa)	195000	**Vertical FRP on the Wall**	
b_c (mm)	150	f_{ywk} (Mpa)	241		
h_c (mm)	100	f_{yk} (Mpa)	347	ε_{FRP}	0.0045
A_s (mm^2)	201	f_{ck} (Mpa)	8.9	E_{FRP} (Mpa)	230000
s_c (mm)	95	f_{ctk} (Mpa	1.04	t_{FRP} (mm)	0.13
d_c (mm)	80	N_d (kN)	14.7	b_{wFRP} (mm)	50

$$\theta = \tan^{-1}(\frac{750}{730}) = 0.799 \; radian$$

$$f_{bm} = 0.1063 \times 5.2 + 3.8875 = 4.4 \text{ MPa}$$ Linear Regression

$$f_p = f_m = 5.2 \text{ MPa}$$ Experimental Test

$$f_{bmp} = 4.4 \times \frac{70}{70 + 2 \times 8.5} + 5.2 \times \frac{2 \times 8.5}{70 + 2 \times 8.5} = 4.6 \text{ MPa}$$

k=1.49 (Equation 5.26)

$$f_{bmpF} = 4.6 \times 1.49 = 6.82 \text{ MPa}$$ (Equation 5.21)

$$E_{bm} = 750 \times 4.4 = 3330.2 \text{ MPa}$$ (Equation 5.1)

$$E_p = 5500\sqrt{5.2} = 12541.9 \text{ MPa}$$ (Equation 5.2)

$$E_{bmp} = 3330.2 \times \frac{70}{70 + 2 \times 8.5} + 12541.9 \times \frac{2 \times 8.5}{70 + 2 \times 8.5} = 5130 \text{ MPa}$$ (Equation 5.3)

$$\tau_{bm} = (0.0133 \times 5.2 + 1.3783) \times 0.3 = 0.43 \text{ MPa} \quad \text{(Equation 5.23)}$$

$$\tau_p = 0.15 \times (5.2 \times 0.30) = 0.23\ MPa \quad \text{(Equation 5.25)}$$

R_s=14917.65 N (Equation 5.10)

$$Cos(0.799) = 0.697$$
$$Sin(0.799) = 0.717$$

$$R_s = \frac{1}{0.697 - 0.3 \times 0.717} \begin{Bmatrix} 0.43 \times 730 \times 70 + 0.23 \times 730 \times 17 \\ +2 \times 0.3 \times 0.13 \times 200 \times (0.0045 \times 230000) \times 0.717 \\ +4 \times 0.3 \times 0.13 \times 50 \times (0.0045 \times 230000) \\ -2 \times 0.13 \times 200 \times (0.0045 \times 230000) \times 0.697 \end{Bmatrix} = 14917.65\ N$$

$$V_f = \frac{(14917.65 \times 0.697 + 2 \times 0.13 \times 200 \times (0.0045 \times 230000) \times 0.697)}{1000} = 47.94\ kN \quad \text{(Eq. 5.9)}$$

Stresses in reinforcing steel and corresponding plastic moments at different elevations can be calculated as follows:

$$f_{s\_bottom} = \frac{20 \times 8}{0.67 \times 0.24 \times 8 \times \frac{347}{1.04}} \times 347 = 130.5\ MPa \qquad M_{p\_bottom}=1.46 \text{ kN-m} \quad \text{(Eq. 5.6)}$$

$$f_{s\_middle} = \frac{46.9 \times 8}{0.67 \times 0.24 \times 8 \times \frac{347}{1.04}} \times 347 = 305.9\ MPa \qquad M_{p\_middle}=2.51 \text{ kN-m} \quad \text{(Eq. 5.6)}$$

$$f_{s\_top} = \frac{39 \times 8}{0.67 \times 0.24 \times 8 \times \frac{347}{1.04}} \times 347 = 254.5\ MPa \qquad M_{p\_top}=2.2 \text{ kN-m} \quad \text{(Eq. 5.6)}$$

Increasing deformations caused separation between columns and masonry panel and columns carried shear and moments. When sliding developed at the mid-height of the panel, shear due to plastic hinge moments at the top of the left column and at the bottom of the right column can be calculated as follows:

$$V_{up} = \frac{2.2 + 2.51}{(0.75/2)} = 12.56\ kN \qquad \text{(Equation 5.15)}$$

$$V_{down} = \frac{1.46 + 2.51}{(0.75/2)} = 10.59\ kN \qquad \text{(Equation 5.16)}$$

Shear capacity of column under compression (Equation 5.14);

$$V_{column\_comp.} = \frac{25.13}{95} \times 241 \times 80 + 0.8 \times (0.65 \times 1.04 \times 150 \times 80 \times \left[1 + 0.07 \times \frac{14700}{150 \times 100}\right]) = 12.06\ kN$$

Shear capacity of column under tension (Equation 5.14);

$$V_{column\_tension} = \frac{25.13}{95} \times 241 \times 80 + 0.8 \times (0.65 \times 1.04 \times 150 \times 80 \times \left[1 - 0.3 \times \frac{14700}{150 \times 100}\right]) = 9.70\ kN$$

Total shear force that can be carried by column under the combined action of moment, shear and axial loads;

$$V_{f-column} = 9.70 + 10.59 = 20.3\ kN \qquad \text{(Equation 5.17)}$$

Sliding shear failure load;

$$V_i = 47.94 + 20.3 = 68.2\ kN \qquad \text{(Equation 5.18)}$$

Contact length between column and panel;

$$z_{clm} = \frac{\pi}{2}\left(\frac{4 \times 23696 \times 1.25e + 7 \times 750}{5130.2 \times (70 + 17) \times \sin(2 \times 0.799)}\right)^{\frac{1}{4}} = 331.8\ mm \qquad \text{(Equation 5.19)}$$

The coefficient used to modify compressive strength of the masonry can be found as follows;

$$f_{bmpF} = f_{bmp} \times \left[\frac{0.67}{(830/825)} \times \left(\frac{280+280+200}{1046} \right) + 1 \right] = 4.6 \times 1.49 = 6.82\ MPa \quad \text{(Equation 5.21)}$$

Compression failure load of the diagonal strut;

$$R_c = \frac{2}{3} \times 331.8 \times (70+17) \times 6.82 \times \sec(0.799) = 188.3\ kN \quad \text{(Equation 5.20)}$$

Overturning failure load;

$$P = \frac{1}{\frac{825+2\times1725}{3}} \begin{Bmatrix} 14700\times830 + (100.5\times2)\times130.5\times830 \\ +2\times50\times0.13\times1035\times745 \\ +2\times50\times0.13\times1035\times605 \\ +2\times200\times0.13\times1035\times0.697\times825 + 1460000 \end{Bmatrix} = 59.3\ kN \quad \text{(Eq. 5.22)}$$

Minimum of V_i (68.2 kN), P (59.3 kN), and R_c*cos(0.799) (131.3 kN) is called the analytical failure load.

B.2. Capacity Calculation of Specimen SA2.3-CCM

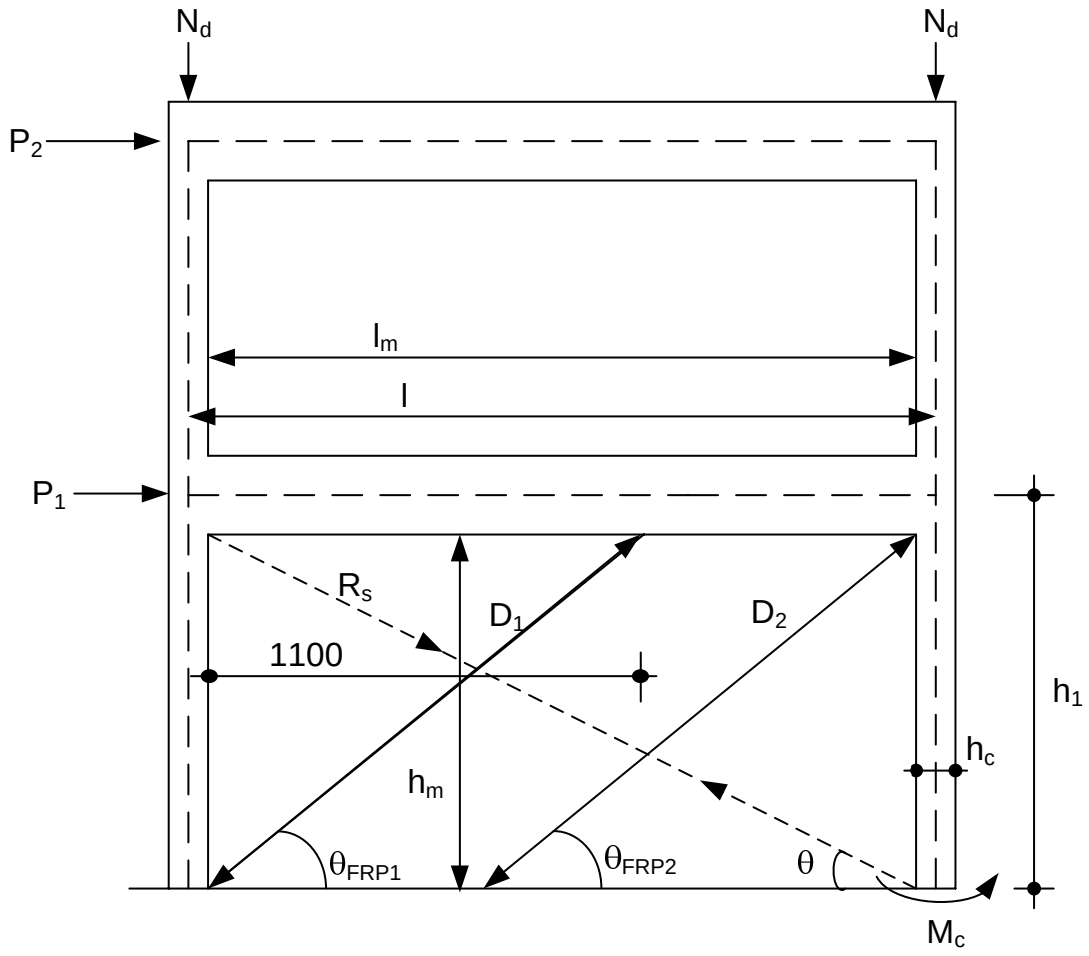

Figure B.2. Variables of specimen SA2.3-CCM

Table B.2. Mechanical and geometric properties of specimen SA2.3-CCM

Geometric Properties (SA2.3-CCM)		**Mechanical Properties (SA2.3-CCM)**			
Infill		**Masonry, Steel, Concrete**		**Cross FRP_1**	
		E_{bmp} (Mpa)	6630.5		
l_m (mm)	1800	f_{bmp} (Mpa)	6.1		
h_m (mm)	750	f_m (Mpa)	10.5	ε_{FRP1}	0.0045
d_m (mm)	1950.0	μ	0.3	E_{FRP1} (Mpa)	230000
θ_strut (rad)	0.395	τ_{bm} (Mpa)	0.46	t_{FRP1} (mm)	0.13
Frame		τ_p (Mpa)	0.47	b_{wFRP1} (mm)	200
		E_c (Mpa)	27000	$\theta_{FRP1,}$ θ_{FRP2} (rad)	0.598
l (mm)	1900	I_g (mm^4)	12500000	**Cross FRP_2**	
h_1 (mm)	825	E_s (Mpa)	195000		
b_c (mm)	150	f_{ywk} (Mpa)	241		
h_c (mm)	100	f_{yk} (Mpa)	347	ε_{FRP2}	0.0045
A_s (mm^2)	201	f_{ck} (Mpa)	16	E_{FRP2} (Mpa)	230000
s_c (mm)	95	f_{ctk} (Mpa	1.40	t_{FRP2} (mm)	0.13
d_c (mm)	80	N_d (kN)	24.0	b_{wFRP2} (mm)	200

$f_{bm} = 0.1063 \times 10.5 + 3.8875 = 5.0$ MPa — Linear Regression

$f_p = f_m = 10.5$ MPa — Experimental Test

$$f_{bmp} = 5.0 \times \frac{70}{70 + 2 \times 9.0} + 10.5 \times \frac{2 \times 9.0}{70 + 2 \times 9.0} = 6.1 \text{ MPa}$$

k=1.14 (Equation 5.26)

$f_{bmpF} = 6.1 \times 1.14 = 6.96$ MPa (Equation 5.21)

$E_{bm} = 750 \times 5.0 = 3752.7$ MPa (Equation 5.1)

$E_p = 5500\sqrt{10.5} = 17822.0$ MPa (Equation 5.2)

$$E_{bmp} = 3752.7 \times \frac{70}{70 + 2 \times 9.0} + 17822.0 \times \frac{2 \times 9.0}{70 + 2 \times 9.0} = 6630.5 \text{ MPa}$$ (Equation 5.3)

$\tau_{bm} = (0.0133 \times 10.5 + 1.3783) \times 0.3 = 0.46$ MPa (Equation 5.23)

$$\tau_p = 0.15 \times (10.5 \times 0.30) = 0.47\ MPa$$ (Equation 5.25)

R_s=2.41 kN (Equation 5.30)

$$R_s = \frac{1}{0.923 - 0.3 \times 0.385} \left\{ \begin{array}{l} 0.4554 \times 1800 \times 70 + 0.4725 \times 1800 \times 18 \\ + \sum_{i=1}^{2} 2 \times 0.3 \times 0.13 \times 200 \times 1035 \times \sin(0.598^R) \\ - \sum_{i=1}^{2} 2 \times 0.13 \times 200 \times 1035 \times Cos(0.598^R) \end{array} \right\} = 2.41\ kN$$

$$V_f = 2406 \times 0.923 + \sum_{i=1}^{2} 2 \times 0.13 \times 200 \times 1035 \times 0.826 = 91.2\ kN$$ (Equation 5.29)

$$f_{s\_bottom} = \frac{20 \times 8}{0.67 \times 0.24 \times 8 \times \frac{347}{1.40}} \times 347 = 175\ MPa$$ M_{p_bottom}=2.18 kN-m (Equation 5.6)

$$f_{s\_middle} = \frac{46.9 \times 8}{0.67 \times 0.24 \times 8 \times \frac{347}{1.40}} \times 347 > 347; \Rightarrow f_{s\_middle} = 347\ MPa$$; M_{p_middle}=3.22 kN-m (5.6)

$$f_{s\_top} = \frac{39 \times 8}{0.67 \times 0.24 \times 8 \times \frac{347}{1.40}} \times 347 = 341.3\ MPa$$ M_{p_top}=3.18 kN-m (Equation 5.6)

$$V_{up} = \frac{3.18 + 3.22}{(0.75/2)} = 17.07\ kN$$ (Equation 5.15)

$$V_{down} = \frac{2.18 + 3.22}{(0.75/2)} = 14.40\ kN$$ (Equation 5.16)

Shear capacity of column under compression (Equation 5.14);

$$V_{column\_comp.} = \frac{25.13}{95} \times 241 \times 80 + 0.8 \times (0.65 \times 1.40 \times 150 \times 80 \times \left[1 + 0.07 \times \frac{24000}{150 \times 100} \right]) = 14.82 \ kN$$

Shear capacity of column under tension (Equation 5.14);

$$V_{column\_tension} = \frac{25.13}{95} \times 241 \times 80 + 0.8 \times (0.65 \times 1.40 \times 150 \times 80 \times \left[1 - 0.3 \times \frac{24000}{150 \times 100} \right]) = 9.64 \ kN$$

Total shear force that can be carried by column under the combined action of moment, shear and axial loads;

$$V_{f-column} = 9.64 + 14.40 = 24.0 \ kN \qquad \text{(Equation 5.17)}$$

$$V_i = 91.2 + 24.0 = 115.2 \ kN \qquad \text{(Equation 5.18)}$$

Contact length between column and panel;

$$z_{clm} = \frac{\pi}{2} \left(\frac{4 \times 27000 \times 1.25e + 7 \times 750}{6630.5 \times (70 + 18) \times \sin(2 \times 0.395)} \right)^{\frac{1}{4}} = 349.2 \ mm \qquad \text{(Equation 5.19)}$$

The coefficient used to modify compressive strength of the masonry can be found as follows;

$$f_{bmpF} = f_{bmp} \times \left[\frac{0.67}{(1900/825)} \times \left(\frac{217 + 217 + 239 + 239}{1950} \right) + 1 \right] = 6.1 \times 1.14 = 6.96 \text{ MPa} \quad \text{(Eq. 5.21)}$$

Compression failure load of the diagonal strut;

$$R_c = \frac{2}{3} \times 349.2 \times (70 + 18) \times 6.96 \times \sec(0.395) = 154.6 \ kN \qquad \text{(Equation 5.20)}$$

Overturning failure load (Equation 5.31);

$$P = \frac{1}{\frac{825+2\times1725}{3}} \left\{ \begin{array}{l} 24000\times1900+2\times100.5\times175\times1900 \\ +2\times200\times0.13\times1035\times0.826\times825 \\ +2\times200\times0.13\times1035\times0.563\times(1900-1100-\frac{100}{2}-110) \\ +2\times200\times0.13\times1035\times0.826\times825+2188000 \end{array} \right\} = 145.55\ kN$$

Failure load should be the minimum of (P=145.55 kN, R_c*cos(0.395)=142.7 kN, V_i=115.2 kN).

B.3. Capacity Calculation of Specimen SA2.3-CFM

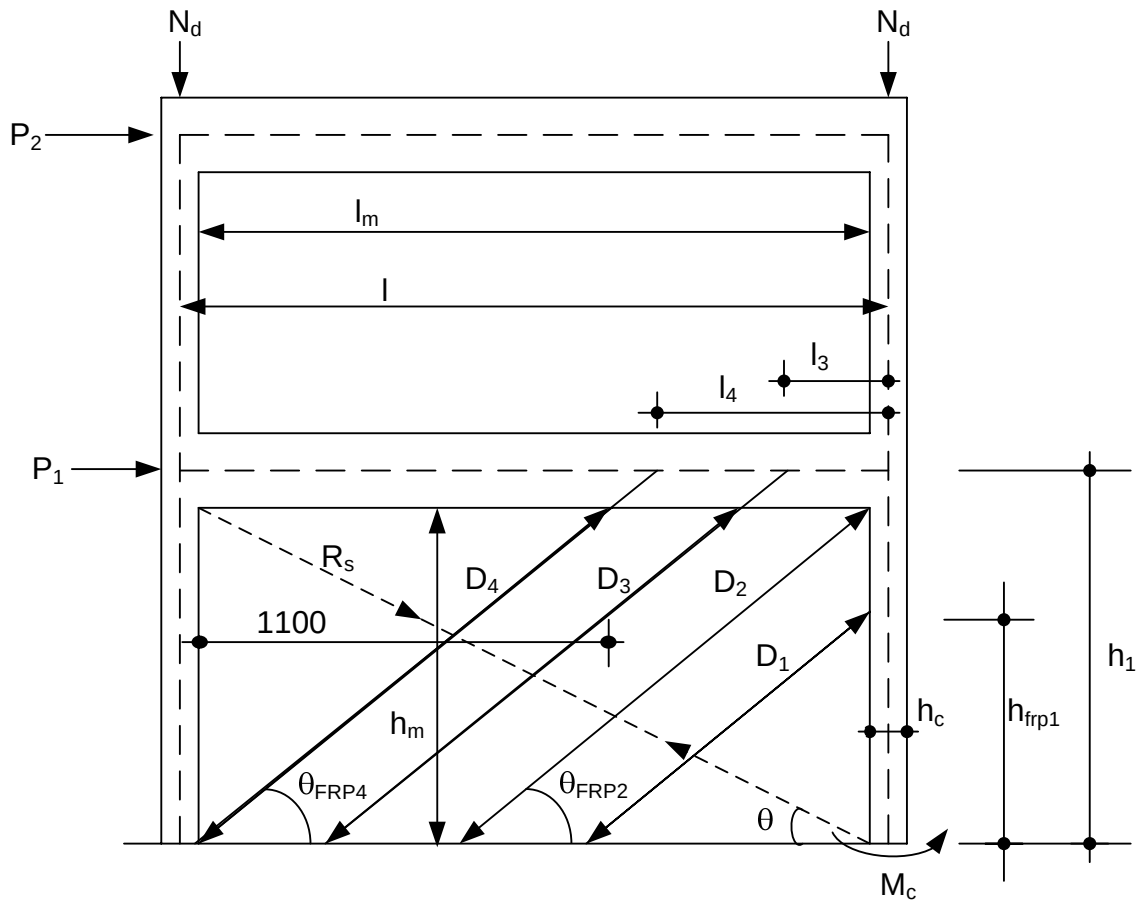

Figure B.3. Variables of specimen SA2.3-CFM

Table B.3. Mechanical and geometric properties of specimen SA2.3-CFM

Geometric Properties (SA2.3-CFM)		**Mechanical Properties (SA2.3-CFM)**			
Infill		**Masonry, Steel, Concrete**		**Cross FRP_1 and 2**	
		E_{bmp} (Mpa)	5786.8		
l_m (mm)	1800	f_{bmp} (Mpa)	5.0		
h_m (mm)	750	f_m (Mpa)	6.5	ε_{FRP1-2}	0.0045
d_m (mm)	1950.0	μ	0.3	E_{FRP1-2} (Mpa)	230000
θ_strut (rad)	0.395	τ_{bm} (Mpa)	0.44	t_{FRP1-2} (mm)	0.13
Frame		τ_p (Mpa))	0.29	$b_{wFRP1-2}$ (mm)	80
		E_c (Mpa)	27789	θ_{FRP1-2}, θ_{FRP3-4} (rad)	0.598
l (mm)	1900	I_g (mm^4)	12500000	**Cross FRP_3 and 4**	
h_1 (mm)	825	E_s (Mpa)	195000		
b_c (mm)	150	f_{ywk} (Mpa)	241		
h_c (mm)	100	f_{yk} (Mpa)	347	ε_{FRP3-4}	0.0045
A_s (mm^2)	201	f_{ck} (Mpa)	18	E_{FRP3-4} (Mpa)	230000
s_c (mm)	95	f_{ctk} (Mpa	1.48	t_{FRP3-4} (mm)	0.13
d_c (mm)	80	N_d (kN)	27.0	$b_{wFRP3-4}$ (mm)	80

$f_{bm} = 0.1063 \times 6.5 + 3.8875 = 4.6$ MPa — Linear Regression

$f_p = f_m = 6.5$ MPa — Experimental Test

$$f_{bmp} = 4.6 \times \frac{70}{70 + 2 \times 10} + 6.5 \times \frac{2 \times 10}{70 + 2 \times 10} = 5.0 \text{ MPa}$$

k=1.14 (Equation 5.26)

$f_{bmpF} = 5.0 \times 1.14 = 5.69$ MPa (Equation 5.21)

$E_{bm} = 750 \times 4.6 = 3433.8$ MPa (Equation 5.1)

$E_p = 5500\sqrt{6.5} = 14022.3$ MPa (Equation 5.2)

$$E_{bmp} = 3433.8 \times \frac{70}{70 + 2 \times 10} + 14022.3 \times \frac{2 \times 10}{70 + 2 \times 10} = 5786.8 \text{ MPa} \quad \text{(Equation 5.3)}$$

$$\tau_{bm} = (0.0133 \times 6.5 + 1.3783) \times 0.3 = 0.44 \text{ MPa} \quad \text{(Equation 5.23)}$$

$$\tau_p = 0.15 \times (6.5 \times 0.30) = 0.29 \ MPa \quad \text{(Equation 5.25)}$$

R_s=11.5 kN (Equation 5.34)

$$R_s = \frac{1}{0.923 - 0.3 \times 0.38462} \left\{ \begin{array}{l} 0.44 \times 1800 \times 70 + 0.29 \times 1800 \times 20 \\ + \sum_{i=1}^{4} 2 \times 0.3 \times 0.13 \times 80 \times 1035 \times \sin(0.598^R) \\ - \sum_{i=1}^{4} 2 \times 0.13 \times 80 \times 1035 \times \cos(0.598^R) \end{array} \right\} = 11.5 \ kN$$

$$V_f = 11500 \times \cos(0.395) + \sum_{i=1}^{4} 2 \times 0.13 \times 80 \times 1035 \times \cos(0.598) = 81.8 \ kN \quad \text{(Equation 5.33)}$$

$$f_{s\_bottom} = \frac{20 \times 8}{0.67 \times 0.24 \times 8 \times \frac{347}{1.48}} \times 347 = 185.6 \ MPa \quad M_{p\_bottom}=2.39 \text{ kN-m} \quad \text{(Equation 5.6)}$$

$$f_{s\_middle} = \frac{46.9 \times 8}{0.67 \times 0.24 \times 8 \times \frac{347}{1.48}} \times 347 > 347; \Rightarrow \ f_{s\_middle}=347 \ MPa \ ; M_{p\_middle}=3.36 \text{ kN-m} \ (5.6)$$

$$f_{s\_top} = \frac{39 \times 8}{0.67 \times 0.24 \times 8 \times \frac{347}{1.48}} \times 347 > 347 \text{ thus } f_{s\_top}=347 \ MPa \quad M_{p\_top}=3.36 \text{ kN-m} \ \text{(Eq. 5.6)}$$

$$V_{up} = \frac{3.36 + 3.36}{(0.75/2)} = 17.9 \ kN \quad \text{(Equation 5.15)}$$

$$V_{down} = \frac{2.39 + 3.36}{(0.75/2)} = 15.3 \ kN \quad \text{(Equation 5.16)}$$

Shear capacity of column under compression (Equation 5.14);

$$V_{column\_comp.} = \frac{25.13}{95} \times 241 \times 80 + 0.8 \times (0.65 \times 1.48 \times 150 \times 80 \times \left[1 + 0.07 \times \frac{27000}{150 \times 100} \right]) = 15.5 \ kN$$

Shear capacity of column under tension (Equation 5.14);

$$V_{column\_tension} = \frac{25.13}{95} \times 241 \times 80 + 0.8 \times (0.65 \times 1.48 \times 150 \times 80 \times \left[1 - 0.3 \times \frac{27000}{150 \times 100} \right]) = 9.36 \ kN$$

Total shear force that can be carried by column under the combined action of moment, shear and axial loads;

$$V_{f-column} = 9.36 + 15.3 = 24.7 \ kN \qquad \text{(Equation 5.17)}$$

$$V_i = 81.8 + 24.7 + (100 \times 0.13 \times 4 \times 230000 \times 0.003 / 1000) = 142.4 \ kN \quad \text{(Eq. 5.18 and Eq. 5.36)}$$

Contact length between column and panel;

$$z_{clm} = \frac{\pi}{2} \left(\frac{4 \times 27789 \times 1.25e + 7 \times 750}{5786.8 \times (70 + 20) \times \sin(2 \times 0.395)} \right)^{\frac{1}{4}} = 361.9 \ mm \qquad \text{(Equation 5.19)}$$

The coefficient used to modify compressive strength of the masonry can be found as follows;

$$f_{bmpF} = f_{bmp} \times \frac{0.67}{(1900/825)} \times \left(\frac{217 + 217 + 95 \times 5}{1950} \right) + 1 = 5.0 \times 1.14 = 5.69 \ MPa \quad \text{(Equation 5.21)}$$

Compression failure load of the diagonal strut;

$$R_c = \frac{2}{3} \times 361.9 \times (70 + 20) \times 5.69 \times \sec(0.395) = 133.7 \ kN \qquad \text{(Equation 5.20)}$$

Overturning failure load (Equation 5.35);

$$P = \frac{1}{\frac{2\times 1725+825}{3}} \left\{ \begin{array}{l} 27000\times 1900 + 201\times 185.6\times 1900 + 2390000 \\ +2\times 0.13\times 80\times 1035\times \cos(0.598^R)\times 508 \\ +2\times 0.13\times 80\times 1035\times \cos(0.598^R)\times 825 \\ +2\times 0.13\times 80\times 1035\times (\cos(0.598^R)\times 825 + \sin(0.598^R)\times 290) \\ +2\times 0.13\times 80\times 1035\times (\cos(0.598^R)\times 825 + \sin(0.598^R)\times 640) \end{array} \right\} = 132.6\ kN$$

Failure load=min(P=132.6 kN, R_c*cos(0.395)=123.5 kN, V_i=142.4 kN)

APPENDIX C: BASE SHEAR VERSUS SHEAR DISTORTION ANGLE GRAPHS

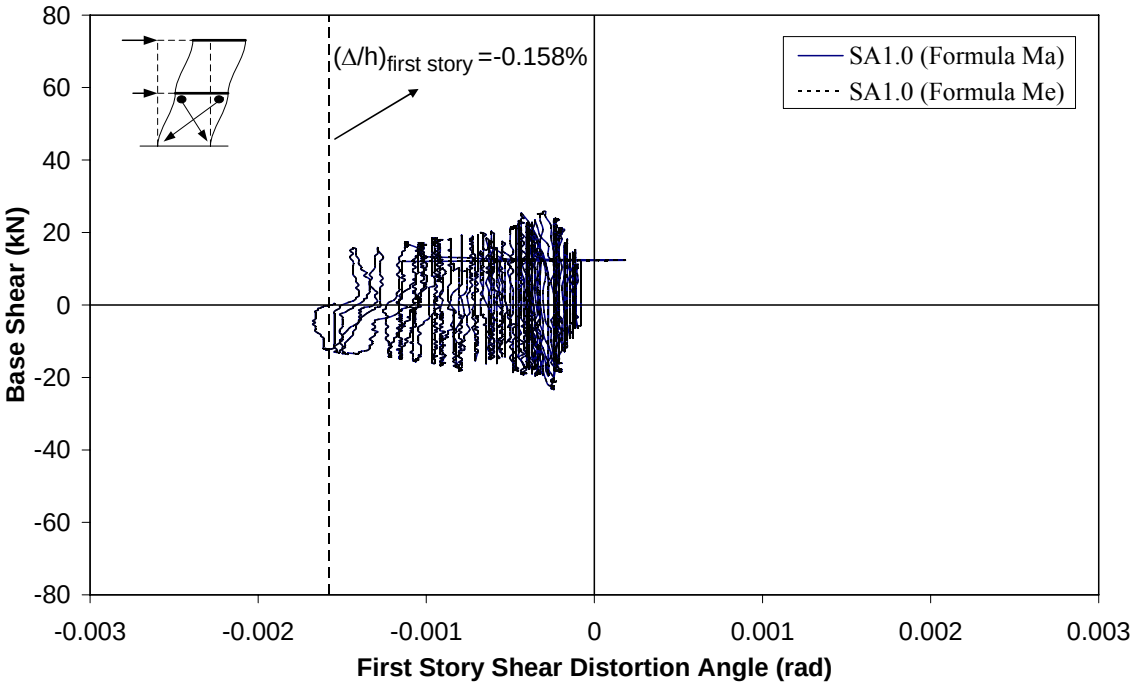

Figure C.1. Base shear versus 1st story shear distortion angle of specimen SA1.0

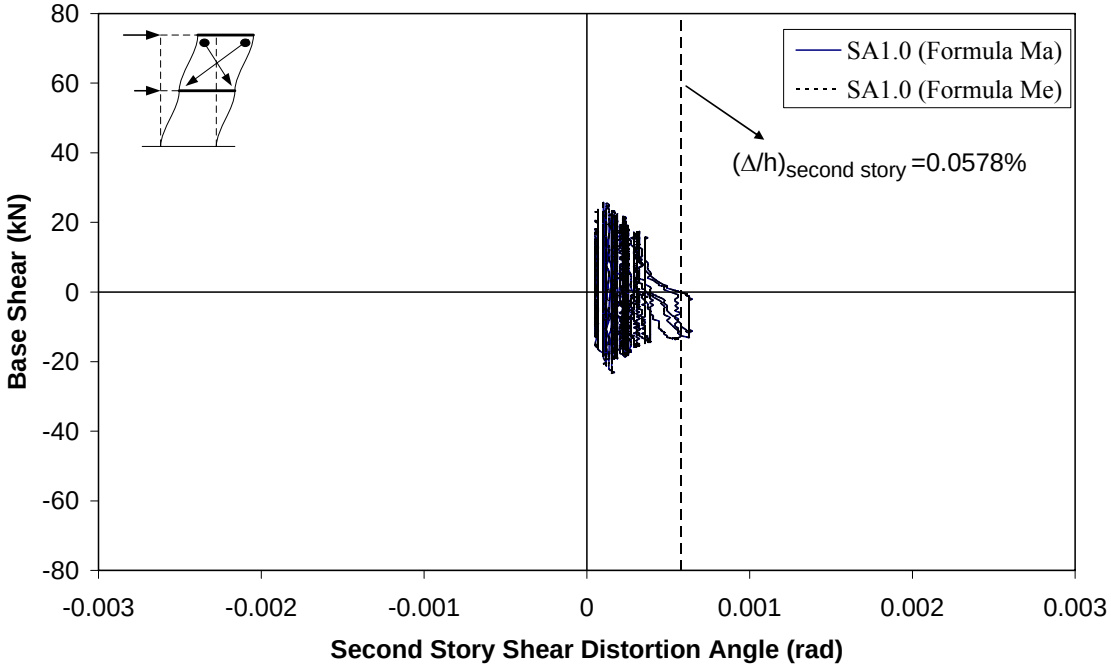

Figure C.2. Base shear versus 2nd story shear distortion angle of specimen SA1.0

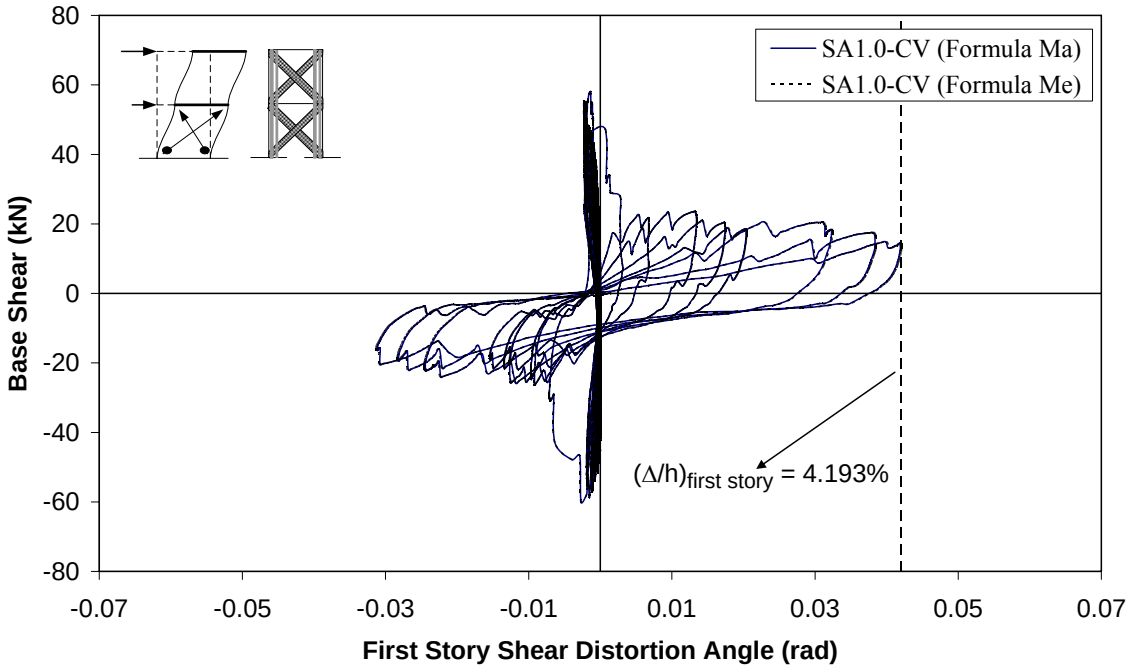

Figure C.3. Base shear versus 1st story shear distortion angle of specimen SA1.0-CV

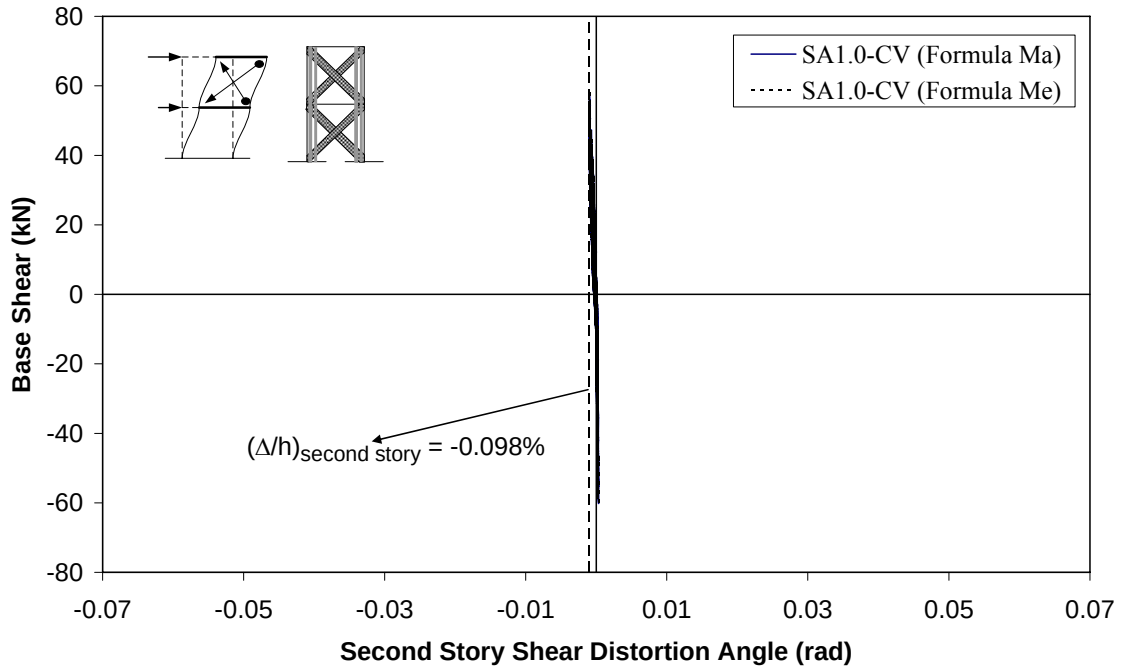

Figure C.4. Base shear versus 2nd story shear distortion angle of specimen SA1.0-CV

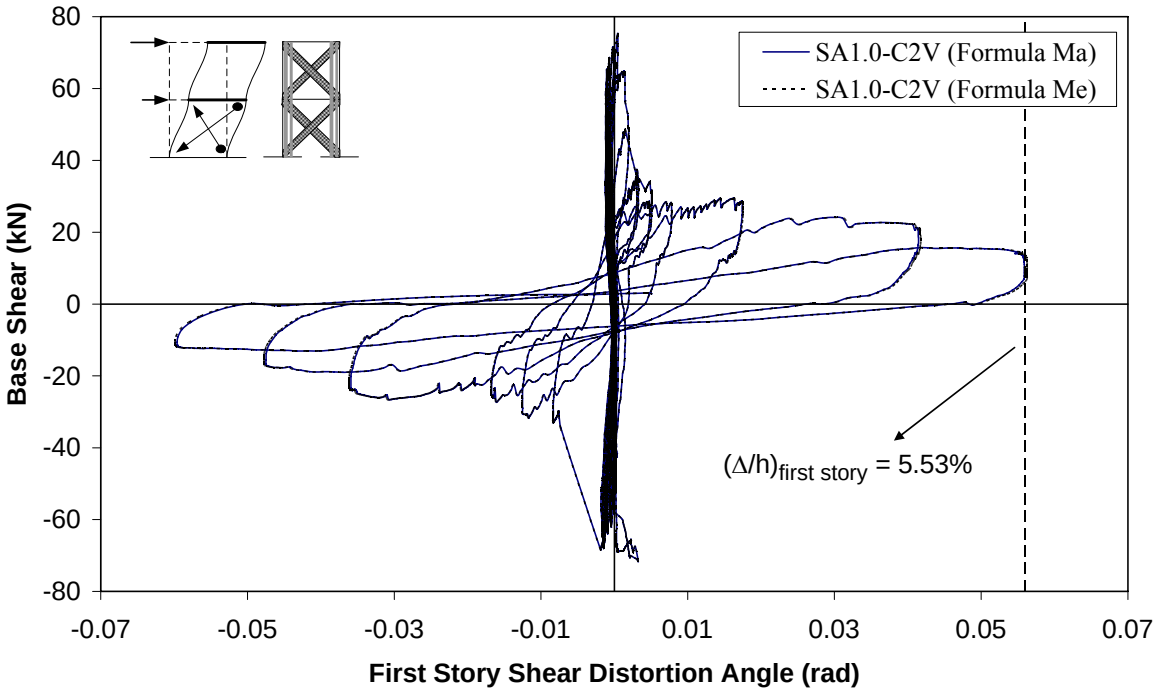

Figure C.5. Base shear versus 1st story shear distortion angle of specimen SA1.0-C2V

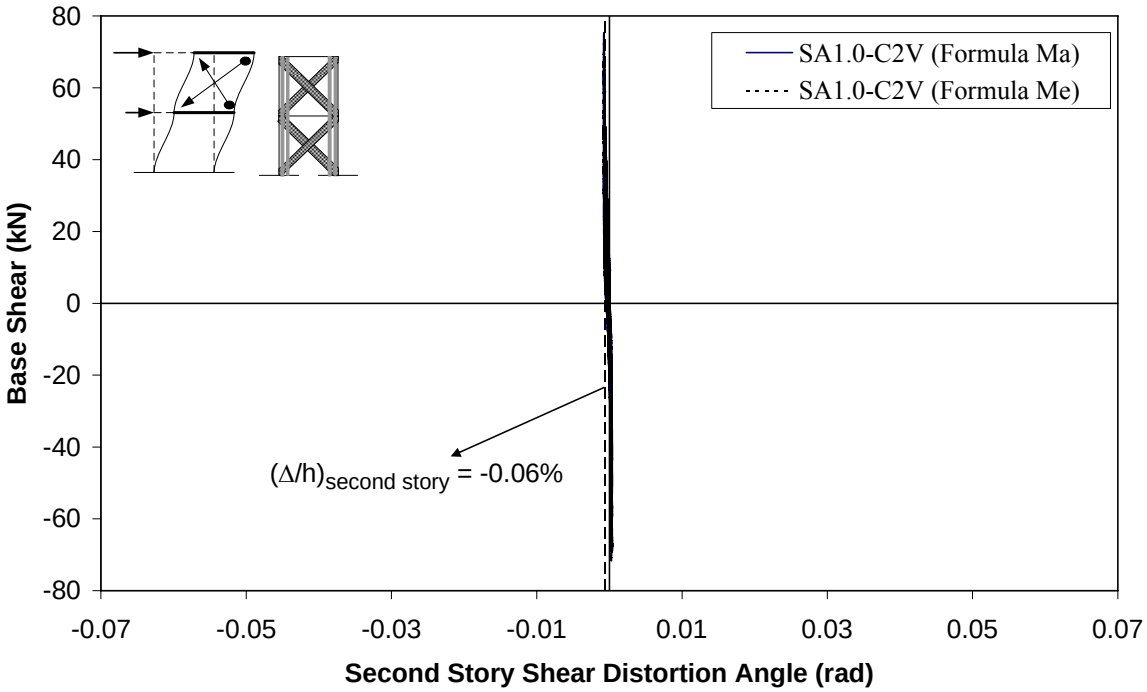

Figure C.6. Base shear versus 2nd story shear distortion angle of specimen SA1.0-C2V

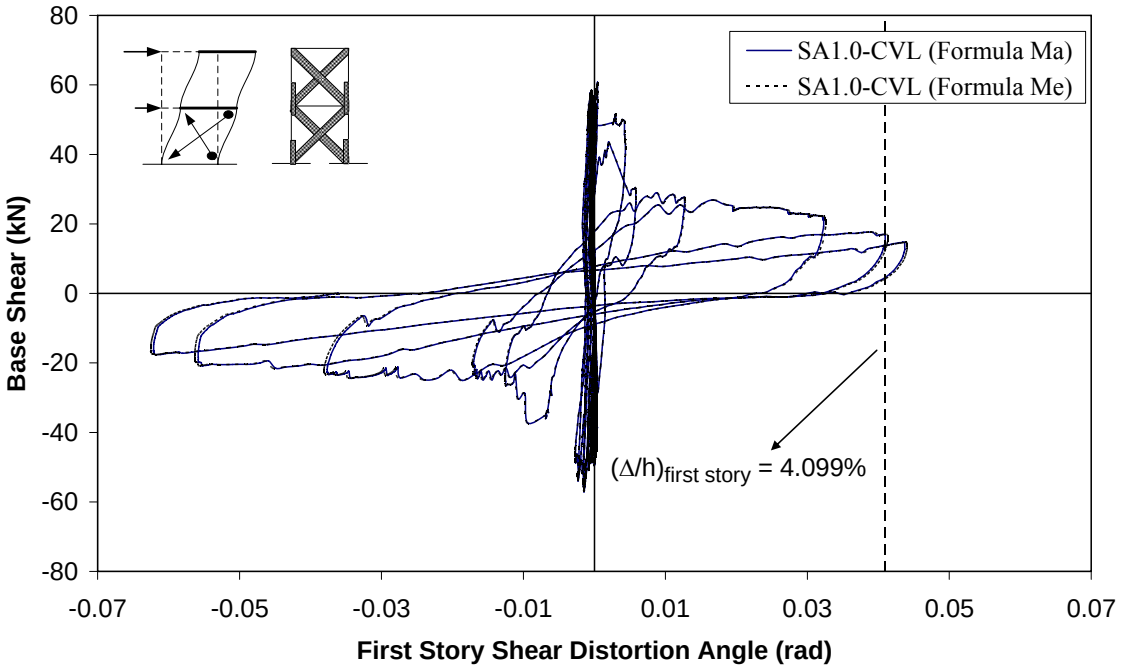

Figure C.7. Base shear versus 1st story shear distortion angle of specimen SA1.0-CVL

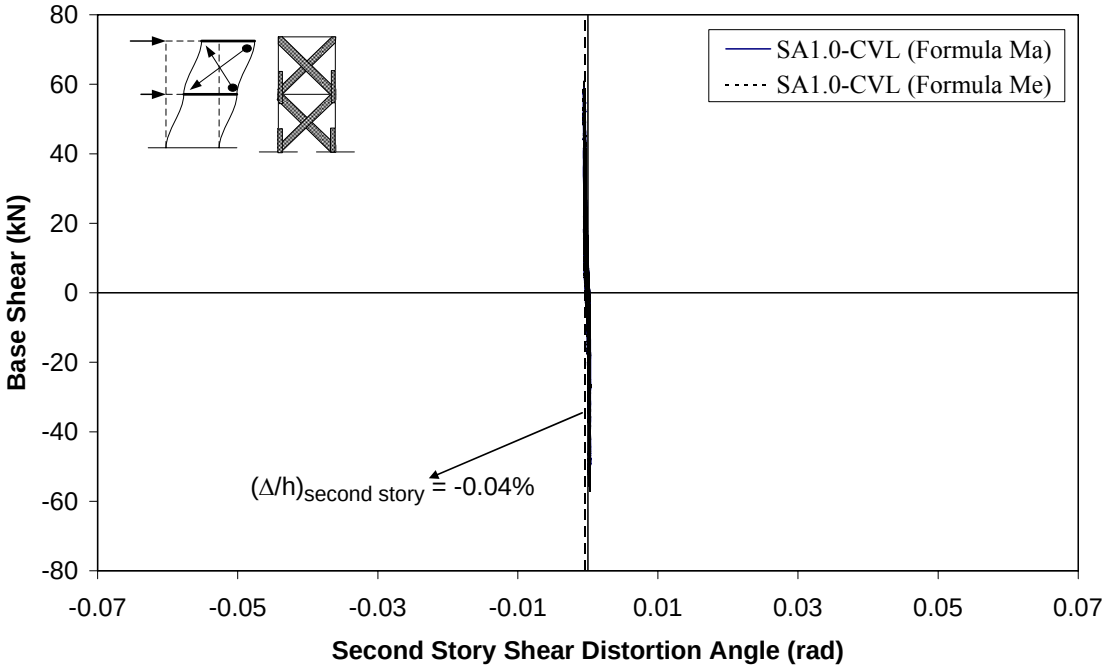

Figure C.8. Base shear versus 2nd story shear distortion angle of specimen SA1.0-CVL

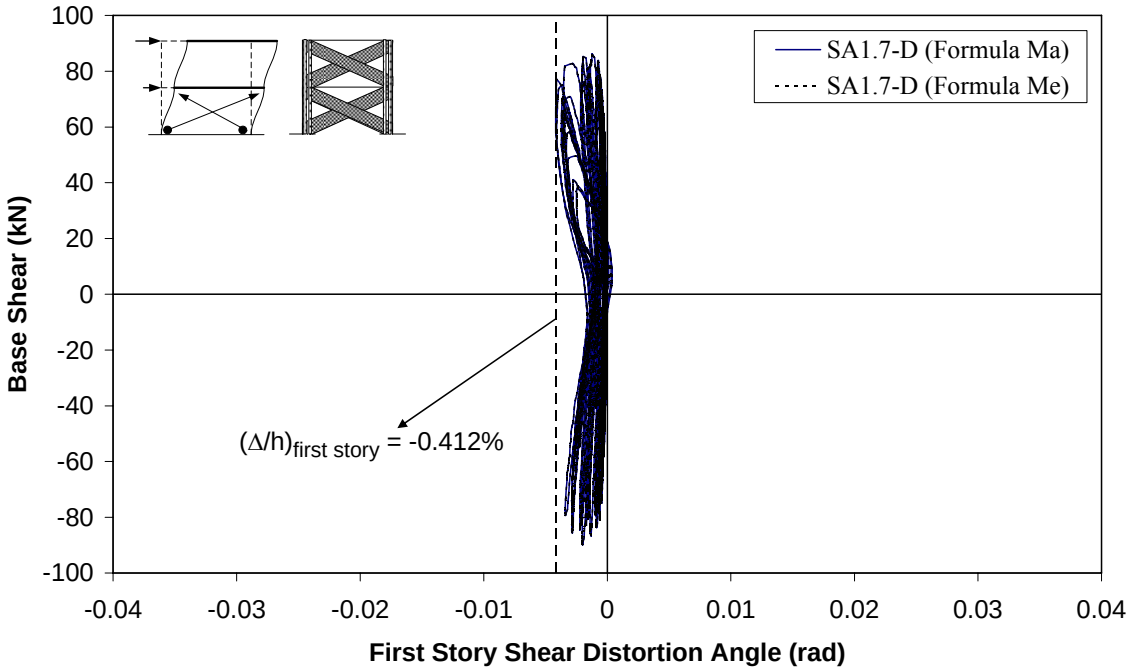

Figure C.9. Base shear versus 1st story shear distortion angle of specimen SA1.7-D

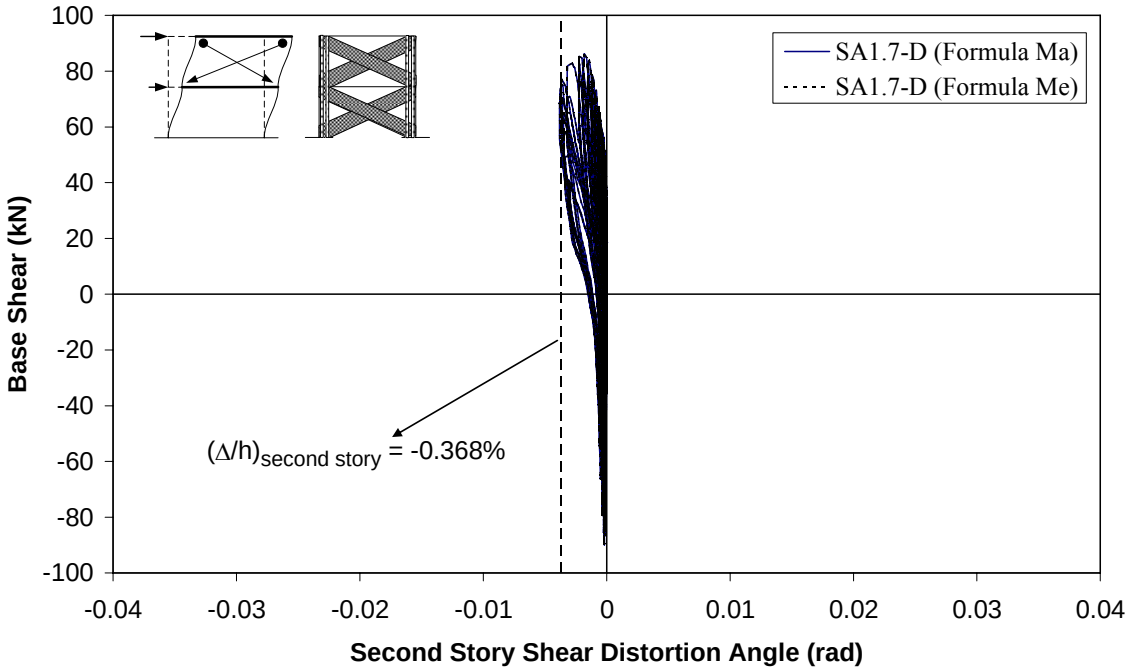

Figure C.10. Base shear versus 2nd story shear distortion angle of specimen SA1.7-D

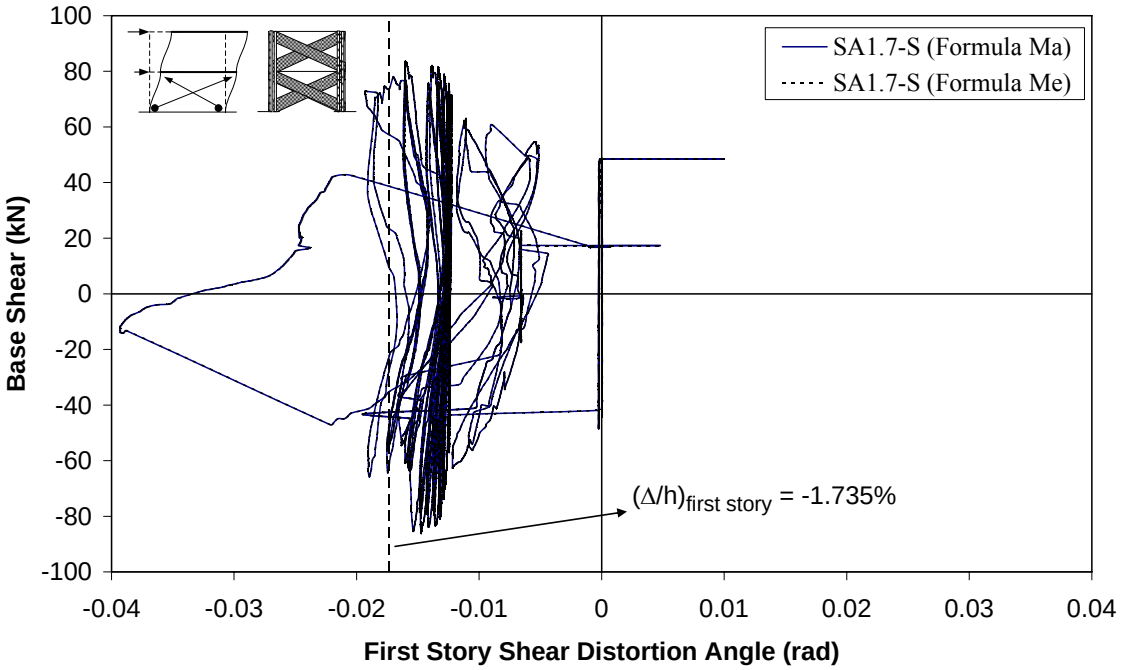

Figure C.11. Base shear versus 1st story shear distortion angle of specimen SA1.7-S

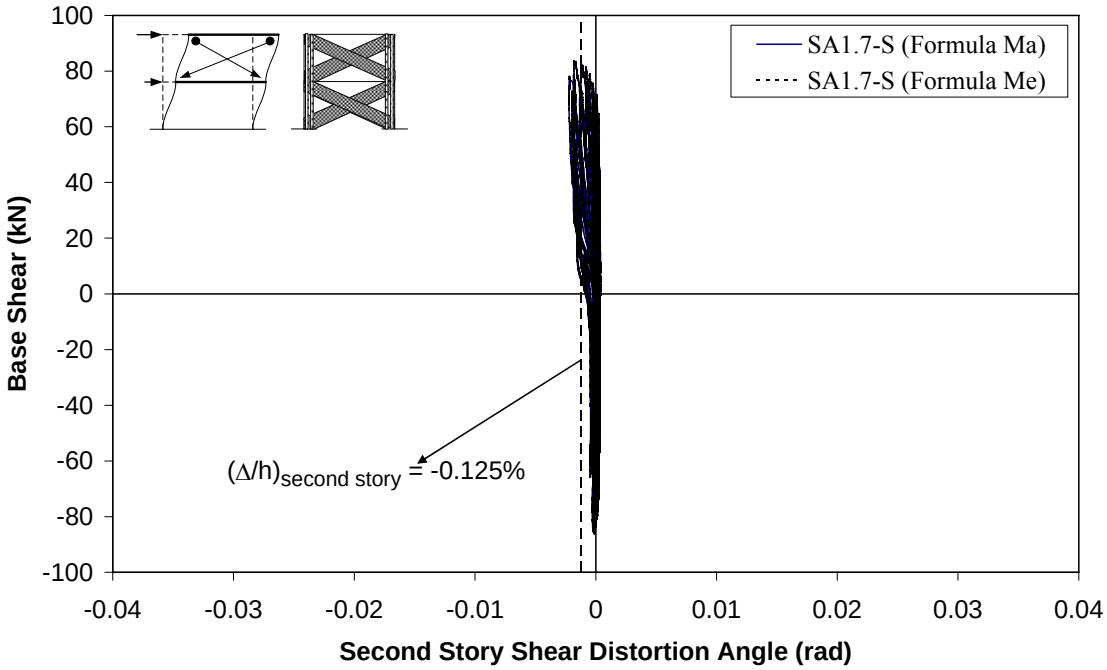

Figure C.12. Base shear versus 2nd story shear distortion angle of specimen SA1.7-S

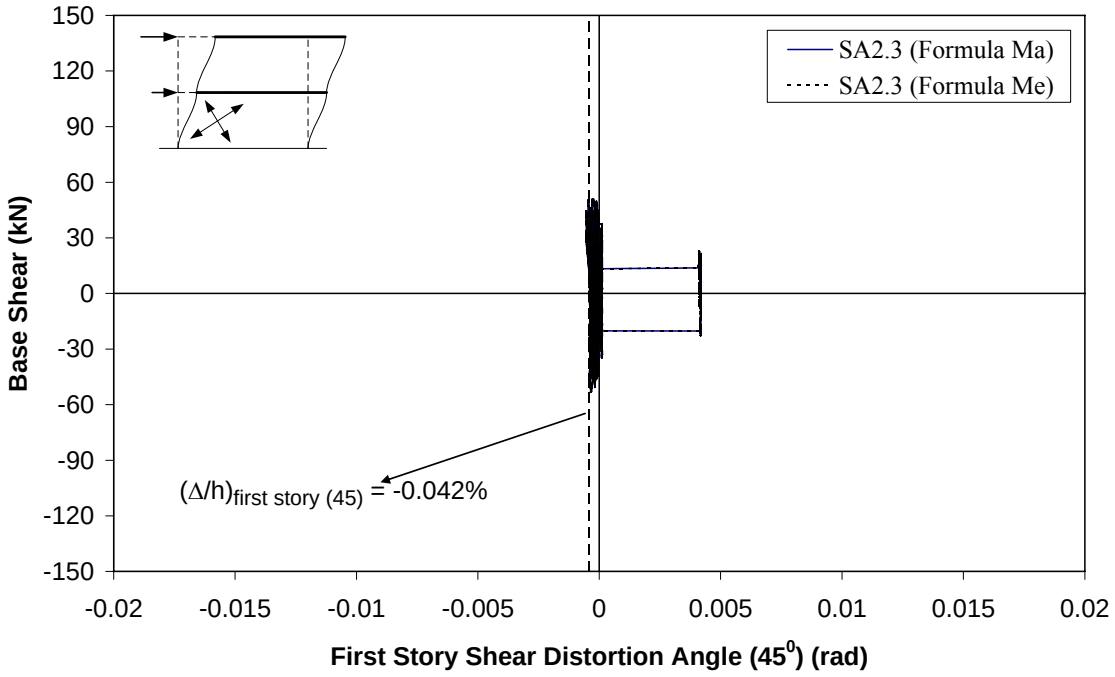

Figure C.13. Base shear versus 1st story shear distortion angle (45^0) of specimen SA2.3

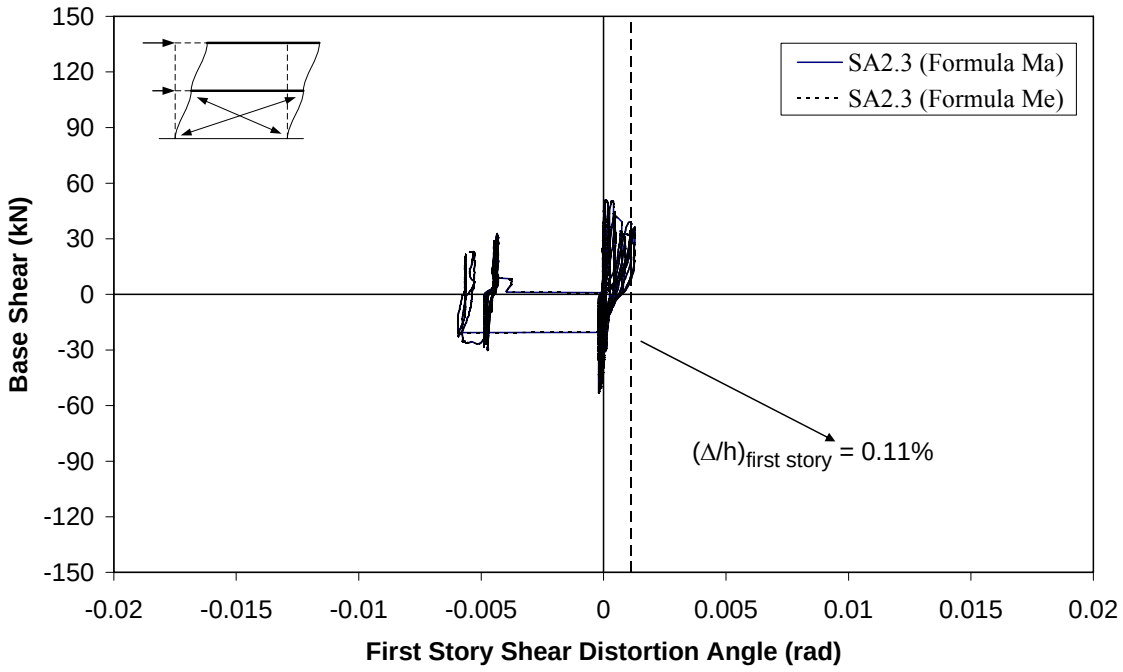

Figure C.14. Base shear versus 1st story shear distortion angle of specimen SA2.3

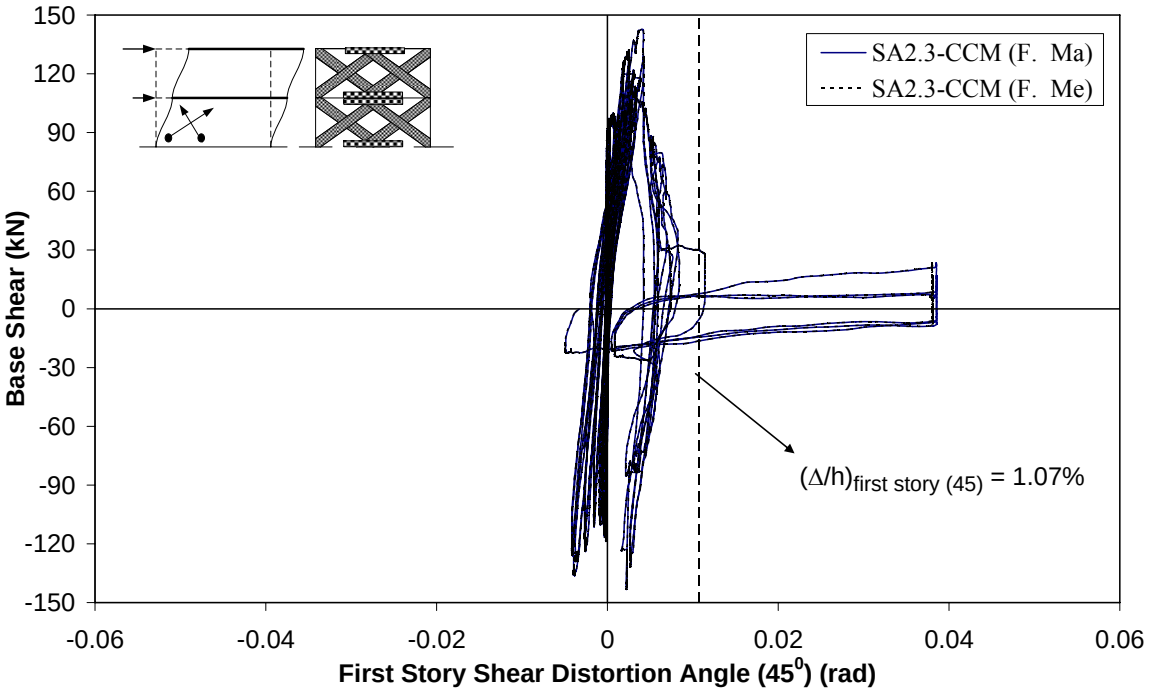

Figure C.15. Base shear versus 1st story shear distortion angle (45^0) of specimen SA2.3-CCM

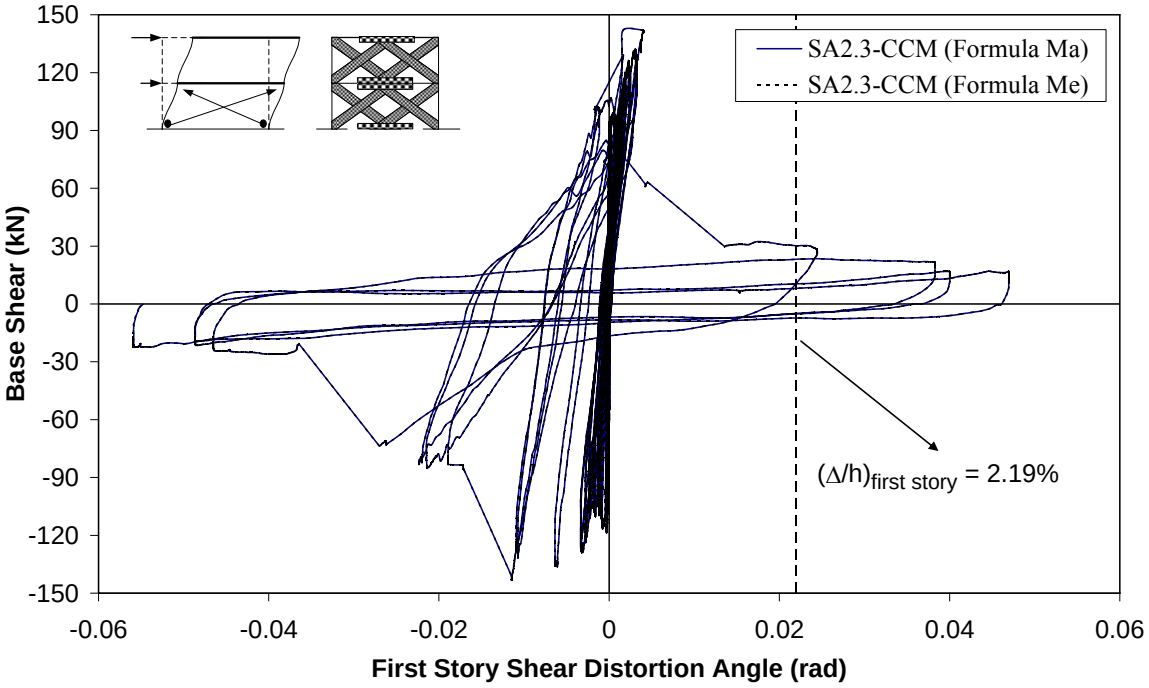

Figure C.16. Base shear versus 1st story shear distortion angle of specimen SA2.3-CCM

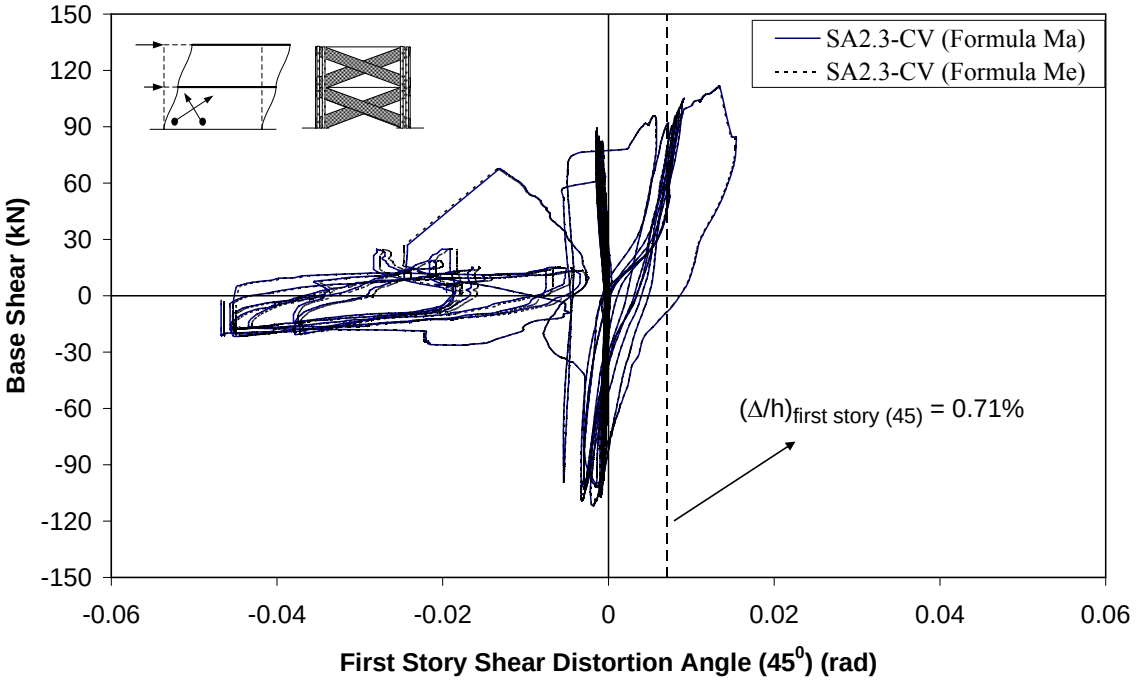

Figure C.17. Base shear versus 1st story shear distortion angle of specimen (45^0) SA2.3-CV

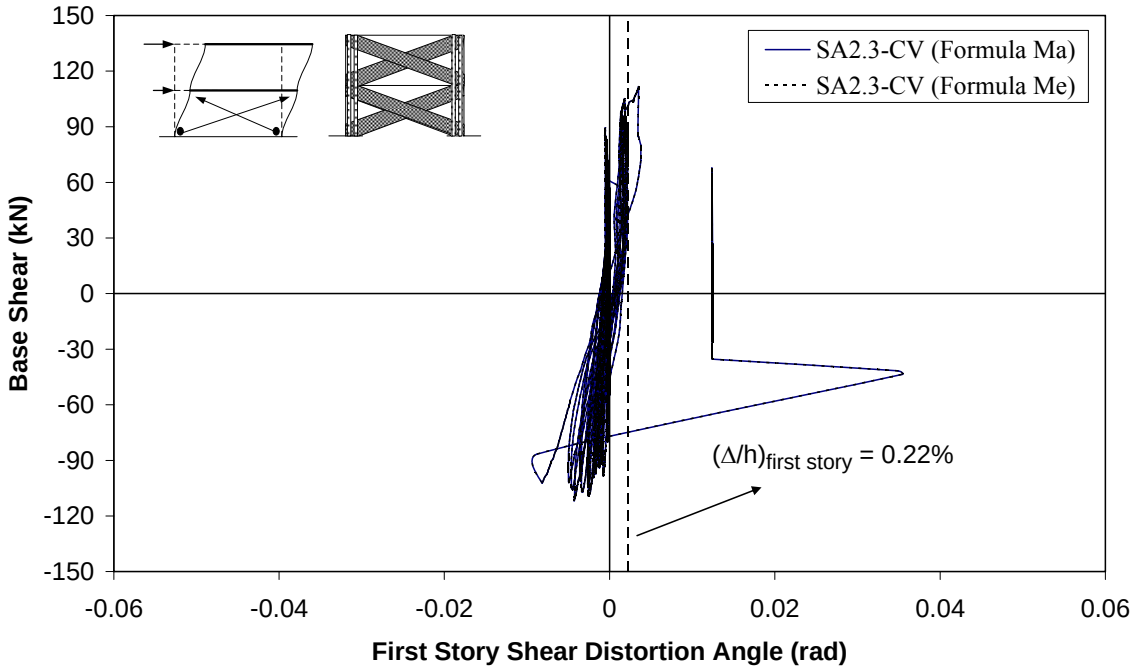

Figure C.18. Base shear versus 1st story shear distortion angle of specimen SA2.3-CV

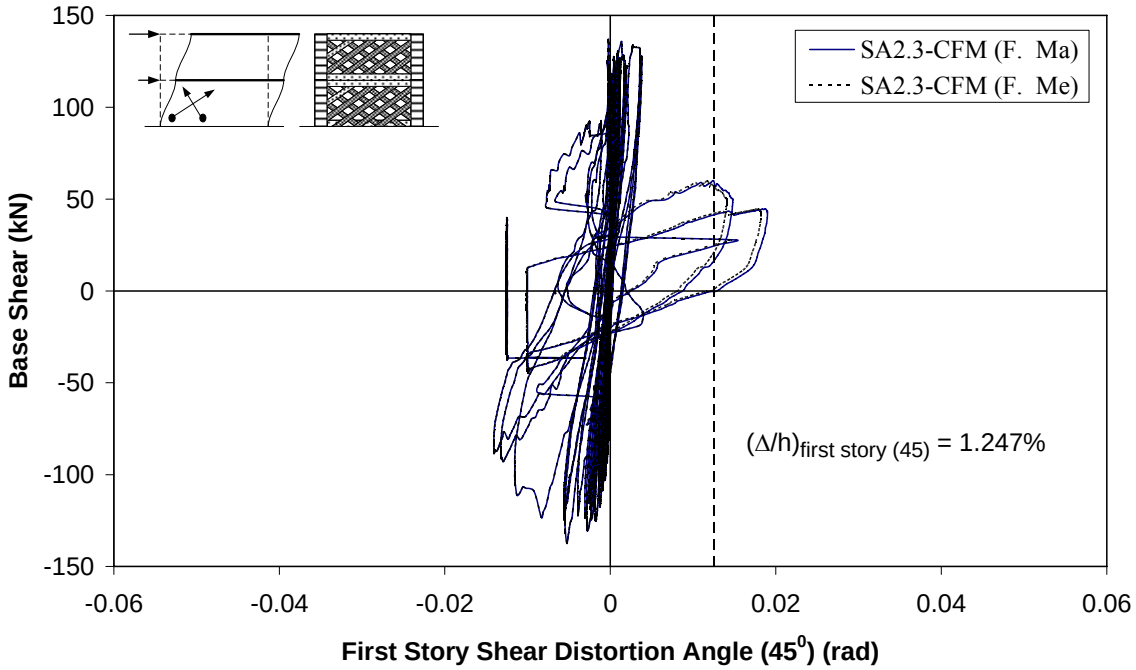

Figure C.19. Base shear versus 1st story shear distortion angle (45^0) of specimen SA2.3-CFM

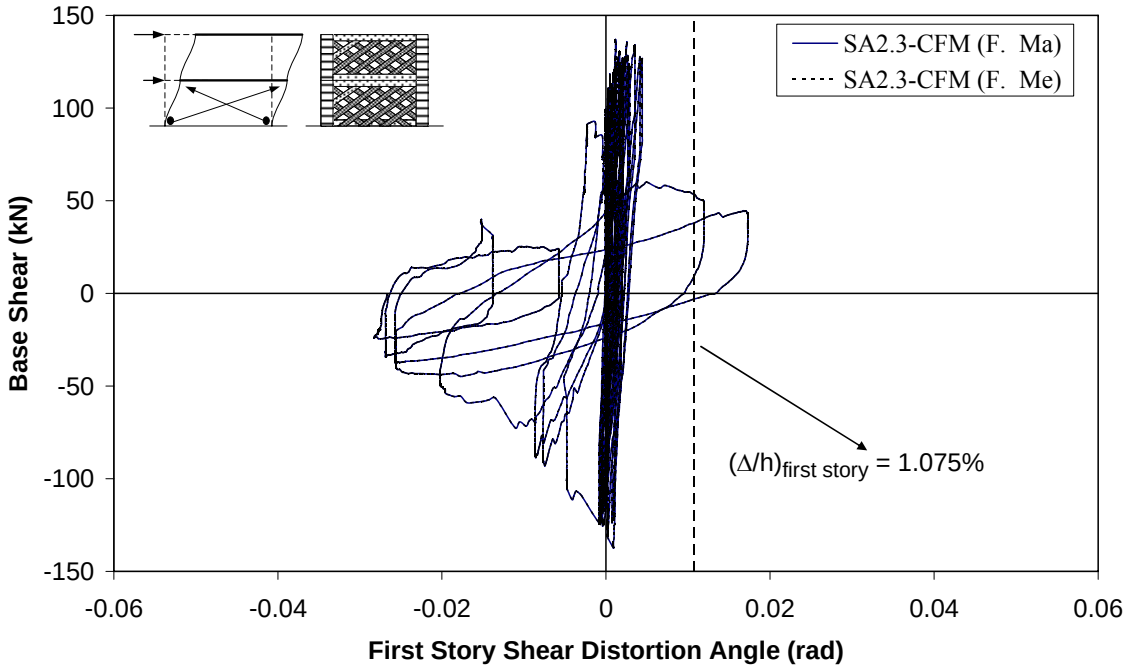

Figure C.20. Base shear versus 1st story shear distortion angle of specimen SA2.3-CFM

REFERENCES

1. Tomazeviç, M., *Earthquake-Resistant Design of Masonry Buildings*, Imperial College Press, 2000.

2. Paulay, T. and M.J.N. Priestley, *Seismic Design of Reinforced Concrete and Masonry Buildings*, John Wiley, New York, 1992.

3. Mehrabi, A.B., P.B. Shing, M.P Schuller and J.L Noland, "Experimental Evaluation of Masonry-Infilled RC Frames", *ASCE Journal of Structural Engineering*, Vol. 122, No. 3, pp. 228-237, March 1996.

4. Chamber of Civil Engineers, *Engineering Reports of Marmara and Duzce Earthquakes*, Minpa Press, Ankara, 2000.

5. Wallace, J.W., "Building Performance in the 17 August 1999 Izmit, Turkey Earthquake", *Los Angeles Tall Building Conference*, May 2000.

6. Specification for the Structures to be Built in Disaster Regions (Turkish Seismic Code), Ministry of Public Works and Settlement, Ankara, 1998.

7. Specification for the Structures to be Built in Disaster Regions (Turkish Seismic Code), Ministry of Public Works and Settlement, Ankara, 2007.

8. Bracci, J.M., A.M. Reinhorn and J.B. Mander, "Seismic Retrofit of Reinforced Concrete Buildings Designed for Gravity Loads: Performance of Structural Model", *ACI Structural Journal*, Vol. 92, No. 6, pp. 711-723, November-December 1995.

9. El-Attar, A.G., R.N. White and P. Gergely, "Behavior of Gravity Load Designed Reinforced Concrete Buildings Subjected to Earthquakes", *ACI Structural Journal*, Vol. 94, No. 2, pp. 133-145, March-April 1997.

10. Sezen, H. and J.P. Moehle, "Seismic Tests of Concrete Columns with Light Transverse Reinforcement", *ACI Structural Journal*, Vol. 103, No. 6, pp. 842-849, November-December 2006.

11. Valluvan, R., M.E. Kreger and J.O. Jirsa, "Strengthening of Column Splices for Seismic Retrofit of Nonductile Reinforced Concrete Frames", *ACI Structural Journal*, Vol. 90, No. 4, pp. 432-440, July-August 1993.

12. Hassan, A.F. and M.A. Sozen, "Seismic Vulnerability Assessment of Low-Rise Buildings in Regions with Infrequent Earthquakes", *ACI Structural Journal*, Vol. 94, No. 1, pp. 31-39, January-February 1997.

13. Gulkan, P. and M.A. Sozen, "Procedure for Determining Seismic Vulnerability of Building Structures", *ACI Structural Journal*, Vol. 96, No. 3, pp. 336-342, May-June 1999.

14. Ozcebe, G., M. S. Yucemen, A. Yakut and V. Aydogan, *Seismic Vulnerability Assessment Procedure for Low to Medium Rise Reinforced Concrete Buildings*, Technical Report 2003/2, October 2003.

15. Canbay, E., U. Ersoy and G. Ozcebe, "Contribution of Reinforced Concrete Infills to Seismic Behavior of Structural Systems", *ACI Structural Journal*, Vol. 100, No. 5, pp. 637-643, September-October 2003.

16. Benjamin, J.R. and H.A. Williams, "The Behavior of One-Story Brick Shear Walls", *ASCE Journal of the Structural Division*, Vol. 84, No. ST4, paper 1723, July 1958.

17. Holmes, M., "Steel Frames with Brickwork and Concrete Infilling", *Proceedings of the Institute of Civil Engineers*, Vol. 19, August 1961, pp. 473-478.

18. Holmes, M., "Combined Loading on Infilled Frames", *Proceedings of the Institute of Civil Engineers*, Vol. 25, pp. 31-38, 1963.

19. Smith, B.S., "Lateral Stiffness of Infilled Frames", *ASCE Journal of the Structural Division*, Vol. 88, No. ST6, pp. 183-199, December 1962.

20. Smith, B.S., "Behavior of Square Infilled Frames", *ASCE Journal of the Structural Division*, Vol. 92, No. ST1, pp. 381-403, February 1966.

21. Mallick, D.V. and R.T. Severn, "The Behavior of Infilled Frames Under Static Loading", *Proceedings of the Institute of Civil Engineers*, Vol. 38, pp. 639-656, September/December 1967.

22. Mallick, D.V. and R.T. Severn, "Dynamic Characteristics of Infilled Frames", *Proceedings of the Institute of Civil Engineers*, Vol. 39, pp. 261-289, January/April 1968.

23. Smith, B.S. and C. Carter, "A Method of Analysis for Infilled Frames", *Proceedings of the Institute of Civil Engineers*, Vol. 44, Part 2, pp. 31-48, 1969.

24. Liauw, T.C., "Elastic Behavior of Infilled Frames", *Proceedings of the Institute of Civil Engineers*, Vol. 46, pp. 343-349, 1970.

25. Ersoy, U and S. Uzsoy, *The Behavior and Strength of Infilled Frames*, Report No. MAG 205 Tubitak, Ankara, Turkey, 1971 (In Turkish).

26. Mallick, D.V. and R.P. Garg, "Effect of Openings on the Lateral Stiffness of Infilled Frames", *Proceedings of the Institute of Civil Engineers*, Vol. 49, pp. 193-209, June 1971.

27. Mainstone, R.J., "On the Stiffness and Strength of Infilled Frames" *Proceedings of the Institute of Civil Engineers*, Vol. 49, Supplementary Paper 7360S, pp. 57-90, 1971.

28. Liauw, T.C. and S.W. Lee, "On the Behavior and the Analysis of Multi-Storey Infilled Frames Subjected to Lateral Loading", *Proceedings of the Institute of Civil Engineers*, Vol. 63, Part 2, pp. 641-656, September 1977.

29. Wood, R.H., "Plasticity, Composite Action and Collapse Design of Unreinforced Shear Wall Panels in Frames", *Proceedings of the Institute of Civil Engineers*, Vol. 65, Part 2, pp. 381-411, June 1978.

30. Klingner, R.E. and V.V. Bertero, "Earthquake resistance of Infilled Frames", *ASCE Journal of the Structural Division*, Vol. 104, No. ST6, pp. 973-989, June 1978.

31. Kahn, L.F. and R.D. Hanson, "Infilled Walls for Earthquake Strengthening", *ASCE Journal of the Structural Division*, Vol. 105, No. ST2, pp. 283-296, February 1979.

32. Liauw, T.C., "Tests on Multistory Infilled Frames Subjected to Dynamic Lateral Loading", *ACI Structural Journal*, Vol. 76, No. 4, pp. 551-563, April 1979.

33. Bertero, V. and S. Brokken, "Infills in Seismic Resistant Building", *ASCE Journal of Structural Engineering*, Vol. 109, No. 6, pp. 1337-1361, June 1983.

34. Liauw, T.C. and K.H. Kwan, "Nonlinear Behavior of Non-integral Infilled Frames", *Computers and Structures*, Vol. 18, No. 3, pp. 551-560, 1984.

35. Liauw, T.C. and K.H. Kwan, "Plastic Design of Infilled Frames" *Proceedings of the Institute of Civil Engineers*, Vol. 77, Part 2, pp. 367-377, September 1984.

36. Liauw, T.C. and K.H. Kwan, "Unified Plastic Analysis for Infilled Frames", *ASCE Journal of Structural Engineering*, Vol. 111, No. 7, pp. 1427-1448, July 1985.

37. Liauw, T.C. and C.Q. Lo, "On Multibay Infilled Frames" *Proceedings of the Institute of Civil Engineers*, Vol. 85, Part 2, pp. 469-483, September 1988.

38. Liauw, T.C. and K.H. Kwan, "Non-linear Analysis of Multistorey Infilled Frames" *Proceedings of the Institute of Civil Engineers*, Vol. 73, Part 2, pp. 441-454, June 1982.

39. Altın, S., U. Ersoy and T. Tankut, "Hysteretic Response of Reinforced Concrete Infilled Frames", *ASCE Journal of Structural Engineering*, Vol. 118, No. 8, pp. 2133-2150, August 1992.

40. Marjani, F., *Behavior of Brick Infilled Reinforced Concrete Frames Under Reversed Cyclic Loading*, Ph.D. Thesis, Department of Civil Engineering, Middle East Technical University, September 1997.

41. Mosalam, K.M., R.N. White and P. Gergely, "Static Response of Infilled Frames Using Quasi-static Experiments", *ASCE Journal of Structural Engineering*, Vol. 123, No. 11, pp. 1462-1469, November 1997.

42. Schneider, S.P., B.R. Zagers and D.P. Abrams, "Lateral Strength of Steel Frames With Masonry Infills Having Large Openings", *ASCE Journal of Structural Engineering*, Vol. 124, No. 8, pp. 896-904, August 1998.

43. Turk, A.M., *Rehabilitation of Reinforced Concrete Frames by Reinforced Concrete Infills*, Ph.D. Thesis, Department of Civil Engineering, Bogazici University, 1998.

44. Chaker, A.A and A. Cherifati, "Influence of Masonry Infill Panels on the Vibration and Stiffness Characteristics of RC Frame Buildings", *Earthquake Engineering and Structural Dynamics*, Vol. 28, pp. 1061-1065, 1999.

45. Flanagan, R.D. and R.M. Bennett, "In-Plane Behavior of Structural Clay Tile Infilled Frames" , *ASCE Journal of Structural Engineering*, Vol. 125, No. 6, pp. 590-599, June 1999.

46. Seah, C.K., *A Universal Approach for the Analysis and Design of Masonry Infilled Frame Structures*, Ph.D. Thesis, Graduate Academic Unit of Civil Engineering, University of New Brunswick, December 1998.

47. Al-Chaar, G., M. Issa and S. Sweeney, "Behavior of Masonry-Infilled Nonductile Reinforced Concrete Frames", *ASCE Journal of Structural Engineering*, Vol. 128, No. 8, pp. 1055-1063, August 2002.

48. Asteris, P.G., "Lateral Stiffness of Brick Masonry Infilled Plane Frames" , *ASCE Journal of Structural Engineering*, Vol. 129, No. 8, pp. 1071-1079, August 2003.

49. Sonuvar, M.O., G. Ozcebe and U. Ersoy, "Rehabilitation of Reinforced Concrete Frames with Reinforced Concrete Infills" *ACI Structural Journal*, Vol. 101, No. 4, pp. 494-500, July-August 2004.

50. Sonuvar, M.O., *Hysteretic Response of Reinforced Concrete Frames Repaired by Means of Reinforced Concrete Infills*, Ph.D. Thesis, Department of Civil Engineering, Middle East Technical University, June 2001.

51. Kara, M.E. and S. Altin, "Behavior of Reinforced Concrete Frames with Reinforced Concrete Partial Infills", *ACI Structural Journal*, Vol. 103, No. 5, pp. 701-709, September-October 2006.

52. Singh, H., D.K. Paul and V.V. Sastry, "Inelastic Dynamic Response of Reinforced Concrete Infilled Frames", *Computers and Structures*, Vol. 69, pp. 685-693, 1998.

53. Ghosh, A.K. and A.M. Amde, "Finite Element Analysis of Infilled Frames", *ASCE Journal of Structural Engineering*, Vol. 128, No. 7, pp. 881-889, July 2002.

54. Dhanasekar, M. and A.W. Page, "The Influence of Brick Masonry Infill Properties on the Behavior of Infilled Frames", *Proceedings of the Institute of Civil Engineers*, Vol. 81, Part 2, pp. 593-605, December 1986.

55. Neuenhofer, A., "Lateral Stiffness of Shear Walls with Openings", *ASCE Journal of Structural Engineering*, Vol. 132, No. 11, pp. 1846-1851, November 2006.

56. Cofer, W.F., *Documentation of Strengths and Weaknesses of Current Computer Analysis Methods for Seismic Performance of Reinforced Concrete Members*, Technical Report PEER-99-07, University of California, Berkeley.

57. Zarnic, R., "Modelling of Response of Masonry Infilled Frames", *10th European Conference on Earthquake Engineering*, Duma, pp. 1481-1486, 1995.

58. Madan, A., A.M. Reinhord, J.B. Mander and R.E. Valles, "Modeling of Masonry Infill Panels for Structural Analysis", *ASCE Journal of Structural Engineering*, Vol. 123, No. 10, pp. 1295-1302, October 1997.

59. El-Dakhakhni, W.W., M. Elgaaly and A.A. Hamid, "Three-Strut Model for Concrete Masonry-Infilled Steel Frames", *ASCE Journal of Structural Engineering*, Vol. 129, No. 2, pp. 177-185, February 2003.

60. Christensen, J.B., J. Gilstrap and C.W. Dolan, "Composite Materials Reinforcement of Existing Masonry Walls", *ASCE Journal of Architectural Engineering*, Vol. 2, No. 2, pp. 63-70, June 1996.

61. Marshall, Jr., O.S., S.C. Sweeney and J.C. Trovilion, *Performance Testing of Fiber-Reinforced Polymer Composite Overlays for Seismic Rehabilitation of Unreinforced Masonry Walls,* U.S. Army Construction Engineering Research Laboratories (USACERL), Technical Report 00/18, June 2000.

62. Ehsani, M.R., H. Saadatmanesh and A. Al-Saidy, "Shear Behavior of URM Retrofitted with FRP Overlays", *ASCE Journal of Composites for Construction*, Vol. 1, No. 1, pp. 17-25, February 1997.

63. Triantafillou, T.C., "Strengthening of Masonry Structures Using Epoxy-Bonded FRP Laminates", *ASCE Journal of Composites for Construction*, Vol. 2, No. 2, pp. 96-104, May 1998.

64. Kolsch, H., "Carbon Fiber Cement Matrix (CFCM) Overlay System for Masonry Strengthening", *ASCE Journal of Composites for Construction*, Vol. 2, No. 2, pp. 105-109, May 1998.

65. Velazquez-Dimas, J.I., M.R. Ehsani and H. Saadatmanesh, "Out of Plane Behavior of Brick Masonry Walls Strengthened with Fiber Composites", *ACI Structural Journal*, Vol. 97, No. 3, pp. 377-387, May-June 2000.

66. Velazquez-Dimas, J.I. and M.R. Ehsani, "Modeling Out of Plane Behavior of URM Walls Retrofitted with Fiber Composites", *ASCE Journal of Composites for Construction*, Vol. 4, No. 4, pp. 172-181, November 2000.

67. Albert, M.L., A.E. Elwi and J.J.R. Cheng, "Strengthening of Unreinforced Masonry Walls Using FRPs", *ASCE Journal of Composites for Construction*, Vol. 5, No. 2, pp. 76-84, May 2001.

68. Hamilton, H.R. III and C.W. Dolan, "Flexural Capacity of Glass FRP Strengthened Concrete Masonry Walls", *ASCE Journal of Composites for Construction*, Vol. 5, No. 3, pp. 170-178, August 2001.

69. Valluzzi, M.R., D. Tinazzi and C. Modena, "Shear Behavior of Masonry Panels Strengthened by FRP Laminates", *Construction and Building Materials*, Vol. 16, pp. 409-416, 2002.

70. Hanoglu, K.B., *Fiber Reinforced Plastic Overlay Retrofit of Hollow Clay Tile Masonry Infilled Reinforced Concrete Frames*, Ph.D. Dissertation, Department of Civil Engineering, Bogazici University, 2002.

71. Akguzel, U., *Seismic Retrofit of Brick Infilled RC Frames with Lap Splice Problem In Columns*, M.S. Thesis, Department of Civil Engineering, Bogazici University, 2003.

72. Ozcebe, G., U. Ersoy, T. Tankut, E. Erduran, O. Keskin and H.C. Mertol, *Strengthening of Brick-Infilled RC Frames with CFRP*, Technical Report, 2003/1, Middle East Technical University, Ankara.

73. Stratford, T., G. Pascale, O. Manfroni and B. Bonfiglioli, "Shear Strengthening Masonry Panels with Sheet Glass-Fiber Reinforced Polymer", *ASCE Journal of Composites for Construction*, Vol. 8, No. 5, pp. 434-443,October 2004.

74. El-Dakhakhni, W.W., A.A. Hamid and M. Elgaaly, "Seismic Retrofit of Concrete-Masonry-Infilled Steel Frames with Glass Fiber-Reinforced Polymer Laminates", *ASCE Journal of Structural Engineering*, Vol. 130, No. 9, pp. 1343-1352, September 2004.

75. Yuksel, E., A. Ilki, G. Erol, C. Demir and H. F. Karadogan, "Seismic Retrofit of Infilled Reinforced Concrete Frames With CFRP Composites", *Advances in Earthquake Engineering for Urban Risk Reduction,* S.T. Wasti and G. Ozcebe (editors), pp. 285-300, Springer, Amsterdam, Netherlands, 2006.

76. Erdem, I., U.Akyuz, U. Ersoy and G. Ozcebe, "An Experimental Study on Two Different Strengthening Techniques for RC Frames", *Engineering Structures*, Vol. 28, pp. 1843-1851, 2006.

77. ElGawady, M.A., P. Lestuzzi and M. Badoux, "Static Cyclic Response of Masonry Walls Retrofitted with Fiber-Reinforced Polymers", *ASCE Journal of Composites for Construction*, Vol. 11, No. 1, pp. 50-61, February 2007.

78. Erdik, M., *Report on 1999 Kocaeli and Düzce (Turkey) Earthquakes*, www.koeri.edu.tr/depremmuh/eqspecials/kocaeli/kocaelireport.pdf, 1999.

79. Ellul F. and Dina D'ayala, *The Bingol, Turkey Earthquake of the 1st of May 2003*, www.istructe.org/eefit/files/BingolFieldReport.pdf, 2003.

80. Scrawthorn, C., *Earhquakes of 1999-Issues for Catastrophe Risk Management,* www.iiasa.ac.at/Research/RMS/july2000/papers/scawthorn.pdf, July 2000.

81. Harris, H.G. and Gajanan M. Sabnis, *Structural Modelling and Experimental Techniques*, CRC Press LLC, Florida, 1999.

82. American Society for Testing and Materials, ASTM C39-96, *Standard Test Method for Compressive Strength of Cylindrical Concrete Specimens*, Annual Book of ASTM Standards, Vol. 04.02, West Conshohocken, Pennsylvania.

83. American Society for Testing and Materials, ASTM C496-96, *Standard Test Method for Splitting Tensile Strength of Cylindrical Concrete Specimens*, Annual Book of ASTM Standards, Vol. 04.02, West Conshohocken, Pennsylvania.

84. American Society for Testing and Materials, ASTM-A706/A706M-06a, *Standard Specification for Low-Alloy Steel Deformed and Plain Bars for Concrete Reinforcement*, Annual Book of ASTM Standards, West Conshohocken, Pennsylvania.

85. American Society for Testing and Materials, ASTM C109/C109M-95, *Standard Test Method for Compressive Strength of Hydraulic Cement Mortars*, Annual Book of ASTM Standards, Vol. 04.01, West Conshohocken, Pennsylvania.

86. American Society for Testing and Materials, ASTM E447-97, *Standard Test Method for Compressive Strength of Laboratory Constructed Masonry Prisms*, Annual Book of ASTM Standards, Vol. 04.05, West Conshohocken, Pennsylvania.

87. Angel, R. E., *Behavior of Reinforced Concrete Frames with Masonry Infill Walls*, Ph.D. Thesis, Department of Civil Engineering, University of Illinois at Urbana Champaign, 1994.

88. ACI 440R-96, *State of the Art Report on Fiber Reinforced Plastic (FRP) Reinforcement for Concrete Structures,* ACI Commitee 440, American Concrete Institute, 1996.

89. Özdemir, G. *Mechanical Properties of CFRP Anchorages*, M.S. Thesis, Department of Civil Engineering, Middle East Technical University, January 2005.

90. Massone, L.M. and J.W. Wallace, "Load Deformation Responses of SlenderReinforced Concrete Walls", *ACI Structural Journal*, Vol. 101, No. 1, pp. 103-113, January-February 2004.

91. Melek, M., J.W. Wallace and J.P. Conte, *Experimental Assessment of Columns with Short Lap Splices Subjected to Cyclic Loads*, PEER Report 2003/04, College of Engineering, University of California, Berkeley, April 2003

92. ACI T1.1-01, *Acceptance Criteria for Moment Frames Based on Structural Testing,* American Concrete Institute, Michigan, 2001.

93. UBC, "Uniform Building Code: Vol. 2, Structural Engineering Design Provisions", *International Conferences of Building Officials*, Whittier, California, 1997.

94. TS500, *Requirements for Design and Construction of Reinforced Concrete Structures,* Turkish Stndard Institute, 2000.

95. FEMA 356, *Pre-standard And Commentary For The Seismic Rehabilitation Of Buildings*, American Society Of Civil Engineers, Reston, November 2000.

96. Beres, A.B., *Experimental and Analytical Study of the Performance of Reinforced Concrete Frames with Non-Ductile Details*, Ph.D. Dissertation, Cornell University, 1994.

97. Ersoy, U., G. Ozcebe and T. Tankut, *Reinforced Concrete*, Middle East Technical University, Ankara, 2006.

98. Hakam, Z. H-R., *Retrofit of Hollow Concrete Masonry Infilled Steel Frames Using Glass Fiber Reinforced Plastic Laminates*, Ph.D. Dissertation, Drexel University, 2000.

99. Park, R., "Evaluation of Ductility of Structures and Structural Assemblages From Laboratory Resting", *Bulletin of the New Zealand National Society for Earthquake Engineering*, Vol. 22, No:3, pp. 155-166, September 1989.

100. Priestley, M.J.N., and R. Park, "Strength and Ductility of Concrete Bridge Columns Under Seismic Loading", *ACI Structural Journal*, Vol. 84, No. 01, pp.61-76, January-February 1987.

101. Newmark, N.M. and W.J. Hall, "Earthquake Spectra and Design", *Engineering Monograph*, Earthquake Engineering Research Institute, Berkeley, California, 1982.

102. Tomazeviç, M., M. Lutman and L. Petkoviç, "Seismic Behavior of Masonry Walls: Experimental Simulation" *ASCE Journal of Structural Engineering*, Vol. 122, No. 9, pp. 1040-1047, September 1996.

103. Altın, S., U. Ersoy and T. Tankut, *Seismic Strengthening of Reinforced Concrete Frames With Reinforced Concrete Infills*, Report No. METU/SML-90/01,Ankara, June 1990.

104. Atmaca, S., Strengthening of Reinforced Concrete Beams Using Externally Bonded FRP Plates, M.S. Thesis, Dept. of Civil Engineering, Boğazici University, 2001.

105. Chopra, A.K., *Dynamics of Structures,* Prentice-Hall, New Jersey, 2001.

106. Mosalam, K.M., *Experimental and Computational Strategies for the Seismic Behavior Evaluation of Frames with Infill Walls*, Ph.D. Dissertation, Cornell University, 1996.

107. Mehrabi, A.B. and P.B. Shing, "Finite Element Modeling of Masonry-Infilled RC Frames", *ASCE Journal of Structural Engineering*, Vol. 123, No. 5, pp. 604-613, May 1997.

108. Cavaleri, L., M. Fossetti and M. Papia, "Infilled Frames: Developments in the Evaluation of Cyclic Behavior Under Lateral Loads", *Structural Engineering and Mechanics*, Vol. 21, No.4, pp. 469-494, 2005.

109. Klingner, R.E. and V.V. Bertero, *Infilled Frames in Earthquake-Resistant Construction*, Technical Report, EERC 76-32, December 1976, University of California Berkeley, California.

110. Al-Chaar, G.K. and G.E. Lamb, *Design of Fiber Reinforced Polymer Materials for Seismic Rehabilitation of Infilled Concrete Structures*, Technical Report, US Army Corps of Engineers, Technical Report, ERDC/CERL TR-02-33, December 2002.

111. Polyakov, S.V., "On the Interaction Between Masonry Filler Walls and Enclosing Frame When Loaded in Plane of the Wall", *Translation in Earthquake Engineering, Earthquake Engineering Research Institute,* San Francisco, CA, pp. 36-42, 1960.

112. Hendry A.W., *Structural Masonry,* Macmillan, 1990.

113. Drysdale, R. G., A.A. Hamid and L. R.Baker, *Masonry Structures: Behavior and Design*, The Masonry Society, Colorado, 1999.

114. Dawe, J.L. and C.K. Seah, "Behavior of Masonry Infilled Steel Frames", *Canadian Journal of Civil Engineering*, Vol. 16, 1989.

115. Durrani, A.J. and Y.H. Luo, *Seismic Retrofit of Flat-Slab Buildings With Masonry Infills,* NCEER Workshop on Seismic Response of Masonry Walls, Technical Report, NCEER-94-0004, San Francisco, 1994.

116. Perera, R., "Performance Evaluation of Masonry-Infilled RC Frames Under Cyclic Loading Based on Damage Mechanics", *Engineering Structures*, Vol. 27, pp. 1278-1288, 2005.

117. Combescure, D., "Some Contributions of Physical and Numerical Modeling to the Assessment of Existing Masonry Infilled RC Frames Under Extreme Loading", *1st European Conference on Earthquake Engineering and Seismology*, Paper No:370, Geneva, Switzerland, September 2006.

118. Buonopane, S.G. and R.N. White, "Pseudodynamic Testing of Masonry Infilled Reinforced Concrete Frame", *ASCE Journal of Structural Engineering,* Vol. 125, No. 6, pp. 578-589, June 1999.

119. Saneinejad, A. and B. Hobbs, "Inelastic Design of Infilled Frames", *ASCE Journal of Structural Engineering,* Vol. 121, No. 4, pp. 634-650, April 1995.

120. Binici, B., G. Ozcebe and R. Ozcelik, "Analysis and Design of FRP Composites for Seismic Retrofit of Infill Walls in Reinforced Concrete Frames", *Composites: Part B,* Vol. 38, pp. 575-583, 2007.

121. Binici, B. and G. Ozcebe, "Seismic Evaluation of Infilled Reinforced Concrete Frames Strengthened with FRPs", *Proceedings of the 8th U.S. National Conference on Earthquake Engineering,* Paper No:1717, San Francisco, 2006.

122. Priestley, M.J.N., F. Seible and G.M. Calvi, *Seismic Design and Retrofit of Bridges,* John Wiley and Sons, New York, 1996.

123. SAP2000 v10.0.1, Structural Analysis Program, Computers and Structures, Inc., Berkeley.

124. XTRACT, *Cross-sectional Structural Analysis of Components,* Imbsen Software Systems, 2006

125. Cosenza, E., G. Manfredi and G.M. Verderame, "A Fibre Model for Push-over Analysis of Underdesigned Reinforced Concrete Frames", *Computers and Structures*, Vol. 84, pp. 904-916, 2006.

126. Mostafaei, H. and T. Kabeyasawa, "Effect of Infill Masonry Walls on the Seismic Response of Reinforced Concrete Buildings Subjected to the 2003 Bam Earthquake Strong Motion: A Case Study of Bam Telephone Center", *Bull. Earthq. Res. Inst.*, University of Tokyo, Vol. 79, pp. 133-156, 2004.

127. El-Dakhakhni, W.W., *Experimental and Analytical Seismic Evaluation of Concrete Masonry-Infilled Steel Frames Retrofitted Using GFRP Laminates*, Ph.D. Dissertation, Drexel University, 2002.

128. Marshall, O.S., S.C. Sweeney and J.C. Trovillion, *Performance Testing of Fiber-Reinforced Polymer Composite Overlays for Seismic Rehabilitation of Unreinforced Masonry Walls*, Technical Report, US Army Corps of Engineers, ERDC/CERL TR-00-18, June 2000.

129. FEMA 306, *Evaluation of Earthquake Damaged Concrete and Masonry Wall Buildings*, Applied Technology Council, Redwood City, California, 1998.